



THE HONG KONG  
POLYTECHNIC UNIVERSITY

香港理工大學

Pao Yue-kong Library

包玉剛圖書館

---

## Copyright Undertaking

This thesis is protected by copyright, with all rights reserved.

**By reading and using the thesis, the reader understands and agrees to the following terms:**

1. The reader will abide by the rules and legal ordinances governing copyright regarding the use of the thesis.
2. The reader will use the thesis for the purpose of research or private study only and not for distribution or further reproduction or any other purpose.
3. The reader agrees to indemnify and hold the University harmless from and against any loss, damage, cost, liability or expenses arising from copyright infringement or unauthorized usage.

### IMPORTANT

If you have reasons to believe that any materials in this thesis are deemed not suitable to be distributed in this form, or a copyright owner having difficulty with the material being included in our database, please contact [lbsys@polyu.edu.hk](mailto:lbsys@polyu.edu.hk) providing details. The Library will look into your claim and consider taking remedial action upon receipt of the written requests.

**INTERLAYER ENGINEERING AND SURFACE  
MODIFICATION OF  $Ti_3C_2T_x$  MXENE FOR HIGH-  
PERFORMANCE SUPERCAPACITORS**

**LI HAO**

**PhD**

**The Hong Kong Polytechnic University**

**2023**

**The Hong Kong Polytechnic University**

**Department of Applied Physics**

**Interlayer engineering and surface modification of  
 $\text{Ti}_3\text{C}_2\text{T}_x$  MXene for high-performance  
supercapacitors**

**LI Hao**

**A thesis submitted in partial fulfilment of the requirements for the  
degree of Doctor of Philosophy**

**December 2022**

## **CERTIFICATE OF ORIGINALITY**

I hereby declare that this thesis is my own work and that, to the best of my knowledge and belief, it reproduces no material previously published or written, nor material that has been accepted for the award of any other degree or diploma, except where due acknowledgement has been made in the text.

\_\_\_\_\_ **Signed**

**LI Hao** \_\_\_\_\_ **Name of student**



## Abstract

Pseudocapacitors are a kind of promising energy storage devices due to simultaneous possession of high-power densities, high energy densities and robust cyclic stability. Their energy storage behaviors and ability are critically determined by electrode materials that should be redox-active, highly conductive and strong for cycling test.  $\text{Ti}_3\text{C}_2\text{T}_x$  MXene has aroused an upsurge of worldwide research on its various applications including energy storage since its discovery in 2011. This novel two-dimensional material exhibits pseudo-capacitance in aqueous acid electrolytes and has metallic conductivity, which make it a good candidate for supercapacitor electrode material. However, its wide application is restricted by the sluggish ion diffusion within the interlayer channel of assembled MXene film, unsatisfactory capacitance, and low oxidation resistance in air. This research is focused on solving the above mentioned issues.

Firstly, the restacking of MXene sheets is inevitable when they are assembled into a freestanding film electrode, which hinders electrolyte ion diffusion to active sites and results in sluggish energy storage kinetics. Herein, the volumetrically expanded ester reaction between ethanol and phosphoric acid is exploited to improve interlayer path within  $\text{Ti}_3\text{C}_2\text{T}_x$  film. These two kinds of molecules jointly intercalate into interlayer space of  $\text{Ti}_3\text{C}_2\text{T}_x$  film and then react to produce phosphate under heating, leading to molecular scale expanded but uniform interlayer gallery. The optimized film shows enhancement in both gravimetric and volumetric capacitances along with better rate capability. It exhibits a capacitance of  $297 \text{ F g}^{-1}/965 \text{ F cm}^{-3}$  at  $2 \text{ mV s}^{-1}$  and retains  $108 \text{ F g}^{-1}/300 \text{ F cm}^{-3}$  at  $200 \text{ mV s}^{-1}$ , which are greatly superior to those of the pristine film without the treatments. The assembled symmetric and asymmetric supercapacitors with optimized film structure can deliver an energy density of  $6.33$  and  $7 \text{ Wh Kg}^{-1}$ ,



respectively. This work demonstrates a novel yet simple method to ameliorate restacking of MXene sheets for its better supercapacitor application.

Secondly,  $\text{Ti}_3\text{C}_2\text{T}_x$  MXene is regarded as a promising supercapacitor electrode material due to its high conductivity and pseudocapacitive nature. Its capacitance can be improved via nitrogen or sulfur heteroatom doping due to the ability to donate surface electrons. Phosphorus possesses a lower electronegativity than nitrogen and sulfur so that it is believed to enable greater performance enhancement once being doped. Herein, phosphorus is incorporated onto  $\text{Ti}_3\text{C}_2\text{T}_x$  to boost its electrochemical performance and the underlying enhancement mechanism is revealed. The results show that doped phosphorus exists with the formation of Ti-O-P terminations on MXene surface, and 2.1 at. % P-doped  $\text{Ti}_3\text{C}_2\text{T}_x$  delivers a capacitance enhancement of 30% ( $328 \text{ F g}^{-1}$  at  $2 \text{ mV s}^{-1}$ ) in comparison with pristine MXene and outstanding cyclic stability, comparable to N- and S-doped MXene. Multiple *in situ* and *ex situ* characterization methods along with DFT calculations collectively reveal that the formed Ti-O-P species are new active sites for a two-proton bonding-debonding process, contributing to the enhanced charge storage and capacitive performance in MXene. However, higher surface phosphorus doping would destroy crystal integrity of MXene and leads to performance deterioration.

Finally,  $\text{Ti}_3\text{C}_2\text{T}_x$  MXene delivers high pseudo-capacitance in acid solution via surface -O terminations bonding with protons. Numerous efforts have been devoted to engineer more -O for improved charge storage or expand interlayer gallery of MXene to boost ion intercalation. However, narrow interlayer space favors proton transport with Grotthuss mechanism and strengthens the interaction between intercalated protons and material interface, which is commonly neglected in optimizing MXene supercapacitive performance. Herein, a novel strategy combining surface modification and interlayer shrinkage of MXene is proposed to boost its energy storage ability. The modified



MXene is rich in -O surface groups along with substantial removal of detrimental -F species, and the interlayer space becomes narrower than its pristine counterpart. It exhibits not only a high capacitance of  $375 \text{ F g}^{-1}$  ( $338 \text{ C g}^{-1}$ ), but also much enhanced oxidation resistance and excellent cyclic stability. Multiple *in situ* and *ex situ* characterization results reveal that only monolayer interstitial water is formed during its charge/discharge process, which boosts proton transport into interlayer space and strengthens host-ion interaction, contributing to the charge storage. And the rich oxygen groups are responsible for its superior oxidation resistance. The assembled asymmetric supercapacitor with modified MXene and Prussian blue analogue can deliver a high energy density of  $19.7 \text{ Wh Kg}^{-1}$ . This work proposes a novel strategy to simultaneously enhance the energy storage capability and oxidation resistance of MXene for supercapacitor applications.



## List of publications

### Published papers

1. **Hao Li**, Hanmo Zhou, Lyuchao Zhuang, Tiancheng Liu, Wei Han, and Haitao Huang. **2022**. Enhanced Ion Diffusion in Flexible  $Ti_3C_2T_x$  MXene Film for High-Performance Supercapacitors, *Advanced Energy and Sustainability Research*, 3: 2100216.
2. Hanmo Zhou, **Hao Li**, Liuqing Li, Tiancheng Liu, Gao Chen, Yanping Zhu, Limin Zhou, and Haitao Huang. **2022**. Structural composite energy storage devices — a review, *Materials Today Energy*, 24: 100924.
3. Hanmo Zhou, Yiyin Su, Jing Zhang, **Hao Li**, Limin Zhou, Haitao Huang. **2023**. A novel embedded all-solid-state composite structural supercapacitor based on activated carbon fiber electrode and carbon fiber reinforced polymer matrix, *Chemical Engineering Journal*, 454:140222.
4. Liuqing Li, Haifa Qiu, Yanping Zhu, Gao Chen, Sixuan She, Xuyun Guo, **Hao Li**, Tiancheng Liu, Zezhou Lin, Hanmo Zhou, Ye Zhu, Ming Yang, Baomin Xu, Haitao Huang, **2023**. 'Atomic ruthenium modification of nickel-cobalt alloy for enhanced alkaline hydrogen evolution', *Applied Catalysis B: Environmental*, 331:122710.
5. Hanmo Zhou, Anchalee Duongthipthewa, Jing Zhang, **Hao Li**, Luwei Peng, Yu Fu Haitao Huang, Limin Zhou, **2023**. A composite structural supercapacitor based on Ni-Co-layered double hydroxide-coated carbon cloth electrodes. *Composites Science and Technology*, 240: 110068.

### Paper in preparation

1. **Hao Li**, Ke Fan, Pei Xiong, Hanmo Zhou, Zezhou Lin, Keyu Tao, Tiancheng Liu, Xuyun Guo, Ye Zhu, Lyuchao Zhuang, Wei Han, Chen Yang, Yan Liu, Chen Yang, Molly Meng-Jung Li, Haitao Huang. ' Grafted phosphorous in  $Ti_3C_2T_x$  MXene as



active site for enhanced charge storage via a two-proton bonding/debonding process' Submitted.

2. **Hao Li**, Jing Zhang, Keyu Tao, ZeZhou Lin, Liuqing Li, Tiancheng Liu, Yunduo Yao, Ye Zhu, Haitao Huang 'Oxygen-rich surface and narrow interlayer space endow  $Ti_3C_2T_x$  MXene with enhanced capacitance and oxidation resistance ability' under preparation.

## Conference presentation

### Oral presentation

1. **Hao Li**, Ke Fan, Hanmo Zhou, Tiancheng Liu, Di Zu, Haitao Huang. 'Grafted phosphorus atoms on  $Ti_3C_2T_x$  MXene providing extra capacitance for improved super capacitive performance' MRS Spring Meeting & Exhibit, May 23-25, **2022**, Virtual, Honolulu, Hawaii, US.



## Acknowledgements

The three-year learning experience in Hong Kong Polytechnic University taught me a lot, and there are too many persons who I need to express sincere appreciation.

First of all, I would express my sincere gratitude to my chief supervisor, Prof. Haitao Huang, for giving me careful and invaluable instruction, which leads me continuous improvements in academics. He always makes his every effort to train me and help me to become an independent researcher. More importantly, his administration offers me a free and flexible atmosphere to conduct research work, making me gradually fall in love with research work and develop a positive but responsible attitude to solve each academic issue. Meanwhile, I admire his approachable and patient personality and regard him as my role model who I want to become in the future. No words can fully express my feeling of appreciation to him. In addition, I would also like to thank Dr. Wing Man Tang for giving me the inestimable opportunity to study and undertake research in PolyU.

I would like to thank my group members, Dr. Yan Liu, Hanmo Zhou, Luwei Peng, Tiancheng Liu, Lu Li, Xinyou Zhang, Zezhou Lin, Liuqing Li, Haifa Qiu, Dr. Dui Ma, Dr. Ke Fan, Dr. Ming Xu, Dr. Shanshan Shi, Zihan Hu, Dr. Sixuan She, Dr. Huilin You for their assistance in my experiments, data discussions and life. I would also express



my special appreciation to some members in the Department of Applied Physics, Dr. Wei Han, Dr. Honfai, Wong, Dr. Sinyi Pang, Dr. Zhen Hou, Dr. Lyuchao Zhuang, Pei Xiong, Dr. Guangchao Li to assist my experiments and give me suggestions how to conduct research work.

Gratitude is also conveyed to my best friends, Dr. Keyu Tao for selflessly sharing his experience on supercapacitors and knowledge about electrochemistry and materials characterization, Dr. Chengguang Lang, Zhihao He, Mingjun Chen for their support. I would also thank my master supervisor, Prof. Wanqi Qiu in South China University of Technology for giving me encouragement to insist academics and life suggestions.

Finally, I would like to thank my respected father Mr. Shuisheng Li, my younger brother Mr. Jun Li for their understanding and support of my study. In the meantime, I would be here thanking my departed mother, Mrs. Mane Li, for her patient but selfless guide, with which I developed positive and responsible attitudes to cope with life difficulties and challenges. I also express my appreciation to my other dear relatives, elder brother Mr. Linfeng Cai, elder sister Mrs. Ailing Li and Mrs. Meihua Zhou for their life assistance and supports.



## Table of contents

Abstract.....	I
List of publications .....	IV
Acknowledgements.....	VI
Table of contents .....	VIII
List of Figures.....	X
List of Tables.....	XVII
Chapter 1 Introduction .....	1
1.1 Background.....	1
1.2 Research motivation and scope.....	7
1.3 Synopsis of thesis.....	12
Chapter 2 Literature review of supercapacitors and MXene for supercapacitor applications.....	15
2.1 Supercapacitors and electrode materials .....	15
2.1.1 Electrical double-layer capacitors (EDLCs).....	16
2.1.2 Pseudocapacitors (PCs).....	24
2.1.3 Hybrid supercapacitors (HCs).....	31
2.2 Inactive components in supercapacitors.....	33
2.2.1 Electrolytes.....	33
2.2.2 Current collectors.....	37
2.2.3 Separators.....	37
2.3 Review of MXenes synthesis methods.....	38
2.3.1 Fluorine-involved liquid etching.....	41
2.3.2 Alkaline etching .....	44
2.3.3 Electrochemical etching.....	46
2.3.4 Molten salt etching.....	48
2.3.5 Other methods.....	51
2.4 $Ti_3C_2T_x$ MXene for the supercapacitor electrode material .....	57
2.4.1 $Ti_3C_2T_x$ MXene energy storage behavior in different electrolyte.....	58
2.4.2 Surface modification to boost performance .....	65
2.4.3 Interlayer engineering of $Ti_3C_2T_x$ MXene.....	69
2.4.4 Porous formation strategy to boost rate capability .....	72
2.3.5 Construction of $Ti_3C_2T_x$ MXene based hybrid for supercapacitors.....	76
2.4 Summary .....	76
Chapter 3 Experiments and characterization methods .....	78
3.1 Experiments for enhanced ion diffusion within flexible $Ti_3C_2T_x$ film for supercapacitors applications .....	79
3.2 Experiments for grafting phosphorus on $Ti_3C_2T_x$ MXene for enhanced supercapacitive performance .....	82
3.3 Experiments for synthesizing $Ti_3C_2T_x$ with oxygen-rich and narrow interlayer space .....	86



Chapter 4 Enhanced ion diffusion in flexible $Ti_3C_2T_x$ MXene film for high performance supercapacitors.....	89
4.1 Introduction.....	90
4.2 Results and discussions.....	93
4.3. Conclusion.....	110
Chapter 5 Unravel boosted supercapacitive performance of $Ti_3C_2T_x$ MXene due to grafted phosphorous atoms.....	111
5.1 Introduction.....	112
5.2 Results and discussions.....	116
5.3 Conclusions.....	143
Chapter 6 Oxygen-rich surface and narrow interlayer space endow $Ti_3C_2T_x$ MXene with enhanced capacitance and oxidation resistance ability.....	145
6.1 Introduction.....	146
6.2 Results and discussions.....	150
6.3 Conclusions.....	179
Chapter 7 Conclusions and Prospect.....	180
7.1 Conclusions.....	180
7.2 Prospects.....	184
References.....	186

## List of Figures

<b>Figure 1.1</b> development course and future of carbon emission around the world. <sup>[1]</sup> .....	2
<b>Figure 1.2</b> Specific power vs. specific energy density (Ragone plot) for various energy storage devices. <sup>[7]</sup> .....	4
<b>Figure 1.3</b> Elements for MXene composition <sup>[24]</sup> .....	6
<b>Figure 2.1</b> Schematic diagram of supercapacitors. <sup>[6]</sup> .....	16
<b>Figure 2.2</b> The development of EDL model. (a) Helmholtz model, (b) Gouy–Chapman model and (c) Stern model. <sup>[8]</sup> .....	17
<b>Figure 2.3</b> (a) CV and (b) GCD curves of EDLCs at different scan rates and current densities. <sup>[49]</sup> .....	19
<b>Figure 2.4</b> (a) Snapshot plot for BMI-PF6 ionic liquid electrolyte between two graphite electrodes at potential of 2V (top), and long-range layered structure due to charge overscreening (middle) is suppressed when adding an organic solvent (bottom). pion, ion density. (b) Formation of a superionic state results from the formation of co-ion pairs when the ionic liquid EMI-TFSI is confined in pores with a comparable size to the electrolyte ions (top). The first solvation shell surrounding an anion involves up to 24% anions without polarization (middle), which leads to increased ion population in the pores (bottom). (c) The charge stored per carbon in nanopores of 3D porous carbons enhances with the decrement of the curvature radius, resulting from stronger or closer interactions between confined ions and the carbon walls. <sup>[7]</sup> .....	23
<b>Figure 2.5</b> Schematic for energy storage mechanism of (a)-(c) Pseudocapacitors with energy storage mechanism of (a) underpotential deposition, (b) fast surface redox reactions, (c) cation intercalation. <sup>[11]</sup> .....	25
<b>Figure 2.6</b> (a), (c) Schematic for a Li-ion capacitor (LIC), which combines a battery-type negative graphite electrode with a positive porous carbon EDLC electrode. (b),(d) Concepts of HCs that pseudocapacitive Nb <sub>2</sub> O <sub>5</sub> or MXene negative electrode with a defective LFP positive electrode. <sup>[7]</sup> .....	32
<b>Figure 2.7</b> Classification of electrolytes for supercapacitors. <sup>[16]</sup> .....	33
<b>Figure 2.8</b> Crystal structure of four common kinds of MXenes. <sup>[156]</sup> .....	39
<b>Figure 2.9</b> (a) the fabrication process of MXene, and (b) the history of fabricating MXene with different methods. ....	41
<b>Figure 2.10</b> (a) HF etching process, <sup>[25]</sup> (b) clay like MXene can be rolled into flexible film, <sup>[154]</sup> (c)surface Ti <sub>3</sub> AlC <sub>2</sub> was etched with NH <sub>4</sub> HF <sub>2</sub> aqueous solution, <sup>[165]</sup> (d) colloidal solution from MILD method can be collected by vacuum filtration, <sup>[167]</sup> (e) MXene was fabricated in NH <sub>4</sub> HF <sub>2</sub> PC solution. <sup>[169]</sup> .....	44
<b>Figure 2.11</b> (a) TMAOH etching mechanism, <sup>[171]</sup> (b)NaOH etching principle <sup>[170]</sup> .....	46
<b>Figure 2.12</b> (a) the electrochemical etching mechanism of Ti <sub>2</sub> AlC in 1M HCl <sup>[172]</sup> , (b) fabrication of Ti <sub>3</sub> C <sub>2</sub> T <sub>x</sub> MXene with electrochemical etching in TMAOH +NH <sub>4</sub> Cl mixed solution, <sup>[173]</sup> (c) the 3D MXene fabricated from electrochemical etching strengthen by	

heating and application. <sup>[174]</sup> In addition, LiCl and LiOH mixed solution can also be used as electrochemical etching liquid to synthesize Ti<sub>3</sub>C<sub>2</sub>T<sub>x</sub> MXene, which also bypass the use of hazardous intercalant. <sup>[176]</sup> ..... 48

**Figure 2.13** (a) etching process of Ti<sub>4</sub>N<sub>3</sub>T<sub>x</sub> in molten LiF + KF + NaF, <sup>[177]</sup> (b) the element replacement of Ti<sub>3</sub>AlC<sub>2</sub> in molten ZnCl<sub>2</sub> and further conversion to Ti<sub>3</sub>C<sub>2</sub>Cl<sub>2</sub> MXene<sup>[179]</sup>, (c) (d) Ti<sub>3</sub>SiC<sub>2</sub> was etched in molten CuCl<sub>2</sub> and corresponding redox potential to proves the underlying mechanism of general Lewis method to etch MAX for MXene. <sup>[180]</sup> ..... 50

**Figure 2.14** Synthesis process of TMN in ammonium gas atmosphere. <sup>[181]</sup> ..... 51

**Figure 2.15** (a) the mechanism of Lithiation–Expansion–Microexplosion etching method, <sup>[182]</sup> (b) the etching process of Mo<sub>2</sub>GaC under hydrothermal process in HCl solution, <sup>[161]</sup> (c) UV irradiation to assist the selective etching Ga in Mo<sub>2</sub>GaC in phosphoric acid solution, <sup>[183]</sup> (d) the principle of Mechanical-energy-assisted etching method, <sup>[185]</sup> (e) the process of halogen etching Al in Ti<sub>3</sub>AlC<sub>2</sub> and<sup>[187]</sup> (f) CVD method to grow Mo<sub>2</sub>C MXene/graphene and Mo<sub>2</sub>C MXene on pure copper foil. <sup>[189]</sup>..... 56

**Figure 2.16** (a) Schematic diagram of MXene structure,<sup>[140]</sup> (b) SEM figure for accordion like multilayer Ti<sub>3</sub>C<sub>2</sub>T<sub>x</sub> MXene,<sup>[25]</sup> (c) SEM few-layered Ti<sub>3</sub>C<sub>2</sub>T<sub>x</sub>,<sup>[36]</sup> (d) Photo for Ti<sub>3</sub>C<sub>2</sub>T<sub>x</sub> MXene aqueous colloidal solution shows Tyndall effect when a laser transmits it , (e) SEM figure for cross section of Ti<sub>3</sub>C<sub>2</sub>T<sub>x</sub> MXene free-standing film,<sup>[194]</sup> and inset shows the good flexibility of the film.<sup>[193]</sup>..... 58

**Figure 2.17** CV curves for (a)Ti<sub>3</sub>C<sub>2</sub>T<sub>x</sub> MXene etched with HF (Ti<sub>3</sub>C<sub>2</sub>T<sub>x</sub>) , followed by treating with KOH (KOH-Ti<sub>3</sub>C<sub>2</sub>) or KOAc(KOAc-Ti<sub>3</sub>C<sub>2</sub>) and being delaminated with assistance of DMSO,<sup>[196]</sup> (b) HF-synthesized Ti<sub>3</sub>C<sub>2</sub>T<sub>x</sub> and treated with 400 °C heating (400-Ti<sub>3</sub>C<sub>2</sub>T<sub>x</sub>), KOH(KOH-Ti<sub>3</sub>C<sub>2</sub>T<sub>x</sub>) and KOH+400°C heating(400-KOH-Ti<sub>3</sub>C<sub>2</sub>) ,<sup>[163]</sup> (c)HF-synthesized Ti<sub>3</sub>C<sub>2</sub>T<sub>x</sub> (Ti<sub>3</sub>C<sub>2</sub>T<sub>x</sub>-HF),and followed by treating with CaCl<sub>2</sub> solution to expand interlayer space (HF-Ti<sub>3</sub>C<sub>2</sub>T<sub>x</sub>-CaCl<sub>2</sub>), HCl+LiF synthesized MXene(Ti<sub>3</sub>C<sub>2</sub>T<sub>x</sub> -(HCl/LiF)) and followed by heating at 400°C in ammonia atmosphere(Ti<sub>3</sub>C<sub>2</sub>T<sub>x</sub> -(HCl/LiF)-400) ,<sup>[41]</sup> (d) delaminated MXene sheets assemble a free-standing film(Ti<sub>3</sub>C<sub>2</sub>T<sub>x</sub> film) and KOH + annealing treated film (ak-Ti<sub>3</sub>C<sub>2</sub>T<sub>x</sub> film-A), whose collectors are Pt clamp for EC performance measurement ,<sup>[197]</sup> (e) delaminated MXene free-standing film whose current collector is glass carbon EC EC characterization electrochemical measurement,<sup>[140]</sup> (f) freeze-dried MXene powder<sup>[34]</sup> ..... 61

**Figure 2.18** CV curves of HCl+LiF etched Ti<sub>3</sub>C<sub>2</sub>T<sub>x</sub> MXene tested with different collector collectors. .... 61

**Figure 2.19** CV plots for Ti<sub>3</sub>C<sub>2</sub>T<sub>x</sub> MXene in (a) 1M LiCl,<sup>[35]</sup> (b) alkaline electrolytes (LiOH, NaOH, KOH),<sup>[205]</sup> (c) 1-ethyl-3-methylimidazolium bis-(trifluoromethylsulfonyl)-imide (EMIMTFSI) and its 1M acetonitrile (ACN) solution,<sup>[206]</sup> (d) lithium bis(trifluoromethylsulfonyl) amine (LiTFSI) solution with dimethyl sulfoxide (DMSO), propylene carbonate(PC) and acetonitrile (ACN) as solvents.<sup>[207]</sup>..... 63

**Figure 2.20** (a)schematic diagrams for KOH alkalization and heating treatment of Ti<sub>3</sub>C<sub>2</sub>T<sub>x</sub> MXene,<sup>[163]</sup> (b) modifying Ti<sub>3</sub>C<sub>2</sub>T<sub>x</sub> MXene with N-Butyllithium to decrease surface -F and changes surface -OH into -O groups,<sup>[36]</sup> (c) Partial oxidation of MXene to decrease -F and engineer more surface -O,<sup>[211]</sup> (d) crystal structure of N-doped MXene,<sup>[41]</sup> (e)

Schematic diagram for N,S co-doped  $Ti_3C_2T_x$  MXene,<sup>[43]</sup> and (f) V-doping process of  $Ti_3C_2T_x$  MXene.<sup>[201]</sup> .....67

**Figure 2.21** (a) intercalating CNTs into the interlayer of MXene sheets,<sup>[40]</sup> (b) MXene sheets sandwiched by reduced graphene oxides,<sup>[216]</sup> (c) activated carbon used for alleviating restacking of MXene sheets,<sup>[52]</sup> (d) Schematic diagram for intercalating PANI into the interlayer space of MXene,<sup>[218]</sup> (e) preintercalation of metal ions into interlayer space of MXene,<sup>[198]</sup> (f) comparison of MXene films from vacuum filtration and natural sedimentation.<sup>[222]</sup> ..... 72

**Figure 2.22** (a) SEM figures for vacuum filtration assembled MXene film(top) and synthesized macroporous MXene films via template method,<sup>[140]</sup> (b) schematic diagram for ice template for constructing 3D porous structure,<sup>[227]</sup> (c) the formation process of MXene hydrogel with assistance of  $Fe^{2+}$ ,<sup>[34]</sup> (d) the assembling process of 3D MXene/ Bacterial cellulose,<sup>[31]</sup> (e) the ion diffusion within horizontally stacked and vertically aligned MXene films and schematic diagram for preparing vertically aligned MXene films,<sup>[233]</sup> (f) comparison of ion diffusions within large MXene restacked film and the small MXene sheets with nano pores restacked film. <sup>[234]</sup> ..... 75

**Figure 3.1** flow chart of the experiments in this research ..... 78

**Figure 4.1** Schematic illustration of fabrication process of (a)  $Ti_3C_2T_x$  MXene sheets and (b) MXene freestanding film with optimized interlayer path ..... 93

**Figure 4.2** Cross-sectional SEM images of (a) PMF, and (b) OMF ..... 96

**Figure 4.3** SEM image of (a) PMF surface and (b) OMF surface, photos of PMF (c) and (d) PMX..... 96

**Figure 4.4** (a) XRD spectra, (b) Raman spectra and (c) cross-section EDS results of PMF and OMF. Insets in (c) are cross-section SEM images of the two films; ..... 98

**Figure 4.5** (a) XPS survey spectra of PMF and OMF. (b) O 1s and (c) Ti 2p XPS spectra of the two films, d) P 2p high resolution spectra of OMF. .... 99

**Figure 4.6** (a) CV curves of pristine and optimized films at a scan rate of  $20\text{ mV s}^{-1}$ . (b) GCD curves of PMF and OMF at  $1\text{ A g}^{-1}$ . CV curves of (c) PMF, and (d) OMF under scan rates from 2 to  $200\text{ mV s}^{-1}$  ..... 102

**Figure 4.7** (a) Gravimetric & volumetric capacitance versus scan rates for PMF and OMF. (b) Percentage of capacitive contribution of PMF and OMF. (c) Electrochemical impedance spectroscopy data of PMF and OMF, inset shows their equivalent circuit. (d) Cyclic test of OMF at  $10\text{ A g}^{-1}$ ..... 103

**Figure 4.8** (a) CV curves for OMF-based symmetric supercapacitors at scan rates from 2 to  $100\text{ mV s}^{-1}$ . (b) Gravimetric capacitance against scan rates for PMF-based and OMF-based symmetric supercapacitors. (c) Cyclic stability of OMF-based symmetric supercapacitor at a current density of  $5\text{ A g}^{-1}$  for 10000 cycles. (d) Ragone plot displaying energy density versus power density for PMF, OMF and some reported  $Ti_3C_2T_x$  film based symmetric supercapacitors. .... 106

**Figure 4.9** (a) CV curves, (b) specific capacitance vs. scan rates, (c) GCD curves at current densities from 1 to  $10\text{ A g}^{-1}$ , and (d) rate performance of activated carbon electrode... 108

**Figure 4.10** (a) CV curves of OMF and activated carbon at  $20\text{ mV s}^{-1}$ . (b) CV curves of an

- OMF//activated carbon asymmetric supercapacitor at scan rates ranging from 2 to 200  $\text{mV s}^{-1}$ . (c) GCD curves of the device at current densities from 1 to 10  $\text{A g}^{-1}$ . (d) Rate performance of the asymmetric supercapacitor. (e) Cyclic stability of the device at 2  $\text{A g}^{-1}$ . (f) Ragone plot of the device. Inset is the photo showing that two devices in series can light up a red LED bulb with working potential of 1.8 to 2.2 V..... 109
- Figure 5.1** Schematic illustration for (a) phosphorus doping strategy, (b) proton interaction with surface of pristine  $\text{Ti}_3\text{C}_2\text{T}_x$ , and (c)-(d) proton interaction with surface of PMX. 115
- Figure 5.2** (a)  $\text{Ti}_3\text{C}_2\text{T}_x$  MXene colloidal solution shows Tyndall effect. (b) SEM image of  $\text{Ti}_3\text{C}_2\text{T}_x$  sheets on silicon substrate. (c) AFM image of  $\text{Ti}_3\text{C}_2\text{T}_x$  sheets, inset shows height profile of the selected line on the upper sheet. (d) Photograph of  $\text{Ti}_3\text{C}_2\text{T}_x$  MXene aerogel. .... 116
- Figure 5.3** SEM images of (a) MX, (b) PMX1, (c) PMX2 and (d) CMX. (e) XRD patterns of the samples. (f) Enlarged (002) peak in (e). .... 117
- Figure 5.4** (a) Nitrogen isothermal adsorption/desorption curves and (b) corresponding pore width distribution curves of MX, PMX1, PMX2 and CMX. .... 120
- Figure 5.5** HRTEM images and corresponding SAED patterns of (a) MX, (b) PMX1, (c) PMX2 and (d) CMX, respectively..... 121
- Figure 5.6** (a) HRTEM image and (b) SAED pattern of PMX8. (c) HRTEM image and (d) SAED pattern of PMX20. (e) FFT pattern of A region in (c)..... 122
- Figure 5.7** (a) Ti  $L_{2,3}$  edge and (b) O K edge EELS spectra of MX, PMX2 and CMX, in which EELS intensities of two elements in each sample were normalized with their separate highest peak values in Ti  $L_{2,3}$  edge EELS spectra. (c) O K edge spectra for the three samples normalized with the first peak intensity. (d) EELS elemental mapping results (Ti, O, P) of PMX2. .... 123
- Figure 5.8** (a) Composition analysis of MX, PMX1, PMX2 and CMX from XPS survey spectra. (b) High resolution P2p XPS spectra of PMX1 and PMX2. (c) Top and (d) side views of the  $\text{Ti}_3\text{C}_2\text{O}_2\text{-P}$  system; (e) Differential charge density distributions of  $\text{Ti}_3\text{C}_2\text{O}_2\text{-P}$ , yellow and blue regions indicate electron accumulation and depletion, respectively; (f) Electron localization function (ELF) maps of  $\text{Ti}_3\text{C}_2\text{O}_2\text{-P}$ , the scale bar shows the isodensity values of ELF. Ti, C, O, and P atoms are represented in blue, brown, red, and purple, respectively. .... 125
- Figure 5.9** Before and after optimization of different P concentrations  $\text{Ti}_3\text{C}_2\text{O}_2\text{-P}$  system. (a)  $\text{Ti}_3\text{C}_2\text{O}_2\text{P}_{0.11}$ , (b)  $\text{Ti}_3\text{C}_2\text{O}_2\text{P}_{0.33}$  and (c)  $\text{Ti}_3\text{C}_2\text{O}_2\text{P}$  ..... 126
- Figure 5.10** High resolution (a) O1s and (b) Ti2p XPS spectra of MX, PMX1, PMX2 and CMX. .... 128
- Figure 5.11** (e) Raman spectrum of MX, PMX1, PMX2 and CMX. (b) Ti K-edge of EXAFS spectra of MX and PMX2. EXAFS fitting results for (c) MX and (d) PMX2. (e) WT-EXAFS profiles for MX and PMX2 ..... 130
- Figure 5.12** (a) CV curves of MX, PMX1, PMX2 and CMX at the scan rate of 20  $\text{mV s}^{-1}$  and (b) GCD curves at the current density of 1  $\text{A g}^{-1}$  for the four samples. Specific capacitances of the samples at (c) scan rates from 2 to 1000  $\text{mVs}^{-1}$  and (d) current densities of 2 ~ 20  $\text{A g}^{-1}$ . (e) EIS spectra for the samples at -0.2V vs. Ag/AgCl. Insets are the enlarged EIS

- spectra at intercept with real axis and fitted equivalent circuit. (f) Capacitive contributions of the four samples at  $2 \text{ mV s}^{-1}$ . (g) Cyclic test of PMX2 at  $10 \text{ A g}^{-1}$ , the inset shows its GCD curves at different cycles. .... 132
- Figure 5.13** (a) CV curves of PMX8 and PMX20 at  $20 \text{ mV s}^{-1}$ , (b) GCD curves of the two samples at  $1 \text{ A g}^{-1}$ , (c) EIS plots of MX, PMX1, PMX2, PMX8, PMX20 and CMX, (6) capacitance vs. scan rates for the six samples, (e) gravimetric capacitance of the six samples at current densities from 2 to  $20 \text{ A g}^{-1}$ , (f) cyclic stability of PMX8 and PMX20 at  $10 \text{ A g}^{-1}$ ..... 133
- Figure 5.14** Capacitive contribution of MX, PMX1, PMX2 and CMX at scan rates from 2 to  $50 \text{ mV s}^{-1}$  ..... 136
- Figure 5.15** *Ex situ* XRD spectra of (a) MX, (b) PMX2 and (c) CMX. .... 137
- Figure 5.16** (a) Photo for in-situ Raman device. *In situ* Raman spectra of (b) MX and (c) PMX2 at potential range of  $-0.25 \sim 0.3 \text{ V}$  versus Ag/AgCl reference electrode. (d) Raman shift of  $A_{1g}$  band of MX and PMX2 with applied potential. (e) Ti K-edge XANES spectra of MX and PMX2 at  $-0.35$  and  $0.30 \text{ V}$  versus Ag/AgCl, and (f) enlarged profile of the rectangular area in (e)..... 139
- Figure 5.17** Ti2p XPS spectra of (a) MX, (b) PMX2 and (c) CMX at potentials of  $-0.35$  and  $0.3 \text{ V}$  vs. Ag/AgCl reference electrode. (d) P 2p XPS spectrum of PMX2 at  $-0.35$  and  $0.3 \text{ V}$  versus Ag/AgCl. (e) Top and side views of the hydrogen adopted in  $\text{Ti}_3\text{C}_2\text{O}_2\text{-P}$  system. .... 140
- Figure 5.18** Differential charge density distributions of  $\text{Ti}_3\text{C}_2\text{O}_2\text{-P}$  before (a) and after (b) the surface P bonding with two protons. The yellow and blue regions indicate electron accumulation and depletion, respectively..... 141
- Figure 5.19** (a) CV curves of MX and PMX2 based symmetric supercapacitors at  $2 \text{ mV s}^{-1}$ , (b) specific capacitance vs. scan rates for MX and PMX2 assembled symmetric supercapacitors, (c) cyclic stability of PMX2-based supercapacitors at  $10 \text{ A g}^{-1}$ , its inset shows GCD curves at 1<sup>st</sup>, 5000<sup>th</sup> and 10000<sup>th</sup> cycles (d) energy density vs. power density plot for MX and PMX2 based symmetric supercapacitors. .... 142
- Figure 6.1** Side view of (a) pristine MXene and (b) modified  $\text{Ti}_3\text{C}_2\text{T}_x$  MXene with interlayer water molecules. Top view of water molecules between pristine  $\text{Ti}_3\text{C}_2\text{T}_x$  (c) and modified  $\text{Ti}_3\text{C}_2\text{T}_x$  (d) interlayer space. .... 150
- Figure 6.2** SEM figures for (a) MX, (b) PMX600, (c) PMX700 and (d) CMX600 ..... 151
- Figure 6.3** (a) XRD plots of the samples, (b) enlarged (002) peak in (a), (c) nitrogen isothermal adsorption/desorption curves and (d) corresponding pore width distribution ..... 154
- Figure 6.4** HRTEM images and corresponding SAED patterns for (a) MX, (b) PMX600, (c)PMX700 and (d) CMX600. .... 155
- Figure 6.5** (a) Raman spectra for MX, PMX600, PMX700 and CMX600. (b) composition analysis for the samples from XPS survey spectra. High resolution O1s (c) and Ti2p (d) of MX, PMX600, PMX700 and CMX600..... 158
- Figure 6.6** (a) P2p high resolution spectra of PMX600 and PMX700 ..... 159
- Figure 6.7** Electrochemical performance of MX, PMX600, PMX700 and CMX600. (a) CV curves at the scan rate of  $2 \text{ mV s}^{-1}$ . (b) GCD plots at the current density of  $2 \text{ A g}^{-1}$ . (c), (d)

- capacity of the samples at various scan rates (c) and (d) current densities. (e) EIS plot and its inset shows intercept with real axis. (f) capacitive contributions of the sample at scan rates from 2 to 50  $\text{mV s}^{-1}$  and (f) shows the capacity composition at the scan rate of 2  $\text{mV s}^{-1}$ . (h) cyclic test of PMX600 and CMX600 at 10  $\text{A g}^{-1}$  and its inset shows the CV and GCD plots of PMX600 after different cycle times. (i) Specific capacity vs. scan rates for PMX600 and the plots of capacities using other modified methods. .... 163
- Figure 6.8** CV curves of MX (a) and PMX600 (b) at different cycle times within potential window of -0.6-0.6V vs. Ag/AgCl. .... 165
- Figure 6.9** ex situ XRD patten of (a) MX and PMX600. (c) (002) peak value vs. potential plots for MX and PMX600. CV curves of MX and PMX600 in 3M HCl, 1M  $\text{Li}_2\text{SO}_4$  and LiCl at 20 the scan rate of 20  $\text{mV s}^{-1}$  ..... 166
- Figure 6.10** Electrochemical impedance spectra of MX (a) and PMX600 (b) at different potentials. (c) CV curves of MX and PMX600 at the scan rate of 2  $\text{mV s}^{-1}$  to elucidate the difference of energy storage behavior between them. (d)-(f) Rate capability of MX and PMX600 in 3M HCl(d), 1M  $\text{Li}_2\text{SO}_4$  (e) and 3M LiCl (f)..... 169
- Figure 6.11** CV curves of MX-based symmetric supercapacitors at the scan rate of 2  $\text{mV s}^{-1}$  with 1C (a), 2C (b) and 3C (d) separating film. (d) The schematic diagram of proton transport within the device when charged. (e)-(g) CV curves of the supercapacitor at 2  $\text{mV s}^{-1}$  and with 1V voltage window using 3C (e), Nafion117 (f) and Nafion117+GF (g) as separating films respectively. (h) specific capacitance vs. scan rate plots for two MX based symmetric supercapacitors with Nafion117 and Nafion117+GF as separating films, respectively. (i) self-discharge behavior of the two energy storage devices. .... 172
- Figure 6.12** Electrochemical performance of MX, PMX600 and CMX600 based symmetric supercapacitors. CV curves at the scan rate of 2  $\text{mV s}^{-1}$  for the samples with voltage window of 0.6V (a), 0.8V (b) and 1V (c). GCD plots at the current density of 0.5  $\text{A g}^{-1}$  for 0.6V (d), 0.8V (e) and 1V (f) voltage window. Specific capacities of the symmetric supercapacitors at the scan rates from 2 to 200  $\text{mV s}^{-1}$  with 0.6V (g), 0.8V(h) and 1V (i) voltage windows, respectively..... 173
- Figure 6.13** self-discharge behavior of MX and PMX600 and CMX600 based symmetric supercapacitors with 0.6V(a), 0.8V(b) and 1V(c) voltage windows. (d) Ragone plots for the assembled devices with different voltage windows. .... 175
- Figure 6.14** (a) XRD patterns of PBA. (b) CV curve of PBA in 1M  $\text{H}_2\text{SO}_4$  at 5  $\text{mV s}^{-1}$  and (c) its GCD plots at current density from 1 to 20  $\text{A g}^{-1}$ . (d) The plots of specific capacity vs. current density for PBA. .... 176
- Figure 6.15** Electrochemical performance of PMX600-PBA supercapacitors. (a) CV curve at 5  $\text{mV s}^{-1}$  and GCD plot at 0.1  $\text{A g}^{-1}$  of the assembled device. (c) CV curves of the device at scan rates from 2 to 200  $\text{mV s}^{-1}$ , and (d) GCD curves at current density from 0.1 to 5A  $\text{g}^{-1}$  for the supercapacitor. (e) EIS spectra for the PMX600-PBA supercapacitor. (f) Specific capacitance vs. scan rates for the device. (g) the plot of open circuit potential vs. time for the device. (h) Ragone plots of the energy density vs. power density for PMX600-PBA supercapacitor and other reported device. (i) The photo of two in-series PMX600-PBA devices lighting a red and a green LED bulb..... 178



**Figure 7.1** (a) Rate capability of OMF, PMX2, PMX600. (b)-(c) Self-discharge behavior of MX-, PMX2- and PMX600-based symmetric supercapacitors with voltage windows of 0.6 V (b) and 0.8 V (c). (d) The plots of open-circuit potential vs. time for MX, PMX2 and PMX600-based symmetric supercapacitors with 1V voltage window and PMX600-PBA asymmetric supercapacitor. .... 180

**Figure 7.2** Comparison of cyclic stability between MX and other modified samples..... 181



## List of Tables

<b>Table 4.1</b> deconvolution results for O1s of PMF and OMF .....	100
<b>Table 4.2</b> deconvolution results for Ti2p of PMF and OMF .....	100
<b>Table 5.1</b> Ti K-edge EXAFS fitting results .....	130
<b>Table 5.2</b> Comparison in terms of capacitance of PMX2 along with other heteroatoms doped Ti <sub>3</sub> C <sub>2</sub> T <sub>x</sub> MXene.....	132
<b>Table 5.3</b> EIS fitting results for MX, PMX1, PMX2 and CMX .....	135
<b>Table 6.1</b> deconvolution results for O1s XPS spectra. ....	158



## Chapter 1 Introduction

### 1.1 Background

Four industrial revolutions in human history have greatly enhanced and enriched our standards of living, which include the first with the signal of invention of steam engines by James Watt in 1875, the second time marked by the wide utilization of electricity in 1850, the third referring to the automatic production brought by the computer in 1946, and the last one labelled by the formation of first worldwide web in 1984.<sup>[1]</sup> Throughout the development progress in recent 250 years, it can be summarized as a history about the exploitation of energy. For example, when steam engines in the first revolution were applied into trains for goods delivery etc., they put a higher demand for energy provision, which causes the extensive exploitation and use of coal.<sup>[2]</sup> The posterior three revolutions are closely connected with superior energy consumption using fossil fuels, such as petroleum, coal and natural gas etc., as main energy resources. Although tremendous advancements of science and technologies have been achieved in these processes, worldwide atmosphere accordingly tends to become warmer due to emission of carbon dioxide that is a product from combustion of fossil fuels. Earth history tells us that the sea level varies with air temperature and the sensitivity is 20 m per °C.<sup>[3]</sup> Therefore, it can be expected that continuous rise of sea level will be a huge disaster for human beings if no relevant measures were adopted to reverse the trend. Carbon

neutrality was first proposed in 1997 with the meaning that net-zero emissions of carbon dioxide is achieved through balancing the release of carbon dioxide and its removals. As of February 2021, 124 countries including China have promised to achieve carbon neutrality by 2050 or 2060.<sup>[4]</sup> Carbon neutrality seems have become the fifth industrial revolution for the whole human society, as shown in **Figure 1.1**.

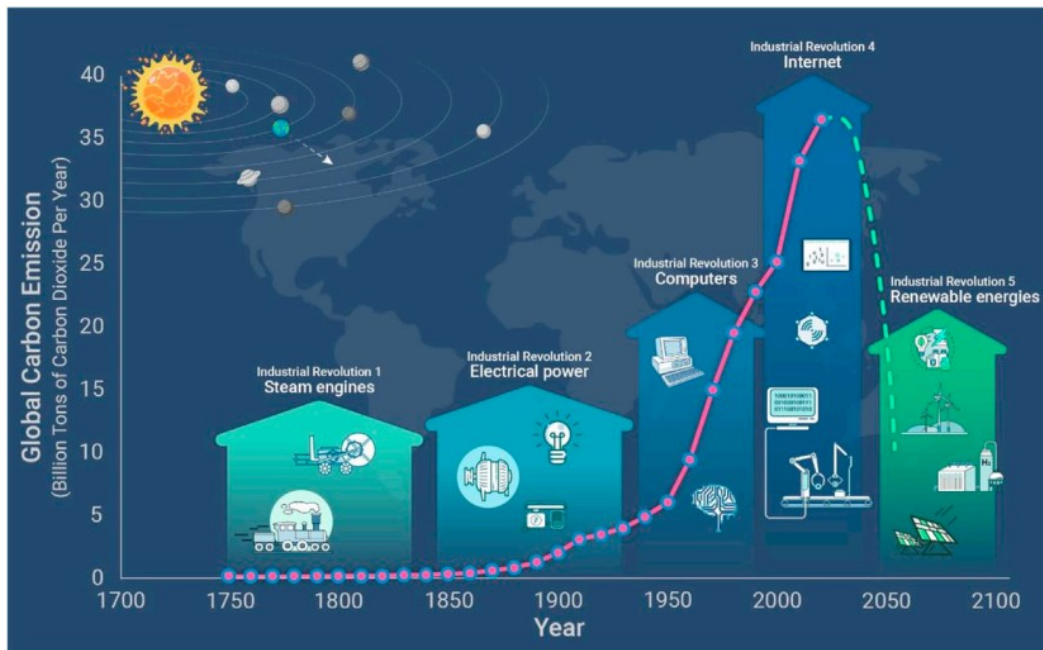


**Figure 1.1** development course and future of carbon emission around the world.<sup>[1]</sup>

Thus far, renewable energy sources like solar energy, wind energy, tidal energy and hydro energy etc. have been developed to generate electricity for reducing the use of fossil fuels and emission of greenhouse gases, which can immensely contribute to carbon neutrality.<sup>[5]</sup> Efficient energy storage systems are required to store energy from these intermittent sources to grid and should be equipped with high-rate harvesting, storage and deliverability of electrical energy.<sup>[6, 7]</sup> **Figure 1.2** depicts the power density vs. energy density of several common energy storage systems, which is known as



Ragone plot. Batteries locate the region with high energy density but low power density, featuring with a time constant (working time) varying from one to tens of hours. They are proverbially used in various applications, such as grid storage, powering electronics etc. due to high energy density.<sup>[6, 8]</sup> However, the energy storage process of batteries is diffusion-controlled and involves in phase transformation along with volume changes, which leads to inferior rate capability and only sustains a few thousand cycles life.<sup>[9, 10]</sup> Therefore, batteries are not ideal devices to directly crop energy from renewable resources because of incapable fast discharge and discharge. Electrochemical capacitors (ECs), also known as supercapacitors, are another main kind of energy storage systems. They can provide much higher power density but lower energy density than batteries and endures long cycles ( up to  $10^6$  cycles) .<sup>[11]</sup> ECs are regarded as complementary energy storage devices for batteries, which store energy via physical ion adsorption/desorption on electrode surface or fast redox reaction on electrode surface/subsurface. Supercapacitors can be used alone or combined with batteries to achieve the high-rate charge/discharge performance of whole energy storage systems,<sup>[6, 8]</sup> and are applied into grid energy storage for power quality and smoothing,<sup>[12]</sup> collecting braking energy of vehicles,<sup>[13]</sup> and electrical pitch control system of wind turbines etc. fields that require high power density for a short time.<sup>[14]</sup> Therefore, it can be conclude that available batteries and ECs cannot alone achieve high power density, high energy density and robust cycling life simultaneously. From the perspective of batteries, it is expected to deliver higher power but maintain originally outstanding

energy density. But for ECs, more efforts should be paid to enhance their energy density under no loss of rate performance and cycling stability. These two goals indicate that the boundary between batteries and ECs may gradually become blurred, as shown in the blue star of **Figure 1.2**. Note that here both the power and energy densities are normalized by the total mass of the assembled devices including current collectors, electrode materials, separators and electrolyte.<sup>[7]</sup>

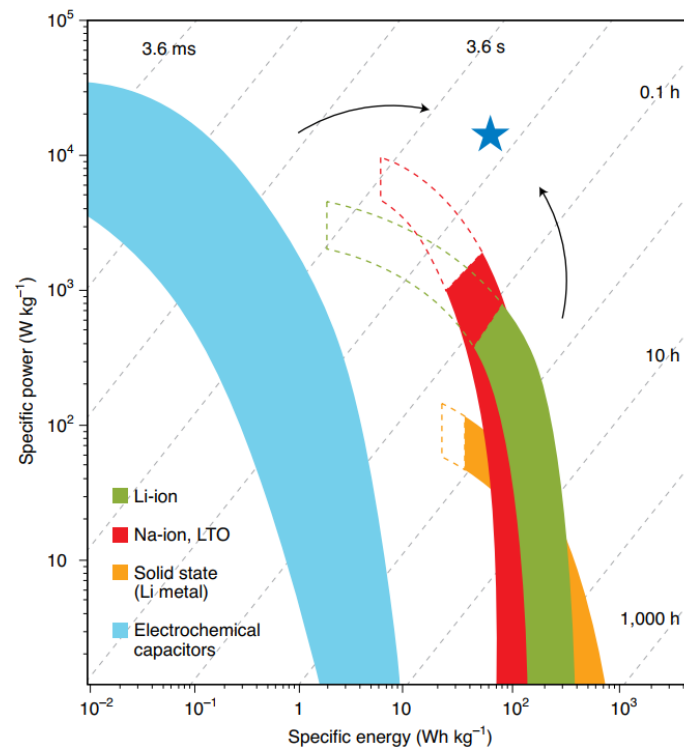


**Figure 1.2** Specific power vs. specific energy density (Ragone plot) for various energy storage devices.<sup>[7]</sup>

Supercapacitors are selected as the research theme in this work due to their more important role in fast energy harvesting of renewable energy resources than batteries. Similar with batteries, supercapacitors are also composed of two electrodes sandwiched by a separating film, which are packaged into a cell filled with electrolyte. Electrode materials fundamentally determine the energy storage ability of supercapacitors. The



devices store energy via either fast redox reactions on electrode surface/near surface or ion adsorption on electrode surface, which corresponds to pseudocapacitors (PCs) and electric double layer capacitors (EDLCs), respectively.<sup>[11, 15]</sup> PCs can deliver higher energy density than EDLCs due to more charge stored at redox active sites of electrode materials, leading to its reception of higher attention than EDLCs. The ideal pseudocapacitor electrode materials should be equipped with high conductivity, redox activity, and robust stability in electrolyte according to its charge/discharge characteristics.<sup>[16]</sup> Thus far, conventional pseudocapacitive electrode materials include transition metal oxides/hydroxides ( $\text{MnO}_2$ ,  $\text{RuO}_2$ ,  $\text{TiO}_2$ ,  $\text{NiO}$ ,  $\text{CoO}$  etc.),<sup>[17-21]</sup> conducting polymer (polyaniline, polypyrrole, poly(3,4-ethylenedioxythiophene and Polythiophene etc.).<sup>[22, 23]</sup> These materials can deliver high capacitance than EDLCs electrode materials, but their applications are restricted by low conductivity and inferior cycling stability. Therefore, electrode materials with superior capacitance, high conductivity and robust stability for supercapacitors are still urgently desired.

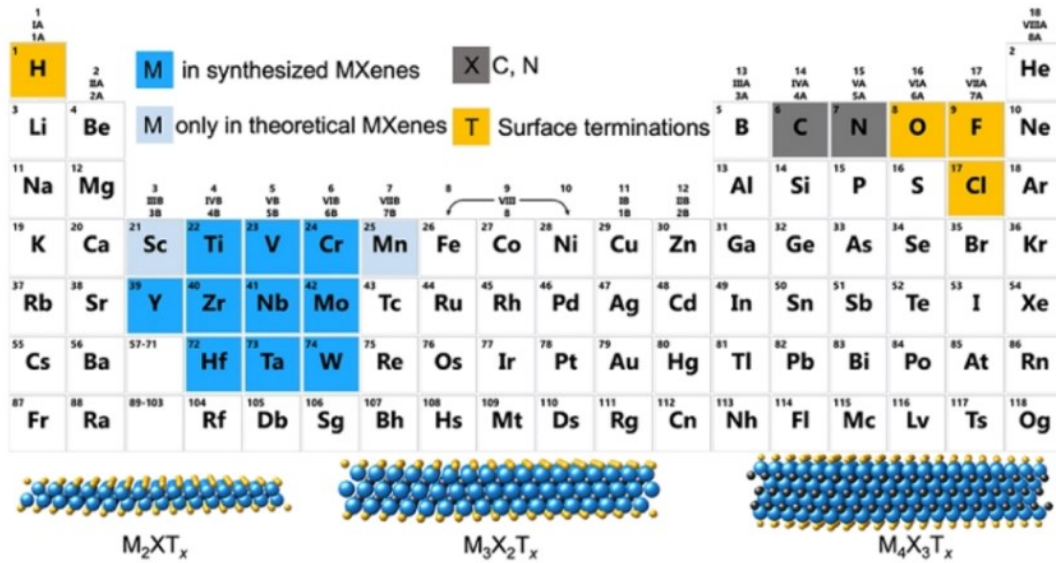


Figure 1.3 Elements for MXene composition<sup>[24]</sup>

MXenes are a novel kind of two-dimensional (2D) materials and have aroused an upsurge of worldwide research on their various applications due to their unique physicochemical properties since its discovery in 2011.<sup>[25, 26]</sup> MXenes refers to 2D transition metal carbides/nitrides/carbonitrides, and have a general formula of  $M_nX_{n+1}T_x$  ( $x$  ranges from 2 to 4), where  $M$  refers to transition metal (Ti, Cr, V, Mo, Nb, Zr, Hf, Ta, Sc, W, Y),  $X$  is carbon and/or nitrogen, and  $T$  denotes functional groups (-F, -Cl, -O and -OH) linked with surface metal atoms, shown in **Figure 1.3**.<sup>[24-27]</sup> One can observe that some MXenes have not been experimentally prepared but theoretically predicted. The inner part of MXenes sheets is transition metal carbides and their outer section resemble transition metal oxides/hydroxides, which endows them with simultaneously high conductivity and redox-active nature, respectively. Given this, MXenes are believed as the promising candidates for supercapacitor electrode materials. Thus far,  $Ti_3C_2T_x$  MXene is the most investigated and delivers the highest capacitance



in acid electrolytes among all found MXene.<sup>[26]</sup>  $Ti_3C_2T_x$  stores charge via the proton bonding with its surface -O functional groups and exhibits an intercalation pseudo capacitance mechanism.<sup>[28, 29]</sup> It is therefore to conclude that the supercapacitive performance of  $Ti_3C_2T_x$  MXene is jointly dependent on its surface chemistry and interlayer space. For boosting the supercapacitive applications of  $Ti_3C_2T_x$ , delamination,<sup>[30]</sup> adding interlayer spacers,<sup>[31, 32]</sup> construction of macroporous structure,<sup>[33, 34]</sup> and surface modification with alkalis or nucleophilic agents etc.,<sup>[35, 36]</sup> and heteroatom (N, S etc.) doping have been adopted. <sup>[37-39]</sup> These methods can be classified as two main categories, interlayer engineering and increasing active sites. Incorporation of spacer and pores into  $Ti_3C_2T_x$  MXene and conducting delamination belong to interlayer engineering and are to enable easier accessibility of electrolyte ions to active sites. And surface modification and heteroatom doping are assigned to 'increasing active sites', with which more active sites or charge transfer are achieved. Though a great amount of progress on  $Ti_3C_2T_x$  MXene for the high-performance supercapacitor's electrode material was reaped in recent years, it is still far from practical applications due to high production cost, inferior oxidation resistance etc. issues.

## 1.2 Research motivation and scope

Delaminated  $Ti_3C_2T_x$  MXene sheets can be assemble into flexible free-standing films



for supercapacitor application,<sup>[33, 38]</sup> but the restacking among the flakes will cause sluggish energy storage kinetics. To facilitate the ion diffusion within MXene electrodes, adding spacers (carbon nanotubes, bacterial cellulose etc.) or construction of porous structure have been proved to be feasible.<sup>[31, 40]</sup> But the introduction of inactive parts and formation of pores will decrease gravimetric and volumetric capacitance of the electrodes, respectively. Thus, it is highly desired to improve rate capability but also maintains pristine volumetric capacitance of  $Ti_3C_2T_x$  MXene.

The low electronegativity of MXene surface functional groups can boost its electron donor behavior, favorable for the charge transfer at MXene/electrolyte interface.<sup>[41]</sup> Therefore, heteroatoms with low electronegativity, like N and S have been doped onto  $Ti_3C_2T_x$  to modify its surface electron band structure. The resultant doped MXenes indeed exhibit improved supercapacitive performance.<sup>[42, 43]</sup> Given this, P incorporation onto  $Ti_3C_2T_x$  MXene should contribute to a greater promotion due to its superior electron donor ability to N and S.

The redox charge storage of  $Ti_3C_2T_x$  MXene is through the proton bonding/debonding with surface -O functional groups and the transport of protons to the active sites proceeds with Grotthuss mechanism within the interlayer space.<sup>[28, 44]</sup> Numerous efforts have been devoted to engineer more -O and decrease detrimental -F species on  $Ti_3C_2T_x$  surface for improved charge storage, along with expanding interlayer gallery of MXene



to boost ion intercalation. However, narrow interlayer space favors proton transport with Grotthuss mechanism and strengthens the interaction between intercalated protons and material interface,<sup>[28, 45]</sup> which is commonly neglected in optimizing MXene supercapacitive performance. Therefore, for the sake of boosting the energy storage ability of  $Ti_3C_2T_x$  MXene, not only should its surface functional groups be elaboratively designed, but also interlayer path could be modulated carefully. Thus far, most attention is focused on the surface modification, design of narrow interlayer path for boosting its capacitive performance is scarcely reported.

Based on previous issues discussed, this research mainly focuses on following three motivations.

- (1) To design a facile technology that can alleviate sheets restacking in MXene freestanding films but maintains their high volumetric capacitance.
  
- (2) To research the effect of doped phosphorus with lower electronegativity than nitrogen and sulfur on supercapacitive performance of  $Ti_3C_2T_x$  MXene and unravel underlying mechanism how hybrid element contributes to energy storage ability of MXene.
  
- (3) Validate the strategy that simultaneously eliminate the detrimental terminations (-F) on  $Ti_3C_2T_x$  MXene and shrink interlayer path in boosting the energy storage of



MXene and uncover the fundamental enhancement mechanism in modified MXene.

Following strategies are proposed to accomplish above three objectives.

The volumetrically expanded ester reaction between ethanol and phosphoric acid was exploited in this research to solve the first challenge.  $\text{Ti}_3\text{C}_2\text{T}_x$  MXene free-standing films from vacuum filtration were heated in the mixture of the two substances, leading to atomic scale interlayer expansion and improved interlayer uniformity due to the ester reaction. Boosted ion diffusion along with ameliorative rate capability are finally reaped in the optimized MXene film and its volumetric capacitance has not degraded but instead shows an increment due to this interlayer structure, which is seldom found in other methods to resist MXene sheets restacking.

To confirm the boosted role of doped phosphorus for energy storage ability of  $\text{Ti}_3\text{C}_2\text{T}_x$ , phosphorus was firstly doped onto  $\text{Ti}_3\text{C}_2\text{T}_x$  MXene via heating in phosphine ( $\text{PH}_3$ ) and argon mixed atmosphere. The energy storage ability of P-doped MXene was then characterized through electrochemical characterization. And the surface formed Ti-O-P functional groups are revealed to serve as new active sites to lead to more charge storage using *in situ* Raman, *ex situ* X-ray Absorption Spectroscopy (XAS), *ex situ* X-ray photoelectron spectroscopy (XPS) and *ex situ* X-ray diffraction (XRD). In addition, it is also confirmed that lattice distortion appears simultaneously with phosphorus doping, and higher phosphorus content will even lead to amorphization of MXene.



These results elucidate the facilitated role of phosphorus for energy storage performance of P-doped MXene and also explain why its energy storage ability cannot be further promoted by increasing surface grafted phosphorus on  $Ti_3C_2T_x$  MXene.

To simultaneously modulate surface functional groups and interlayer space (3<sup>rd</sup> objective), few-layer  $Ti_3C_2T_x$  MXene aerogel was heated in the mixed atmosphere of  $PH_3$  and Ar at a higher temperature (600°C) than that of P-doping in the second strategy of this research. The surface -F was greatly eliminated after the heating process and the interlayer path becomes narrower due to the removal of surface functional groups. But the heating procedure with presence of  $PH_3$  also cause the formation Ti-O-P terminals on MXene surface, which serve as pillars to resist the further shrinkage of interlayer path. The oxidation of MXene is also suppressed due to the existence of  $PH_3$  in the heating atmosphere. The resulting MXene shows a much-enhanced capacitance along with better rate capability. More importantly, modified  $Ti_3C_2T_x$  MXene exhibits a greatly strengthened oxidation resistance ability in comparison to pristine MXene. Multiple characterizations were also conducted to unravel the boosted energy storage ability in the modified samples. It is finally concluded that the monolayer interlayer water molecules lead to its ameliorative capacitance and rate capability and the rich oxygen terminals and strengthen chemical bonds are responsible for its much-improved oxidation resistance ability.



### 1.3 Synopsis of thesis

This thesis focuses on design of interlayer path and surface modulation of  $Ti_3C_2T_x$  MXene for boosting its supercapacitor applications, which could be divided into three works. The broaden but uniform interlayer path within MXene free-standing film is prepared by exploiting the expansion effect of ester reaction between ethanol and phosphoric acid in the first work. And the electron donor ability of  $Ti_3C_2T_x$  MXene was modulated by surface grafting phosphorus atoms for enhanced capacitance in the second job. The final work is removing the unfavorable surface functional groups of  $Ti_3C_2T_x$  MXene and changing the interlayer path to be narrower to boost the proton transport within the confined interlayer space and increase the interaction between intercalated ions and MXene surface.

The thesis is organized as follows.

**Chapter1** mainly introduces research background and research objectives of this research. The carbon neutrality goal is first presented to highlight the exploitation of renewable resources, which is followed by introduction of common energy storage systems and emphasizing the importance of supercapacitors for harvesting renewable resources. Afterwards, MXenes are briefly introduced as a kind of promising supercapacitor electrode material. Finally, relevant challenges on MXenes' supercapacitor applications and research motivations in the research are presented.



**Chapter 2** is literature review about supercapacitors, energy storage mechanism of supercapacitors and electrode materials, MXenes synthesis methods, MXenes applications in supercapacitors and improved strategies.

In **chapter 3**, the experimental approaches of this research are introduced in detail, which comprise materials synthesis, characterization, fabrication of electrodes, device assembly, electrochemical measurements and the methods of Density Functional Theory calculation.

**Chapter 4** presents using the ester reaction between phosphoric acid to optimize the interlayer path of  $Ti_3C_2T_x$  MXene free-standing films for enhanced capacitive performance.

**Chapter 5** introduces that incorporation of phosphorus onto  $Ti_3C_2T_x$  MXene to improve its energy storage ability and revealing the underlying enhanced mechanism. Why further capacitance improvement cannot be achieved by purely increasing surface doping amount is also disclosed.

**Chapter 6** studies the synergistic modulation of  $Ti_3C_2T_x$  surface functional groups and interlayer path to strengthen its energy storage ability and uncover the fundamental reasons about ameliorative capacitance, rate capability and oxidation resistance in the



modified MXene.

**Chapter 7** summarizes the conclusions of this research and gives the prospect of outcomes in this work for practical application.



## Chapter 2 Literature review of supercapacitors and MXene for supercapacitor applications

In this chapter, the classification of supercapacitors, underlying mechanism of supercapacitors are first introduced. Classical electrode materials for supercapacitors and synthesis methods of MXene are then summarized. The final attention moves on the application of  $Ti_3C_2T_x$  MXene for supercapacitors electrode materials and optimized strategies.

### 2.1 Supercapacitors and electrode materials

Supercapacitors deliver higher power density but lower energy density than batteries due to their unique energy storage mechanism. They can be categorized into electrical double-layer capacitors (EDLCs), pseudocapacitors (PCs) and hybrid supercapacitors (HSCs) according to underlying energy storage principles. The architecture of supercapacitors resembles batteries and are mainly composed of two electrodes including current collectors, a separator and electrolyte, as shown in **Figure 2.1**. The charging in supercapacitors is a process that let electrons flow from cathode to anode, forced by external potential field, which is accompanied by the ion rearrangements or redox reactions on electrode surface.<sup>[46]</sup> The discharging of supercapacitors is a reversed process. In addition, the energy storage/release process of supercapacitors does not

involve in phase transformation and solid diffusion process that proceeds in batteries and this feature is often used to judge battery-type or capacitive behavior in an energy storage device.<sup>[7, 47]</sup> Therefore, electrode/electrolyte interface plays the vital role in energy storage process of supercapacitors, which will be further elucidated in terms of energy storage mechanism in the following sections.

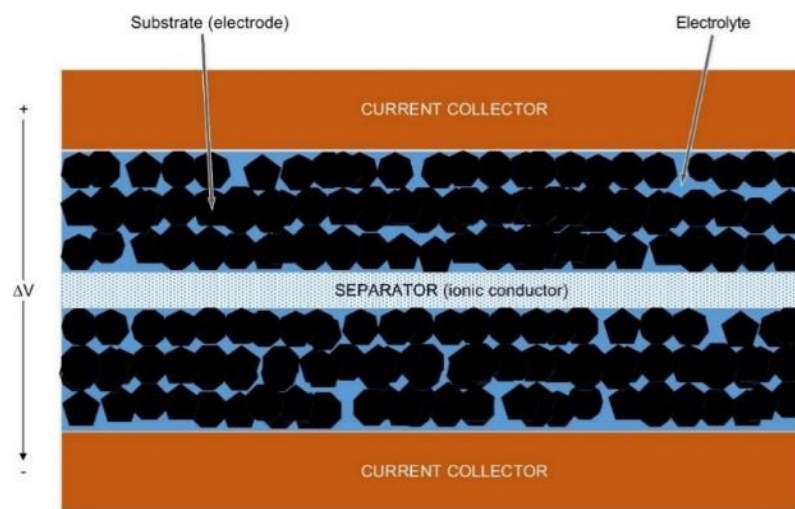


**Figure 2.1** Schematic diagram of supercapacitors.<sup>[6]</sup>

### 2.1.1 Electrical double-layer capacitors (EDLCs)

EDLCs stores charge via physical adsorption of electrolyte ions on electrode surface, and no charge transfer occurs across electrolyte/electrode interface, similar to that of typical dielectric capacitor.<sup>[48]</sup> The capacitance of EDLCs is generated due to this true capacitance effect. The ion adsorption on electrode surface can be described with electrical double layer (EDL) model, which is used to explain the phenomenon that counter charge forms on a charged object when it is placed into liquids. The simplest mode is Helmholtz model that considers a solid layer with opposite charge forming at

a  $d$  distance from electrode surface (**Figure 2.2a**). But it cannot adequately explain what happens in the real electrode-electrolyte interface. So, Helmholtz model was then replaced by Gouy–Chapman model. The new one believes that the counter ions are not rigidly absorbed on electrode surface but forms diffusing layer with solvent molecules, as shown in **Figure 2.2b**. The ion in diffuse layer in Gouy–Chapman model follows Maxwell-Boltzmann’s distribution. However, this optimized mode cannot fit for highly charged electrodes and the experimentally measured thickness of diffuse layer is higher than the calculated value. Finally, Stern proposed a new explanation mode by combining the merits of the previous two models shown in **Figure 2.2c**, which assumes that counter charge layer near electrode surface is composed of the inner strongly absorbed stern layer (specifically absorbed ions) and outer diffuse layer (nonspecifically adsorbed counter-ions).

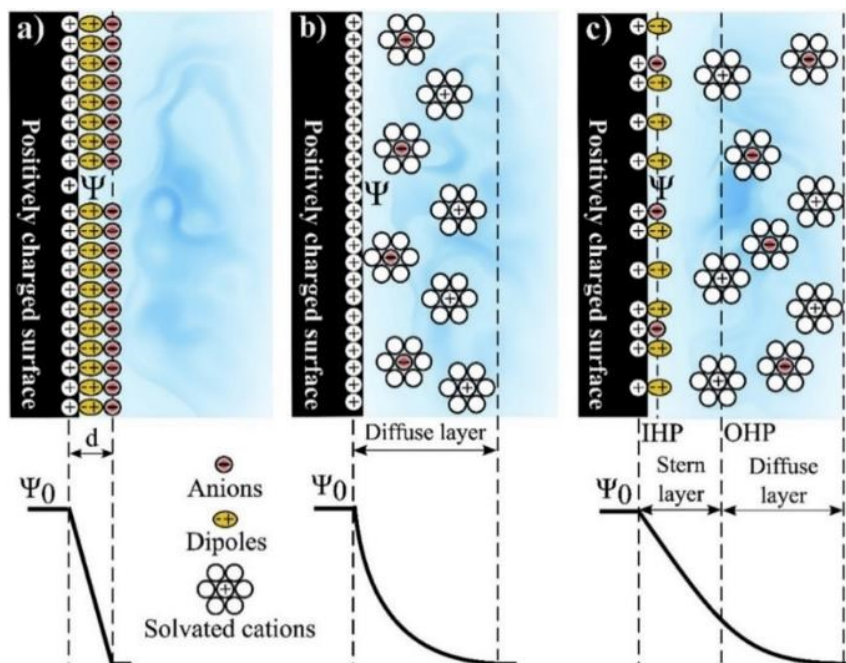


**Figure 2.2** The development of EDL model. (a) Helmholtz model, (b) Gouy–Chapman model and (c) Stern model.<sup>[8]</sup>



Given the electrical double layer structure of electrode/electrolyte interface in EDLCs, their capacitance of EDL can be described with equation below.

$$C_{dl} = \frac{Q}{V} = \frac{\epsilon_r \epsilon_0 A}{d} \quad (2-1)$$

Where  $C_{dl}$  is the capacitance of EDL interface,  $Q$  is the stored charge at potential  $V$ .  $\epsilon_r$  and  $\epsilon_0$  refer to dielectric constants of the electrolyte and vacuum, respectively. The  $A$  in the formula represents the electrode surface area.

If the  $C_{dl}$  is constant in EDLCs, the response current ( $I$ ) of capacitors can be derived from equation 2-1, with the following formula.

$$I = \frac{dQ}{dt} = C_{dl} \frac{dV}{dt} \quad (2-2)$$

Where  $t$  indicates the charge time. And if the applied voltage changes linearly with time  $t$  through a sweep rate of  $v$ , the equation 2-2 can be changed into

$$I = C_{dl} v \quad (2-3)$$

Equation 2-2 indicates the response current at a certain scan rate is constant, which corresponds to almost rectangular shape in cyclic voltammetry (CV) profiles, and the increasing scan rates contribute to the linear increment of currents or current densities, from equation 2-3, as shown in **Figure 2.3a**. Similarly, if a constant current is applied to EDLCs, their voltages will linearly vary with the time, resulting in a triangular galvanostatic charge /discharge (GCD) shape (**Figure 2.3b**). Since the charge storage of EDLCs only occur on electrode surface, high-power density can be achieved. But their low energy density restricts the large-scale applications. Carbon-based materials, like activated carbon,<sup>[49-52]</sup> carbon nanotube<sup>[53]</sup> carbide-derived carbon,<sup>[54, 55]</sup> and

graphene<sup>[56, 57]</sup>, are typical electrode materials to fabricate EDLCs.

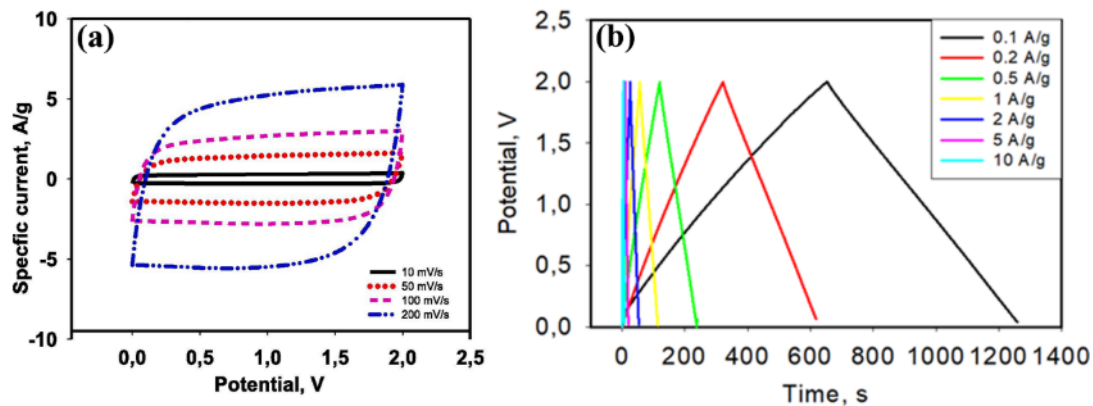


**Figure 2.3** (a) CV and (b) GCD curves of EDLCs at different scan rates and current densities.<sup>[49]</sup>

Activated carbon (AC) is the most widely used carbon materials for EDLCs, which is synthesized by heating carbon-rich organic precursors and subsequent activation process. The first heating process is for producing amorphous carbon and the second activation process using physical or chemical methods endows the material with high specific area (up to  $3000 \text{ m}^2 \text{ g}^{-1}$ ).<sup>[58]</sup> However, not all of the pores in AC can be used for charge storage since some pores are inaccessible to electrolyte. Thus far, most of commercial EDLCs are assembled with AC and organic solution as electrode materials and electrolyte respectively, which can exhibit a potential window of 2.7 V, whereby delivering much higher energy density than aqueous devices due to wider voltage window.<sup>[6, 59]</sup>

Carbon nanotubes (CNTs) are another kind of electrode material for EDLCs and can be



synthesized by catalytic decomposition of certain hydrocarbons.<sup>[53, 60]</sup> The number of carbon-layer in CNTs can be controlled by modification of synthesis parameters, resulting in the formation of single walled carbon nano tubes (SWCNTs) or multi-walled carbon nano tubes (MWCNTs). Similar to AC, CNTs also possess high specific area (200-400 m<sup>2</sup> g<sup>-1</sup>) and the capacitance of purified CNTs ranges from 20 to 80 Fg<sup>-1</sup>. A further treating CNTs with nitric acid or potassium hydroxide can greatly increase their specific area, greatly contributing to the charge storage ability.<sup>[61, 62]</sup>

Carbide derived carbons (CDCs) are produced by extracting metal atoms of carbides at high temperature heating under vacuum conditions<sup>[63]</sup> or using chlorination.<sup>[54, 64]</sup> The appealing feature of CDCs for electrode materials of EDLCs is its controllability of porous structure within these carbon materials. The common strategy is changing carbide precursors and synthesis temperature. For example, titanium carbide derived carbons own the larger pore size than that derived from silicon carbide at the same heating temperature (1200°C).<sup>[65]</sup> And the pore size in CDCs increases with elevating heating temperature but the porous structure tends to collapse when the synthesis temperature surpasses 1300°C.<sup>[66]</sup> Titanium carbide derived carbon which can delivers a highest capacitance of 220 Fg<sup>-1</sup> in aqueous electrolyte among all CDCs and 120 F g<sup>-1</sup> in organic solution. The investigation on the effect of pore size on capacitance reveals the pore less than 1 nm in CDCs can be more favorable for their higher capacitance than those pore with size larger than 1 nm,<sup>[67]</sup> which is explained as a confinement



effect.<sup>[7]</sup>

Graphene is a two-dimensional (2D) material wholly composed of  $sp^2$  bonded carbon atoms and exhibits high conductivity, extensive specific area (theoretically  $2630 \text{ m}^2 \text{ g}^{-1}$ ) and excellent chemical stability.<sup>[56, 68]</sup> This novel 2D material can be fabricated via mechanical exfoliation of highly oriented pyrolytic graphite with tapes,<sup>[69]</sup> chemical vapor deposition,<sup>[70]</sup> and liquid phase exfoliation method,<sup>[71]</sup> among which the third method has been used for mass production.<sup>[68]</sup> Monolayer graphene sheets theoretically can deliver an ultrahigh power density due to intrinsically high conducting behavior, but the restacking between graphene sheets will impede the diffusion of electrolyte, leading to sluggish energy storage kinetics.<sup>[72]</sup> Given this issue, incorporation of micropores in graphene sheets,<sup>[73]</sup> and 3D porous structure<sup>[74]</sup> are utilized to alleviate the detrimental effect from the sheets restacking. Graphene based EDLCs were reported to show a higher capacitance ( $200\sim 300 \text{ F g}^{-1}$ ) in aqueous electrolyte than in ionic liquid ( $75 \text{ F g}^{-1}$ ).<sup>[6, 75]</sup> But the devices with ionic liquid electrolyte can operate up to 4.5 V, contributing to high power density up to  $130 \text{ Wh Kg}^{-1}$ .<sup>[76]</sup>

Except the previous discussion about EDLCs and their typical electrode materials, there are also great achievements on the underlying mechanism on the formation and charge of double layer in nanoporous carbon electrodes. It is found that the subnano pores in carbon materials contribute to enhanced capacitance.<sup>[67]</sup> Various *in situ* characterization



methods and theoretical calculation collectively reveal that the increment in capacitance is ascribed to that partially desolvated ions enter into those subnano meter pores, leading to special organization of electrolyte in the confined space, creation of images charges on carbon surface, and more concentrated ion packing.<sup>[77-85]</sup> As for the planar electrode in pure ionic liquid, the charge overscreening makes the ionic liquid exhibit long-range layered structure, and the presence of solvent disturbs the electrolyte organization, as shown in **Figure 2.4a**.<sup>[7]</sup> By contrast, the confinement of pure ionic liquid in those pores with comparable size of ion results in the formation of superionic state and formation of co-ion pairs, eventually contributing to the improved capacitance (**Figure 2.4b**).<sup>[86]</sup> In addition, the confined ions in these subnano meter pores lacks overscreening due to the geometric constrictions of the pores ( $< 1$  nm), which makes the thickness of diffusion layer within the pores decrease, whereby leading to the stronger interaction between ions and carbon host, as shown in **Figure 2.4c**.<sup>[87, 88]</sup> The revealment of this increasing mechanism guides the manufacture of activated carbon with an average pore size in the nano meter range, boosting the energy density of commercial EDLCs (up to  $10 \text{ Wh Kg}^{-1}$ ).

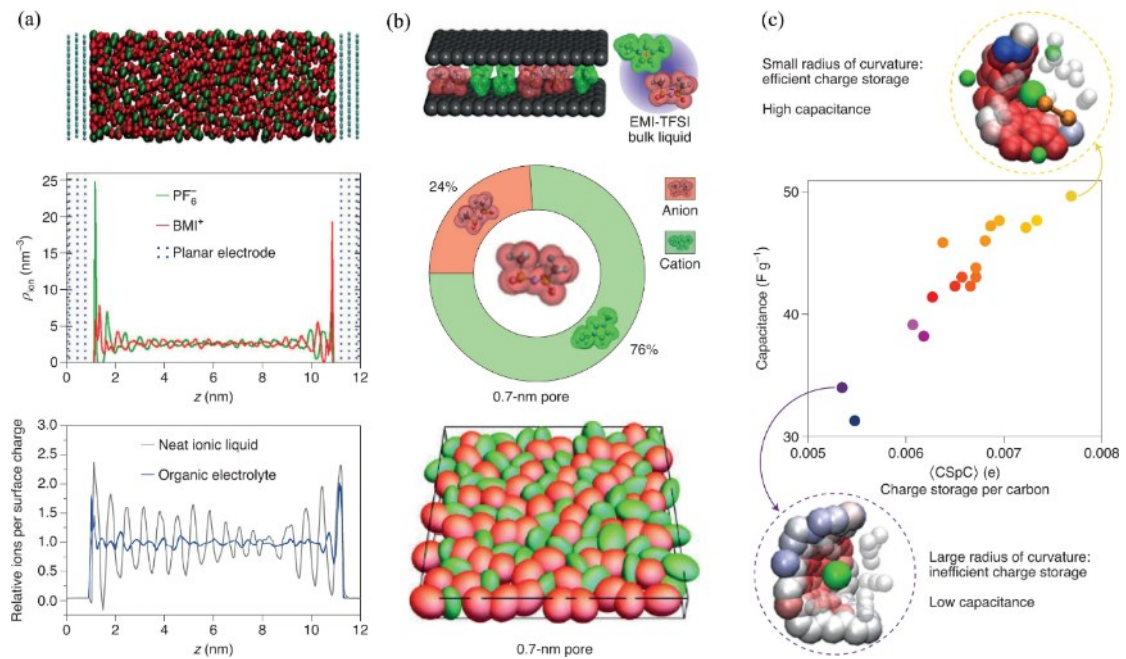


**Figure 2.4** (a) Snapshot plot for BMI-PF<sub>6</sub> ionic liquid electrolyte between two graphite electrodes at potential of 2V (top), and long-range layered structure due to charge overscreening (middle) is suppressed when adding an organic solvent (bottom).  $\rho_{ion}$ , ion density. (b) Formation of a superionic state results from the formation of co-ion pairs when the ionic liquid EMI-TFSI is confined in pores with a comparable size to the electrolyte ions (top). The first solvation shell surrounding an anion involves up to 24% anions without polarization (middle), which leads to increased ion population in the pores (bottom). (c) The charge stored per carbon in nanopores of 3D porous carbons enhances with the decrement of the curvature radius, resulting from stronger or closer interactions between confined ions and the carbon walls.<sup>[7]</sup>

In summary, EDLCs store charge through ion absorption on electrode surface without redox reactions, which can be well described with stern EDL model. Carbon materials with high specific area and high conductivity are widely used for electrode materials of EDLCs. The sub-nano meter pores in carbon materials play vital roles for boosting its capacitance, which is achieved through the entrance of desolvated ions, formation of superionic state, and exclusion of overscreening in the pores, leading to higher ion-carbon wall interaction.



### 2.1.2 Pseudocapacitors (PCs)

The supercapacitors that store energy through underpotential deposition on metal electrode, fast and invertible redox reactions on electrode surface, or fast ion intercalation into layered electrode materials are believed to belong to pseudocapacitors (PCs). Those devices storing charge via fast ion intercalation process have a special name, intercalation pseudocapacitors. The characteristic feature for PCs includes (1) the stored charge varies with applied potential, (2) no solid-state diffusion due to the charge storage only occurring electrode surface or near surface, (3) absence of phase transformation during its charge/discharge process. It should be noted that C/g and mA<sub>g</sub>/g is more suitable for describing the energy storage ability of PCs.<sup>[7]</sup> In comparison to EDLCs, PCs can deliver higher energy density due to existence of Faradic redox charge transfer at electrode-electrolyte interface.<sup>[7, 11]</sup> **Figure 2.5** summarizes the schematic diagrams of three energy storage mechanisms for pseudocapacitors, which include underpotential deposition, redox pseudocapacitance, and intercalation pseudocapacitance.<sup>[11]</sup>

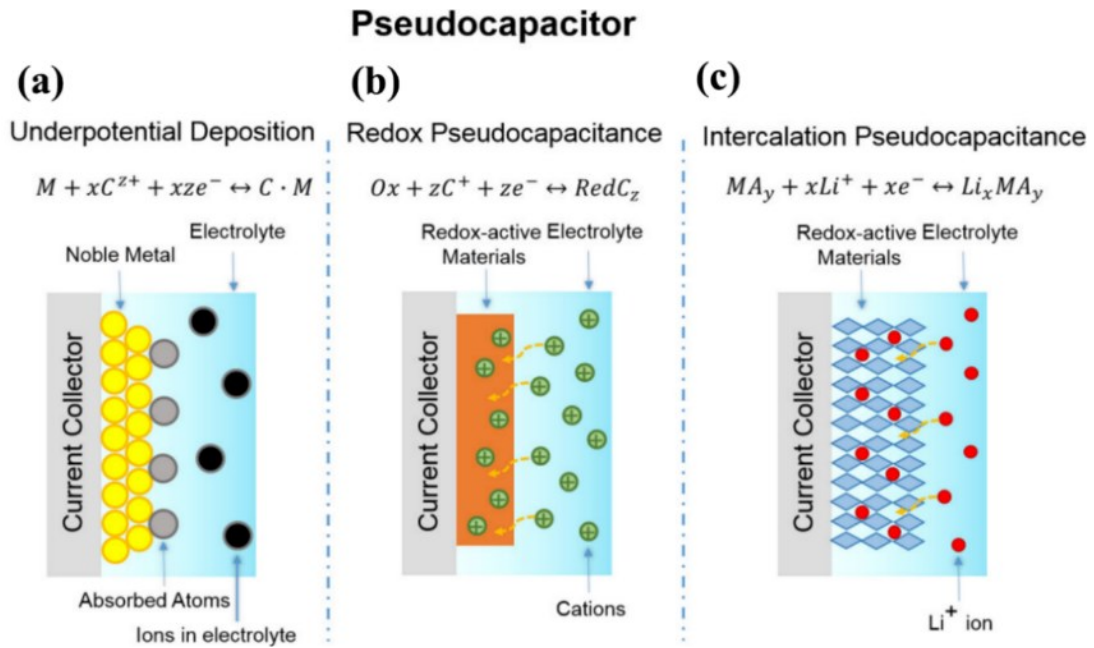


**Figure 2.5** Schematic for energy storage mechanism of (a)-(c) Pseudocapacitors with energy storage mechanism of (a) underpotential deposition, (b) fast surface redox reactions, (c) cation intercalation.<sup>[11]</sup>

Underpotential deposition (UPD) refers to that ions deposit on a metal-electrolyte surface at potentials higher than their reversible redox potential, as shown in **Figure 2.5a**. The process can be expressed by the equation 2-4,

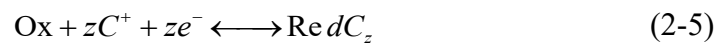


where M is precious metal electrode (Pt, Au, Ir),  $C^{z+}$  refers to absorbed atoms ( $H^{+}$  or  $Pd^{2+}$ ) and x denotes the number of absorbed ions during the process.<sup>[89]</sup> The typical characteristic for the underpotential deposition of ions is that the applied potential should be always positive to their reversible redox potential. A very high areal can be achieved through UPD mechanism. For example, the areal capacitance for hydrogen underpotential deposition on Pt electrode can reach up to  $\sim 2200 \mu F \text{ cm}^{-2}$ .<sup>[11]</sup> However, the narrow potential window (only 0.3-0.6 V) and high cost noble metal electrodes of



UPD restricts its wide application.<sup>[47, 90]</sup>

Supercapacitors that store charge via fast surface redox reactions are categorized into redox pseudocapacitors. The ions in electrolyte absorb/desorb on electrode surface, leading to the valence state change of certain elements in electrode materials along with charge transfer. The typical electrode materials with this scheme includes transition metal oxides (RuO<sub>2</sub>, MnO<sub>2</sub> etc.) and doped conducting polymer (polyaniline, polypyrrole, poly 3,4-ethylenedioxythiophene and Polythiophene etc.).<sup>[22, 23]</sup> Their energy storage process also can be described with the equation 2-5.

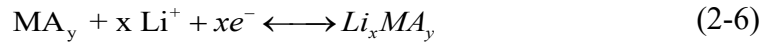


Ox in the equation is electrode materials, C<sup>+</sup> refers to the surface-absorbed ions (H<sup>+</sup>, Li<sup>+</sup>, Na<sup>+</sup>, K<sup>+</sup> etc.), RedC<sub>z</sub> indicates the reduced C species, and z is the number of transferred electrons. For example, hydrous RuO<sub>2</sub> can deliver a highest capacitance of 900 F g<sup>-1</sup> (theoretically 1358 F g<sup>-1</sup>) with this mechanism,<sup>[91, 92]</sup> but its expensive price cannot fit the demand of large-scale commercialization. MnO<sub>2</sub> is also equipped with a high theoretical capacitance of 1370F g<sup>-1</sup>,<sup>[93]</sup> but its inferior conductivity limits its rate capability. Conducting polymers enable redox capacitance behavior in acid electrolyte, whereas they exhibit the obvious capacitance decay with the cycling times,<sup>[23]</sup> also restricting its wide application.

Intercalation pseudocapacitance occurs in layered materials via fast ion intercalation



(Figure 2.5c) into their interlayer space. The energy storage process can be described with the equation below.<sup>[94]</sup>



Where  $MA_y$  is layered materials ( $MoS_2$ , MXene etc.),  $Li^+$  corresponds to the intercalated ions and can also be replaced by other cations, like  $H^+$  and  $K^+$ .<sup>[95]</sup> It should be pointed out that the intercalation of those cations does not lead to phase change of host materials, which proceeds in lithium ion batteries to store charge. The preconditions for intercalation pseudocapacitance are facile 2D diffusion path for intercalated ions and little lattice change upon ion intercalation. The materials with intercalation pseudocapacitance involve Faradic charge transfer, thus they also can achieve high capacitance.  $Ti_3C_2T_x$  MXene with proton intercalation mechanism to store energy delivers a highest capacitance of  $927 F g^{-1}$  in sulfuric acid electrolyte. And the capacitance of nanocrystal  $T-Nb_2O_5$  store charge in lithium ion organic electrolyte by fast lithium insertion and its energy storage is independent of scan rates and a high capacity of  $130 mAh g^{-1}$  was obtained at a 10 C discharge rate.<sup>[94]</sup>

In addition to materials that intrinsically show pseudocapacitive performance, nano scaling electrodes material or modifying electrode materials with defect can make some battery-type electrode materials ( $LiFePO_4$ ,<sup>[96, 97]</sup>  $LiCoO_2$ ,<sup>[98]</sup>  $MoO_3$ <sup>[99, 100]</sup>) present pseudocapacitive energy storage behavior. The incorporation structural water molecules into metal oxides ( $MoO_3$   $WO_3$  etc.) was also proved to be an efficient



approach to change them into pseudocapacitive materials.<sup>[101]</sup> The incorporated water molecules locate at the interlayer space, which isolate structural transformation to two dimensions and stabilize the structure along the third direction. These confined and ordered structural water provide a highway for proton intercalation, enable extremely facile phase transformation and litter change of interlayer distance. Incorporation of confined fluid into the interlayer space of redox-active electrode materials is a promising modified strategy to simultaneously achieve its high energy densities and power densities.

Although a great number of transition metal oxides and  $Ti_3C_2T_x$  MXenes have been investigated for pseudocapacitive materials, but the underlying reason why rate-independent behavior can be observed in these materials are worthy to be further studied. Therefore, similar with research work on insight into the ion absorption in subnano meter pores of carbon materials, *in situ* characterization methods and density functional theory (DFT) calculations have also been applied to reveal the underlying mechanism of layered materials.<sup>[28, 102]</sup> The interlayer water in transition metal oxides and MXene is revealed to critically affect the transport of the intercalated cations within the interlayer gallery. For example, the interlayer water in birnessite ( $MnO_2 \cdot yH_2O$ ) can reduce the interaction between intercalated  $K^+$  and oxide surface, which is beneficial for the intercalation of the ions and leads to minimal structural changes.<sup>[102]</sup> In addition, the confinement of  $K^+$  ions in the interlayer space can exhibit more charge transfer than



that the planar interface absorbs  $K^+$  ions.<sup>[102]</sup> Overall, the hydration and nanoscale channels collectively contribute to high-rate ion transport and charge storage.<sup>[95, 103]</sup> Another instance is that the interlayer gallery of  $Ti_3C_2T_x$  MXene critically determines its energy storage behavior. It is demonstrated that the protons transport with the help of hydrogen bond network formed between water molecules, which is known as Grothuss mechanism.<sup>[28, 104]</sup> One-layer interlayer water molecules in  $Ti_3C_2T_x$  MXene can provide faster redox rate than two- or more-layer of interlayer water.<sup>[44]</sup> Since protons transporting within the one-layer of interlayer water has more chances to encounter active on upper or down MXene sheets.<sup>[44]</sup> However, surface -OH and -F on MXene would disturb the continuity of hydrogen bond network formed between water molecules at interlayer space. Therefore, more uniform hydrogen network can be formed within few -OH functionalized MXene interlayer space, which facilitates proton transport with Grothuss mechanism and boosts the charge storage and rate capability of  $Ti_3C_2T_x$  MXene.<sup>[28]</sup> The network of hydrogen bonded lattice water is also critical for the high proton conduction in Prussian blue analogues cathode materials of proton batteries, which resembles to the energy storage behavior of MXene.<sup>[104]</sup> It could be concluded that the hydrated but narrow interlayer space are responsible for the high rate capability and capacitance, respectively in layered pseudocapacitive materials.

But as for 2D pseudocapacitive electrode materials ( $MoS_2$ , MXene,), the narrow but hydrated interlayer path is not enough for to achieve high-rate capability when mass



loading is applied. The ion transport channel can be reduced by decreasing the size of 2D sheets, which has been proved an efficient way to achieve good rate performance for high mass loading 2D materials electrodes. <sup>[95]</sup> The narrow, short and hydrated interlayer path are the critical factors for achieving fast intercalation of cations into interlayer path and achieve higher capacitance in layered materials.

In summary, pseudocapacitors store charge via fast redox reaction on/near electrode surface or fast ion intercalation into interlayer space of layered electrode materials. And a great number of experiments and research reveal that the hydrated waters and confined effect of these materials collectively contribute to the intercalation pseudocapacitance. Finally, the ideal interlayer path structure is summarized for intercalation-type materials in aqueous electrolyte, which should be (1) hydrated, (2) short and (3) suitably narrow. Nowadays, a great amount work is focused on the aqueous electrolyte. And the energy densities of supercapacitors are more sensitive to potential window than capacitance of electrodes due the equation  $E=1/2 CU^2$ , where E is energy density of devices, C refers to the capacitance and U denotes the potential window. More attentions should be moved on non-aqueous based pseudocapacitors due to broader voltage windows.



### 2.1.3 Hybrid supercapacitors (HCs)

Considering that batteries can deliver high energy density and supercapacitors show high rate capability, hybrid supercapacitors (HCs) are a kind of energy storage device that combine a battery type electrode and a supercapacitor electrode, enabling not only high energy density but also outstanding power density.<sup>[105]</sup> Nowadays, most HCs are composed of a Li-ion battery graphite anode and porous activated carbon cathode, which is also known as lithium-ion capacitors (LICs), as shown in **Figure 2.6** a,c.<sup>[7]</sup> The working potential for the LICs with this scheme can reach up to 4.2V. However, graphite anode in LICs cannot achieve high-rate performance so the assembled HCs cannot reach to the high-power densities comparable to EDLCs. To further increase the power performance of hybrid supercapacitors, T-Nb<sub>2</sub>O<sub>5</sub><sup>[94]</sup> and Ti<sub>3</sub>C<sub>2</sub>T<sub>x</sub> MXene<sup>[106]</sup> etc. that possess high rate charge/discharge ability are proposed to replace graphite anode and defective LiFePO<sub>4</sub> serves as capacitive and high-energy cathode,<sup>[96,97]</sup> as shown in (**Figure 2.6** b,d). In general, HCs are now at the infancy stage of investigation, which still have numerous challenges to be solved, like their cycling stability is far behind both EDLCs and PCs, and their energy densities are also much inferior to battery-type energy storage systems (Li, Na, K-ion batteries).<sup>[7]</sup>

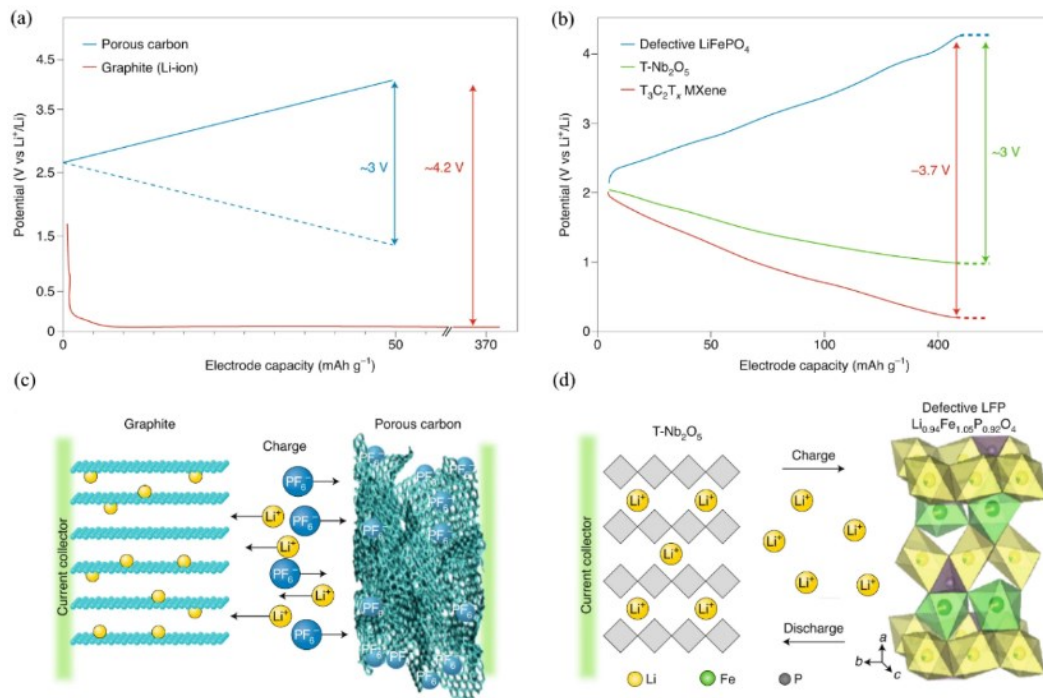


**Figure 2.6** (a), (c) Schematic for a Li-ion capacitor (LIC), which combines a battery-type negative graphite electrode with a positive porous carbon EDLC electrode. (b),(d) Concepts of HCs that pseudocapacitive Nb<sub>2</sub>O<sub>5</sub> or MXene negative electrode with a defective LFP positive electrode.<sup>[7]</sup>

To sum up, EDLCs, PCs and HCs are characterized by their own natures. PCs and HCs can deliver superior energy densities but lower power performance than EDLCs. In addition, supercapacitors are expected to exhibit multifunctional applications, like deformable supercapacitors, self-charge supercapacitors, self-healable supercapacitors, shape memory supercapacitors and electrochromic supercapacitors etc., which have been another research hotspot in recent years.<sup>[107]</sup>

## 2.2 Inactive components in supercapacitors

### 2.2.1 Electrolytes

The charge storage within supercapacitors proceed via the interaction between electrolyte ions and materials surface. Therefore, electrolyte also play the key role in determining the energy storage of supercapacitors. Electrolytes can be classified into liquid electrolyte, solid or quasi-solid-state electrolyte and redox-active electrolyte based on their own features, as shown in **Figure 2.7**. Liquid electrolyte can be further subcategorized into aqueous electrolyte and nonaqueous electrolyte.

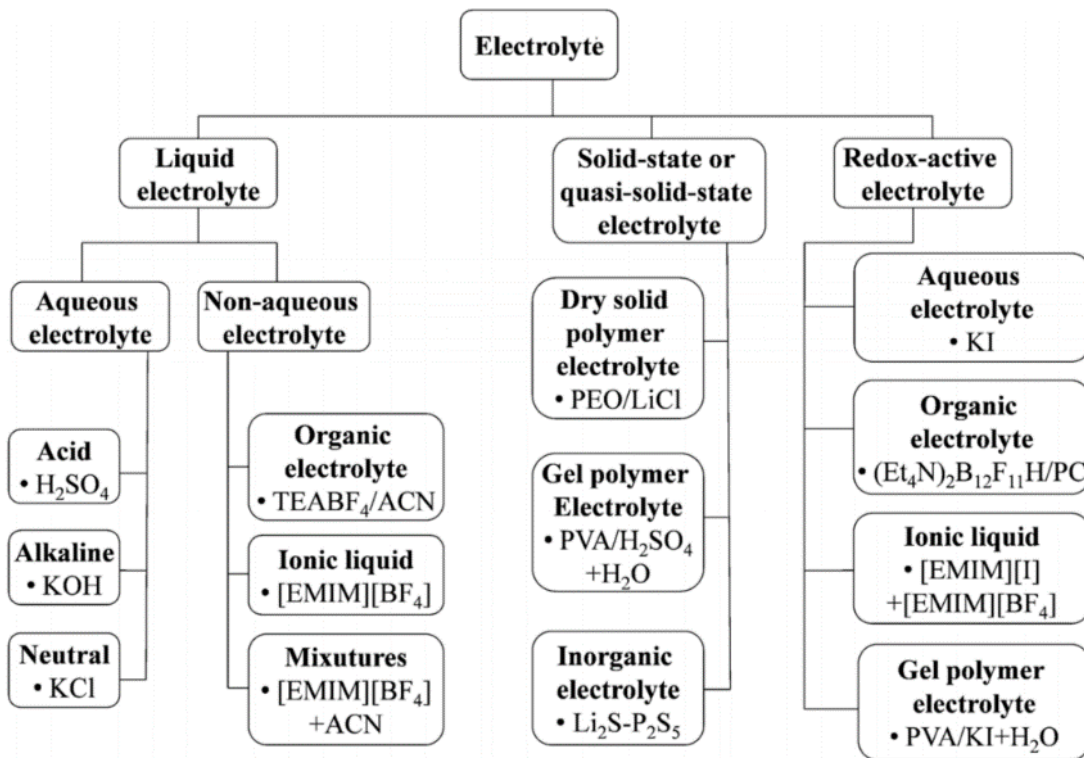


**Figure 2.7** Classification of electrolytes for supercapacitors.<sup>[16]</sup>



Aqueous electrolytes include acid, alkaline and neutral solutions. Acid aqueous electrolytes ( $\text{H}_2\text{SO}_4$ ,  $\text{H}_3\text{PO}_4$ ) can endow the supercapacitors with lower equivalent series resistance (ESR) than other neutral electrolytes due to higher ionic conductivity. KOH is the mostly used alkaline electrolyte for transition metal oxides and sulfides and phosphide electrode materials.<sup>[17, 108, 109]</sup> And the size of cations ( $\text{Li}^+$ ,  $\text{Na}^+$ ,  $\text{K}^+$ ) in alkaline electrolytes also affects the capacitance of transition metal oxides ( $\text{Co}_2\text{P}_2\text{O}_7$ ,  $\text{MnFe}_2\text{O}_4$  and  $\text{Bi}_2\text{WO}_6$ ).<sup>[16]</sup> N-doped carbon can exhibit the highest capacitance in alkaline electrolytes.<sup>[110]</sup> However, alkaline electrolytes might lead to the decay of capacitance due to the dissolution of electrode material.<sup>[111]</sup> Neutral electrolytes ( $\text{LiCl}$ ,  $\text{Na}_2\text{SO}_4$ ,  $\text{Li}_2\text{SO}_4$  etc.) exhibit lower ionic conductivity but can achieve the wider potential window (up to 2.2V) in symmetric supercapacitors than both acidic and alkaline electrolytes.<sup>[112]</sup>

Organic electrolytes and ionic liquids (ILs) deliver the lower capacitance than aqueous electrolytes when the electrode materials are the same due to inferior ionic conductivity. But wider potential window, 2.5~2.8V for organic electrolytes, and above 3V for ILs can be achieved in devices with these kinds of electrolytes than in those with aqueous electrolytes.<sup>[16]</sup> Therefore, nonaqueous electrolytes-contained supercapacitor can lead to the significant improvement of energy and power densities. Organic electrolytes are composed of salt and solvents. Typical organic electrolytes are prepared by dissolving Li ion salts,  $\text{LiClO}_4$  and  $\text{LiPF}_6$ , into PC, ACN, or a mixed liquid of different solvents,



like EC-DEC, EC-DMC, EC-EMS, EC-DMC-EMC and ECX-DMC-DEC to prepare typical electrolytes for supercapacitors.<sup>[113-115]</sup> Some organic electrolytes in Li-ion batteries can also be used in supercapacitors. Ionic liquids can deliver the relatively wider cell voltage in supercapacitors than organic electrolytes and avoid the safety issue of organic solvents. However, there are still some defects for ILs, such as high viscosity, inferior ionic conductivity, and high price, which restricts its practical application in supercapacitors.<sup>[116]</sup> ILs of common use in lab comprise [EMIM][BF<sub>4</sub>],<sup>[117]</sup> [BMIM][BF<sub>4</sub>],<sup>[116]</sup> [EMIM][FSI],<sup>[118]</sup> [EMIM][PO<sub>2</sub>F<sub>2</sub>],<sup>[119]</sup> and [EMIM][B(CN)<sub>4</sub>]<sup>[120]</sup> etc.

Solid-state electrolytes of supercapacitors are developed to meet the demand of powers for flexible electronics, wearable electronics, portable electronics, and printable electronics.<sup>[121]</sup> The application of solid-state electrolytes can simplify the package and fabrication process of supercapacitors and avoid the issue of liquid-leakage. Thus far, main attention is focused on polymer-based solid-state electrolytes, which can be further grouped into gel polymer electrolytes (GPE), solid polymer electrolytes (SPE) and polyelectrolytes.<sup>[16]</sup> GPE is the most studied and delivers the highest ionic conductivity among the three kinds of electrolytes. To prepare a GPE, a polymer matrix (also named host polymer) and a liquid electrolyte are mixed. Various polymer matrices, have been applied in the synthesis of GPE, like poly(vinyl alcohol) (PVA),<sup>[122]</sup> poly(ether ether ketone) (PEEK),<sup>[123]</sup> potassium polyacrylate (PAAK),<sup>[124]</sup>



poly(acrylonitrile)-block-poly(ethylene glycol)-block-poly(acrylonitrile)(PAN-b-PEG-b-PAN),<sup>[125]</sup> poly(vinylidene fluoride-co-hexafluoropropylene) (PVDF-HFP),<sup>[126]</sup> poly(ethyl oxide) (PEO),<sup>[127]</sup> and poly-(methylmethacrylate) (PMMA)<sup>[128]</sup>. The liquid electrolyte could be aqueous electrolyte or organic solvent containing conducting salt and ionic ILs. The GPE with aqueous solution is also named as hydrogel. Hydrogel tends to suffer from fluidity issues with increasing temperatures,<sup>[129]</sup> thus additives like , SiO<sub>2</sub> and TiO<sub>2</sub> etc. were added to improve its high-temperature rigidity.<sup>[130, 131]</sup> Similar with aqueous electrolytes, hydrogel electrodes also endow supercapacitor with limited voltage window. GPE with organic solvent named as organogel can achieve much wider cell voltage for supercapacitors (2.5~3V) than hydrogel.<sup>[132]</sup> GPE with ionic liquids is named as also ionogel, which can achieve a broader working potential range (3.5V) than both organogel and ionogel.<sup>[133]</sup> Note that some solid-state electrolytes, like the mixture of IL and epoxy, can serve as structural electrolytes for supercapacitors,<sup>[134]</sup> which can not only play the role of charge storage, but also serve as the components of bearing stress.<sup>[135]</sup> The feature of solid-state electrolytes greatly determine the mechanical performance of structural supercapacitors.

The final category is redox-active electrolyte which can provide extra redox reactions for charge storage in addition to the pseudocapacitance on the electrode surface. KI, HQ, teropoly acids, K<sub>3</sub>Fe(CN)<sub>6</sub>, etc. have been successfully applied as redox-active electrolytes for supercapacitors.<sup>[16, 136]</sup>



### 2.2.2 Current collectors

Current collectors refer to substrate that load active materials. The common substrate that can be used as current collectors comprises, golden sheet, silver sheet, copper sheet(foam), nickel sheet(foam), titanium sheet, carbon paper(cloth), graphite paper and glass sheet coated with indium tin oxide (ITO) etc.<sup>[137]</sup> As for some 2D materials, like MXene and graphene, free-standing films can be assembled with delaminated sheets, which can avoid the used of current collectors.<sup>[33, 138]</sup> The selection of current collector should follow the principle that the selected material cannot react with electrolyte during charge/discharge process and exhibits high electrical conductivity. Carbon materials and ITO are commonly used current collector in acid electrolyte. Nickle metal is applicable for the current media in alkaline solution due to its relatively low cost. Various material can be used for current collectors, such as, Ni,<sup>[139]</sup> Ti,<sup>[140]</sup> stainless steel<sup>[141]</sup> because of the much less corrosive nature of neutral electrolytes. Aluminum is widely applied in organic electrolytes and ionic electrolytes.<sup>[16]</sup>

### 2.2.3 Separators

Separator within supercapacitors locates between two electrodes, which serves as role to prevent direct contact and electron transfer between cathode anode of the devices. A qualified separator should be equipped with the features: (1) having low ion diffusion resistance, (2) possessing excellent chemical and electrochemical stability in



electrolytes, (3) exhibiting good mechanical performance to ensure its durability. The pore size, chemical composition and thickness of separator have been proved to greatly affect the performance of the assembled supercapacitor.<sup>[142]</sup> Both Nafion and GO film deliver high proton conductivity, thus is suitable to be applied as separator in supercapacitors with H<sub>2</sub>SO<sub>4</sub> electrolyte.<sup>[143, 144]</sup> In this research, we have also demonstrated that nafion film plays the key role for suppressing the self-discharge of Ti<sub>3</sub>C<sub>2</sub>T<sub>x</sub> MXene-based supercapacitors

## 2.3 Review of MXenes synthesis methods

Two-dimensional (2D) materials can exhibit some unique properties due to their atomic thickness and editable surface. Since successful synthesis of 2D graphene from graphite by mechanical exfoliation in 2004,<sup>[145]</sup> there have been a research upsurge on various 2D materials all over the world. As a new member of low-dimensional materials, MXenes are equipped with metal conductivity, hydrophilic surface, high tensile strength and outstanding stability in acid solution,<sup>[25, 27, 146]</sup> which makes them be investigated for various applications, such as supercapacitors,<sup>[38, 140]</sup> catalysts,<sup>[147]</sup> electromagnetic shielding<sup>[148]</sup> and batteries (including lithium ion, sodium ion, potassium ion and zinc batteries).<sup>[149-152]</sup> MXenes refer to 2D transition metal carbides/nitrides/carbonitrides and have a general formula of M<sub>n+1</sub>X<sub>n</sub>T<sub>x</sub>, where M is transition metal element (Ti, Cr, V, Mo, Sc, Nb), X denotes C and/or N, and T represents functional groups linked with surface metal atoms. **Figure 2.8** shows crystal structure

of four kinds of common MXenes,  $M_2XT_x$ ,<sup>[153]</sup>  $M_3X_2T_x$ ,<sup>[154]</sup>  $M_4X_3T_x$ <sup>[155]</sup> and  $M_5X_4T_x$ <sup>[156]</sup>. It can be observed that inner part of each MXene sheet is transition metal carbide/nitrides/carbonitrides which can makes it good electrical conductor, like  $Ti_3C_2T_x$  MXene possess a conductivity up to  $2.4 \times 10^6 \text{ S m}^{-1}$ ,<sup>[18, 157]</sup> and the surface -O groups endow MXenes with the properties of transition metal oxides. Surprisingly, surface -T terminations can be modified with N, S, Br, Cl, S etc. to modulate its physiochemical properties.<sup>[38, 106, 158, 159]</sup> Note that more metal layers in an individual MXene sheet can lead to better electrical conductivity.<sup>[160]</sup> Namely,  $M_5X_4T_x$  is the best electrical conductor within four kinds of structure when M and X are the same.

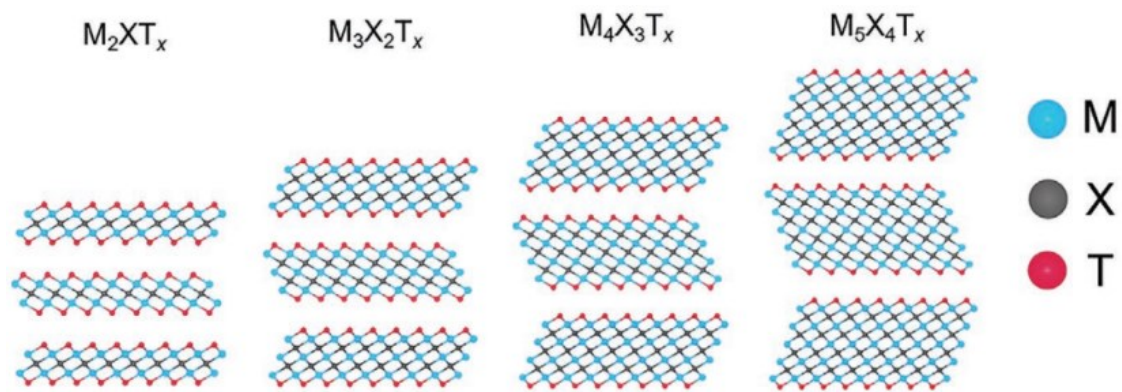


**Figure 2.8** Crystal structure of four common kinds of MXenes.<sup>[156]</sup>

The fascinating properties of MXenes inspire to explore easy, environmental and safe fabrication methods for their future large-scale application. Hexagonal  $M_{n+1}AX_n$  (MAX) phases are the precursors for synthesizing MXenes. The key point to prepare a kind of MXene is how to selectively etch off A-layer in its corresponding MAX precursor.

**Figure 2.9a** shows the typical process of MXenes, A-layer is deintercalated from the precursor in the first step via etching to obtain multilayered MXene, which is followed



by a further delamination procedure to obtain monolayer or few-layer MXene sheets.

**Figure 2.9b** depicts the fabrication history of MXene from its very first discovery with HF as etchant to recent HCl-hydrothermal method to eliminate Ga-layer in  $\text{Mo}_2\text{GaC}$ .<sup>[25, 161]</sup> Selective etching of MAX phase is due to metal bond between M and A, which is energetically active than the M-X. It is the feature that endow the MAX phase with selective etching ability and obtain corresponding MXenes.<sup>[162]</sup>

According to the development process, the synthesis of MXenes could be classified as (1) fluorine-involved liquid state etching, (2) alkaline etching, (3) electrochemical etching, (4) molten salt etching and (5) other etching methods.

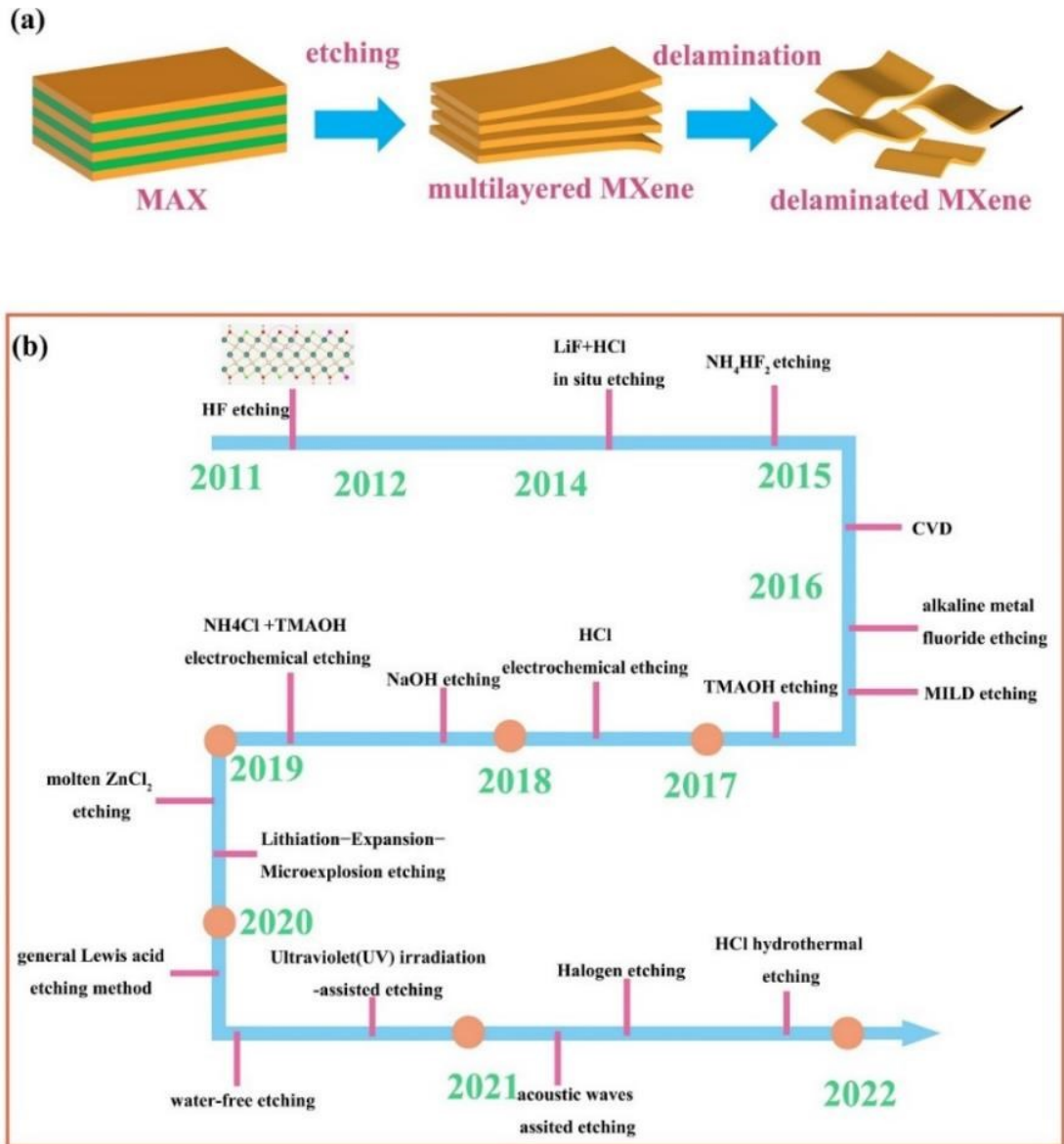


**Figure 2.9** (a) the fabrication process of MXene, and (b) the history of fabricating MXene with different methods.

### 2.3.1 Fluorine-involved liquid etching

Hydrofluoric (HF) acid solution was firstly exploited to remove A (Al, Si, Ga) element of precursors (**Figure 2.10a**).<sup>[25]</sup> MXenes fabricated through HF etching are abundant in surface -F, which is not favorable for its energy storage ability if applied as electrode



material in lithium ion batteries and supercapacitors.<sup>[149, 163]</sup> Thus, a subsequent heat treatment or alkalization was normally conducted to reduce surface fluorine concentration to boost the charge storage behavior.<sup>[164]</sup> To lower down the risk of operation of HF-etching method, an *in situ* HF-forming strategy with lithium fluoride and hydrochloric acid as etchant to etch A-layer in MAX phase was discovered.<sup>[154]</sup> In this method, the reaction between fluoride and acid can *in situ* form HF to achieve the selective etching of A-layer element of precursors. Thanks to absence of HF, the operation is safer and resultant MXene is clay-like, also called clay-method, and can be pressed into flexible films (**Figure 2.10b**) which can exhibit a high volumetric capacitance of  $900 \text{ mF cm}^{-3}$  ( $245 \text{ F g}^{-1}$ ).<sup>[154]</sup> In addition, to avoid the direct use of HF, ammonium dihydrogen fluoride aqueous solution was also applied to etch MAX phase. The  $\text{NH}_4\text{HF}_2$ -etched MXene shows the stronger oxidation-resistance than that etched through HF solution (**Figure 2.10c**), which can keep stable in air at temperature up to  $350^\circ\text{C}$ .<sup>[165]</sup> A intercalation along with sonication process is necessary for delaminating multilayered MXene, which inevitably reduce lateral size of MXene sheets and introduce extra defects.<sup>[166]</sup> The oxidation of MXene starts at edge or defects.<sup>[167, 168]</sup> Therefore it had better get rid of sonication process during the fabrication process of MXene sheets. Given this, minimally intensive layer delamination method (MILD) was proposed, which was optimized from the previous clay method.  $\text{Ti}_3\text{AlC}_2$  was also etched in the mixed  $\text{LiF} + \text{HCl}$  liquid, but both of them have higher concentrations in the etchant liquid than those in the clay method ( $12\text{M LiF}/9\text{M HCl}$  vs.  $5\text{M LiF}/6\text{M}$



HCl).<sup>[167]</sup> Here, extra lithium ions intercalate the interlayer space of MXene during etching process and only hand shaking enables its delamination after washing until the PH of supernatant reaches to ~6, resulting in stable colloidal solution (**Figure 2.10d**).

Ti<sub>3</sub>C<sub>2</sub>T<sub>x</sub> MXene is a good candidate for anode material of lithium ions batteries due to layered configuration and high conductivity.<sup>[149]</sup> And it has good application prospect in some anhydrous fields. It is expected to develop method to synthesize MXene in organic solvent for battery etc. applications with high sensitivity of humidity. Ammonium dihydrogen fluoride was dissolved in propylene carbonate (PC), acetonitrile (ACN), dioxane (DXN), N, N-dimethylformamide(DMF), N-methyl-2-pyrrolidone (NMP) and DMSO serving as etchant liquids to eliminate Al layer in Ti<sub>3</sub>AlC<sub>2</sub>, as shown in **Figure 2.10e**. Resultant MXene is equipped with abundant surface -F terminations and delivers two-time capacity of sodium storage than those synthesized in aqueous etching agent, which highlights the importance of anhydrous fabrication of MXene for battery applications.<sup>[169]</sup>

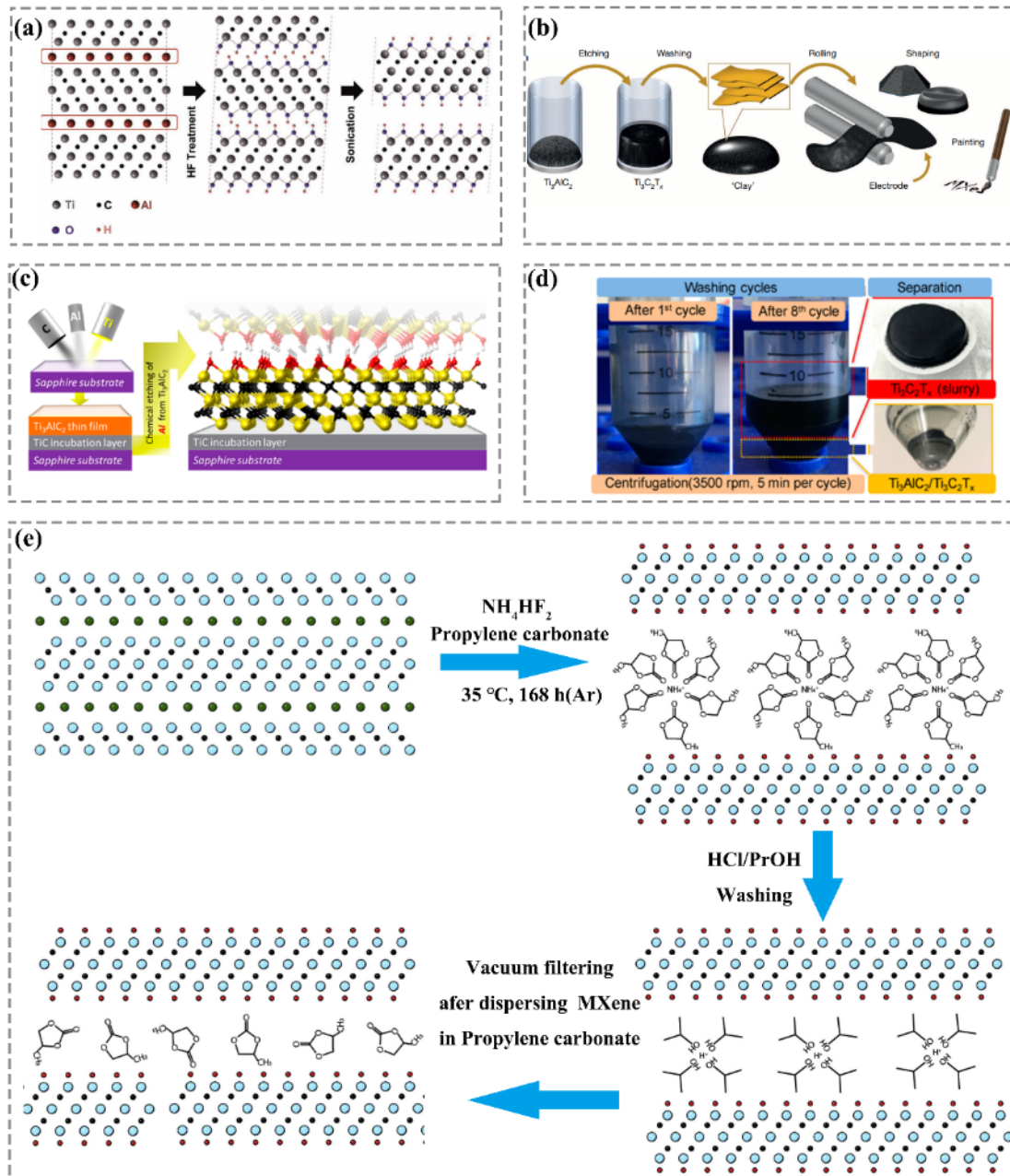


**Figure 2.10** (a) HF etching process,<sup>[25]</sup> (b) clay like MXene can be rolled into flexible film,<sup>[154]</sup> (c) surface  $Ti_3AlC_2$  was etched with  $NH_4HF_2$  aqueous solution,<sup>[165]</sup> (d) colloidal solution from MILD method can be collected by vacuum filtration,<sup>[167]</sup> (e) MXene was fabricated in  $NH_4HF_2$  PC solution.<sup>[169]</sup>

### 2.3.2 Alkaline etching

TMAOH was the first alkaline to etch MAX for obtaining  $Ti_3C_2T_x$  MXene. But before



alkaline etching,  $\text{Ti}_3\text{AlC}_2$  precursor was firstly washed by  $0.1\text{ g mL}^{-1}$  HF. Here HF washing is attempted to eliminate the surface titanium oxide, which expose Al for TMAOH's etching effect (**Figure 2.11a**). The resultant  $\text{Ti}_3\text{C}_2\text{T}_x$  MXene free-standing film electrode delivers a capacitance of  $173.5\text{ F g}^{-1}$  at  $2\text{ mV s}^{-1}$  in  $1\text{ M KOH}$  electrolyte. This work proves that the  $\text{Ti}_3\text{C}_2\text{T}_x$  MXene is a good candidate of efficient photothermal agent due to rich surface terminated  $\text{Al}(\text{OH})_4^-$  functional groups.<sup>[170]</sup> But this etching strategy is doubtful due to absence of repeatability.<sup>[167]</sup> In the light of amphoteric feature of aluminum in  $\text{Ti}_3\text{AlC}_2$  precursors, high concentration NaOH solution was used to selectively eliminate aluminum layer in the precursor.  $\text{Ti}_3\text{AlC}_2$  can be etched in  $27.5\text{ M NaOH}$  at  $270^\circ\text{C}$  using hydrothermal method (**Figure 2.11b**). Note that the Ar bubbling treatment before etching is necessary for the elimination of Al in  $\text{Ti}_3\text{AlC}_2$ . Eventually,  $52\text{ }\mu\text{m}$  NaOH-treated MXene can yield a capacitance of  $314\text{ F g}^{-1}$  ( $514\text{ F cm}^{-3}$ ) at  $2\text{ mV s}^{-1}$  in  $1\text{ M H}_2\text{SO}_4$ .

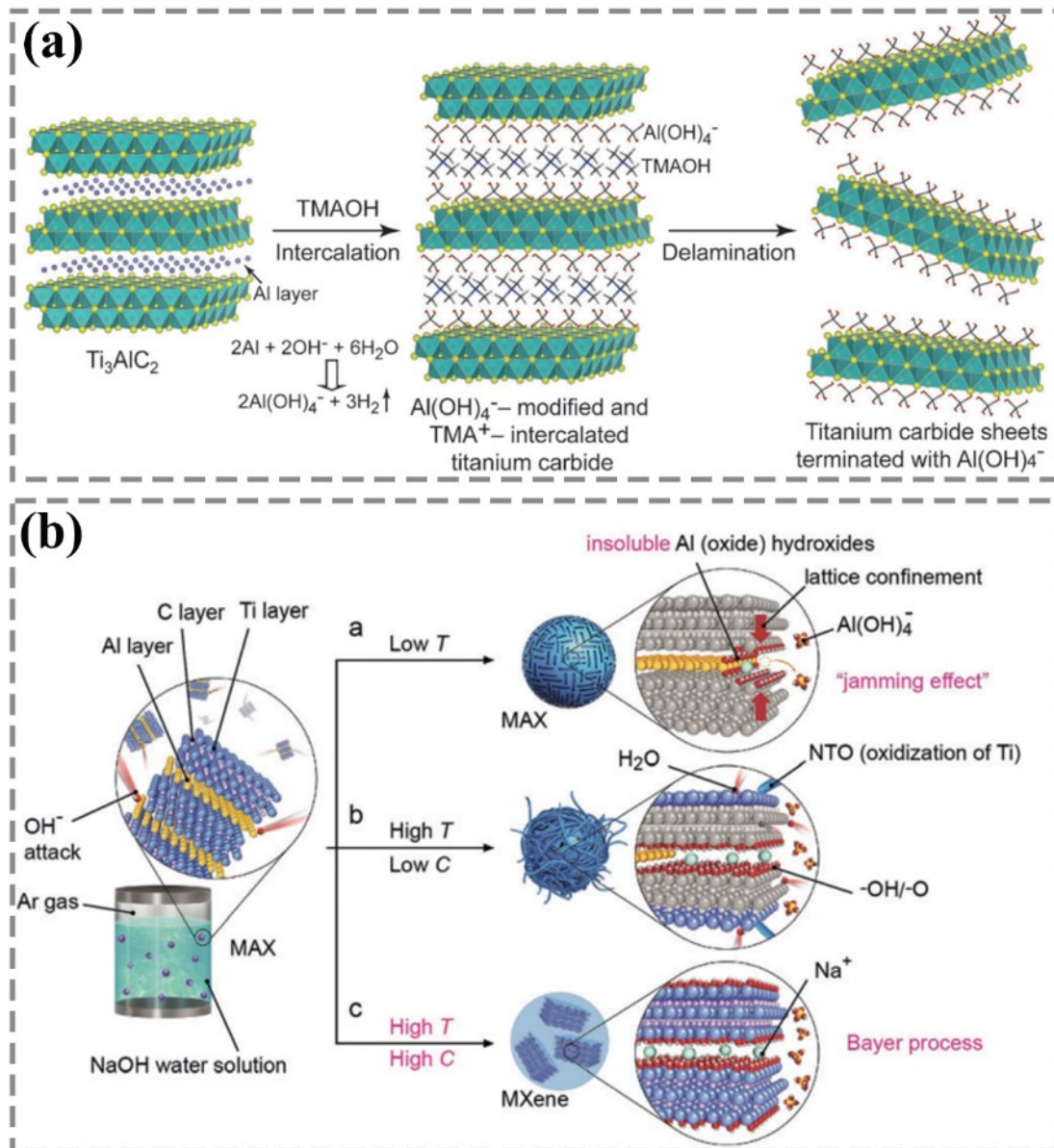


Figure 2.11 (a) TMAOH etching mechanism,<sup>[171]</sup> (b)NaOH etching principle<sup>[170]</sup>

### 2.3.3 Electrochemical etching

Electrochemical etching was first exploited to eliminate aluminum layer of  $Ti_2AlC$  in 2M HCl, contributing to the products of  $Ti_2CT_x$  MXene. But its further etching of precursor is restrained by the formed surface carbide derived carbon(CDC), as



elucidated in **Figure 2.12a**.<sup>[172]</sup> Thus the it is hard to be used for large-scale production of MXene. Given this, an optimized strategy was that  $Ti_3AlC_2$  block was etched in the mixed ammonium chloride and tetramethylammonium hydroxide (TMAOH) electrolyte. The outside Al was first deintercalated by  $Cl^-$  under a potential of 5V, followed by  $NH_4OH$  and  $TMA^+$  intercalation to facilitate further etching (**Figure 2.12b**).<sup>[173]</sup> With this method, the etching of aluminum layer in precursor can be finished within 5 hours. However, the intercalants like TMA are toxic. Thus, heating was applied to replace poisonous intercalant and open interlayer space of prepared MXene to assist the etching of underneath MAX phase during fabrication process (**Figure 2.12c**).<sup>[174]</sup> In addition,  $V_2AlC$  MAX phase can be etched in the mixed 21 M LiTFS and 1M  $Zn(OTf)_2$  electrolyte through respective CV cycling process within potential window of 0-2V.<sup>[175]</sup> Note that  $V_2AlC$  serves as cathode and Al layer was removed by  $F^-$  within charging process, driven by electric field of battery systems. It could be summarized that any electrolyte containing ions that have strong binding ability with Al may could be tried to conduct electrochemical etching of MAX precursors.

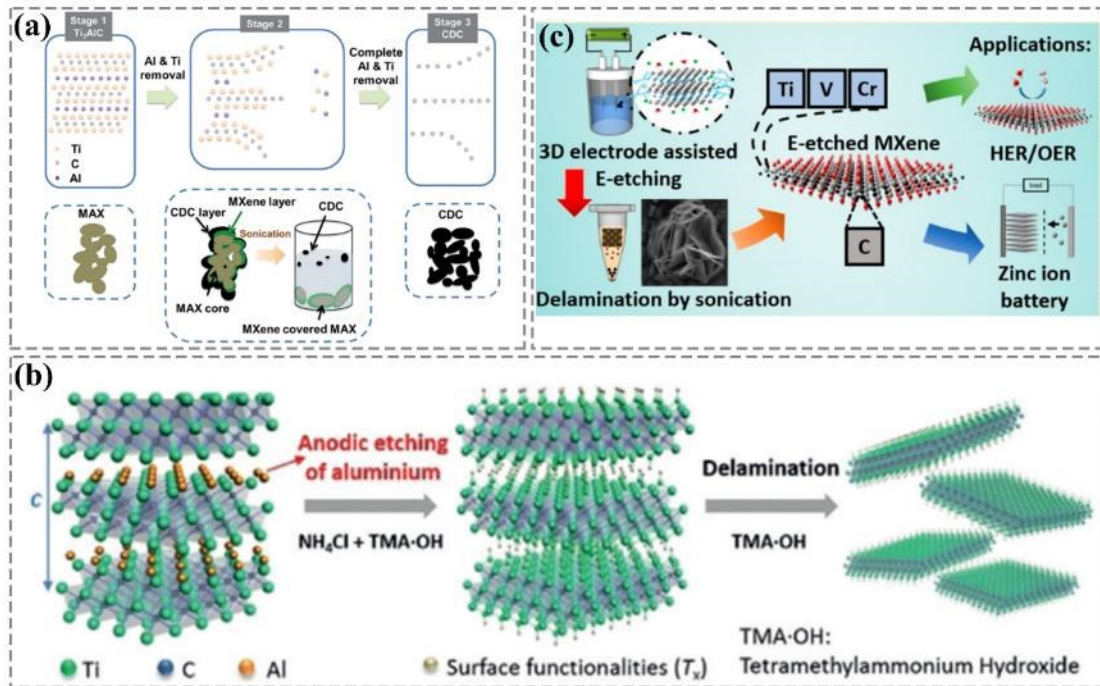


**Figure 2.12** (a) the electrochemical etching mechanism of  $Ti_2AlC$  in 1M HCl<sup>[172]</sup>, (b) fabrication of  $Ti_3C_2T_x$  MXene with electrochemical etching in TMAOH +  $NH_4Cl$  mixed solution,<sup>[173]</sup> (c) the 3D MXene fabricated from electrochemical etching strengthened by heating and application.<sup>[174]</sup> In addition, LiCl and LiOH mixed solution can also be used as electrochemical etching liquid to synthesize  $Ti_3C_2T_x$  MXene, which also bypass the use of hazardous intercalant.<sup>[176]</sup>

### 2.3.4 Molten salt etching

The very first molten salt to etch MAX is the mixture of  $LiF + KF + NaF$ . 400 mesh  $Ti_4AlN_3$  was etched in the mixed molten salt (KF: LiF: NaF mass ratio of 0.59: 0.29: 0.12) at 550°C for 30 min in Ar atmosphere (**Figure 2.13a**). Ar-atmosphere is a necessary factor for the successful production of MXene. In air, the resultant substance is rock salt structure of partially ordered vacancies.<sup>[177]</sup> Noble metal can replace Al element of MAX ( $Ti_3AlC_2$ ) though high temperature heat treatment to get  $Ti_3AuC_2$  and  $Ti_3IrC_2$  under the existence of noble-metal source.<sup>[178]</sup> The fabrication of MXene is



similar with the change of A-layer in MAX phase. Thus,  $\text{ZnCl}_2$  was first to be tried to replace Al in  $\text{Ti}_3\text{AlC}_2$ . The results show that Al can be replaced by Zn in the melt and excess  $\text{Zn}^{2+}$  serves etchant to deintercalate interlayer Zn, leaving  $\text{Ti}_3\text{C}_2$  terminated with Cl, as shown in **Figure 2.13b**.<sup>[179]</sup> To figure out the underlying etching mechanism, a general Lewis acid etching method with transition metal chlorides as etchant was proposed in 2020.<sup>[106]</sup> Free transition metal ( $\text{Zn}^{2+}$ ,  $\text{Cu}^{2+}$ ,  $\text{Ni}^{2+}$ ,  $\text{Co}^{2+}$ ,  $\text{Ag}^+$ ) ions in molten salt state are good acceptor of electrons and can react with exposed A-element to form volatile A-based chloride. The high temperature (550~750 °C) heating contribution makes the resultant chloride to be vaporized, boosting the underneath etching reaction with residual metal ions in molten salt. It should point out that any Lewis acid (cations) with higher redox potential than A-element can be used for selectively etching A layer in MAX phase precursor under molten state (**Figure 2.13c-d**).<sup>[106]</sup> Since the cation serves as the critical role in etching process, the anions in selected salt can be replaced by  $\text{F}^-$ ,  $\text{Br}^-$ ,  $\text{I}^-$  etc., leading to that resultant MXene is terminated with different function groups. For instance, molten tin fluoride ( $\text{SnF}_2$ ) was proved to be an efficient etchant to eliminate Al-layer in  $\text{Ti}_3\text{AlC}_2$  precursor and the resultant  $\text{Ti}_3\text{C}_2\text{T}_x$  MXene is rich in surface -F groups.<sup>[180]</sup>

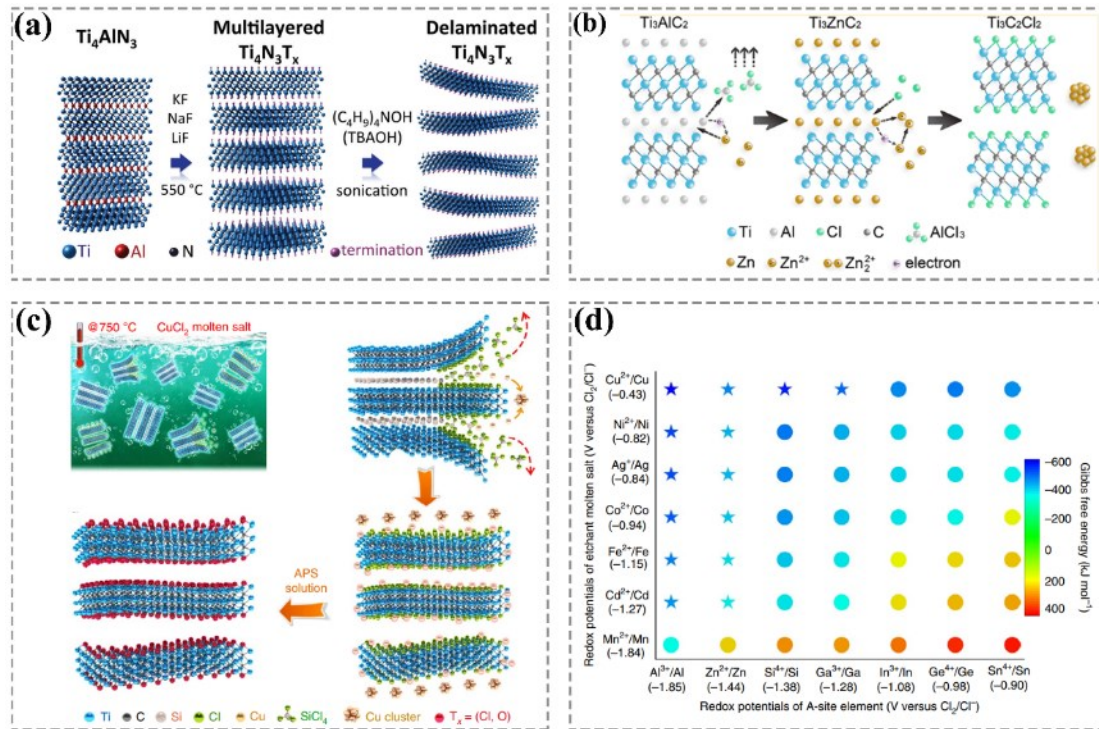


**Figure 2.13** (a) etching process of  $Ti_4N_3T_x$  in molten  $LiF + KF + NaF$ ,<sup>[177]</sup> (b) the element replacement of  $Ti_3AlC_2$  in molten  $ZnCl_2$  and further conversion to  $Ti_3C_2Cl_2$  MXene<sup>[179]</sup>, (c)  $Ti_3SiC_2$  was etched in molten  $CuCl_2$  and corresponding redox potential to proves the underlying mechanism of general Lewis method to etch MAX for MXene.<sup>[180]</sup>

Transition metal oxides were also selected to serve as precursors to synthesize 2D transition metal nitrides (TMNs) with alkaline ions as catalysis under molten state and ammonium gas supply, shown in **Figure 2.14**.<sup>[181]</sup> The resultant tungsten and molybdenum nitride show excellent hydrogen evolution performance.

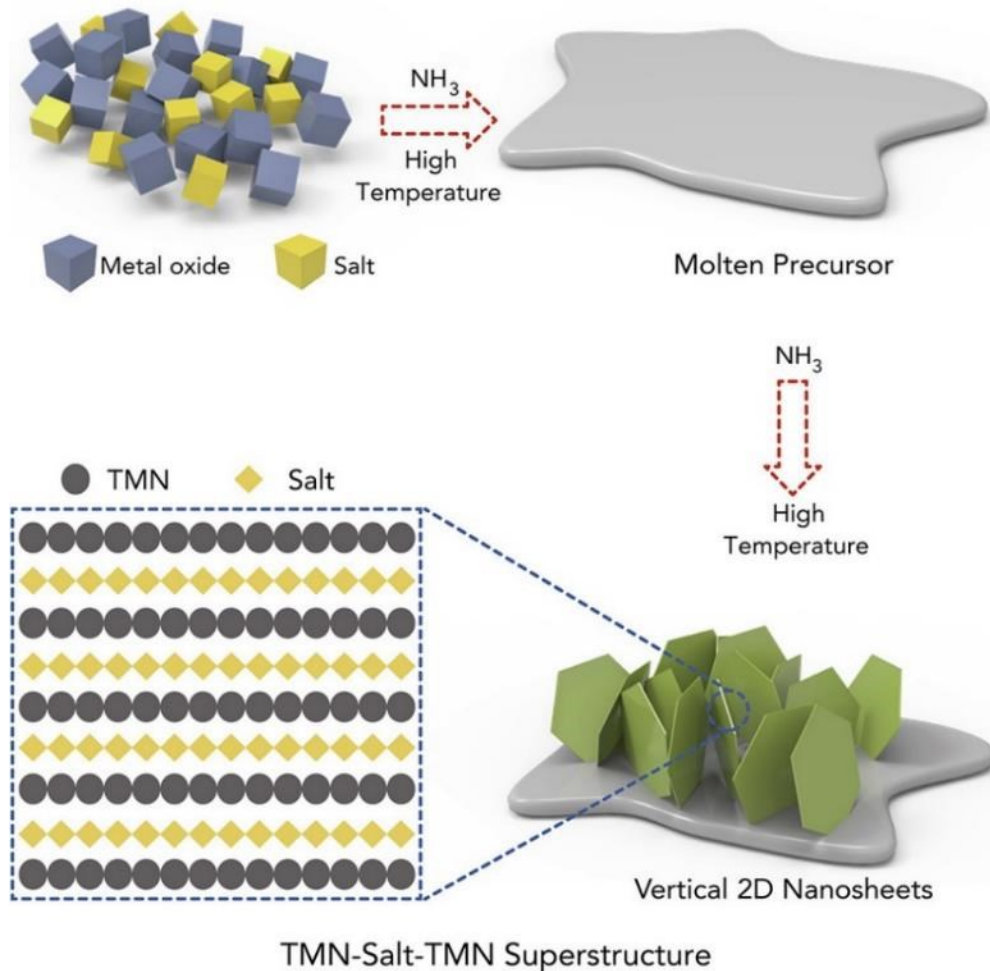


**Figure 2.14** Synthesis process of TMN in ammonium gas atmosphere.<sup>[181]</sup>

### 2.3.5 Other methods

#### (a) Lithiation–Expansion–Micro-explosion method

Lithiation–Expansion–Microexplosion is a method that relies on the lithium-aluminum alloying effect to exclude aluminum of  $\text{Ti}_3\text{AlC}_2$  to synthesize  $\text{Ti}_3\text{C}_2\text{T}_x$  MXene.  $\text{Ti}_3\text{AlC}_2$  and lithium serves as cathode and anode with 1M LiTFSI as electrolyte to assembly a coin cell, followed by applying an electrical potential to intercalate lithium into the A-layer site of MAX phase and the intercalated metal simultaneously form alloys with



aluminum layer. Afterwards, intercalated lithium react with water to produce LiOH and H<sub>2</sub>, which serve as etchant and intercalants, respectively, eliminating interlayer aluminum and leading to the delamination of the resultant MXene (**Figure 2.15a**).<sup>[182]</sup>

### **(b) Hydrothermal method**

Hydrothermal method with HCl as etchant is exploited to etch A-layer in some MAX precursors (Mo<sub>2</sub>GaC and Cr<sub>2</sub>AlC). The first-principle calculations reveal that the feasibility of etching MAX phase in HCl is due to the lower chemical potential of 'A' in AlCl<sub>3</sub> than that in MAX, which is the product when A is selectively etched off from precursors (**Figure 2.15b**).<sup>[161]</sup> The chemical potential of A in AlCl<sub>3</sub> can be regulated via changing reaction temperature and pressure, which exactly can be achieved by hydrothermal method. But only Mo<sub>2</sub>CT<sub>x</sub> was successfully synthesized using this scheme thus far, so the universality of fabricating MXenes using this method is still waiting for further verification.

### **(c) Ultraviolet (UV) irradiation-assisted etching**

Some MAX precursors, like Mo<sub>2</sub>GaC, are good ultraviolet (UV)-absorbing materials. UV light irradiation can boost the elimination of A-layer in this kind of precursor. Ga in Mo<sub>2</sub>GaC can be selectively etched in phosphoric acid under UV irradiation. The synthesized Mo<sub>2</sub>CT<sub>x</sub> MXene with this strategy are porous and can exhibit good rate capability when used as anode of batteries (**Figure 2.15c**).<sup>[183]</sup> Recently, Photon-Feton



(PF) reactions assisted by UV-vis light was also applied to synthesize  $Ti_3C_2T_x$  MXene.<sup>[184]</sup> This UV-Vis assisted method can produce electrophilic  $HO\cdot$  and  $O_2\cdot$  radicals, which can weaken Ti-Al bond in  $Ti_3AlC_2$  phase and promote the formation of high concentrated OH- anions in liquid, eventually leading to the elimination of Al-layer.<sup>[184]</sup> The resultant MXene is free of detrimental -F functional groups and shows strengthened bonding ability with sulfur, thus can be a promising host for sulfur in Li-S batteries applications.

#### **(d) Mechanical-energy-assisted etching**

In addition to UV light energy, mechanical energy can also be exploited to assist the synthesis of MXene. The  $Ti_3AlC_2 + LiF$  mixed solution was dropwise coated on a megahertz (MHz) order surface-localized vibrating plates for obtaining  $Ti_3C_2T_x$  MXene. Surface acoustic waves in the process boost that water decompose into proton and hydroxyl along with the decrement of PH of liquid drop. Due to existence of proton, HF will *in situ* form in the liquid then etch aluminum layer in  $Ti_3AlC_2$  precursor (**Figure 2.15d**). The whole etching process for a drop of liquid can be finished on the order of milliseconds.<sup>[185]</sup>

#### **(e) Halogen etching method**

The A-layer of MAX phase can be etched off in  $I_2 + ACN$  mixed nonaqueous solution for obtaining MXene. However, the etching process is time consuming (up to 5 days)



and electrical conductivity (1250 S/cm) of the prepared MXene through this method is inferior to those etched with HF or HF+LIF. In addition, the MXene sheets size is relatively small (less than 3 micrometers) in comparison to other synthesis methods.<sup>[186]</sup> Other halogen like, Br, ICl, BrI were also utilized to etch off aluminum layer in  $Ti_3AlC_2$  precursor for MXene. The resultant product is terminated with the functional groups that depend on the type of halogen etchant (**Figure 2.15e**). Similarly, the etching with other halogen is needed in organic solvent and additives are necessary for stabilizing etched byproducts. In addition, the whole process should be conducted in inert atmosphere, like in glovebox thus the strategy is hard to be widely applied for the mass production of MXene.<sup>[187]</sup>

#### **(f) Chemical vapor deposition (CVD) method**

By contrast to the strategies that etch MAX phase for MXene (top-down method), chemical vapor deposition (CVD) that is a down-top method is developed for the synthesis of MXene. Methane gas flows to the heated (1085°C) copper foil sitting on molybdenum foil to grow  $Mo_2C$  MXene on its upper surface. During the growth process, low methane concentration is provided to avoid the formation of graphene and rapid cooling to restrict the generation of molybdenum nanocluster.<sup>[188]</sup> Inspired by  $Mo_2C$  on molten copper surface, and high methane concentration leads to the formation of graphene. Kian Ping Loh et al. proposed to grow  $Mo_2C$  MXene on formed graphene under high  $CH_4$  flow rate.<sup>[189]</sup> Benefited from the passivation of graphene, centimeter-



scale Mo<sub>2</sub>C film with nanometer-scale thickness was successfully deposited on graphene (**Figure 2.15f**).<sup>[189]</sup> In addition to Mo<sub>2</sub>C MXene, other 2D transition metal carbides and nitrides have been also prepared using CVD methods, including WC and MoN.<sup>[190]</sup>

In summary, although various methods have been reported to synthesize MXenes. But these methods in hand still cannot meet the demand of large-scale production. In addition, the stability of MXenes in air is still an arduous challenge waiting for solution. It should pay more attention on how to achieve scalable production and increase the stability of MXenes, when developing their synthesis methods.

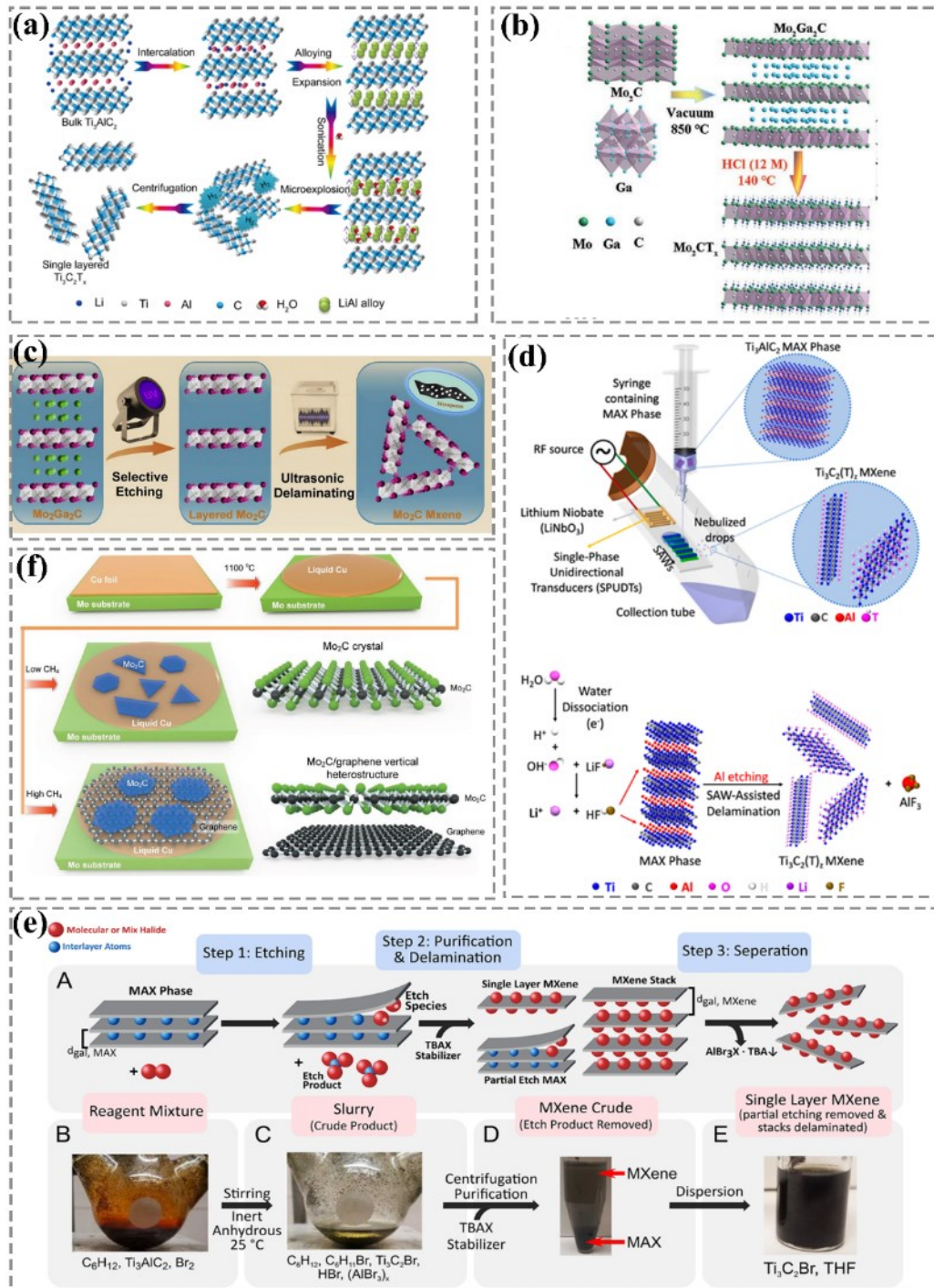


**Figure 2.15** (a) the mechanism of Lithiation–Expansion–Microexplosion etching method, <sup>[182]</sup> (b) the etching process of  $Mo_2GaC$  under hydrothermal process in  $HCl$  solution, <sup>[161]</sup> (c) UV irradiation to assist the selective etching  $Ga$  in  $Mo_2GaC$  in phosphoric acid solution, <sup>[183]</sup> (d) the principle of Mechanical-energy-assisted etching method, <sup>[185]</sup> (e) the process of halogen etching  $Al$  in  $Ti_3AlC_2$  and <sup>[187]</sup> (f) CVD method to grow  $Mo_2C$  MXene/graphene and  $Mo_2C$  MXene on pure copper foil. <sup>[189]</sup>

## 2.4 $\text{Ti}_3\text{C}_2\text{T}_x$ MXene for the supercapacitor electrode material

The inner part (M-C) of 2D MXenes sheets is transition metal carbides, which endows the materials with high conductivity. And the outer section in the crystal structure (M-O) is transition metals oxides serving active sites for redox reactions, shown in Figure 2.16a.<sup>[140]</sup> These unique features make the materials promising pseudocapacitive electrode materials for supercapacitors. Thus far,  $\text{Ti}_3\text{C}_2\text{T}_x$  is the most studied among all synthesized MXenes and delivers the highest capacitance in acid solution.<sup>[191]</sup> The energy storage of  $\text{Ti}_3\text{C}_2\text{T}_x$  MXene in acid electrolyte proceeds with the below mechanism,<sup>[28]</sup>



The resultant  $\text{Ti}_3\text{C}_2\text{T}_x$  is multilayered after the etching of  $\text{Ti}_3\text{AlC}_2$ , which normally shows accordion-like morphology (**Figure 2.16b**).<sup>[25]</sup> To increase the availability of active sites to electrolyte, multilayer MXene is delaminated into few layer counterpart (**Figure 2.16c**) via sonication<sup>[36]</sup> or combining intercalation of intercalants into interlayer space and subsequent sonication processes.<sup>[166, 192]</sup> The resultant aqueous few-layer MXene sheets solution shows Tyndall effect when a laser transmits it, suggesting its colloidal nature, shown in **Figure 2.16d**. These sheets also can be assemble into flexible free-standing films via vacuum filtration (**Figure 2.16e**),<sup>[193, 194]</sup> which can be used for electrodes of flexible energy storage devices.<sup>[33, 43]</sup>

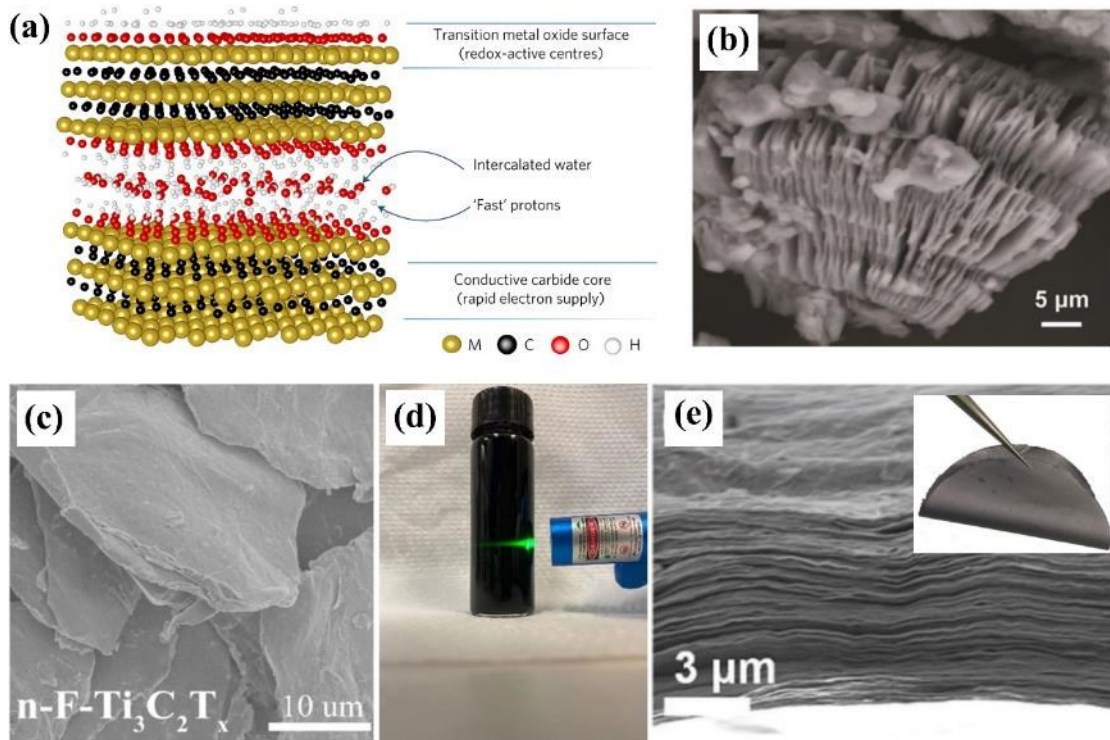


**Figure 2.16** (a) Schematic diagram of MXene structure,<sup>[140]</sup> (b) SEM figure for accordion like multilayer  $Ti_3C_2T_x$  MXene,<sup>[25]</sup> (c) SEM few-layered  $Ti_3C_2T_x$ ,<sup>[36]</sup> (d) Photo for  $Ti_3C_2T_x$  MXene aqueous colloidal solution shows Tyndall effect when a laser transmits it , (e) SEM figure for cross section of  $Ti_3C_2T_x$  MXene free-standing film,<sup>[194]</sup> and inset shows the good flexibility of the film.<sup>[193]</sup>

This subchapter first elucidates the energy storage behavior of  $Ti_3C_2T_x$  MXene in different electrolytes, followed by the introduction of the strategies to alleviate the restacking of MXene sheets and boost its capacitive performance for supercapacitors applications.

### 2.4.1 $Ti_3C_2T_x$ MXene energy storage behavior in different electrolyte

It has been confirmed that the pseudocapacitance of  $Ti_3C_2T_x$  MXene in acid electrolytes originates from the protons bonding/debonding with its surface -O functional groups,



which leads to the variation of titanium valence states.<sup>[28, 195]</sup> However,  $\text{Ti}_3\text{C}_2\text{T}_x$  MXene with different functional groups, interlayer space and current collectors shows various shape of CV curves along with diverse potential windows. The potential window of determine the energy density with more extent than the capacitance according to formula  $E = 1/2 CU^2$ , which is always neglected by researchers of MXene. **Figure 2.17a** is the comparison of CV curves for  $\text{Ti}_3\text{C}_2\text{T}_x$  MXene synthesized by HF etching, the MXene treated with KOH, KOAc and DMSO-assisted delaminated MXene.<sup>[196]</sup> The resultant four samples show different surface functional groups and different integrated area are observed in them, indicating the composition of surface functional groups on  $\text{Ti}_3\text{C}_2\text{T}_x$  MXene determines its energy storage ability. Density functional theory (DFT) calculations results reveal that surface -F and -OH functional groups prohibit ion transport to active sites and lead to the loosen interaction between intercalated ions and MXene surface, whereby contributing to inferior specific capacitance and fast self-discharge behavior.<sup>[28, 45, 149]</sup> Further experiments verify that the elimination of surface -F and -OH of HF-synthesized  $\text{Ti}_3\text{C}_2\text{T}_x$  MXene (HF-  $\text{Ti}_3\text{C}_2\text{T}_x$ ) through the combination of KOH treatment and 400°C annealing can not only boost its redox reaction but also expand the working potential window, shown in **Figure 2.17b**. That is why the LiF-HCl etched  $\text{Ti}_3\text{C}_2\text{T}_x$  that has the less surface -F amount than that prepared by HF exhibits a more broadened potential window but higher capacitance (**Figure 2.17c**).<sup>[41]</sup> In the meantime, it founds that expansion of interlayer space via intercalation of large cations ( $\text{Ca}^+$ ) in HF- $\text{Ti}_3\text{C}_2\text{T}_x$  MXene cannot expand its working potential window,



proving that the surface chemistry nature of MXene plays a more critical role in its stable potential window for energy storage than interlayer space. However, different potential windows for the same MXene free-standing film are also observed. **Figure 2.17d-e** are the CV figures for  $\text{Ti}_3\text{C}_2\text{T}_x$  MXene free-standing films synthesized via LiF+HCl etching but the current collectors for the two figures are platinum clip and glass carbon sheet, respectively.<sup>[197]</sup> Their different potential windows and CV shapes indicates the current collectors should also affect the electrochemical measurements results. A reasonable explanation for the difference is due to that Pt collector will cause hydrogen evolution at low potentials, whose current signal will couple with that from energy storage of MXene, mistakenly show different CV shape or energy storage behavior. This research also measured CV plots (**Figure 2.18**) for HCl-LiF etched multilayer MXene loaded on carbon cloth (PC), oxygen plasma treated carbon cloth (OC), graphite paper (GP) and titanium foil (Ti) with same mass loading. The CV shapes of PC and OC is evidently different from those of GP and Ti, further proving the argument. In addition, the feasibility of electrolyte ions to active sites also influences the energy storage behavior. For example, the pressed MXene electrode with delaminated MXene powder shows a different CV (**Figure 2.17f**) shape from that porous MXene aerogel and low mass loading MXene free-standing film electrodes due to sluggish ion diffusion kinetics.<sup>[34]</sup>

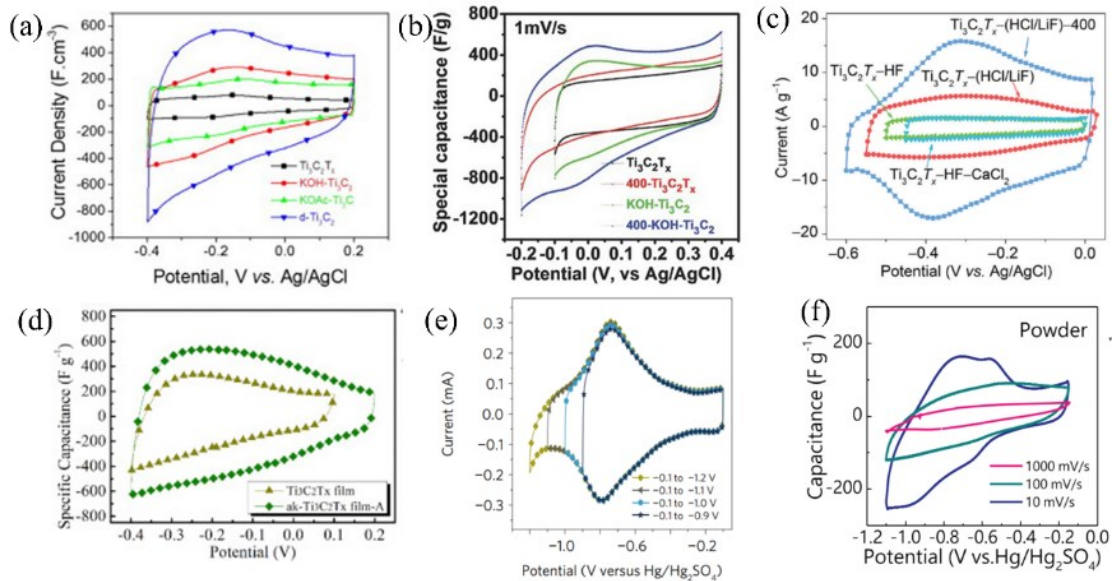


**Figure 2.17** CV curves for (a)  $\text{Ti}_3\text{C}_2\text{T}_x$  MXene etched with HF ( $\text{Ti}_3\text{C}_2\text{T}_x$ ), followed by treating with KOH ( $\text{KOH-Ti}_3\text{C}_2$ ) or KOAc ( $\text{KOAc-Ti}_3\text{C}_2$ ) and being delaminated with assistance of DMSO,<sup>[196]</sup> (b) HF-synthesized  $\text{Ti}_3\text{C}_2\text{T}_x$  and treated with 400 °C heating ( $400\text{-Ti}_3\text{C}_2\text{T}_x$ ), KOH ( $\text{KOH-Ti}_3\text{C}_2\text{T}_x$ ) and KOH+400 °C heating ( $400\text{-KOH-Ti}_3\text{C}_2$ ),<sup>[163]</sup> (c) HF-synthesized  $\text{Ti}_3\text{C}_2\text{T}_x$  ( $\text{Ti}_3\text{C}_2\text{T}_x\text{-HF}$ ), and followed by treating with  $\text{CaCl}_2$  solution to expand interlayer space ( $\text{HF-Ti}_3\text{C}_2\text{T}_x\text{-CaCl}_2$ ), HCl+LiF synthesized MXene ( $\text{Ti}_3\text{C}_2\text{T}_x\text{-(HCl/LiF)}$ ) and followed by heating at 400 °C in ammonia atmosphere ( $\text{Ti}_3\text{C}_2\text{T}_x\text{-(HCl/LiF)-400}$ ),<sup>[41]</sup> (d) delaminated MXene sheets assemble a free-standing film ( $\text{Ti}_3\text{C}_2\text{T}_x$  film) and KOH + annealing treated film ( $\text{ak-Ti}_3\text{C}_2\text{T}_x$  film-A), whose collectors are Pt clamp for EC performance measurement,<sup>[197]</sup> (e) delaminated MXene free-standing film whose current collector is glass carbon EC EC characterization electrochemical measurement,<sup>[140]</sup> (f) freeze-dried MXene powder<sup>[34]</sup>

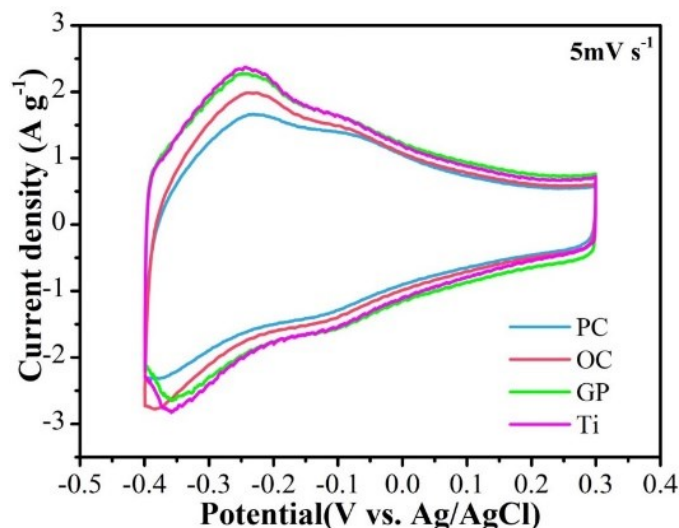
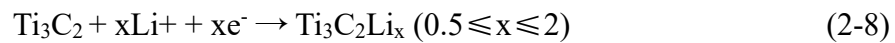


**Figure 2.18** CV curves of HCl+LiF etched  $\text{Ti}_3\text{C}_2\text{T}_x$  MXene tested with different collector collectors.



The energy storage of  $Ti_3C_2T_x$  MXene in neutral aqueous electrolyte with transition metal ions behaves like EDLCs, such as in 1M LiCl, as shown in **Figure 2.19a**, thus leading to inferior capacitances.<sup>[35, 198]</sup> It is believed that the intercalated metal cations ( $Li^+$ ,  $Na^+$ ,  $K^+$ ,  $Al^{3+}$  etc.) is hydrated thus interact with MXene surface with an electrical double layer mode due to the absence of direct interplay between them.<sup>[199]</sup> However, there are still some works believing that the energy storage mechanism in those neutral is pseudocapacitive due to existence of broaden redox peaks, and the corresponding underlying mechanism is shown below,<sup>[200-202]</sup>



Therefore, much deepen work are required to conducted to further reveal the energy storage mechanism of MXene in neutral aqueous electrolytes, which may be used to boost its capacitance.

The charge/discharge behavior of MXene in alkaline solution is similar to that in neutral electrolyte (**Figure 2.19b**). However, Ti-C bonds in  $Ti_3C_2T_x$  MXene are easily broken by the -OH in alkaline electrolyte with the mechanism of hydrolysis reaction, which leads to the unsatisfying cyclic stability.<sup>[202-204]</sup>

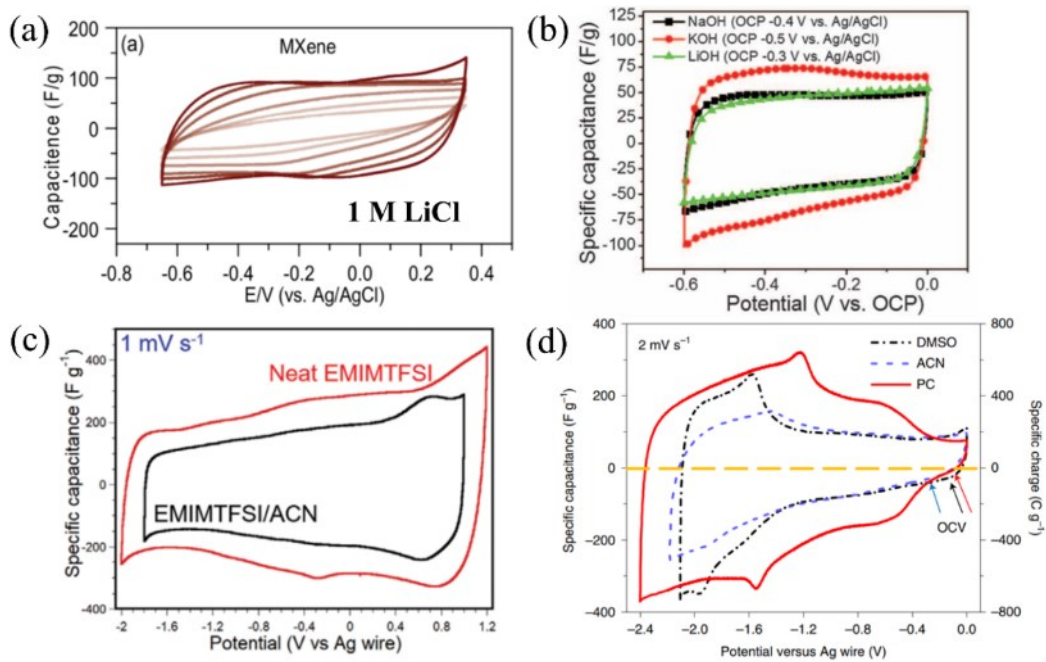


**Figure 2.19** CV plots for  $Ti_3C_2T_x$  MXene in (a) 1M LiCl,<sup>[35]</sup> (b) alkaline electrolytes (LiOH, NaOH, KOH),<sup>[205]</sup> (c) 1-ethyl-3-methylimidazolium bis-(trifluoromethylsulfonyl)-imide (EMIMTFSI) and its 1M acetonitrile (ACN) solution,<sup>[206]</sup> (d) lithium bis(trifluoromethylsulfonyl) amine (LiTFSI) solution with dimethyl sulfoxide (DMSO), propylene carbonate(PC) and acetonitrile (ACN) as solvents.<sup>[207]</sup>

The potential windows of MXene in aqueous electrolyte are limited (<1.23V), thus ionic liquids and organic electrolytes are applied to replace aqueous solution to expand potential window. **Figure 2.19c** shows the CV curves of  $Ti_3C_2T_x$  MXene in pure 1-ethyl-3-methylimidazolium bis-(trifluoromethylsulfonyl)-imide (EMIMTFSI) ionic liquid and its 1M acetonitrile (ACN) solution, which show a potential window of up to 3.2V.<sup>[206]</sup> Obvious redox peaks can be observed in the both electrolytes, indicating the pseudocapacitive energy storage mechanism and intercalated cations in ionic liquid direct interact with MXene surface, contributing to Faradic charge transfer. But the addition of solvent weakens the interplay between MXene and EMIM<sup>+</sup> and decrease



the stable potential window.<sup>[206]</sup> The energy storage of MXene in other nonaqueous electrolytes is also pseudocapacitive, and the charge transfer between intercalated cations and MXene occurs via orbital hybridization.<sup>[199]</sup> Take  $\text{Li}^+$  contained organic electrolyte for example, the  $\text{Li}^+$  ions that are shuttled within the interlayer space will be partially or completely desolvated, contributing to the pseudocapacitance behavior.

**Figure 2.19d** is the CV figures of MXene in lithium bis(trifluoromethylsulfonyl) amine (LiTFSI) solutions with dimethyl sulfoxide (DMSO), propylene carbonate(PC) and acetonitrile (ACN) as solvents.<sup>[207]</sup> Lithium ions in PC solvents are fully desolvated when intercalating interlayer space, resulting in the higher capacitance than those in both DMSO and ACN solvents. That is because that the interlayer space without solvents not only boosts the ion transport, but also strengthen  $\text{Li-Ti}_3\text{C}_2\text{T}_x$  interactions.

The potential window of MXene in water in salt (WIS) will broaden with the increased concentration of salts and MXene also exhibits better oxidation resistance in electrolyte with higher concentrations.<sup>[208]</sup> Desolvation-free cations insertion mechanism was observed in WIS ,which cause a pair of sharp redox peaks with large peak potential separation in CV curves.

To sum up, the energy storage of  $\text{Ti}_3\text{C}_2\text{T}_x$  MXene in acidic aqueous electrolyte is pseudocapacitive, which proceeds through proton bonding/debonding with surface -O functional groups. And the rich surface -F functional groups impede the electrolyte ion



diffusion to active sites, weaken the adsorption force of intercalated ion on MXene surface and decrease the working potential window. For a comprehensive evaluation energy storage ability of MXene in acid solution, suitable current collectors should be selected to avoid hydrogen evolution on current collectors during EC measurements. And the architecture of electrodes and interlayer space greatly affect ion diffusion kinetics. By contrast, charge storage of MXene in both neutral and alkaline aqueous electrolytes proceeds more like EDLCs due to almost rectangular CV shapes. But the underlying energy storage mechanism is waiting for further investigation. Both ionic liquid and organic electrolytes can endow MXene with much broader potential windows than aqueous electrolytes. More obvious redox peaks are shown in the two kinds of electrolytes and solvents in organic electrolytes play the vital for the cation intercalation and the interaction with MXene. And the suitable solvents will lead to the insertion of completely desolvated cations into the  $Ti_3C_2T_x$  MXene interlayer, whereby boosting the energy storage and rate capability.

#### **2.4.2 Surface modification to boost performance**

The functional groups in  $Ti_3C_2T_x$  MXene mainly include -F, -O, -OH and its pseudocapacitance is through the proton bonding/debonding with surface -O terminations. In addition, surface -F and -OH groups block electrolyte ion transport to active sites and lower the adsorption energy of ions, thus are unfavorable for charge storage.<sup>[45, 163]</sup> After understanding the role of each kind of functional groups in energy



storage, surface modification is the first strategy to be undertaken for enhanced capacitance. There are two main directions to modulate MXene surface: (1) engineer more -O and decrease -F on the surface, (2) hetero atom doping to create more active sites and strengthen the interplay between MXene and electrolyte ions. Immersion of  $Ti_3C_2T_x$  into potassium solution along with subsequent annealing in argon atmosphere is the first scheme (**Figure 2.20a**), which can not only eliminate the adverse -F and -OH functional groups but also sustain the interlayer path open with intercalated potassium cations as pillars.<sup>[163]</sup> The resultant MXene shows a great improvement from  $244 F g^{-1}$  to  $500 F g^{-1}$  due to more spacious interlayer space and more active sites. Here, the removal of -F and -OH is believed to cause more Ti exposed to electrolyte,<sup>[163]</sup> but the underlying mechanism is still unclear.<sup>[197]</sup> In addition, washing MXene with alkaline would inevitably lead to the breakage of sheet structure and decrement of conductivity. Given this, nucleophilic reagent, N-butyllithium(n-BuLi), was applied to turn -OH and -F into -O, shown in **Figure 2.20b**.<sup>[36]</sup> Different from alkaline treatment, this method would not destroy crystal structure of MXene but increase the number of active sites (-O) and decrease -F on MXene. Similarly, partial oxidation via treating  $Ti_3C_2T_x$  ammonium persulfate can also achieve the reduction of -F on MXene surface and richer -O surface active sites for enhanced energy storage ability (**Figure 2.20c**). In addition, the -O functional groups on  $Ti_3C_2T_x$  MXene can endow it with greater thermal dynamic stability than other terminals (-F, -Cl, -OH) and also better oxidation resistance ability.<sup>[209, 210]</sup>

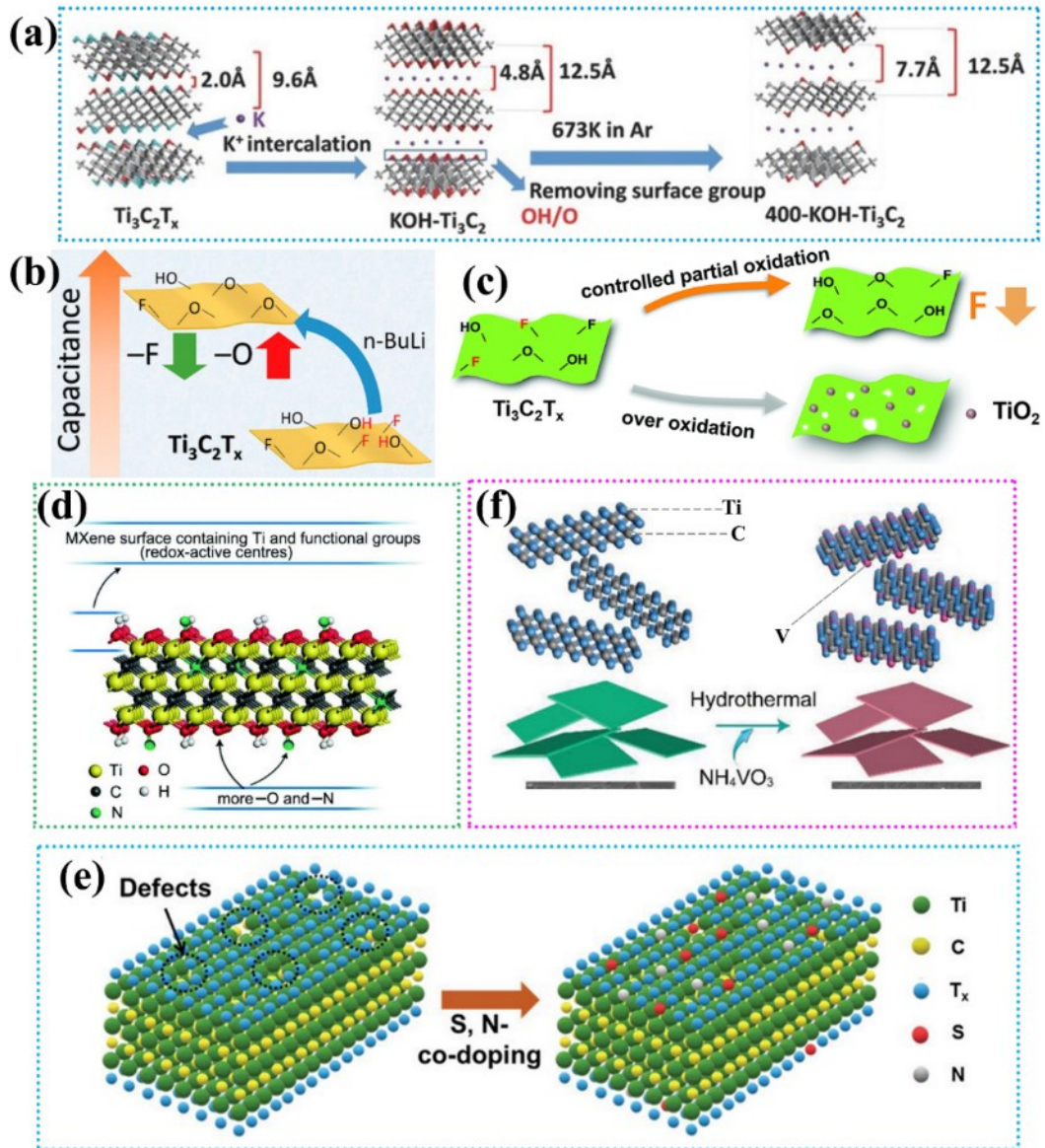


**Figure 2.20** (a) schematic diagrams for KOH alkalization and heating treatment of  $Ti_3C_2T_x$  MXene,<sup>[163]</sup> (b) modifying  $Ti_3C_2T_x$  MXene with N-Butyllithium to decrease surface -F and changes surface -OH into -O groups,<sup>[36]</sup> (c) Partial oxidation of MXene to decrease -F and engineer more surface -O,<sup>[211]</sup> (d) crystal structure of N-doped MXene,<sup>[41]</sup> (e) Schematic diagram for N,S co-doped  $Ti_3C_2T_x$  MXene,<sup>[43]</sup> and (f) V-doping process of  $Ti_3C_2T_x$  MXene.<sup>[201]</sup>

The electronegativity of surface functional groups on  $Ti_3C_2T_x$  MXene determines its electron donor ability, which affects the bonding behavior between MXene and electrolyte ions.<sup>[41]</sup> Heteroatom doping can be used to modulate the electronic band



structure of MXene for boosting the redox reaction between electrode surface and electrolyte ions. Nitrogen has been incorporated into MXene via heating in the ammonium gas and the doped element either replaces the lattice carbon or links with surface oxygen in  $Ti_3C_2T_x$  MXene (**Figure 2.20d**). N-doped MXene exhibits evident increment in capacitance, which is ascribed to newly formed surface -O-N groups that can provide more electrons than pure -O terminations to fulfil more proton bonding. Additionally, the doped elements, like S, can make up fragile surface titanium defects on MXene (**Figure 2.20e**), leading to enhanced environmental stability in addition to contributing to ameliorative energy storage ability. Note that doping element is not limited to N, S etc. light elements, the Ti in  $Ti_3C_2T_x$  can be replaced by other metal atoms using certain doping strategies. V was successfully introduced into the outer metal layers of  $Ti_3C_2T_x$  and locally replace titanium via hydrothermal method (**Figure 2.20f**),<sup>[201]</sup> contributing to highly enhanced pseudocapacitive performance in neutral electrolyte (2M KCl). As mentioned in section 2.3.1, energy storage of  $Ti_3C_2T_x$  MXene in neutral electrolyte resemble that of EDLCs and the intercalated ions interact with MXene surface with an EDL model. The strengthened performance in V-doped  $Ti_3C_2T_x$  MXene is attributed to the stronger electronic donating effect of doped vanadium to surface oxygen that results in upgraded absorbed energy for intercalated ions. It can be summarized that heteroatom doping is efficient way to regulate the electronic band structure of MXene for promoting energy storage and environmental stability.



### 2.4.3 Interlayer engineering of $Ti_3C_2T_x$ MXene

The charge storage of  $Ti_3C_2T_x$  MXene is through cation intercalation, which means the ion diffusion within the interlayer space MXene electrode plays the vital role for the energy storage process. Therefore, designing spacious interlayer path within MXene is an efficient way to improve ion diffusion kinetics. Delaminated MXene sheets tend to restack when assembled into free-standing films, resulting in slow ion transport kinetics. One-dimensional (1D) materials, like carbon nano tubes(CNTs)<sup>[40]</sup>, carbon nanofiber<sup>[212]</sup> and cellulose nanofiber<sup>[213, 214]</sup>, are introduced into the interlayer space between MXene sheets, to alleviate their restacking, just shown in **Figure 2.21a**. It is also noting that the introduction of the 1D materials not only boost the ion transport within the 2D interlayer space of MXene, but also endows the resultant film electrodes exhibiting ameliorative flexibility and mechanical strengthen.<sup>[31, 33, 214]</sup> Some other 2D materials sheets, like  $MoS_2$ <sup>[215]</sup> and reduced graphene oxide (RGO),<sup>[216]</sup> are also incorporated the interlayer path of MXene films, benefiting the ion transport through the interlayer gallery (**Figure 2.21b**). However, the interlayer paths within the composite film fabricated from vacuum filtration usually are curved and have numerous pores, whereby decreasing the volumetric capacitance. By contrast, assembled MXene-RGO composite film assisted by molecular ligand is of 2D sheets ordered assembly and can achieve high packing density and rapid ion transport path.<sup>[217]</sup> Introduction of activated carbon (AC) can also be feasible for boosting MXene supercapacitors application in organic electrolytes (**Figure 2.21c**), which resist restacking of MXene sheets and endows the composite



film high rate performance.<sup>[52]</sup> Given that previous additive components are not redox active, going against the capacitance of capacitance. Therefore, redox active material in acid solution. like polyaniline (PANI) shown in **Figure 2.21d**<sup>[218]</sup> and MoO<sub>3</sub><sup>[219]</sup> etc., are added into the interlayer space, with which not only the rate performance is improved but also a much superior capacitance is obtained in the hybrid films.

In addition to incorporating materials, preintercalation of cations into the interlayer space of MXene can also be feasible. For instance, the freestanding Ti<sub>3</sub>C<sub>2</sub>T<sub>x</sub> films preintercalated with Be<sup>2+</sup> cations exhibits an enhanced capacitance and rate performance in neutral electrolytes (Li<sub>2</sub>SO<sub>4</sub>, K<sub>2</sub>SO<sub>4</sub> etc.), due to the nanopillar effect of Be<sup>2+</sup> ions (**Figure 2.21e**)<sup>[198]</sup> And the pre-intercalation of alkaline metal ions, especially for K<sup>+</sup> and Na<sup>+</sup>, into multilayer MXene also enable sustaining the interlayer open for easier electrolyte diffusion to active sites and the intercalated alkaline metal ions lead to the increased titanium valence state, which is favorable for more charge transfer during charge/discharge process. And the intercalated cations can determine the oxidation resistance ability of MXene.<sup>[220]</sup> Interestingly, this high titanium valence state will reduce to a low valence when immersed into diluted sulfuric acid solution.<sup>[220, 221]</sup> In addition, the intercalation of alkaline metal ions (Na<sup>+</sup>, K<sup>+</sup>) into M<sub>2</sub>CT<sub>x</sub> type MXene can efficiently strengthen its environmental stability.<sup>[153]</sup> The energy storage of MXene in organic electrolyte requires more broaden interlayer gallery, which cannot be achieved by intercalating metal cations. Preintercalation of different chain lengths



alkylammonium (AA) cations can increase the interlayer distance within MXene electrode to ~2.2 nm to boost its application in ionic liquid.<sup>[206]</sup> Nature sedimentation method (**Figure 2.21f**) can be used to assemble MXene free-standing film with broaden interlayer space, which is favorable for the diffusion of lithium ions to the interlayer active sites of the films.<sup>[222]</sup> The length of interlayer path is another factor to influence the energy storage behavior of 2D materials electrodes. The short interlayer path enables the faster ion transport.<sup>[223, 224]</sup> Decreasing the size of MXene sheets to the nanoscale is also proved to be feasible for the better rate capability,<sup>[225]</sup> which is similar to decreasing the lateral size of MoS<sub>2</sub> sheets to the nanometer scale (~6.1 nm), enabling ultrahigh-rate electrochemical capacitance.<sup>[95]</sup> As a whole, the interlayer engineering for boosted capacitance is based on pillar effect of additive substance or cations.

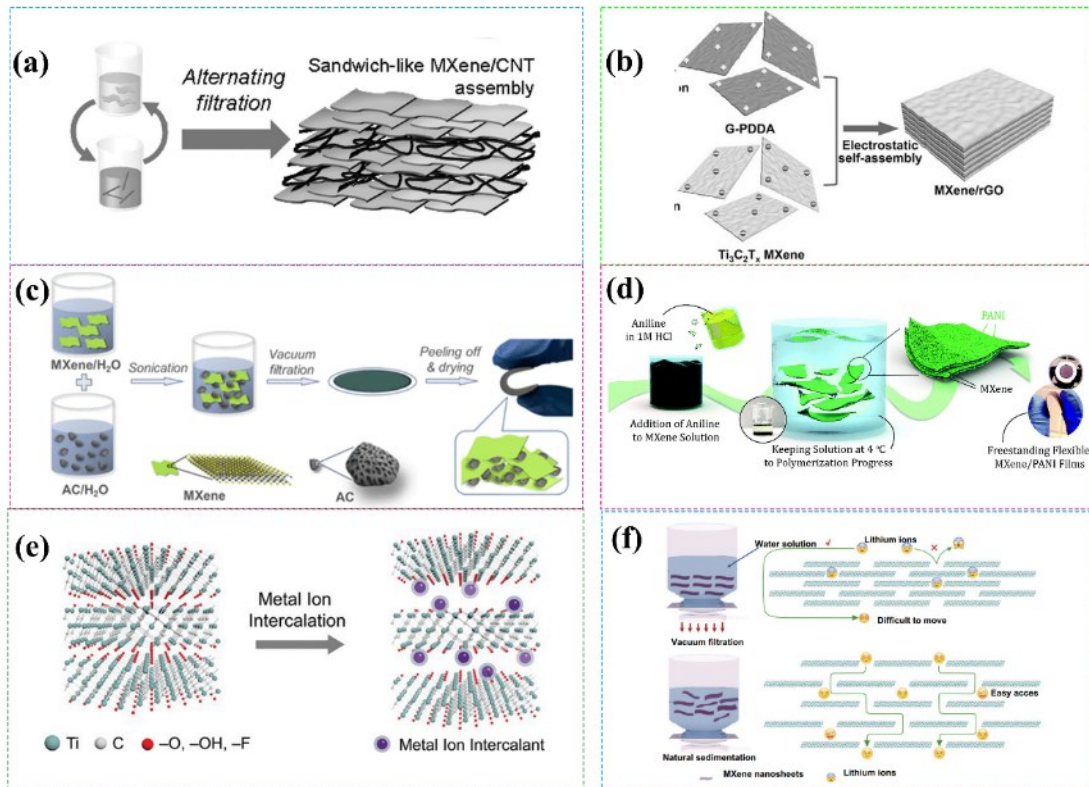


**Figure 2.21** (a) intercalating CNTs into the interlayer of MXene sheets,<sup>[40]</sup> (b) MXene sheets sandwiched by reduced graphene oxides,<sup>[216]</sup> (c) activated carbon used for alleviating restacking of MXene sheets,<sup>[52]</sup> (d) Schematic diagram for intercalating PANI into the interlayer space of MXene,<sup>[218]</sup> (e) preintercalation of metal ions into interlayer space of MXene,<sup>[198]</sup> (f) comparison of MXene films from vacuum filtration and natural sedimentation.<sup>[222]</sup>

### 2.4.4 Porous formation strategy to boost rate capability

The electrolyte ion diffusion barrier within the interlayer space of MXene-based electrodes can also be overcome via construction of 3D network microporous structure.

The formed 3D architecture can resist the restacking of MXene sheets and accelerate the ion transport to active sites. Multiple strategies can be used to construct the 3D porous structure. The macroporous MXene film can be synthesized via template method that first composites MXene sheets with easily removable components, like

(PMMA) spheres, and combines with a subsequent heating procedure.<sup>[140, 226]</sup> The resultant MXene films are composed of hollow MXene spheres, exhibiting much easier ion diffusion behavior than the free-standing film prepared from vacuum filtration (shown in **Figure 2.22a**).<sup>[140]</sup> The delaminated MXene sheets can stably disperse in water and form colloidal solution, as presented in **Figure 2.16d**. The water in the solution can also be used as template for assembling 3D porous MXene electrode (**Figure 2.22b**). The obtained MXene hydrogel via vacuum filtration is first rapidly frozen by liquid nitrogen then a freeze drying procedure is conducted to yield 3D porous MXene film.<sup>[33, 227]</sup> Or MXene colloidal solution is directly flash frozen then experience a subsequent freeze drying process to obtain 3D macroporous MXene aerogel.<sup>[227, 228]</sup> Freeze-assisted tape casting of MXene colloidal solution can also be used to construct vertically aligned MXene films, which show high-rate performance.<sup>[229]</sup>

MXene sheets can be easily assembled into hydrogel in the liquid state, so a follow-up freeze drying can help to change it into 3D porous electrodes. Therefore, the key challenge for obtaining porous configuration in MXene electrodes is how to assemble 3D MXene sheets networks. Transition metal cations ( $\text{Fe}^{2+}$ ,  $\text{Ni}^{2+}$ ,  $\text{Al}^{3+}$  etc.) can assist fast formation of MXene hydrogel in aqueous solution (**Figure 2.22c**).<sup>[34]</sup> To enhance the mechanical performance of resultant electrodes, 1D materials, like CNTs, bacterial cellulose, can be also added (**Figure 2.22d**).<sup>[31]</sup> Assisted with RGO and CNT to assemble 3D porous MXene hydrogel with the assistance of crosslinker (L-cysteine),



followed by freeze drying. It should be noted that the addition of additives into MXene can boost its oxidation resistance and cyclic stability (crosslinker).<sup>[230]</sup> Metal plates can play the same role as metal ions. MXene sheets can be reduced by Zn (or Al, Co, Ni, Fe) plates,<sup>[231]</sup> which will weaken the repulsion between MXene sheets and leads to formation of MXene hydrogel on the metal surface.<sup>[232]</sup> The coherent lamellar layers within liquid crystal will be aligned vertically when an external mechanical shearing force is applied.<sup>[233]</sup> This principle was exploited to construct vertically aligned MXene electrodes, which show thickness independent capacitance energy storage behavior (**Figure 2.22e**). Note that the pores are not limited to the formation among MXene sheet, but also can within MXene sheets.<sup>[234]</sup> The nano pores in MXene sheets can boost electrolyte ion transport, which can show a better rate performance if size of MXene sheets can be decreased, as presented in **Figure 2.22f**.

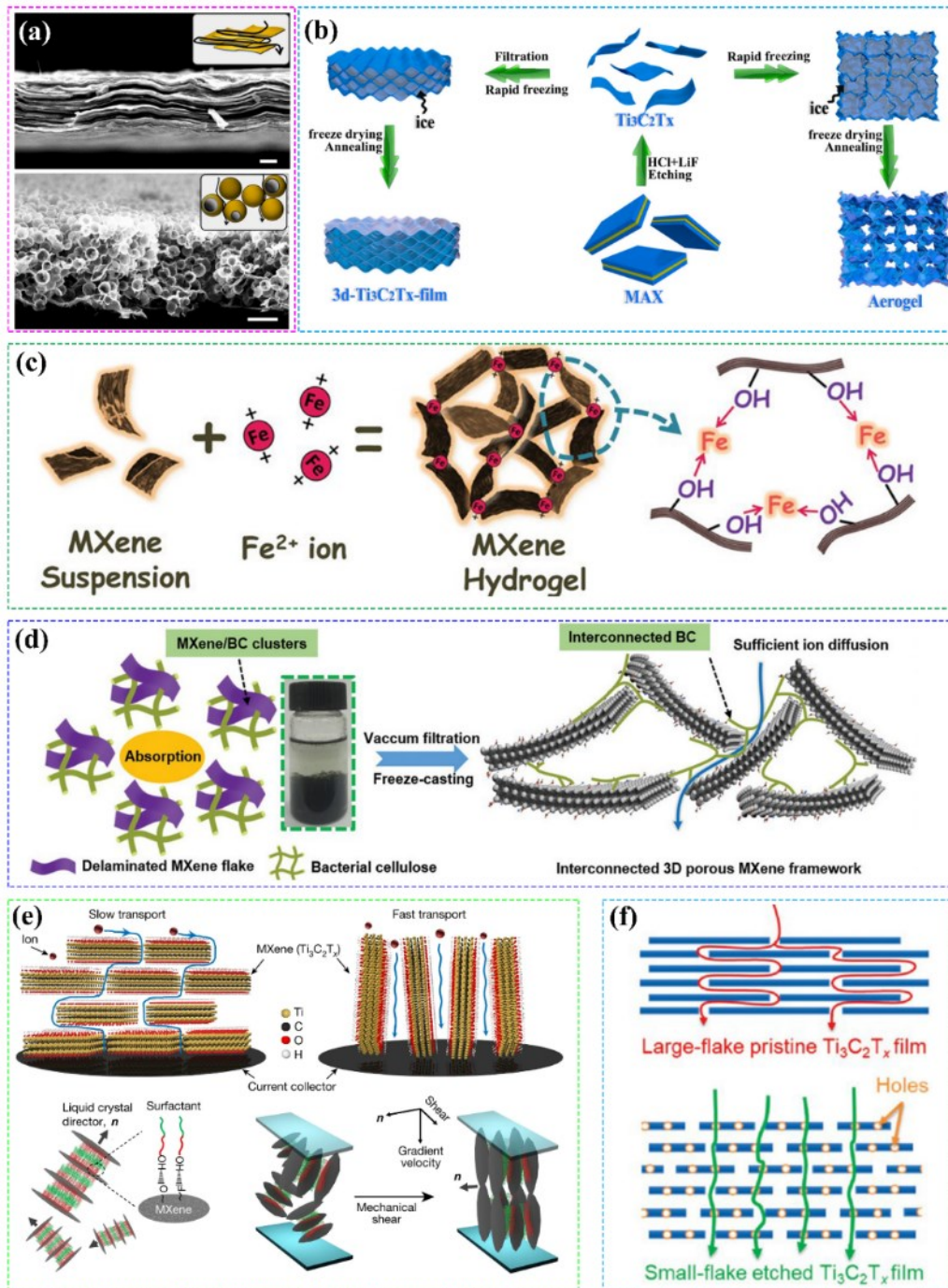


**Figure 2.22** (a) SEM figures for vacuum filtration assembled MXene film(top) and synthesized macroporous MXene films via template method,<sup>[140]</sup> (b) schematic diagram for ice template for constructing 3D porous structure,<sup>[227]</sup> (c) the formation process of MXene hydrogel with assistance of  $Fe^{2+}$ ,<sup>[34]</sup> (d) the assembling process of 3D MXene/Bacterial cellulose,<sup>[31]</sup> (e) the ion diffusion within horizontally stacked and vertically aligned MXene films and schematic diagram for preparing vertically aligned MXene films,<sup>[233]</sup> (f) comparison of ion diffusions within large MXene restacked film and the small MXene sheets with nano pores restacked film.<sup>[234]</sup>



### 2.3.5 Construction of $Ti_3C_2T_x$ MXene based hybrid for supercapacitors

Though  $Ti_3C_2T_x$  MXene can exhibit pseudocapacitance in acid solution, but its capacitance is still much lower than that of transition metal oxides ( $NiO_x$ ,  $CoO_x$  etc.).<sup>[17, 20]</sup> And its inferior capacitance in neutral and alkaline electrolytes also restricts its wide application. Construction of  $Ti_3C_2T_x$  MXene-based composites is a feasible method to get over the issues. Adding redox active materials into  $Ti_3C_2T_x$  MXene with metallic conductivity is expected to further boost the energy storage ability and simultaneously can exhibit high-rate capability due to the high electrical conductivity of  $Ti_3C_2T_x$  MXene. Thus far, the successful cases include MXene/nickel sulfide<sup>[235]</sup>, MXene/Metal–Organic–Framework(MOF),<sup>[236]</sup> MXene/ $MoO_3$ ,<sup>[219]</sup> MXene/ $MnO_2$ ,<sup>[237]</sup> MXene/layered double hydroxides(LDHs)<sup>[238, 239]</sup> ect. In addition,  $Ti_3C_2T_x$  MXene tends to be degraded under the presence of oxygen and water, combination of  $Ti_3C_2T_x$  MXene and reduced graphene oxide and CNT are proved to enable promoting its cyclic stability and oxidation resistance ability,<sup>[43, 230]</sup> which indicates the addition of composite component not only consider to enhance capacitance but also attempt to facilitate the stability of resultant electrode composites.

## 2.4 Summary

This chapter systematically introduces the working mechanisms of supercapacitors,



inactive components of supercapacitors, synthesis methods of MXene, the current progress of about  $Ti_3C_2T_x$  for supercapacitors applications and optimized strategies for boosted energy storage ability. Based on the previous contents, three issues are proposed for better application of MXene for electrode materials of supercapacitors, which will be solved in this research.

- (1) How to alleviate the MXene restacking in film electrodes at no expense of volumetric capacitance with a facile method?
- (2) Can phosphorus with lower electronegativity than nitrogen contribute to the greater enhancement in energy storage ability once being doped into  $Ti_3C_2T_x$  MXene?
- (3) Contrast to the typical methods to boost energy storage ability of MXene, proving the combination of -F removal and shrinking interlayer path of  $Ti_3C_2T_x$  MXene sheets can also be an efficient strategy to boost its super capacitive performance.

## Chapter 3 Experiments and characterization methods

This chapter gives the experiment details for solving the aforementioned three objectives. And the experimental process for the whole research is depicted in **Figure 3.1**

3.1. Three subsections describe them, respectively.

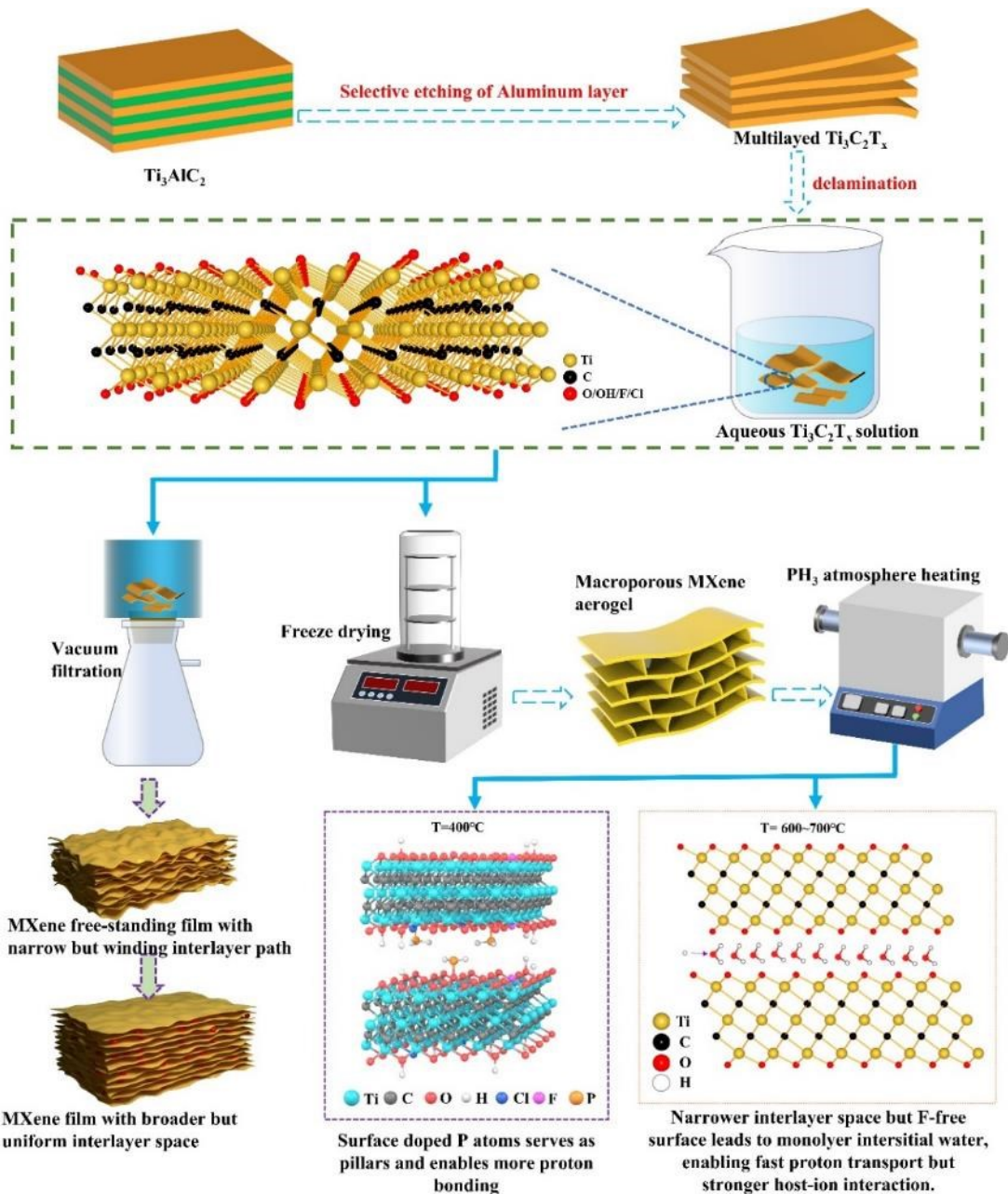


**Figure 3.1** flow chart of the experiments in this research



### 3.1 Experiments for enhanced ion diffusion within flexible $Ti_3C_2T_x$ film for supercapacitors applications

*Preparation of  $Ti_3C_2T_x$  MXene colloidal solution:*  $Ti_3C_2T_x$  MXene sheets were synthesized through reported method.<sup>[240]</sup> 1 g  $Ti_3AlC_2$  precursor was etched in the mixture containing 20 ml 9M HCl and 1.6g LiF at 50 °C for 30 h. The resultant product was then washed with DI water through repetitive centrifugation at 3500 rpm for 5 min until supernatant PH reaches to 6. Afterwards, the obtained sediment was redispersed in DI water and sonicated with ice cooling for 1h under Ar bubbling to avoid MXene oxidation, after which additional centrifugation at 3500 rpm for 1h was conducted to separate delaminated MXene colloidal solution from the mixture. The supernatant was collected.

*Preparation of free-standing MXene film with improved ion diffusion path:* The optimized MXene free-standing film was prepared through a two-step method. 7 ml MXene aqueous solution ( $1.8 \text{ mg ml}^{-1}$ ) was first vacuum filtered using a Celgard 3501 membrane to obtain a densely stacked MXene film. Here, the concentration of MXene solution cannot surpass  $10 \text{ mg ml}^{-1}$ , which will exhibit viscous feature and is adverse to obtaining MXene free-standing film. After drying in a desiccator overnight, the resultant film was then heated in a mixture of 50 mL ethanol and 400 mg phosphoric acid to expand interlayer spacing at 60 °C for 6 h, followed by washing with acetone



and ethanol and dried at room temperature to obtain the film with optimized ion diffusion path.

*Materials Characterization:* The morphology and microstructure of the samples were investigated with a SEM (Tescan MAIA3) equipped with EDS. X-ray diffraction (XRD) data was measured using a powder diffractometer (Rigaku SmartLab) with monochromatic Cu K $\alpha$  radiation ( $\lambda \sim 1.54 \text{ \AA}$ , with a scan speed of  $10^\circ \text{ min}^{-1}$ ). Raman spectra was analyzed on a WITEC Confocal Raman system with a 633 nm laser as an irradiation source. The surface and interlayer chemical composition analysis were conducted on a Nexsa X-Ray Photoelectron Spectrometer (XPS) System with Monochromatic and focused 12 kV Aluminum K $\alpha$  X-ray.

*Electrochemical measurement:* SOLARTRON Electrochemical workstation was used for all electrochemical measurement. The samples were first punched into discs with diameter of 4 mm as working electrodes and then assembled into three-electrode Swagelok cells for EC characterization, where overcapacitive carbon, Ag/AgCl (sat. KCl) and 3M H<sub>3</sub>PO<sub>4</sub> were used as counter electrode, reference electrode, and electrolyte, respectively. EIS measurements were carried out at open circuit potential in the frequency range of 0.01~100000 Hz with an amplitude of 10 mV. Symmetric supercapacitors were assembled with two MXene films with same size ( $\Phi$  5 mm) and mass loading ( $1 \text{ mg cm}^{-2}$ ), which were separated by Celgard 3501 films. Asymmetric



supercapacitors were assembled with OMF and activated carbon as anode and cathode, respectively. Activated carbon electrode was prepared through coating the slurry containing 80 wt% activated carbon (YP50-F, Kuraray), 10 wt% carbon black and 10 wt% Polyvinylidene fluoride (PVDF) along with N-methyl pyrrolidone (NMP) as solvent on carbon cloth, followed by vacuum drying at 100°C overnight.

*The method for calculation of specific capacitance, energy & power densities:* the specific capacitance of working electrodes from CV curves is obtained based on the following formula 3-1.

$$C = \frac{\int idU}{UXv} \quad (3-1)$$

Where U means the potential window(V), X refers to mass(g) or volume(cm<sup>3</sup>) of working electrode, i is current (A) and v represents scan rates (V s<sup>-1</sup>). And gravimetric capacitance from GCD was calculated according to the equation 3-2, shown below.

$$C_g = \frac{I\Delta t}{m} \quad (3-2)$$

Where C<sub>g</sub>, I, Δt and m are gravimetric specific capacitance(F g<sup>-1</sup>), current(A), discharge time(s) and mass of active material, respectively.

The energy density E (Wh Kg<sup>-1</sup>) and power density P (W Kg<sup>-1</sup>) of assembled supercapacitors are calculated according to equation 3-3 and 3-4, respectively.

$$E = \frac{CV^2}{2} \times \frac{1000}{3600} \quad (3-3)$$



$$P = \frac{E}{\Delta t} \times 3600 \quad (3-4)$$

Where C is the specific capacitance of devices based on total mass of two electrodes, V represents the voltage window of the assemble supercapacitors.

Note that all calculations on specific capacitance, energy density and power density throughout this research are based on equations 3-1, 3-2, 3-3 and 3-4.

*Charge balance between cathode and anode of asymmetric supercapacitors:* to assemble the asymmetric device, the mass ratio between cathode and anode is confirmed according to the equation below<sup>[241]</sup>

$$\frac{m_{cathode}}{m_{anode}} = \frac{C_{anode} \cdot U_{anode}}{C_{cathode} \cdot U_{cathode}} \quad (3-5)$$

## 3.2 Experiments for grafting phosphorus on $Ti_3C_2T_x$ MXene for enhanced supercapacitive performance

### 3.2.1 Preparation of $Ti_3C_2T_x$ MXene aerogel

$Ti_3C_2T_x$  MXene aerogel was prepared by a two-step method.  $Ti_3C_2T_x$  colloidal solution was firstly synthesized by the minimal intensive layer delamination (MILD) method.<sup>[240]</sup>

2 g 400 mesh  $Ti_3AlC_2$  precursor was slowly added into 40 ml 9 M HCl + 3.2 g LiF etchant, followed by water bath heating at 50 °C and continuous stirring for 30h. The resultant product was washed via repetitive 3500 rpm × 5min centrifugation procedures until PH of supernatant reaches to 6. Afterwards, decanting the supernatant and extra deionized (DI) water was poured into the centrifugation tube, which was then loaded



onto an orbital shaker for delaminating MXene. Finally, black supernatant in the tube was collected after centrifuging at 3500 rpm for 60min for the next fabrication step. Note that only shaking once is not enough to delaminate all multilayered MXene, so here multiple shaking and collections were conducted to increase the yield. In our experiment, around 600 ml  $2.9 \text{ g ml}^{-1}$  MXene solution was eventually obtained.

The resultant  $\text{Ti}_3\text{C}_2\text{T}_x$  MXene colloidal solution was frozen in liquid nitrogen for 10 min to assemble MXene aerogel framework then vacuum drying at  $-65^\circ\text{C}$  in a freeze-drying machine for five days (pressure  $<1 \times 10^{-3}$  atm) in the second step. The water between MXene sheets was vaporized during this procedure, generating final porous MXene aerogel (Figure S1b).

### 3.2.2 Synthesis of phosphorus doped $\text{Ti}_3\text{C}_2\text{T}_x$

Grafting phosphorus atoms onto  $\text{Ti}_3\text{C}_2\text{T}_x$  was conducted in a tube furnace with two temperature regions. Certain amount of  $\text{NaH}_2\text{PO}_2$  and 50 mg as-prepared  $\text{Ti}_3\text{C}_2\text{T}_x$  aerogel were put at the upstream and downwind temperature regions and heated with  $350^\circ\text{C}$  and  $400^\circ\text{C}$  respectively under continuous 50 sccm argon flow. In details, the phosphine produced in the first region flows to downstream heated MXene to achieve surface phosphorus doping. For the sake of changing the doping quantity in  $\text{Ti}_3\text{C}_2\text{T}_x$ , the mass ratio between  $\text{NaH}_2\text{PO}_2$  and MXene and was controlled as 1, 2, 8 and 20, which correspond samples PMX1, PMX2, PMX8 and PMX20, separately.



### 3.2.3 Materials characterization

The morphologies and microstructure of synthesized samples were characterized by Scanning Electron Microscope (SEM, JEOL Model JSM-6490) equipped with energy dispersive X-ray spectrometry (EDS) system and Scanning Transmission Electron Microscopy (STEM, scanning transmission electron microscopy). X-ray diffraction patterns of the samples were recorded using an X-ray Diffractometer (Rigaku SmartLab) with monochromatic Cu K $\alpha$  X-ray source ( $\lambda=0.15406$  nm). Specific area and pore size distribution of the samples were characterized through a MICROMERITICS surface area and porosity analyzer (ASAP2020). The chemical composition and elemental valence state of the samples were investigated on a Nexsa G2 XPS System equipped with monochromatic and focused 12 kV aluminum K $\alpha$  X-Ray. Raman spectra including in situ Raman spectra were measured in a WITEC Confocal Raman system (Alpha300 R).

### 3.2.4 Electrochemical measurements

The slurry for working electrodes was made through mixing MXene samples, carbon black and PVDF with a mass ratio of 8:1:1 in 600  $\mu$ L N-Methylpyrrolidone (NMP) with continuous grinding for 30min. The resultant slurry was then coated on 2  $\times$  3 cm graphite paper, followed by vacuum drying at 100  $^{\circ}$ C overnight to obtain working electrodes ( $\sim 2.2$  mg cm $^{-2}$  active material loading). It should be pointed that heating time at 100 $^{\circ}$ C should surpass 6h to completely remove NMP. Super-capacitive performance



of working electrodes was investigated through a three-electrode configuration with Ag/AgCl (sat. KCl), graphite bar and 1M H<sub>2</sub>SO<sub>4</sub> as reference electrode, counter electrode and electrolyte respectively, conducted on a SOLARTRON electrochemical workstation. For assembling symmetric supercapacitors, two  $\Phi$ 14 mm working electrodes were separated by Celgard 3501 films and assembled in a Swagelok cell, followed by injecting 200 $\mu$ L 1M H<sub>2</sub>SO<sub>4</sub> electrolyte. The energy storage ability of symmetric supercapacitors was also studied through the SOLARTRON workstation. The cyclic stability of both working electrodes and symmetric supercapacitors was all researched on an Arbin Battery testing system.

### 3.2.5 First-principles calculations

First-principles calculations were performed in the framework of density functional theory (DFT) implemented in the Vienna ab initio simulation package (VASP).<sup>[242, 243]</sup> The exchange-correlation functional was described by generalized gradient approximation (GGA) with the Perdew-Burke-Ernzerhof (PBE) flavor.<sup>[244, 245]</sup> For geometry optimization, the plane-wave cut-off energy was set as 500 eV. The Brillouin zone was sampled using a Monkhorst–Pack  $k$ -point mesh scheme, and the meshes of  $\Gamma$ -centered  $5 \times 5 \times 1$  were used for the  $3 \times 3$  supercell. The convergence criteria for energy and force were set to be  $10^{-6}$  eV and  $0.01$  eV  $\text{\AA}^{-1}$ , respectively. To avoid the interlayer interaction, a vacuum layer added in  $c$ -axis with the distance of 16  $\text{\AA}$ . The charge redistribution and transfer were quantitatively analyzed and estimated by the charge differential analysis and Bader charge method.<sup>[246]</sup>

The formation energy  $\Delta E$  of P atoms on Ti<sub>3</sub>C<sub>2</sub>O<sub>2</sub> monolayer was calculated by:



$$\Delta E = E_{Ti_3C_2O_2P_x} - (x\mu_P + E_{Ti_3C_2O_2}) \quad (3-6)$$

where  $E_{Ti_3C_2O_2P_x}$  and  $E_{Ti_3C_2O_2}$  are the total energies of  $Ti_3C_2O_2$  with and without P atoms,  $\mu_P$  represents the energy per P atom in the bulk form and  $x$  corresponds to the content of phosphorus atoms in the substrate configurations.

The differential charge density was obtained as the difference between the charge density before and after the bonding:<sup>[247]</sup>

$$\Delta\rho(\vec{r}) = \rho_{Ti_3C_2O_2-P}(\vec{r}) - \rho_P(\vec{r}) - \rho_{Ti_3C_2O_2}(\vec{r}) \quad (3-7)$$

where  $\rho_{Ti_3C_2O_2-P}(\vec{r})$ ,  $\rho_P(\vec{r})$ , and  $\rho_{Ti_3C_2O_2}(\vec{r})$  represent the charge density distributions of  $Ti_3C_2O_2$ -P system, P atom, and bare  $Ti_3C_2O_2$  monolayer, respectively.

### 3.3 Experiments for synthesizing $Ti_3C_2T_x$ with oxygen-rich and narrow interlayer space

#### 3.3.1 Synthesis of oxygen-rich but narrower interlayer space few-layer MXene sheets aerogel.

$Ti_3C_2T_x$  MXene aerogel was first prepared using the same procedure with section 3.2. Then  $NaH_2PO_2$  and  $Ti_3C_2T_x$  MXene aerogel with a mass ratio of 1:1 were placed in the two temperature regions of a tube furnace, followed by heating with 350 and 600°C-700°C respectively with continuous argon flow from  $NaH_2PO_2$  to MXene (50 sccm). The resultant samples, namely oxygen-rich but narrower interlayer space few-layer MXene, were named as PMX600 and PMX700 based on their respective heating temperatures. The control sample was prepared with same heating technology (600°C for MXene aerogel) but no addition of  $NaH_2PO_2$  in the uptake temperature region,



named as CMX600.

### 3.3.2 Material characterization

Scanning electron microscope (SEM, JEOL Model JSM-6490) was employed to study the morphology of samples. The detailed change of samples in terms of morphologies and microstructure was studied using field emission transmission electron microscope (TEM, JEOL JEM-2100F). The surface functional groups composition of  $Ti_3C_2T_x$  MXene was characterized through the combination of Raman spectrometer (WITEC, Alpha300 R) and X-ray photoelectron spectrometer (XPS, Nexsa G2). X-ray diffraction (XRD) meter (Rigaku SmartLab 9kW) was utilized to investigate the phase composition and crystalline change of samples. The pore structure and variation of specific area of MXene samples were analyzed via a MICROMERITICS surface area and porosity analyzer (ASAP 2020). The valence state and coordination environment of titanium in  $Ti_3C_2T_x$  MXene were researched via X-ray absorption near-edge spectra (XANES) and extended X-ray absorption fine structure spectra (EXAFS) measurements, which was performed at National Synchrotron Radiation Research Center (NSRRC) in Taiwan.

### 3.3.3 Electrochemical measurements

The supercapacitive performance of samples were characterized with three-electrode configuration, in which MXene aerogel, graphite bar and Ag/AgCl (sat. KCl) serve as working electrode, counter electrode and reference electrode, respectively. The working



electrodes were fabricated by coating the slurry containing active material, carbon black and PVDF (mass ratio 8:1:1) and N-Methylpyrrolidone (NMP) solvent onto 2\*3 cm graphite paper, followed by vacuum drying at 120°C overnight. Self-discharge behavior of supercapacitors is very important for their practical application. To evaluate the property, a device is charged to the highest potential and sustained at the voltage for 10min, then the relationship of open circuit potential vs. time is recorded.<sup>[248, 249]</sup> Here, the reason of applying holding time is to reduce self-discharge rate due to uniform charge distribution.<sup>[250]</sup> PVA serves a critical role for lowering the transport of electrolyte ions, which could greatly be favorable for restricting self-discharge behavior of supercapacitors.<sup>[251]</sup> For assemble Prussian blue analogue(PBA)-MXene asymmetric supercapacitors, PBA working electrode and MXene were sandwiched by Nafion112+glass fiber film in a Swagelok cell, followed by addition of 100  $\mu$ L 1M H<sub>2</sub>SO<sub>4</sub> electrolyte. The energy storage ability of asymmetric proton supercapacitors was also studied through the SOLARTRON workstation.



## Chapter 4 Enhanced ion diffusion in flexible $\text{Ti}_3\text{C}_2\text{T}_x$ MXene film for high performance supercapacitors

$\text{Ti}_3\text{C}_2\text{T}_x$  MXene is a good candidate of electrode materials for supercapacitors due to its high conductivity and outstanding pseudocapacitance. However, restacking among MXene sheets is inevitable when they are assembled into a freestanding film electrode, which hinders electrolyte ion diffusion to active sites and results in sluggish energy storage kinetics. Herein, the volumetrically expanded ester reaction between ethanol and phosphoric acid is exploited to improve interlayer path within  $\text{Ti}_3\text{C}_2\text{T}_x$  film. These two kinds of molecules jointly intercalate into interlayer space of  $\text{Ti}_3\text{C}_2\text{T}_x$  film and then react to produce phosphate under heating, leading to molecular scale expanded but uniform interlayer gallery. The optimized film shows enhancement in both gravimetric and volumetric capacitances along with better rate capability. It exhibits a capacitance of  $297 \text{ F g}^{-1}/965 \text{ F cm}^{-3}$  at  $2 \text{ mV s}^{-1}$  and retains  $108 \text{ F g}^{-1}/300 \text{ F cm}^{-3}$  at  $200 \text{ mV s}^{-1}$ , which are greatly superior to those of the pristine film without the treatments. The assembled symmetric and asymmetric supercapacitors with optimized film structure can deliver an energy density of  $6.33$  and  $7 \text{ Wh Kg}^{-1}$ , respectively. This work demonstrates a novel yet simple method to ameliorate restacking of MXene sheets for its better supercapacitor application.



## 4.1 Introduction

Supercapacitors are regarded as the next generation energy storage devices since they possess high power density, long cycle life and preeminent energy density simultaneously.<sup>[252-254]</sup> From the perspective of energy storage mechanism, supercapacitors can be classified into electron double layer capacitors (EDLCs) and pseudocapacitors. EDLCs normally exhibit relatively low specific capacitance due to ion sorption/desorption on electrode surface, while pseudocapacitors store charge by redox reactions on electrode surface or near surface, delivering much higher capacitance than EDLCs.<sup>[17, 18, 255]</sup>

Since the discovery of two-dimensional (2D) transition metal carbides/nitrides/carbonitrides (MXene) in 2011,<sup>[25]</sup> they have aroused an upsurge of worldwide research on their various applications, such as energy storage,<sup>[140, 256]</sup> electromagnetic interference shielding,<sup>[257]</sup> and catalysis.<sup>[181]</sup> MXene has a generic chemical formula of  $M_{n+1}X_nT_x$ , where M refers to early transition metal element (Ti, V, Cr, Mo, and Nb), X is carbon or nitrogen, and T represents surface functional groups (-O, -OH, -Cl, or -F) linked with M.<sup>[258, 259]</sup> It is synthesized through selectively removal of A-layer in hexagonal stratified MAX phase using liquid-phase,<sup>[25, 154]</sup> molten salt,<sup>[106, 179]</sup> or electrochemical etching methods.<sup>[173, 174]</sup> Different from conventional pseudocapacitive materials, such as transition metal oxides and conducting polymer, MXene not only possesses metallic conductivity but also exhibits highly stable



pseudocapacitance in both organic and aqueous electrolytes,<sup>[199, 260]</sup> making it a better candidate for supercapacitor electrode materials.

Among various MXene,  $\text{Ti}_3\text{C}_2\text{T}_x$  MXene is the most studied and a promising electrode material for supercapacitor application due to its high specific capacitance in acid aqueous electrolyte.<sup>[26, 33]</sup> Nowadays, multilayered  $\text{Ti}_3\text{C}_2\text{T}_x$  particles obtained via etching off Al-layer of  $\text{Ti}_3\text{AlC}_2$  precursor have been directly investigated as active material of supercapacitors.<sup>[37, 41, 154, 163]</sup> A further delamination process is normally conducted to exfoliate multilayered  $\text{Ti}_3\text{C}_2\text{T}_x$  into monolayer or few-layer counterparts for enhanced energy storage capability.<sup>[141, 241, 261]</sup> However, restacking between  $\text{Ti}_3\text{C}_2\text{T}_x$  sheets cannot be avoided due to van der Waals interaction during the electrode fabrication process, which hinders electrolyte ion diffusion to surface active sites at fast charge/discharge rates. To solve this problem, some pillars, like carbon nanotube,<sup>[40]</sup> and activated carbon,<sup>[52]</sup> were introduced into the interlayer space of  $\text{Ti}_3\text{C}_2\text{T}_x$  film to alleviate the restacking. An alternative way is to prepare three-dimensional (3D) macroporous MXene film through template method or multivalent-cation-assisted assembly combined with freeze drying to improve ion diffusion behavior.<sup>[34, 140]</sup> Mechanical shearing was also proved to be able to efficiently construct vertically aligned MXene film which enables fast ion diffusion among MXene sheets and exhibits thickness-independent capacitance.<sup>[233]</sup> Although above methods are feasible against the restacking of MXene sheets, the introduction of inactive components and



construction of porous structure will decrease gravimetric and volumetric capacitances of MXene film, respectively. In addition, complicated processes of these techniques constrain the large-scale application. Therefore, it is still full of challenge to develop an easy strategy that can restrain the restacking of MXene sheets, while maintain the high gravimetric and volumetric capacitances of MXene film.

In this work, the ester reaction between ethanol and phosphoric acid was exploited to expand the interlayer space between  $Ti_3C_2T_x$  sheets against their restacking. The intercalated ethanol and phosphoric acid at interlayer space of densely stacked MXene film react with each other under heating, forming phosphate with larger size, which serves as pillar to broaden the space between MXene sheets. Here the phosphate formed at the interlayer leads to the molecular scale interlayer expansion (without macroscopic cleavage of MXene sheets), and interlayer path becomes more uniform after expansion. Benefiting from the molecular level expanded and uniform interlayer path, the resultant MXene film not only exhibits better rate capability, but also shows improvement in both gravimetric and volumetric capacitances, which can seldom be found in  $Ti_3C_2T_x$  sheets prepared by other methods. Consequently, the optimized  $Ti_3C_2T_x$  MXene film exhibits a high capacitance of  $297\text{ F g}^{-1}$  ( $965\text{ F cm}^{-3}$ ) at  $2\text{ mV s}^{-1}$  in  $3\text{ M H}_3\text{PO}_4$  and maintains  $108\text{ F g}^{-1}$  ( $300\text{ F cm}^{-3}$ ) as the scan rate increases to  $200\text{ mV s}^{-1}$ , which are superior to those of pristine film ( $208\text{ F g}^{-1}/914\text{ F cm}^{-3}$  and  $25\text{ F g}^{-1}/109\text{ F cm}^{-3}$  respectively). The assembled symmetric and asymmetric supercapacitors with the optimized  $Ti_3C_2T_x$  film

deliver energy densities of 6.33 and 7.00 Wh Kg<sup>-1</sup>, respectively, indicating a good prospect as electrode material of supercapacitors. The proposed strategy in this work provides a simple but efficient way to optimize interlayer path of restacked Ti<sub>3</sub>C<sub>2</sub>T<sub>x</sub> freestanding film for better supercapacitor performance, which can be extended to the scalable production of other 2D materials assembled films.

## 4.2 Results and discussions

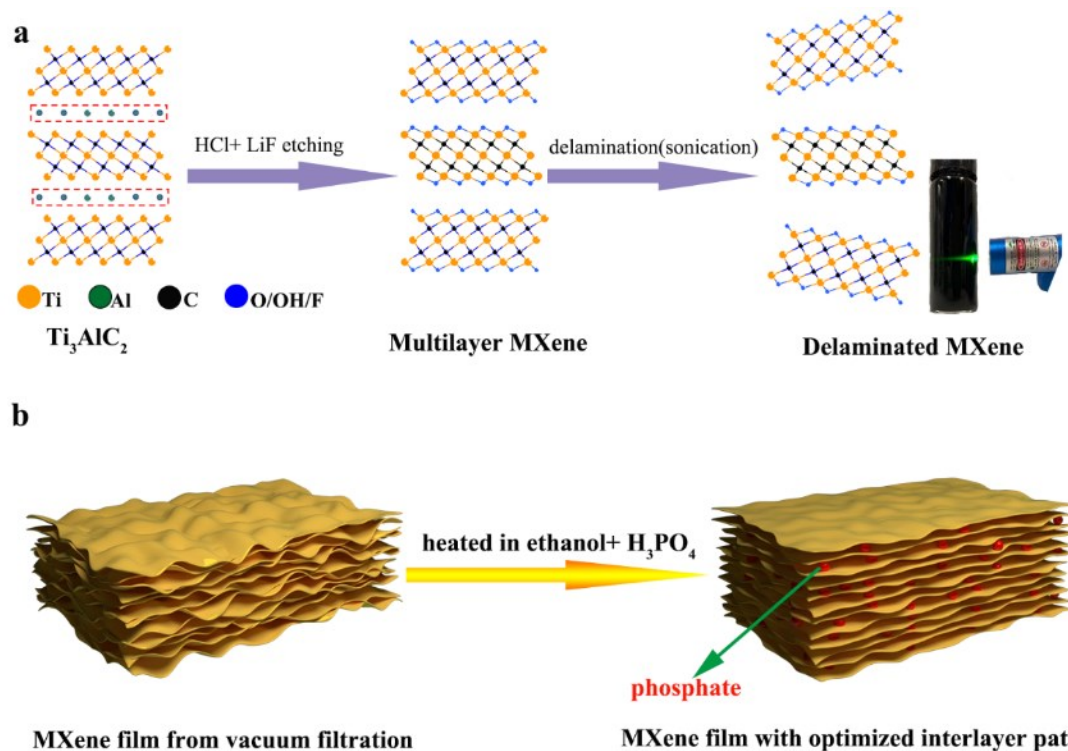


**Figure 4.1** Schematic illustration of fabrication process of (a) Ti<sub>3</sub>C<sub>2</sub>T<sub>x</sub> MXene sheets and (b) MXene freestanding film with optimized interlayer path

**Figure 4.1** depicts the fabrication process of delaminated Ti<sub>3</sub>C<sub>2</sub>T<sub>x</sub> MXene sheets and the MXene free-standing film with optimized interlayer path. Ternary Ti<sub>3</sub>AlC<sub>2</sub>



precursor with layered structure was first etched off aluminum-layer in the heated mixture of hydrochloric acid and lithium fluoride to obtain multilayered  $Ti_3C_2T_x$ , which was subsequently delaminated into  $Ti_3C_2T_x$  MXene sheets through sonication method,<sup>[18, 154]</sup> as shown in **Figure 4.1a**. The resultant aqueous solution of  $Ti_3C_2T_x$  sheets (Figure 1a) shows Tyndall effect, implying its colloidal nature. The  $Ti_3C_2T_x$  free-standing film was prepared via vacuum filtering the colloidal solution followed by a vacuum drying procedure. However, the restacking between MXene sheets is unavoidable during filtration and drying process, which results in the shrinkage of interlayer path due to capillary force. This densely stacked structure can merely afford sluggish ion diffusion to inner active sites of  $Ti_3C_2T_x$  film, thus resulting in low capacitance and inferior rate capability.

The  $Ti_3C_2T_x$  film with optimized interlayer path was prepared through heating the previous  $Ti_3C_2T_x$  film (fabricated from vacuum filtration and drying) in the mixture of ethanol and phosphoric acid, as illustrated in **Figure 4.1b**. Two reactants jointly intercalated into the interlayer gallery of  $Ti_3C_2T_x$  film during the process, then reacted with each other to produce larger-size phosphate, leading to expanded but more uniform interlayer room. Note that the ester reaction between ethanol and phosphoric acid at interlayer is mild due to logy provision of reactants, thus only molecular-scale interlayer expansion was obtained after heating for 6 h. It is the slightly expanded but homogeneous interlayer path that equips the optimized  $Ti_3C_2T_x$  film with superior



gravimetric and volumetric capacitances and better rate capability than pristine counterpart. For convenience, pristine  $\text{Ti}_3\text{C}_2\text{T}_x$  MXene film fabricated from vacuum filtration and  $\text{Ti}_3\text{C}_2\text{T}_x$  MXene film with optimized interlayer path are named PMF and OMF, respectively.

The cross-section microstructure of PMF and OMF is shown in **Figure 4.2**. PMF exhibits a stacked layered structure with a thickness of  $\sim 2.06 \mu\text{m}$  and some porosities are observed between MXene sheets as presented in **Figure 4.2a**, which are left after the evaporation of residual interlayer water in drying process. By contrast, albeit OMF shows stacked cross-section morphology similar to PMF (**Figure 4.2b**), it has a relatively large thickness ( $\sim 2.66 \mu\text{m}$ ), implying more spacious interlayer room in OMF. This result demonstrates that heating  $\text{Ti}_3\text{C}_2\text{T}_x$  film in the mixture of ethanol and phosphoric acid is an efficient way to expand its interlayer path. It is also worth noting that the porous structure in PMF becomes less common in OMF, which should be attributed to the total interlayer expansion of MXene film, alleviating the previous film shrinkage. In addition, high magnification SEM figures in **Figure 4.3 a-b** show that OMF owns a rougher surface than PMF while some nanopores are also exhibited on its surface. These surface nanopores and expanded interlayer gallery synergistically enable the easier ion diffusion to active sites within OMF.<sup>[163, 234]</sup> Surprisingly, the OMF still retains good flexibility notwithstanding increased interlayer distance as shown in **Figure 4.3 c-d**, indicative of its prospect for flexible electrodes of supercapacitors.

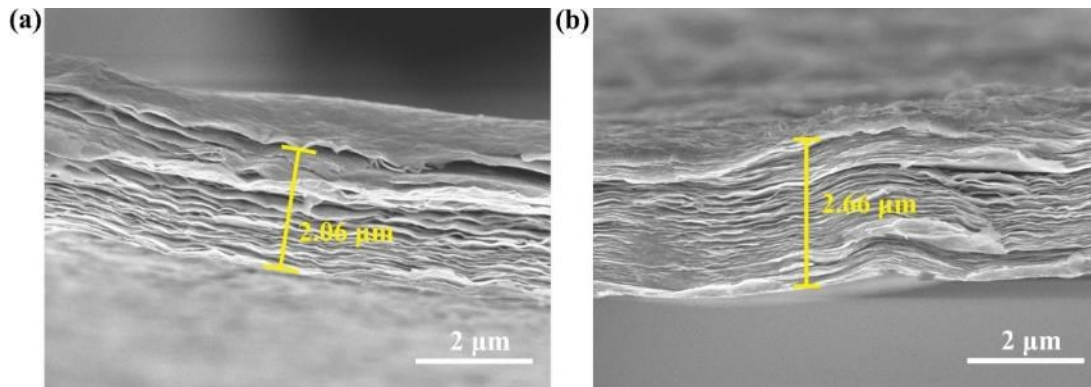


**Figure 4.2** Cross-sectional SEM images of (a) PMF, and (b) OMF

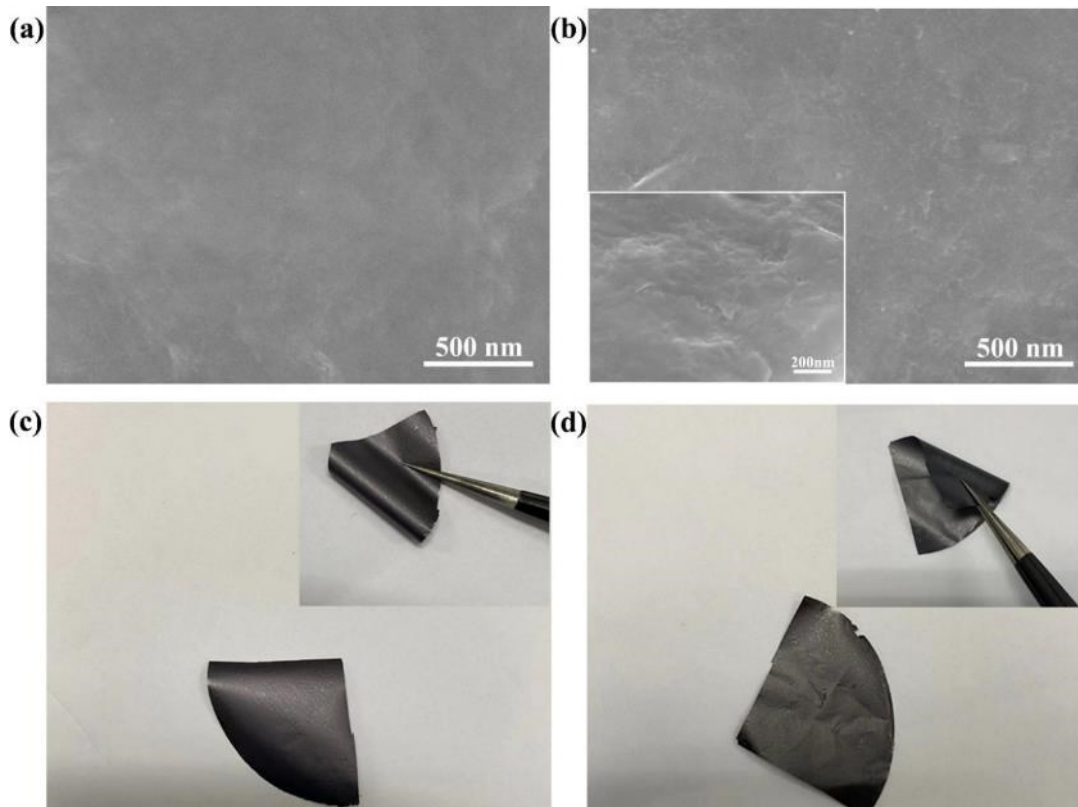


**Figure 4.3** SEM image of (a) PMF surface and (b) OMF surface, photos of PMF (c) and (d) PMX

X-ray diffraction (XRD) was conducted to investigate the interlayer distance of MXene films. XRD spectra for both PMF and OMF are shown in **Figure 4.4a**. As calculated from their (002) peaks, OMF has an average interlayer expansion of 0.15 nm in



comparison to PMF, consistent with the SEM observation (**Figure 4.2**). This molecular scale interlayer expansion is ascribed to interlayer phosphorus species as confirmed from EDS results (**Figure 4.4c**). It should be noted that full width at half maximum (FWHM) of (002) peak can represent uniformity of interlayer space and a more uniform yet open interlayer path can serve as the superhighway for ion diffusion.<sup>[41]</sup> It is obvious that OMF exhibits a smaller FWHM than PMF, indicative of its more uniform interlayer space. Therefore, it is expected that resultant enlarged but uniform interlayer path in OMF can contribute to faster ion diffusion than in PMF. **Figure 4.4b** presents Raman spectra for the two films. A new sharp Raman peak ( $1152\text{ cm}^{-1}$ ) appearing in OMF can be assigned to the stretch vibration of P-O bond of formed phosphate,<sup>[262]</sup> while other Raman bands  $A_{1g}$  and  $E_g$  that correspond to the vibrations of Ti, C and atoms from surface functional groups of  $Ti_3C_2T_x$  are almost the same between the two films.<sup>[33]</sup> In addition, no obvious Raman peak at around  $150\text{ cm}^{-1}$  corresponding to titanium oxide was observed for OMF, indicating no obvious surface oxidation during its heating process.<sup>[263]</sup>

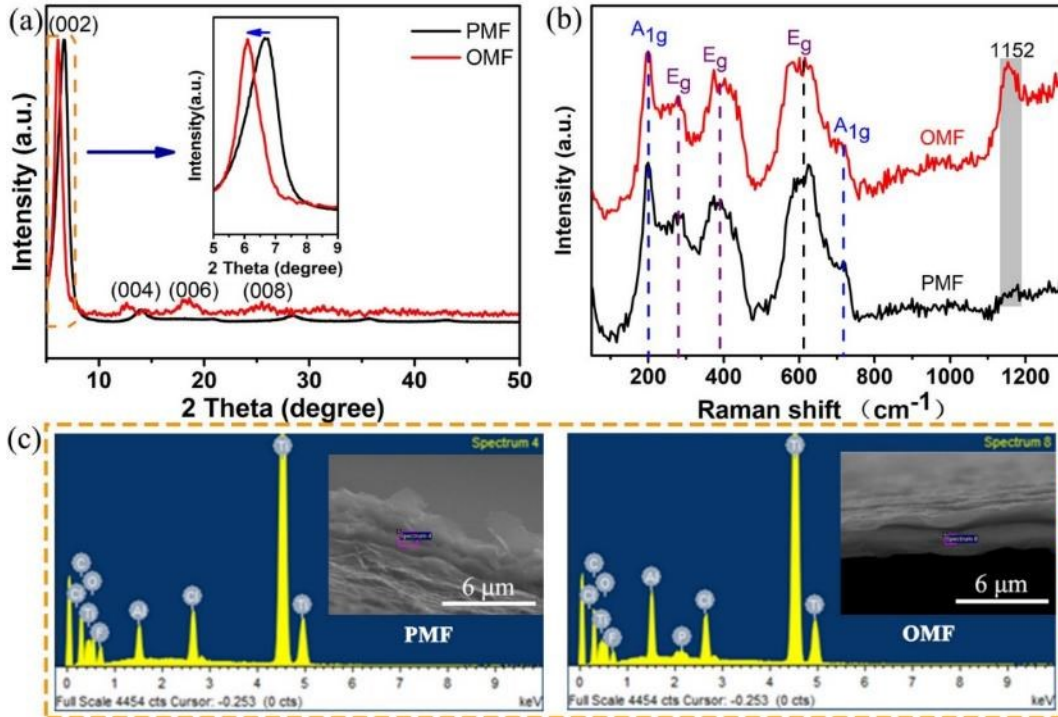


**Figure 4.4** (a) XRD spectra, (b) Raman spectra and (c) cross-section EDS results of PMF and OMF. Insets in (c) are cross-section SEM images of the two films;

X-ray photoelectron spectroscopy (XPS) analysis was conducted to investigate surface chemical composition of MXene films. Survey spectra (**Figure 4.5a**) shows presence of phosphorus on OMF, and its high-resolution P 2p XPS spectrum in **Figure 4.5d** further confirms the additional element phosphorous (133.1 eV), corresponding to phosphate ester.<sup>[264]</sup> Similarly, P=O bond (531.4eV) attributing to phosphate was also detected on OMF from its O 1s spectra (**Figure 4.5b**),<sup>[265]</sup> and deconvolved results reflect more absorbed water and surface -O groups on OMF, as shown in **Table 4.1**. Ti 2p spectrum of OMF (**Figure 4.5c**) exhibits a blue shift (+0.25 eV) in comparison to that of PMF, indicative of increased average valence state of titanium. This increment in valence state could be attributed to the more content of TiO<sub>2</sub> and TiO<sub>2-x</sub>F<sub>x</sub> in OMF

due to slight oxidation, which is confirmed by resolving Ti 2p spectra as shown in **Figure 4.5c** and **Table 4.2**. Pseudocapacitance of  $Ti_3C_2T_x$  is dependent on surface oxygen terminals bonding/debonding with hydronium ions in electrolyte.<sup>[29, 37]</sup> Here both O 1s and Ti 2p spectra confirm more abundance of oxygen on OMF than on PMF, implying that heating MXene film in ethanol and phosphoric acid can lead to more -O active sites, likely contributing to higher pseudocapacitance.

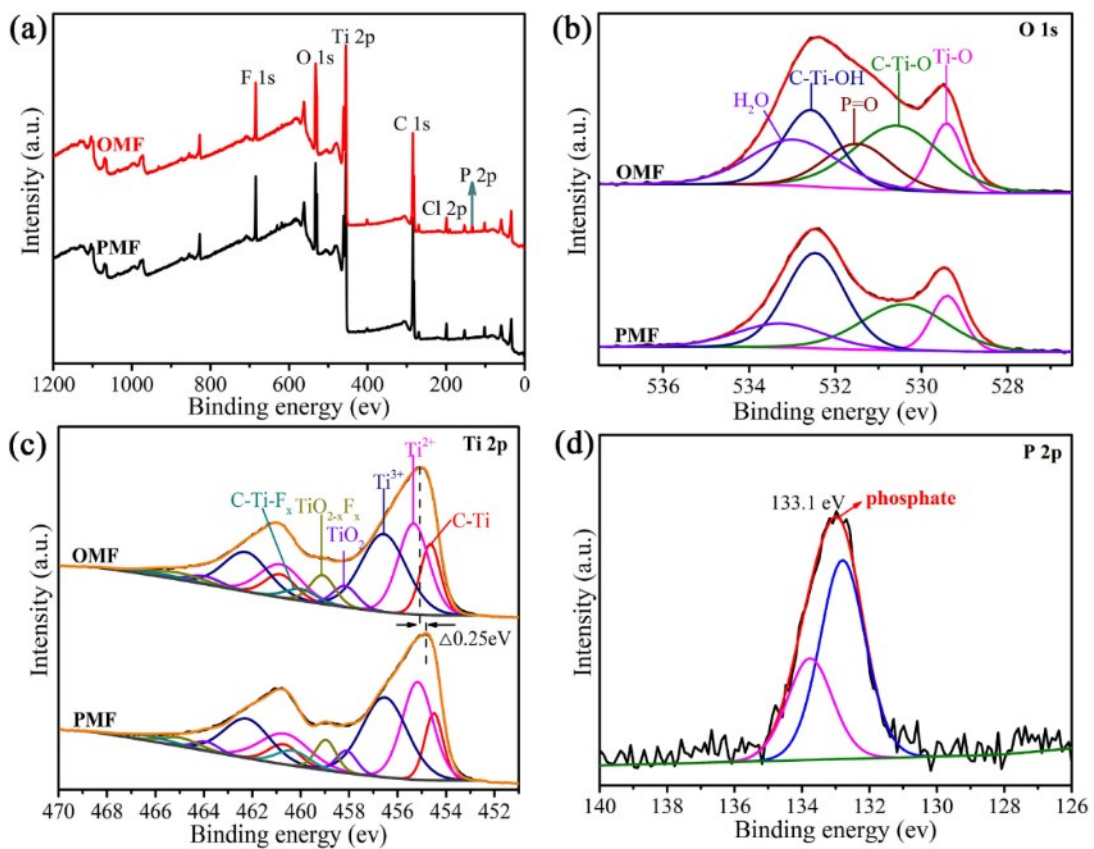


**Figure 4.5** (a) XPS survey spectra of PMF and OMF. (b) O 1s and (c) Ti 2p XPS spectra of the two films, d) P 2p high resolution spectra of OMF.

**Table 4.1** deconvolution results for O1s of PMF and OMF

Sample	Concentration (%)				
	Ti-O	C-Ti-O	P=O	C-Ti-OH	H <sub>2</sub> O
	529.4 eV	530.5eV	531.4eV	532.6 eV	533 eV
PMF	8.69	19.10	-	41.83	6.63
OMF	11.46	29.51	15.67	22.23	7.53
Reference	[266]	[267]	[265]	[30]	[30]

**Table 4.2** deconvolution results for Ti2p of PMF and OMF

Sample	Concentration (%)					
	Ti-C	Ti(II)	Ti(III)	TiO <sub>2</sub>	TiO <sub>2-x</sub> F <sub>x</sub>	C-Ti-F <sub>x</sub>
	2p <sub>3/2</sub>	2p <sub>3/2</sub>				
	454.6 eV	455.4eV	456.6eV	458.5 eV	459.2 eV	460.2 eV
PMF	13.07	31.96	38.26	4.85	6.63	5.24
OMF	15.49	30.05	37.52	5.59	7.53	3.82
Reference	[37]	[30, 37]	[37]	[268]	[268]	[268]

The electrochemical performance of as-prepared films was investigated through a three-electrode configuration in 3 M H<sub>3</sub>PO<sub>4</sub> aqueous electrolyte. **Figure 4.6a** compares the cyclic voltammetry (CV) profiles of both PMF and OMF at a scan rate of 20 mV s<sup>-1</sup>. The emergence of a pair of redox peaks at -0.5 to -0.2 V vs. Ag/AgCl for the two



films indicates their pseudocapacitive nature. Redox peak shift can be observed in both samples, which is due to electrochemical polarization. And the larger integrated area of CV curve of OMF implies its higher specific capacitance than PMF. The galvanostatic charge/discharge (GCD) measurement was also conducted at a current density of  $1 \text{ A g}^{-1}$ , as shown in **Figure 4.6b**. A longer discharging time but smaller internal resistance (IR) drop was observed in OMF, which represents its higher capacitance and smaller internal resistance, respectively.

The comparison of rate capability between PMF and OMF was conducted through measuring their respective CV curves from 2 to  $200 \text{ mV s}^{-1}$ , as shown in **Figure 4.6c-d**. The severely distorted CV shapes with increasing scan rates in PMF manifests its sluggish ion diffusion behavior, whereas less shape distortion is observed on OMF, indicative of the faster ion diffusion kinetics. The specific capacitances of both films at various scan rates are summarized in **Figure 4.7a**. OMF delivers the highest specific capacitance of  $297 \text{ F g}^{-1}$  at  $2 \text{ mV s}^{-1}$  and maintains  $108 \text{ F g}^{-1}$  when the scan rate rises to  $200 \text{ mV s}^{-1}$ , evidently higher than those of PMF at the same scan rates ( $218$  and  $43 \text{ F g}^{-1}$ , respectively), verifying the better rate capability in OMF. These results collectively prove that changing interlayer path to be more spacious and uniform is an efficient way to optimize the energy storage behavior of restacked  $\text{Ti}_3\text{C}_2\text{T}_x$  films. The expanded interlayer path is favorable for the easy access of electrolyte hydronium ions to active sites, while the uniformity of interlayer gallery can boost the transport of these

electrolyte ions, leading to higher capacitance and better rate performance. Note that the volumetric capacitance of OMF is not attenuated due to expanded interlayer path, as shown in upper plot of **Figure 4.7a**. It means that our method not only contributes to increased gravimetric capacitance and better rate capability but also endows  $\text{Ti}_3\text{C}_2\text{T}_x$  film with higher volumetric capacitance.

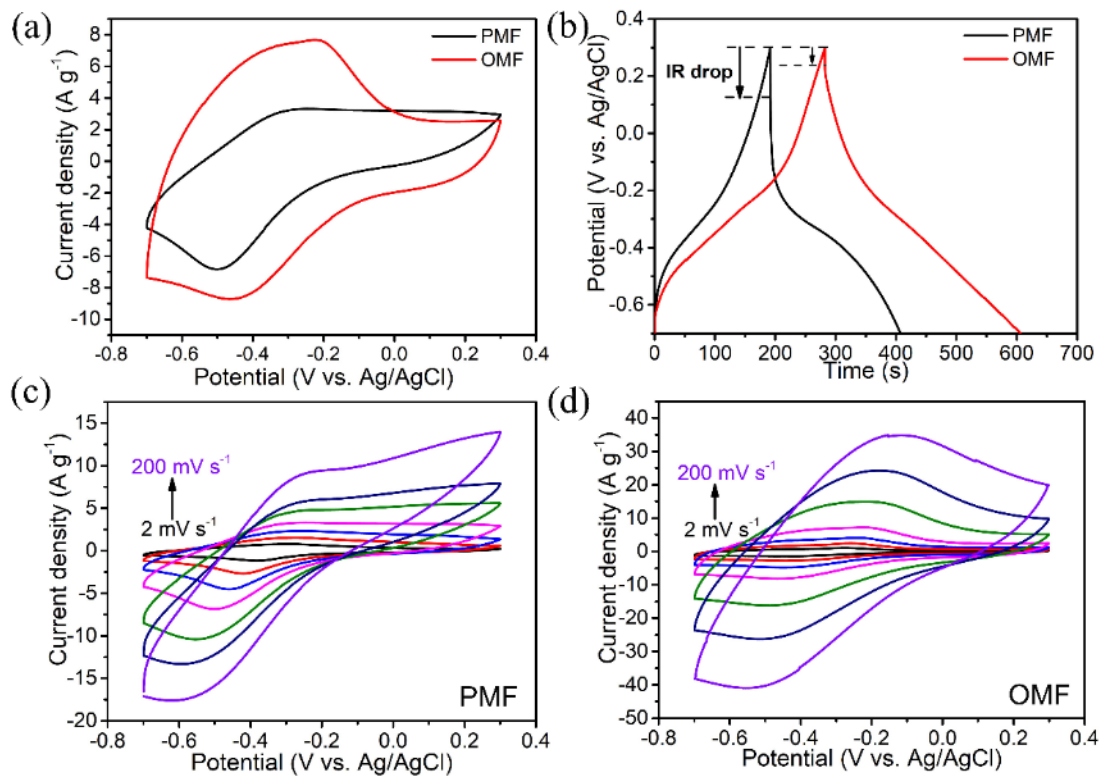


**Figure 4.6** (a) CV curves of pristine and optimized films at a scan rate of 20 mV s<sup>-1</sup>. (b) GCD curves of PMF and OMF at 1 A g<sup>-1</sup>. CV curves of (c) PMF, and (d) OMF under scan rates from 2 to 200 mV s<sup>-1</sup>

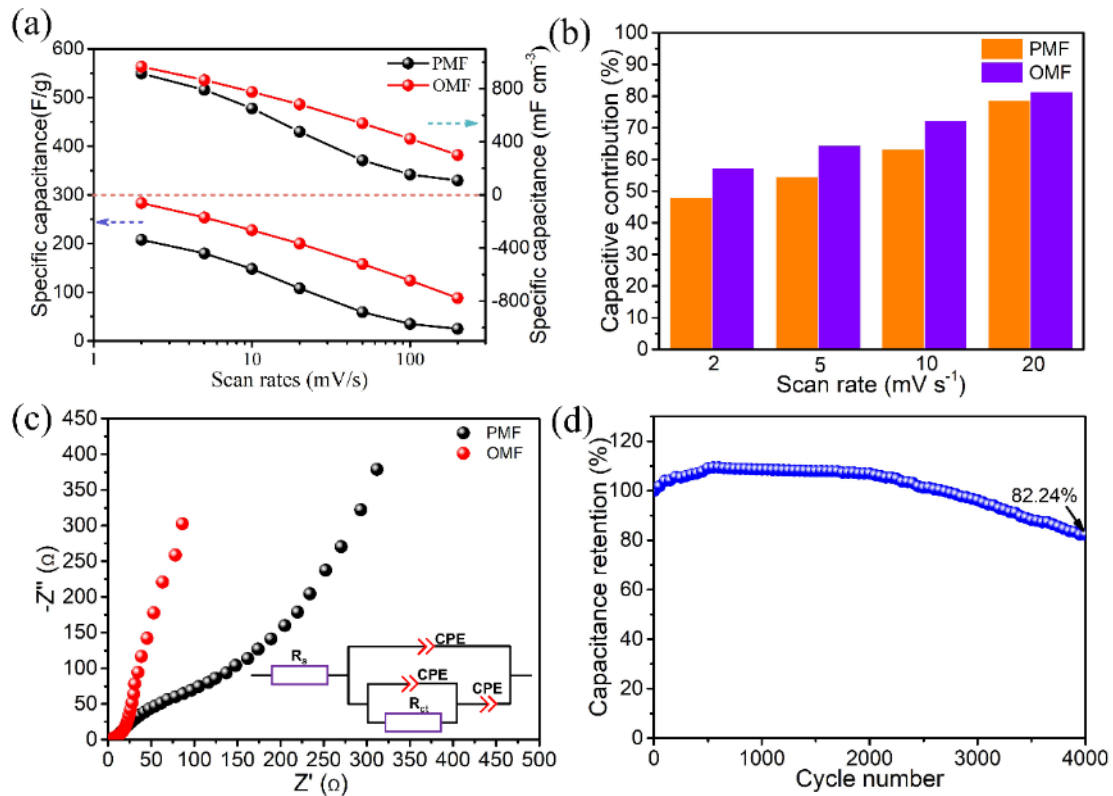


**Figure 4.7** (a) Gravimetric & volumetric capacitance versus scan rates for PMF and OMF. (b) Percentage of capacitive contribution of PMF and OMF. (c) Electrochemical impedance spectroscopy data of PMF and OMF, inset shows their equivalent circuit. (d) Cyclic test of OMF at 10 A g<sup>-1</sup>.

The charge storage mechanism can be studied by dividing the CV current into capacitive and diffusion-controlled contributions according to the equation below,<sup>[269]</sup>

$$i(V) = k_1 v^{0.5} + k_2 v \quad (4-1)$$

where  $i$  is the current at the potential  $V$ ,  $v$  is the scan rate, and  $k_1 v^{0.5}$  and  $k_2 v$  are diffusion-controlled and capacitive contributions to the total currents, respectively. Given this, the capacitive contributions to total capacitances at scan rates from 2 mV s<sup>-1</sup> to 20 mV s<sup>-1</sup> are calculated and summarized in **Figure 4.7b**. The non-diffusion-controlled contribution is 48 % (104 F g<sup>-1</sup>) in PMF at 2 mV s<sup>-1</sup>, while the proportion rises to 57.4% (171 F g<sup>-1</sup>) for OMF at the same scan rate. The capacitive contributions increase with



increasing scan rates for both samples, while OMF always possesses higher capacitive contribution than PMF at same scan rate. The higher capacitive contribution in OMF demonstrates that the expanded but uniform interlayer gallery can be favorable to capacitive behavior of  $\text{Ti}_3\text{C}_2\text{T}_x$  free-standing films. It also further testifies the feasibility of using the ester reaction between ethanol and phosphoric acid to optimize interlayer path of restacked  $\text{Ti}_3\text{C}_2\text{T}_x$  films for easier access of electrolyte ions and enhanced energy storage ability.

**Figure 4.7c** shows electrochemical impedance spectra (EIS) of the two films and their equivalent circuit for the simulation of electrochemical process. The intercept EIS curve on real axis represents equivalent series resistance (ESR), which is the total sum of ionic resistance of electrolyte, electrical resistance of electrode material and the interface resistance between electrode material and electrolyte.<sup>[109]</sup> OMF exhibits a smaller ESR of 4  $\Omega$  than PMF (6.6  $\Omega$ ), consistent with its lesser IR drop in GCD measurements (**Figure 4.6b**). The semi-circle part of the EIS plots can be used to estimate charge transfer resistance ( $R_{ct}$ ) through equivalent circuit fitting (inset of **Figure 4.7c**).  $R_{ct}$  of PMF and OMF are 300 and 18  $\Omega$ , respectively, as confirmed from fitted results, implying faster redox kinetics for charge storage in OMF. This parameter is dependent of available active area to electrolyte and electrical conductivity of electrode materials.<sup>[17]</sup> Since the electrical conductivities for PMF and OMF are identical due to same active material, the smaller  $R_{ct}$  in OMF could be attributed to its



increased available active sites to electrolyte in comparison with PMF. This increased availability of active sites in OMF may be originated from the more surface active -O groups and the optimized interlayer path, with the latter enabling the exposure of more active sites to electrolyte. The slope of the linear part in low frequency range of the EIS plot reveals ion diffusion resistance within electrode materials.<sup>[270]</sup> The much more vertical slope of OMF in **Figure 4.7c** manifests its easier interlayer ion transport behavior. Briefly, EIS analysis shows that OMF has more available active sites for electrolyte and provides faster path for electrolyte ion transport than PMF does.

The cyclic stability of OMF was evaluated through repetitive GCD test at  $10 \text{ A g}^{-1}$  for 4000 cycles, as presented in **Figure 4.7d**. The capacitance experienced an increment at initial stage due to the activation, which is common in MXene-based electrode materials.<sup>[271]</sup> Afterwards, a gradual decay with incremental cycling times was observed. A final capacitance retention of 82.42 % was obtained after the cycling test, indicating its good cyclic stability.

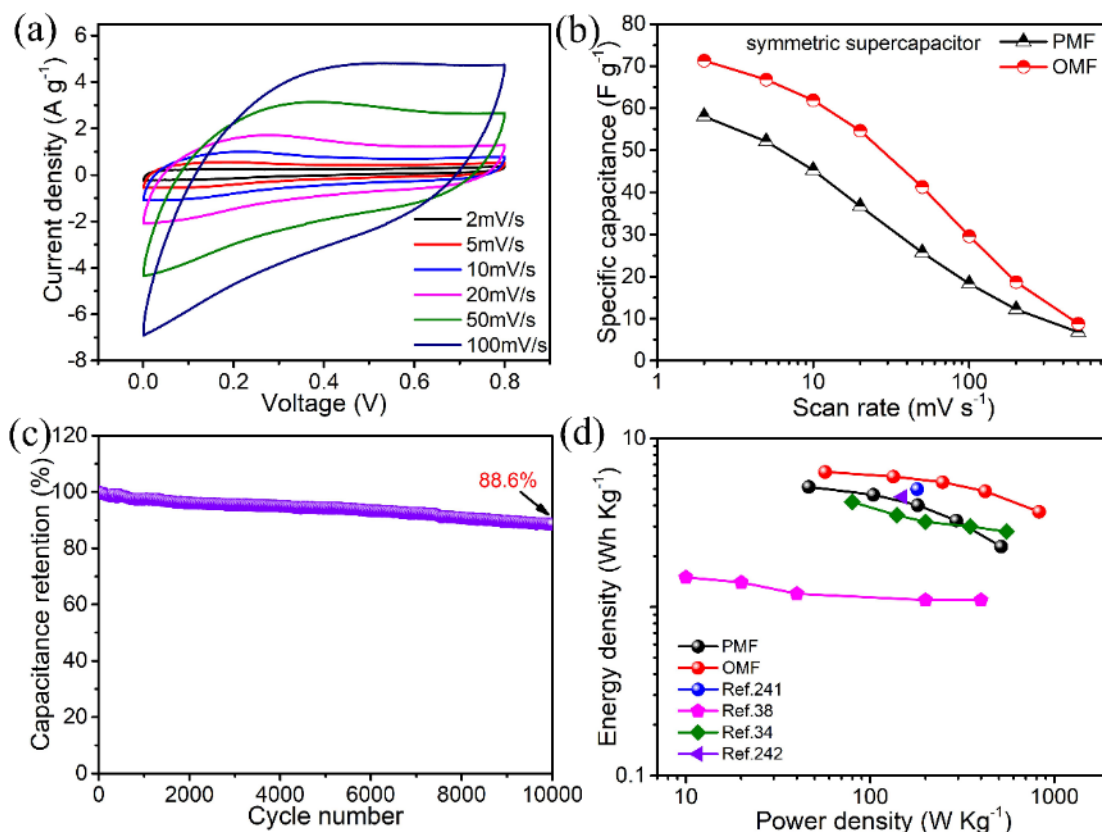


**Figure 4.8** (a) CV curves for OMF-based symmetric supercapacitors at scan rates from 2 to 100 mV s<sup>-1</sup>. (b) Gravimetric capacitance against scan rates for PMF-based and OMF-based symmetric supercapacitors. (c) Cyclic stability of OMF-based symmetric supercapacitor at a current density of 5 A g<sup>-1</sup> for 10000 cycles. (d) Ragone plot displaying energy density versus power density for PMF, OMF and some reported Ti<sub>3</sub>C<sub>2</sub>T<sub>x</sub> film based symmetric supercapacitors.

To verify the practical application of OMF, symmetric supercapacitors with OMF as the electrodes were assembled by using 3M H<sub>3</sub>PO<sub>4</sub> and Celgard 3501 as electrolyte and separator, respectively. **Figure 4.8a** shows that the OMF-based symmetric supercapacitor exhibits similar CV shapes at scan rates ranging from 2 to 100 mV s<sup>-1</sup>, indicating its good rate capability. The device delivers the highest specific capacitance of 71 F g<sup>-1</sup> at 2 mV s<sup>-1</sup> (based on the total mass of two electrodes), superior to that of PMF-based device (58 F g<sup>-1</sup>) at the same scan rate (**Figure 4.8b**). The cyclic stability



was assessed via GCD measurement at  $5 \text{ A g}^{-1}$  for 10000 cycles. **Figure 4.6c** indicates that 88.6 % of original capacitance was maintained after the cycling test, justifying its excellent cyclic stability. The plots of energy density vs. power density for assembled symmetric supercapacitors are shown in **Figure 4.6d**. The OMF-based device exhibits a maximum energy density of  $6.33 \text{ Wh Kg}^{-1}$  at a powder density of  $56.97 \text{ W Kg}^{-1}$  and its energy density still maintains at  $3.67 \text{ Wh Kg}^{-1}$  when the power density increases to  $826 \text{ W Kg}^{-1}$ , which outperforms those reported values on  $\text{Ti}_3\text{C}_2\text{T}_x$  film based symmetric supercapacitors, including Ref. 241<sup>[272]</sup> ( $5 \text{ Wh Kg}^{-1}$  at  $180 \text{ W Kg}^{-1}$ ), Ref. 38<sup>[37]</sup> ( $1.5 \text{ W Kg}^{-1}$  at  $10 \text{ W Kg}^{-1}$ ), Ref. 34<sup>[33]</sup> ( $4.2 \text{ Wh Kg}^{-1}$  at  $80 \text{ W Kg}^{-1}$ ) and Ref. 242<sup>[273]</sup> ( $4.5 \text{ Wh Kg}^{-1}$  at  $150 \text{ W Kg}^{-1}$ ).

In addition, an asymmetric supercapacitor was also assembled with OMF and activated carbon as anode and cathode, respectively, to further increase the energy density. The energy storage performance of activated carbon was first characterized with three-electrode configuration, as shown in **Figure 4.9**. It delivers the highest specific capacitance of  $96 \text{ F g}^{-1}$  at  $2 \text{ mV s}^{-1}$  within potential window of  $0 \sim 0.7 \text{ V}$  vs.  $\text{Ag/AgCl}$ . The mass ratio between anode and cathode materials can be confirmed as 1:4.42 according to charge balance between two electrodes.

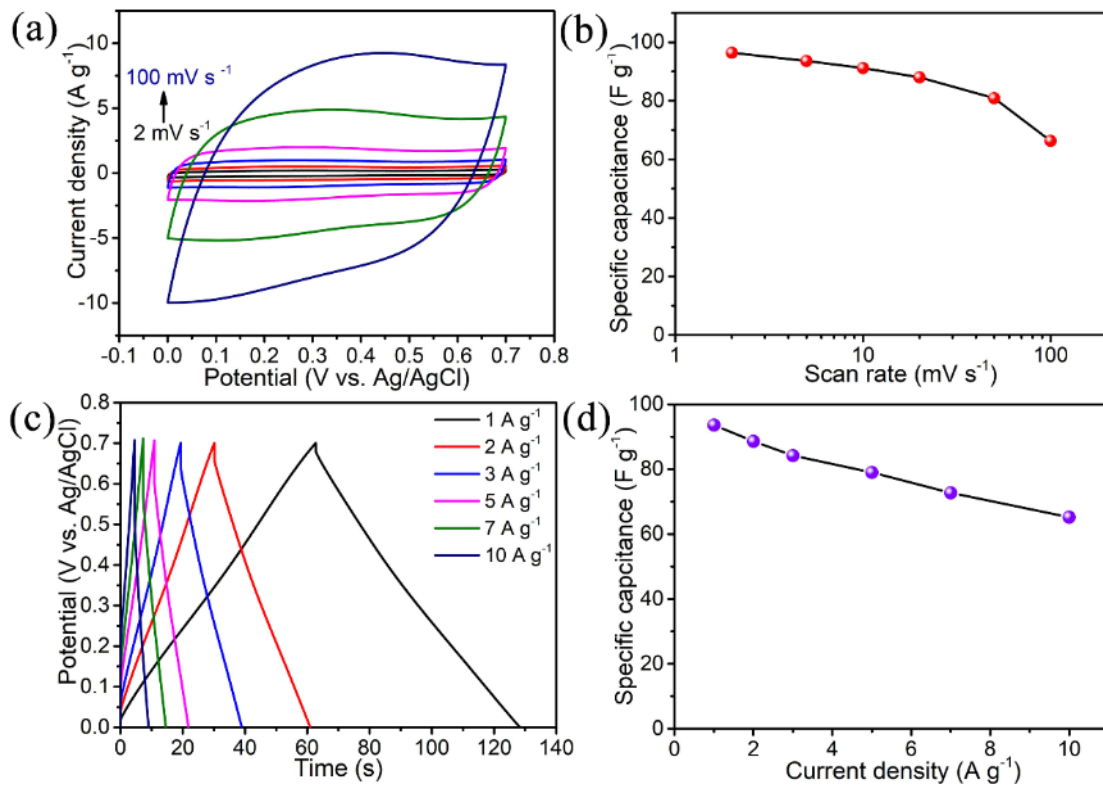


**Figure 4.9** (a) CV curves, (b) specific capacitance vs. scan rates, (c) GCD curves at current densities from 1 to 10 A g<sup>-1</sup>, and (d) rate performance of activated carbon electrode.

The assembled asymmetric device has a stable voltage window of 0 ~ 1.4 V (**Figure 4.10a-b**). Its GCD curves at current densities from 1 to 10 A g<sup>-1</sup> are shown in FigureS7c. A highest specific capacitance of 24 F g<sup>-1</sup> at 1 A g<sup>-1</sup> and 80% of capacitance retention after 3000 cycles at 2 A g<sup>-1</sup> are obtained in the device (**Figure 4.10d-e**). Benefiting from the wider voltage window than symmetric supercapacitor, it delivers the highest energy density of 7 Wh Kg<sup>-1</sup> at a senior power density of 698 W Kg<sup>-1</sup> and still retains an energy density of 4.01 Wh Kg<sup>-1</sup> even if its power density reaches 7007 W Kg<sup>-1</sup> (**Figure 4.10f**). Two asymmetric supercapacitor cells in series were charged at 2 A g<sup>-1</sup> within 17 seconds and can light a red LED bulb with working potential of 1.8~2.2 V (inset of **Figure**

4.10f), again demonstrating the application prospect of OMF. These competitive performances of OMF-based supercapacitors verify the efficiency of the ester reaction between ethanol and phosphoric acid to optimize interlayer path of restacked  $Ti_3C_2T_x$  film for enhanced electrochemical performance, which may be extended to scalable production of other MXene restacked films for better energy storage behavior.

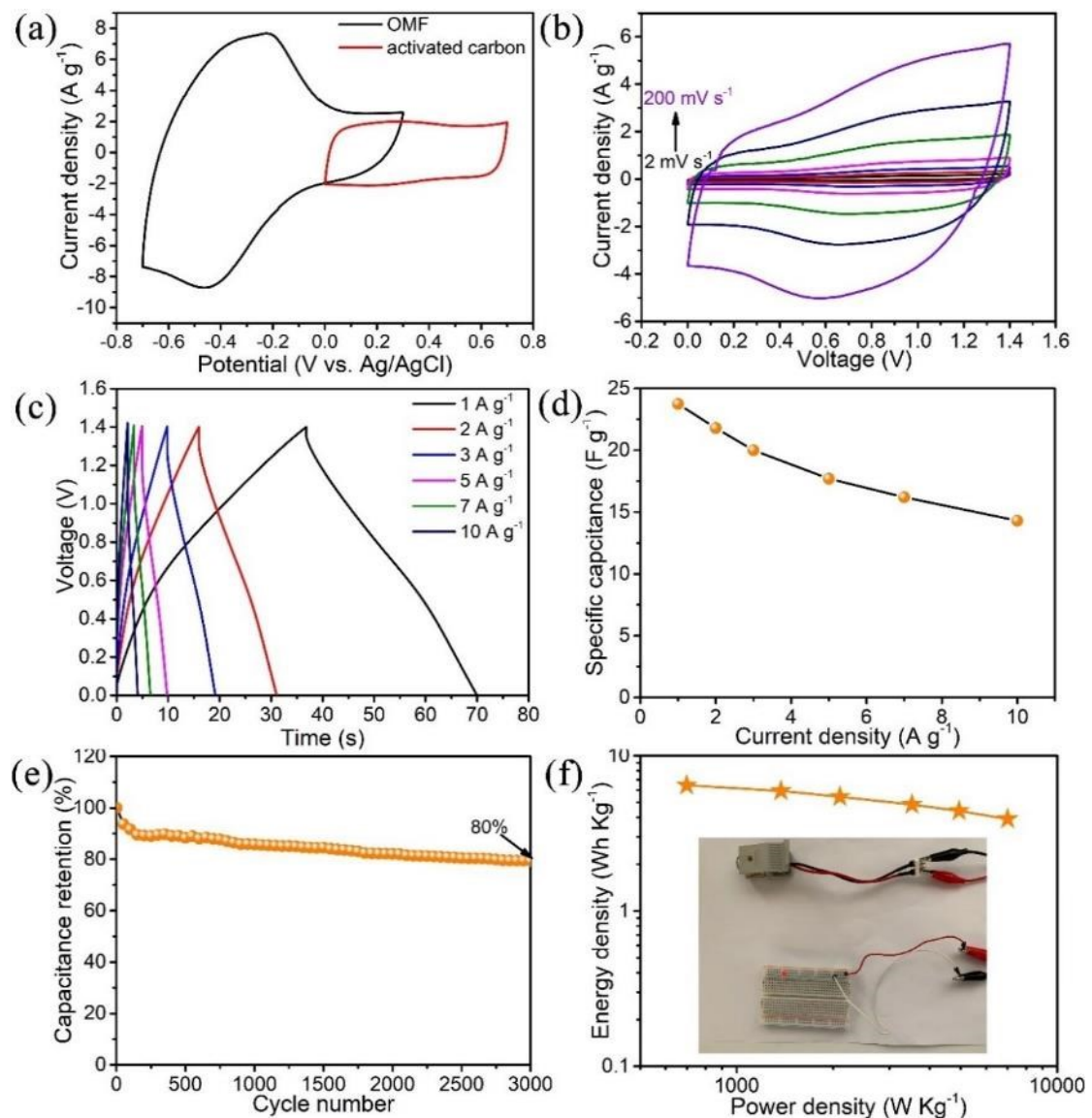


**Figure 4.10** (a) CV curves of OMF and activated carbon at  $20\text{ mV s}^{-1}$ . (b) CV curves of an OMF//activated carbon asymmetric supercapacitor at scan rates ranging from 2 to  $200\text{ mV s}^{-1}$ . (c) GCD curves of the device at current densities from 1 to  $10\text{ A g}^{-1}$ . (d) Rate performance of the asymmetric supercapacitor. (e) Cyclic stability of the device



at  $2 \text{ A g}^{-1}$ . (f) Ragone plot of the device. Inset is the photo showing that two devices in series can light up a red LED bulb with working potential of 1.8 to 2.2 V.

### 4.3. Conclusion

In summary, a facile method employing the ester reaction between ethanol and phosphoric acid to optimize the interlayer path of restacked  $\text{Ti}_3\text{C}_2\text{T}_x$  films is proposed for supercapacitor application. The optimized  $\text{Ti}_3\text{C}_2\text{T}_x$  film owns molecular scale expanded but more uniform interlayer path as compared with pristine film, which endows it with more available active sites to electrolyte, faster ion diffusion kinetics and accelerated redox reaction kinetics, contributing to its enhanced gravimetric capacitance and rate capability. Furthermore, unlike those conventional methods that resist restacking among  $\text{Ti}_3\text{C}_2\text{T}_x$  sheets via constructing porous structure, our method introduces only mild interlayer expansion that will not decrease its volumetric capacitance. Instead, the volumetric capacitance of OMF is raised due to its improved interlayer gallery. Therefore, the proposed strategy is promising to alleviate the restacking of  $\text{Ti}_3\text{C}_2\text{T}_x$  sheets while sustaining high volumetric energy storage ability of the assembled films, capable of being extended to other assembled 2D material films for faster interlayer ion diffusion kinetics and preferable energy storage ability.



## Chapter 5 Unravel boosted supercapacitive performance of $\text{Ti}_3\text{C}_2\text{T}_x$ MXene due to grafted phosphorous atoms

$\text{Ti}_3\text{C}_2\text{T}_x$  MXene is regarded as a promising supercapacitor electrode material due to its high conductivity and pseudocapacitive nature. Its capacitance can be improved via nitrogen or sulfur heteroatom doping due to the ability to donate surface electrons. Phosphorus possesses a lower electronegativity than nitrogen and sulfur so that it is believed to enable greater performance enhancement once being doped. Herein, phosphorus is incorporated onto  $\text{Ti}_3\text{C}_2\text{T}_x$  to boost its electrochemical performance and the underlying enhancement mechanism is revealed. The results show that doped phosphorus exists with the formation of Ti-O-P terminations on MXene surface, and 2.1 at. % P-doped  $\text{Ti}_3\text{C}_2\text{T}_x$  delivers a capacitance enhancement of 30% ( $328 \text{ F g}^{-1}$  at  $2 \text{ mV s}^{-1}$ ) in comparison with pristine MXene and outstanding cyclic stability, comparable to N- and S-doped MXene. Multiple *in situ* and *ex situ* characterization methods along with DFT calculations collectively reveal that the formed Ti-O-P species are new active sites for more proton bonding-debonding, contributing to the charge storage and capacitive performance in MXene. However, higher surface phosphorus doping would destroy crystal integrity of MXene and leads to performance deterioration, explaining why much superior energy storage ability to N- and S- doped MXene cannot be achieved via further increasing phosphorus doping amount.



## 5.1 Introduction

Carbon neutrality has motivated the acceleration of worldwide exploitation of renewable energy resources, such as solar energy, wind energy, hydro energy and tidal energy etc. to reduce the emission of carbon dioxide from the use of fossil fuels. Supercapacitors are regarded as a kind of promising energy storage devices for electricity generated from renewable resources due to its high power density and long cycle life.<sup>[26, 140, 236]</sup> The devices store energy via either fast redox reactions on/near electrode surface or ion adsorption on electrode surface, which corresponds to pseudocapacitors (PCs) or electric double layer capacitors (EDLCs), respectively.<sup>[11, 15]</sup> PCs deliver higher energy densities than EDLCs due to <sup>[189]</sup> more charges stored at redox active sites.<sup>[140, 274]</sup> MXenes have been studied as pseudocapacitive electrode materials since they were discovered in 2011, owing to their metallic conductivity (up to  $2.4 \times 10^6$  S/m), hydrophilic surface, and outstanding capacitance as well as cycling stability in acidic electrolyte.<sup>[25, 26, 154, 157, 205]</sup>

MXenes refer to two-dimensional (2D) transition metal carbides, nitrides and carbonitrides, which have a general formula of  $M_nX_{n+1}T_x$ , where M represents early transition metal (Ti, Cr, V, Mo, Nb, Zr, Hf, Ta, Sc, W, Y), X is C and/or N, and T refers to functional groups linked with surface metal atoms of the material, e.g., -O, -OH, -F, -Cl.<sup>[236, 275]</sup> A typical method for synthesizing MXene is selectively etching off A-layer of hexagonal stratified  $M_{n+1}AX_n$  (MAX) precursors in hydrofluoric acid solution or



mixed etchant of hydrochloric acid and transition metal fluorides.<sup>[167, 275, 276]</sup> Other methods, like molten salt etching,<sup>[106]</sup> electrochemical etching,<sup>[174]</sup> and bottom-up chemical vapor deposition,<sup>[188]</sup> were also developed to successfully fabricate MXenes. The surface functional groups of MXenes vary with synthesis methods and conditions, which make the materials exhibit various physiochemical properties.<sup>[106, 276, 277]</sup>  $Ti_3C_2T_x$ , thus far, is the most studied MXene for supercapacitor electrode material and delivers the highest specific capacitance in acidic electrolyte among all as-made MXenes, which store energy via proton bonding/debonding with surface oxygen terminals.<sup>[28, 195]</sup>

To boost  $Ti_3C_2T_x$  MXene for supercapacitor applications, alkali,<sup>[163]</sup> n-butyllithium,<sup>[36]</sup> and ammonium persulfate,<sup>[211]</sup> etc. were utilized to engineer more surface oxygen functional groups on  $Ti_3C_2T_x$  for enhanced charge storage ability. Heteroatom doping is also an efficient way to modulate MXene electronic band structure to boost charge storage. Nitrogen- and sulfur-doped  $Ti_3C_2T_x$  via heating or solvothermal method<sup>[38, 41, 43]</sup> have shown improved capacitance. Metal elements, such as Nb<sup>[278]</sup> and V<sup>[201]</sup> have also been doped into  $Ti_3C_2T_x$  for enhanced charge storage. But inferior cycling stability was observed in these metal doped MXenes.<sup>[201, 278]</sup> The improved capacitive performance in these heteroatom doped  $Ti_3C_2T_x$  MXene is attributed to ameliorated electron-donor capability after incorporation of heteroatoms.<sup>[37, 38, 41, 42]</sup> Inspired by this, phosphorus with lower electronegativity than nitrogen and sulfur is expected to tune  $Ti_3C_2T_x$  into a more active electron-donor once being doped. Temperature-dependent



phosphorus doping behavior on  $\text{Ti}_3\text{C}_2\text{T}_x$  MXene has been confirmed, and the phosphorus-doped MXene exhibits an improved capacitance.<sup>[39]</sup> However, the underlying mechanism about how doped phosphorus contributes to the enhanced performance and the effect of the doped element amount on  $\text{Ti}_3\text{C}_2\text{T}_x$  MXene crystal structure and capacitive performance is still vague.

Herein, phosphorus was doped into  $\text{Ti}_3\text{C}_2\text{T}_x$  by heating the MXene aerogel in mixed atmosphere of argon and phosphine decomposed from sodium hypophosphite (Figure 1a). The resultant phosphorus-doped  $\text{Ti}_3\text{C}_2\text{T}_x$  MXene (PMX) with 2:1 mass ratio between MXene aerogel and sodium hypophosphite shows a high gravimetric capacitance of  $328 \text{ F g}^{-1}$  at  $2 \text{ mV s}^{-1}$  in  $1 \text{ M H}_2\text{SO}_4$  electrolyte, superior to that of pristine MXene ( $252 \text{ F g}^{-1}$ ). The underlying mechanism for the enhancement of capacitance in PMX was investigated by combining *in situ* Raman spectroscopy, *ex situ* X-ray absorption near edge structure spectra (XANES), *ex situ* X-ray diffraction (XRD) patterns and *ex situ* X-ray photoelectron spectroscopy (XPS). The results show that the phosphorus heteroatoms are grafted onto  $\text{Ti}_3\text{C}_2\text{T}_x$  MXene through oxygen bridging, forming surface Ti-O-P groups, which act as new active sites for more proton bonding/debonding and thereby result in more charge transfer and greater valence state variation of titanium during charge/discharge process (**Figure 5.1b-d**). It is also revealed that the moderate surface phosphorus doping can maintain the MXene crystal structure intact and boost capacitance, but the further increased incorporation of the

hybrid element would injure crystal structure of MXene and even induce amorphization, conversely adverse to its energy storage ability.

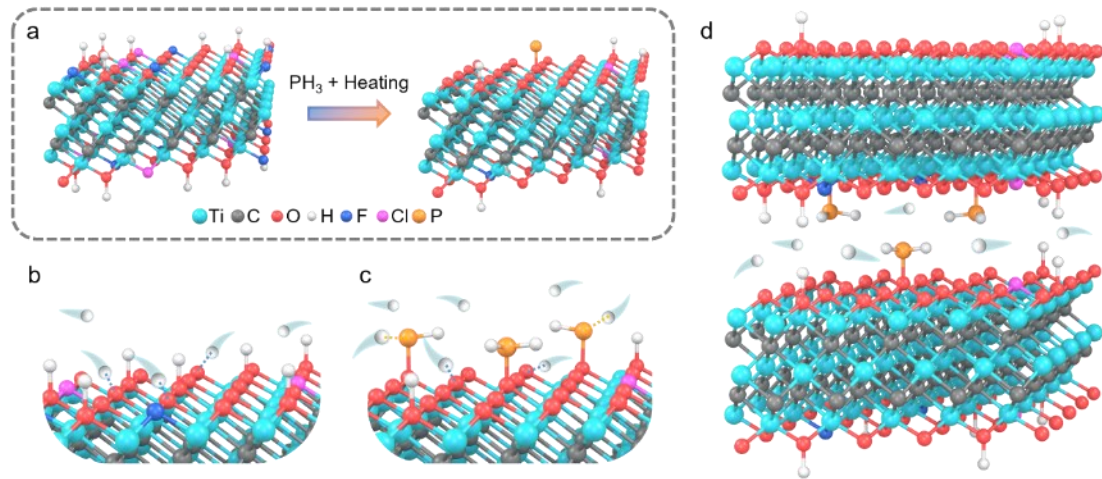


**Figure 5.1** Schematic illustration for (a) phosphorus doping strategy, (b) proton interaction with surface of pristine  $Ti_3C_2T_x$ , and (c)-(d) proton interaction with surface of PMX.

## 5.2 Results and discussions

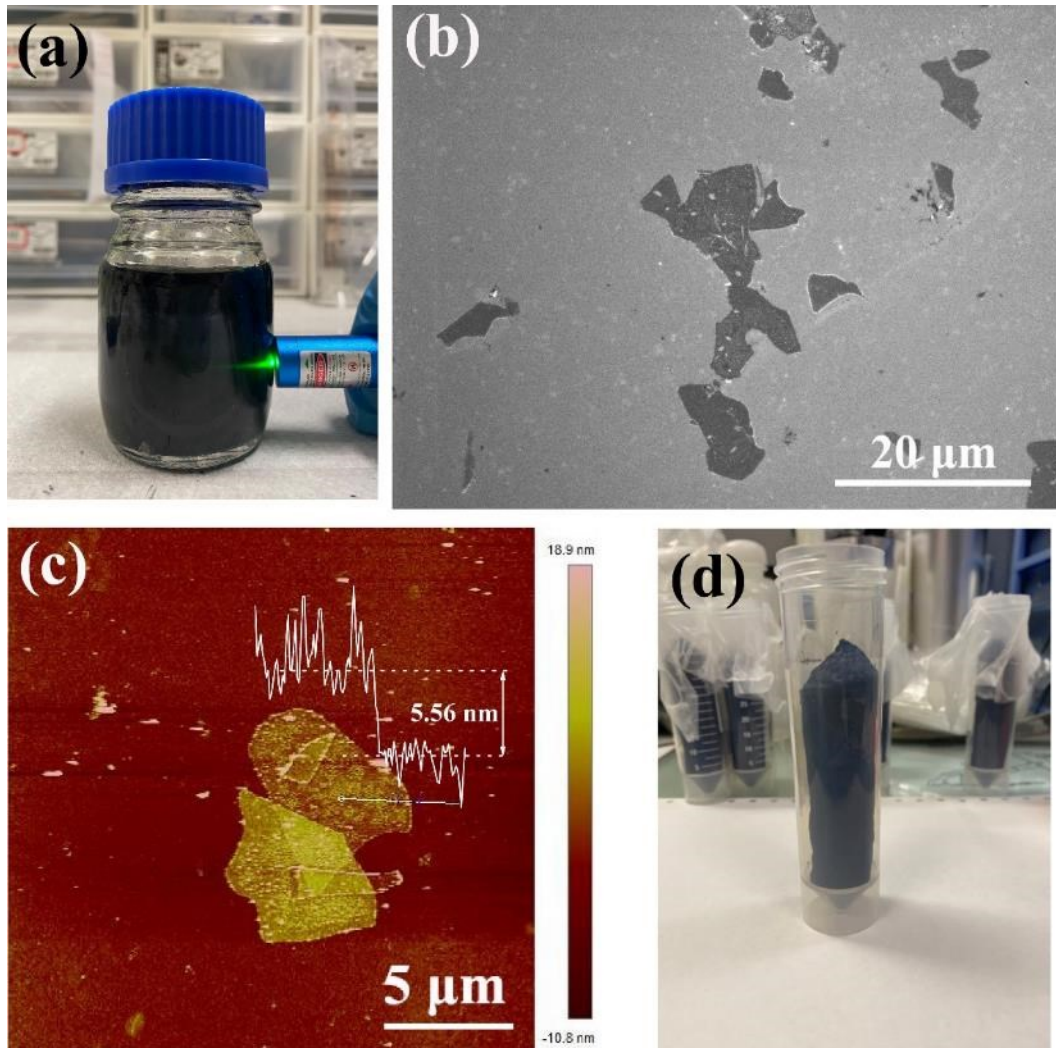


**Figure 5.2** (a)  $\text{Ti}_3\text{C}_2\text{T}_x$  MXene colloidal solution shows Tyndall effect. (b) SEM image of  $\text{Ti}_3\text{C}_2\text{T}_x$  sheets on silicon substrate. (c) AFM image of  $\text{Ti}_3\text{C}_2\text{T}_x$  sheets, inset shows height profile of the selected line on the upper sheet. (d) Photograph of  $\text{Ti}_3\text{C}_2\text{T}_x$  MXene aerogel.

Multilayered  $\text{Ti}_3\text{C}_2\text{T}_x$  MXene was first prepared through selectively etching aluminum layer of  $\text{Ti}_3\text{AlC}_2$  precursor in HCl and LiF mixed liquid, followed by fierce oscillation for its delamination to obtain few-layered MXene. The resultant MXene aqueous solution shows Tyndall effect when a ray transmits through it (**Figure 5.2a**), indicating its colloidal nature. The diameter of MXene sheets is  $0.5\sim 8\ \mu\text{m}$ , as confirmed from the

scanning electron microscope (SEM) image (**Figure 5.2b**). The atomic force microscope (AFM) result shows that MXene sheets have a thickness of 5.56 nm (**Figure 5.3c**), corresponding to a stacking of 5-6 layers. Gas-state doping strategy (**Figure 1a**) was applied in this work for avoiding the subsequent cumbersome washing procedures to remove residual doping source. To increase doping efficiency, MXene sheets were assembled into porous MXene aerogel (**Figure 5.2d** and **Figure 5.3a**) through flash freezing the MXene solution and subsequent freeze-drying.<sup>[228]</sup> Sodium hypophosphite was heated at 350°C to produce phosphine, which was brought by flowing Ar to the downstream MXene aerogel (at 400°C) to fulfill the phosphorus doping. The mass ratio between MXene and NaH<sub>2</sub>PO<sub>2</sub> was varied from 1:1 to 1:2 to tune phosphorus doping amount, named as PMX1 and PMX2, respectively. Meanwhile, a control sample (CMX) was also fabricated by heating pristine Ti<sub>3</sub>C<sub>2</sub>T<sub>x</sub> MXene aerogel (MX) in pure argon under the same heating conditions as those used in the doping process.

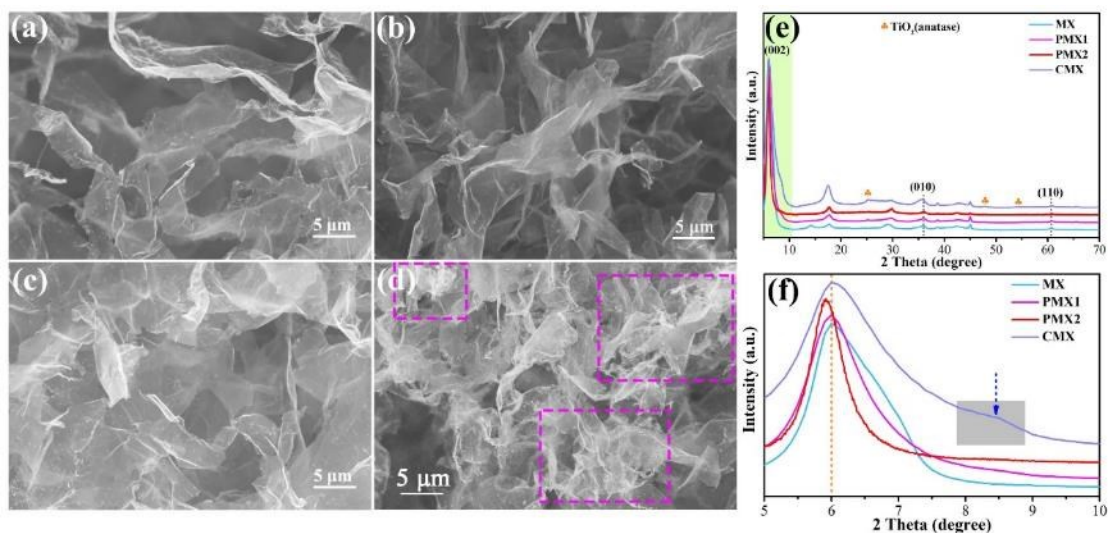


**Figure 5.3** SEM images of (a) MX, (b) PMX1, (c) PMX2 and (d) CMX. (e) XRD patterns of the samples. (f) Enlarged (002) peak in (e).



SEM results show that both PMX1 and PMX2 retain a similar macroporous structure with MX (**Figure 5.3b-c**) after phosphorous incorporation, implying the robust pore structure in the MXene aerogel. Alike porous structure is also observed in CMX, but with some white spots (enclosed by the pink rectangles in **Figure 5.3d**), which could be due to the oxidation of  $Ti_3C_2T_x$ . The existence of titanium oxide in CMX is confirmed from the XRD peaks, while no distinct oxide peaks are detected in both PMX1 and PMX2, as shown in **Fig.5.3e**. This result implies that phosphine not only serve as doping source but also could restrict degradation of  $Ti_3C_2T_x$  being heated. The position and full width at half maximum (FWHM) of the (002) XRD peak of MXene can reveal the changes of interlayer distance ( $d$ ) and crystallinity, respectively, in  $Ti_3C_2T_x$  MXene.<sup>[41]</sup> Enlarged (002) peaks of the samples are shown in Figure 1f. MX shows an unsymmetric but right-tailing (002) peak at  $2\theta$  value of  $6.02^\circ$ , indicating its main interlayer space of  $14.67 \text{ \AA}$  and partial MXene sheets having smaller interlayer distance. The peak value of PMX1 keeps at  $2\theta$  of  $6.02^\circ$  but its FWHM becomes narrower than MX, which implies the increased uniformity of interlayer path. Noticeably, the peak of PMX2 left shifts to  $5.91^\circ$  ( $d=14.94 \text{ \AA}$ ) with smaller FWHM compared to MX, manifesting its more spacious and uniform interlayer path of MXene sheets due to phosphorus doping. This broadened but uniform interlayer path is expected to boost ion diffusion to active sites.<sup>[279]</sup> However, CMX without phosphorus doping shows a much broader (002) peak than the other samples, implying the inferior MXene crystallinity. And a peak shoulder at  $2\theta \approx 8.5^\circ$  in CMX is indicative of the



presence of some MXene sheets with narrower interlayer path, which could originate from interlayer shrinkage of MXene during its heating process.<sup>[280]</sup> Overall, XRD results demonstrate that the phosphorus incorporation not only boosts the interlayer space of MXene but also retards its oxidation during heating process.

Nitrogen gas adsorption/desorption at 77K was conducted to analyze specific surface area and pore size distribution of the samples (**Figure 5.4a-b**). The Brunauer–Emmett–Teller (BET) surface area of MX is  $41.03 \text{ m}^3 \text{ g}^{-1}$ , while those of PMX1, PMX2 and CMX are increased to 43.88, 41.83 and  $47.63 \text{ m}^3 \text{ g}^{-1}$ , respectively (**Figure 5.4a**). These results indicate that the heating procedure ( $400^\circ\text{C}$ ) causes the enhancement of specific surface area of MXene aerogel, while P-doped MXene (PMX1, PMX2) exhibits a lower increment than that with only heating (CMX). The less increment of specific surface area in P-doped MXene can be attributed to their suppressed oxidation. And the larger increment of specific surface area in CMX could be due to its obvious oxidation that leads to the breakage of MXene sheets. **Figure 5.4b** indicates that MX, PMX1, PMX2 and CMX all possess a similar hierarchical pore size distribution (1.5~150 nm). But P-doped samples, especially PMX2, exhibit a higher differential pore volume at pore width of ~1.5 nm (inset of **Figure 5.4b**), probably resulting from the phosphorus incorporation.

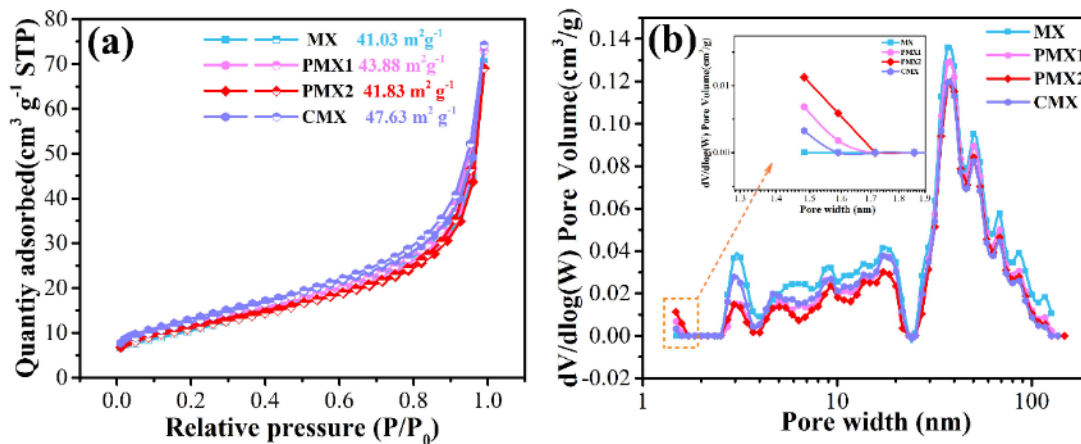


**Figure 5.4** (a) Nitrogen isothermal adsorption/desorption curves and (b) corresponding pore width distribution curves of MX, PMX1, PMX2 and CMX.

To further investigate the crystal structure change of MX after phosphorus doping, high resolution transmission electron microscope (HRTEM) and selected area electron diffraction (SAED) characterizations were carried out (**Figure 5.5**). HRTEM images show that the phosphorus doping of PMX1 and PMX2 has not led to obvious variation of interplanar distance of (010) planes in  $\text{Ti}_3\text{C}_2\text{T}_x$  MXene (**Figure 5.5a-c**), which is consistent with the XRD results of MX, PMX1 and PMX2 showing almost identical (010) peak locations (**Figure 5.3e**). However, CMX possesses a larger (010) interplanar distance (0.256 nm), consistent with its left shifted (010) diffraction peak compared with MX (Figure 1e). The SAED pattern (**Figure 5.5a**) of MX demonstrates the hexagonal symmetry of  $\text{Ti}_3\text{C}_2\text{T}_x$  MXene inherited from  $\text{Ti}_3\text{AlC}_2$  parent phase.<sup>[25]</sup> Its innermost circle of diffraction points corresponds to (010) planes and the second circle of diffraction points originates from (110) planes.<sup>[281]</sup> PMX1 and PMX2 with different doping contents exhibit the identical crystal symmetry with pristine MX, shown in **Figure 5.5b-c**.

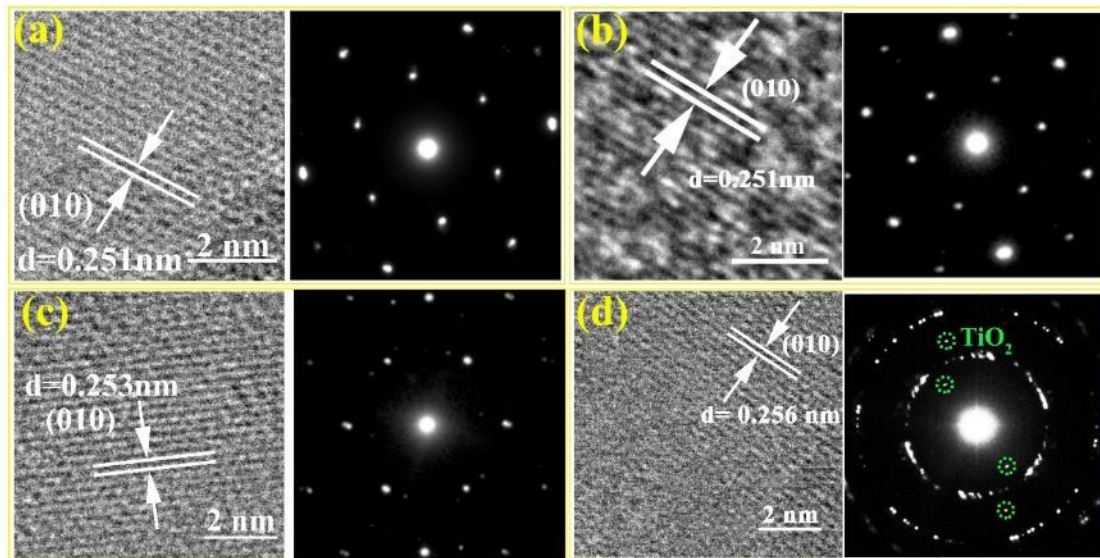


**Figure 5.5** HRTEM images and corresponding SAED patterns of (a) MX, (b) PMX1, (c) PMX2 and (d) CMX, respectively.

However, if the doping amount is further enhanced via increasing  $\text{NaH}_2\text{PO}_2$ : MXene mass ratio to 8 and 20, corresponding to the samples PMX8 and PMX20, respectively, their HRTEM and SAED results show evident difference from MX, shown in Figure S3. The interplanar distance of (010) plane shrinks and new diffraction points appears in PMX8 (**Figure 5.6a-b**), which indicates the changed crystal structure due to the phosphorus incorporation. Amorphization is observed in PMX20 with highest doping extent (**Figure 5.6c-d**), and the six-fold symmetry of (010) planes is disappeared in the area remaining crystal (**Figure 5.6e**). These results conclude that high phosphorus doping amount would break the crystal integrity and symmetry of  $\text{Ti}_3\text{C}_2\text{T}_x$  MXene. By contrast, CMX only exhibits semicontinuous diffraction rings indicating its polycrystalline nature, and some newborn diffraction points corresponding to anatase phase (**Figure 5.5d**), collectively verifying the fragmentation and oxidation of MXene

sheets in the sample, consistent with the foregoing XRD and BET results.

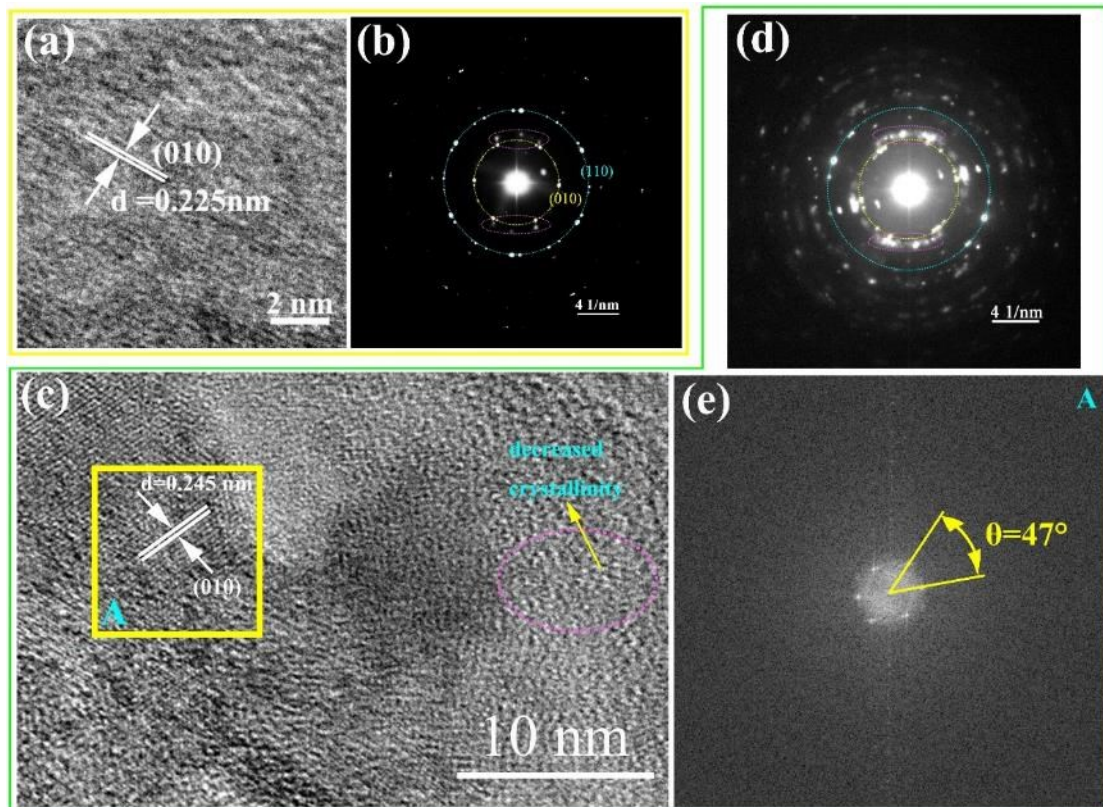


**Figure 5.6** (a) HRTEM image and (b) SAED pattern of PMX8. (c) HRTEM image and (d) SAED pattern of PMX20. (e) FFT pattern of A region in (c)

Electron energy loss spectroscopy (EELS) was conducted to analyze the elemental distribution and change of chemical environment with phosphorus incorporation in P-doped MXene. Here MX, PMX2 and CMX are selected to conduct EELS analysis for simplicity. Both O-K edge and Ti L<sub>2,3</sub> edge spectra of the samples were normalized with their respective Ti L<sub>2</sub> peak intensities, as shown in **Figure 5.7a-b**. PMX2 exhibits the highest O K edge intensity after the normalization (**Figure 5.7b**), implying its richest oxygen composition. It also denotes that the doped phosphorus could be favorable for maintaining more surface oxygen on Ti<sub>3</sub>C<sub>2</sub>T<sub>x</sub>. In addition, asymmetric O K edge is detected in CMX, which can be attributable to the formed titanium oxide (anatase)

within the sample.<sup>[282]</sup> Note that the first peak in O K edge spectra is ascribed to the hybridization between Ti 3d orbitals and surface oxygen terminations.<sup>[283]</sup> To compare the chemical environment of oxygen in samples, their O K edge EELS spectra are normalized with the first peak (**Figure 5.7c**). The almost identical first O-K edge peaks for MX and PMX2 indicate that the original oxygen maintains the bonding with titanium after the phosphorus incorporation. But the difference at peak 2 of oxygen K edge spectra between pristine MX and PMX2 confirms the change of local environment of oxygen atoms in PMX2,<sup>[282]</sup> which could be attributed to the introduced hybrid phosphorus element. The detailed change on chemical valence and environment will be discussed in the following XPS and extended X-ray absorption fine structure (EXAFS) results. The EELS element mapping of PMX2 (**Figure 5.7d**) shows the doped phosphorus is uniformly dispersed at a nanometer scale.

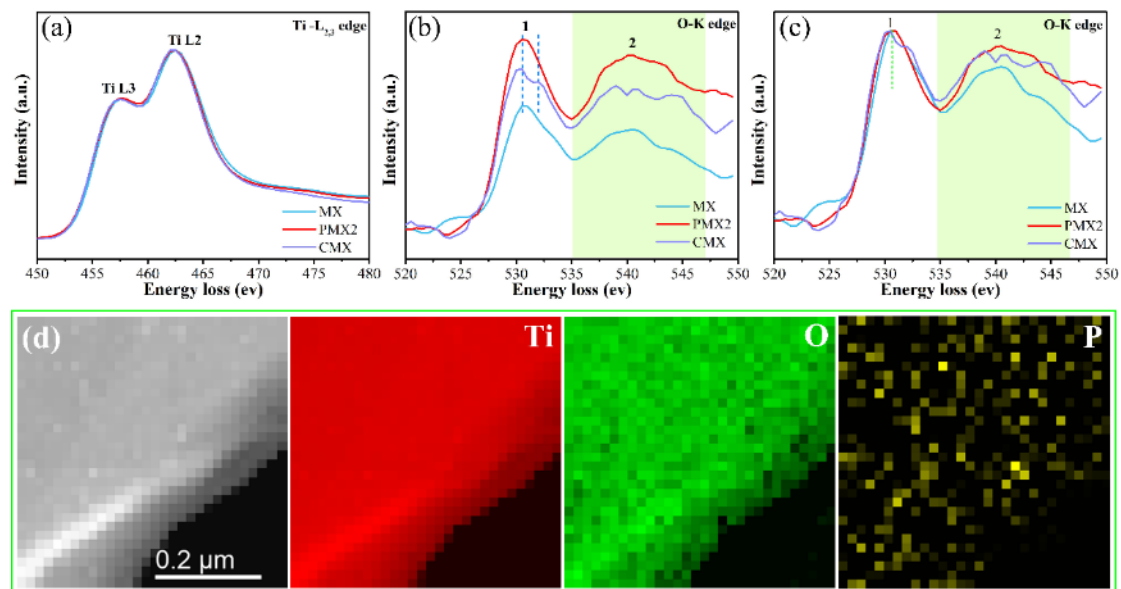


**Figure 5.7** (a) Ti  $L_{2,3}$  edge and (b) O K edge EELS spectra of MX, PMX2 and CMX, in which EELS intensities of two elements in each sample were normalized with their separate highest peak values in Ti  $L_{2,3}$  edge EELS spectra. (c) O K edge spectra for the



three samples normalized with the first peak intensity. (d) EELS elemental mapping results (Ti, O, P) of PMX2.

The composition of samples was investigated by XPS survey spectra and shown in **Figure 5.8a**. PMX1 and PMX2 possess 1.4 and 2.1 at. % phosphorus, respectively, implying the successful phosphorus incorporation and the doping amount increases with increasing amount of  $\text{NaH}_2\text{PO}_2$  added. It is also noted that PMX1 and PMX2 have 20.4 and 25.1 at. % oxygen contents, respectively, which are higher than those of MX and CMX (17.4 and 19.3 at. %, respectively). This indicates the doped phosphorus is favorable for keeping surface oxygen on  $\text{Ti}_3\text{C}_2\text{T}_x$ , consistent with aforementioned EELS results (Figure 5.7b). In the meantime, the less content of -F and -Cl in PMX2 than in MX and CMX indicates that halogen terminations may be more easily eliminated in reducing atmosphere ( $\text{PH}_3$ ). All XPS spectra were calibrated through C-Ti-T<sub>x</sub> bond in C1s for a reliable analysis result in this work.<sup>[284]</sup> P2p high resolution XPS spectra (**Figure 5.8b**) demonstrate the formed P species is P-O bond in both PMX1 and PMX2, corresponding to the binding energy of 133.5 eV.<sup>[285]</sup> Because of the absence of Ti-P bond (129 eV) in P2p,<sup>[285]</sup> the doped phosphorus is only grafted onto  $\text{Ti}_3\text{C}_2\text{T}_x$  MXene via surface oxygen bridging, forming Ti-O-P bond. Ti-O-P is also studied with Density functional theory (DFT) calculations. (**Figure 5.8c-f**) The optimized structure of  $\text{Ti}_3\text{C}_2\text{O}_2$ -P system is shown in **Figure 5.8c** and d, based on the calculation of formation energy between single P atom and  $\text{Ti}_3\text{C}_2\text{O}_2$  substrate, the P atoms can be stably adsorbed above the O atom with a low formation energy of -3.33 eV. Besides, the differential charge density clearly visualizes the charge transfer from

the P atom to the  $\text{Ti}_3\text{C}_2\text{O}_2$  substrates and mainly to the O coordinated with the value of 0.91 electron estimated by the Bader charge method (Figure 5.8e). To better understand the bonding behavior, electron localization function (ELF) has been calculated and the bonds between P–O atoms are covalent in nature (Figure 5.8f). These results confirm that the bond of P–O can stably exist.

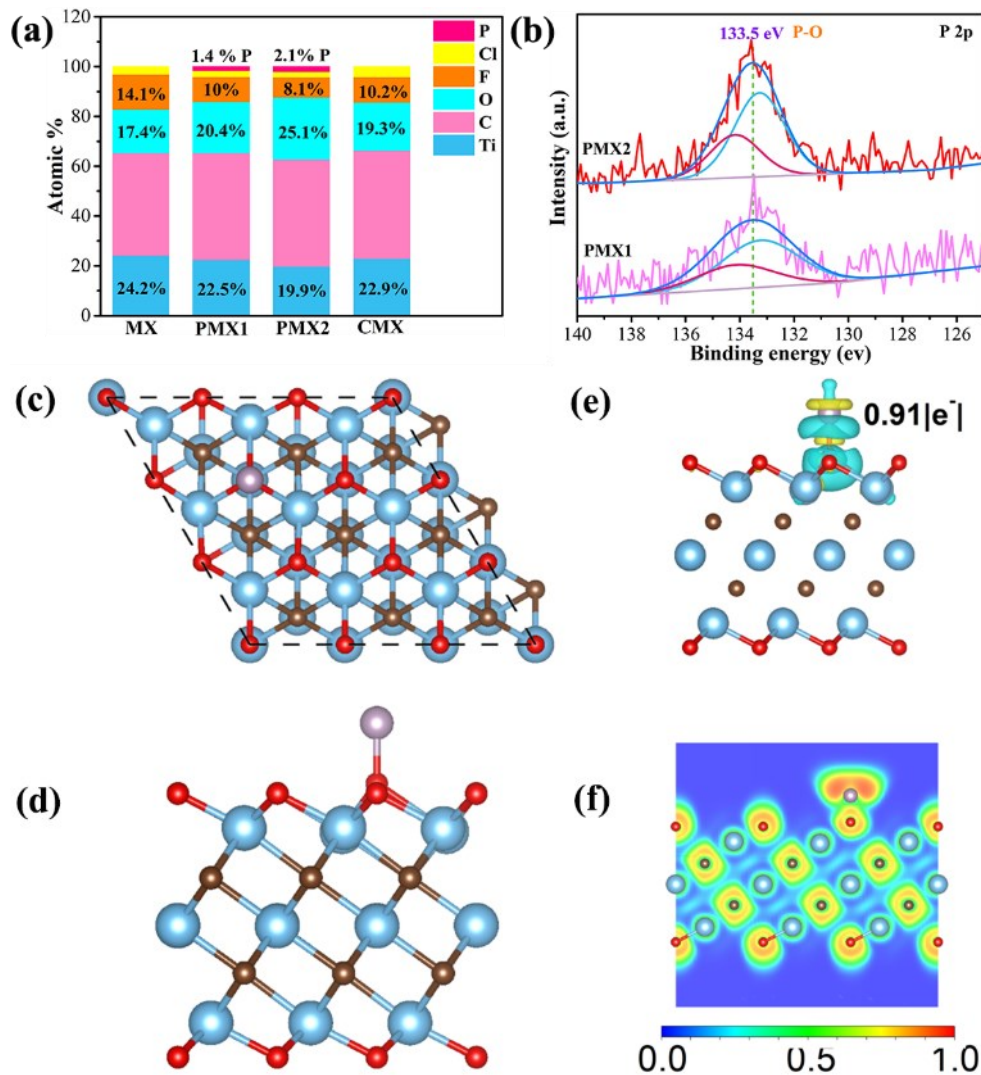


**Figure 5.8** (a) Composition analysis of MX, PMX1, PMX2 and CMX from XPS survey spectra. (b) High resolution P2p XPS spectra of PMX1 and PMX2. (c) Top and (d) side views of the  $\text{Ti}_3\text{C}_2\text{O}_2$ -P system; (e) Differential charge density distributions of  $\text{Ti}_3\text{C}_2\text{O}_2$ -P, yellow and blue regions indicate electron accumulation and depletion, respectively; (f) Electron localization function (ELF) maps of  $\text{Ti}_3\text{C}_2\text{O}_2$ -P, the scale bar shows the isodensity values of ELF. Ti, C, O, and P atoms are represented in blue, brown, red, and

purple, respectively.

And it is also predicted via DFT simulation that the adjacent surface doped phosphorus atoms tend to interact each other and bond together (**Figure 5.9**), which could adversely affect crystal structure of MXene due to lattice stress. This calculation result also explains why high P-doping damages the crystallinity of MXene and even leads to its amorphization.

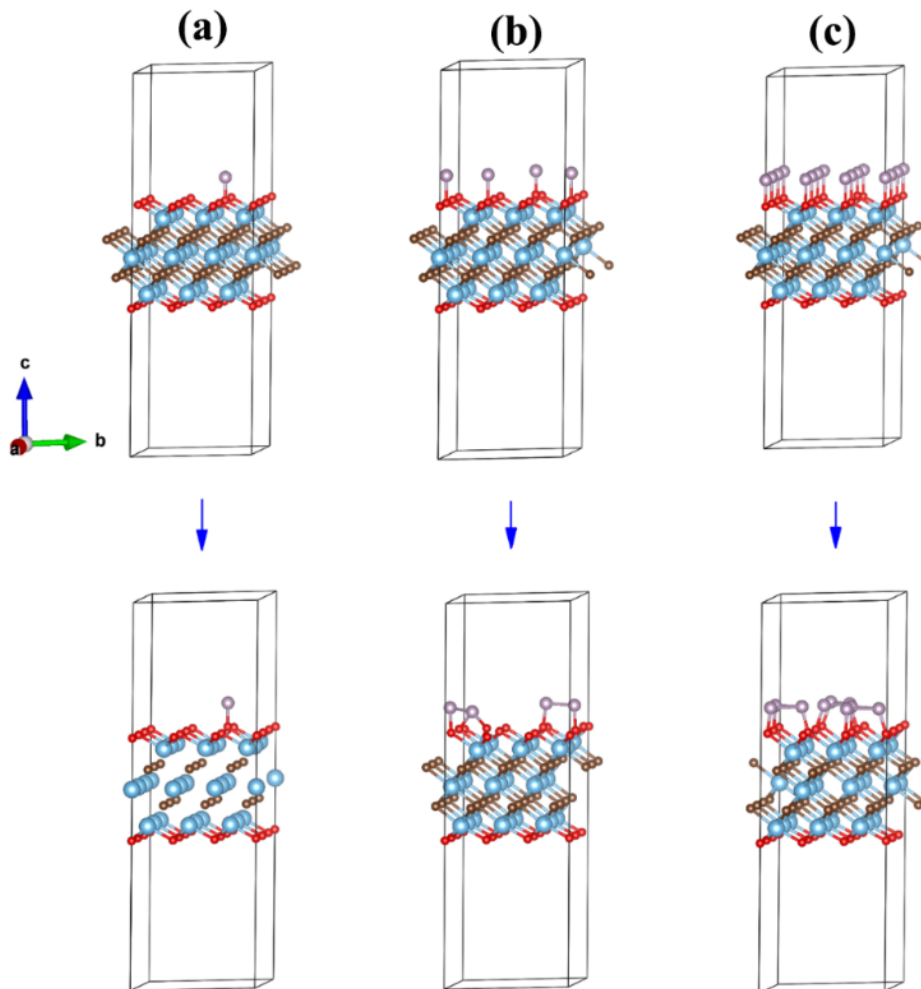


**Figure 5.9** Before and after optimization of different P concentrations  $\text{Ti}_3\text{C}_2\text{O}_2\text{-P}$  system. (a)  $\text{Ti}_3\text{C}_2\text{O}_2\text{P}_{0.11}$ , (b)  $\text{Ti}_3\text{C}_2\text{O}_2\text{P}_{0.33}$  and (c)  $\text{Ti}_3\text{C}_2\text{O}_2\text{P}$

O 1s of MX and CMX (Figure 4c) can be deconvoluted into Ti-O, C-Ti-O, C-Ti-OH,



H<sub>2</sub>O and organics (OR), which correspond to binding energies of 529.8, 531, 532.2, 533.2, and 534.9 eV, respectively.<sup>[268,284]</sup> However, for PMX1 and PMX2, some of their surface C-Ti-O was grafted with phosphorus, leading to the formation of Ti-O-P bond at a higher binding energy (531.6 eV)<sup>[150]</sup>, and the amount of Ti-O-P increases with increasing phosphorus doping amount, as shown in the middle two spectra of Figure 3c. The comparison of Ti 2p of different samples is shown in Figure 4d. The binding energies for Ti 2p<sub>3/2</sub> peak of PMX1 and PMX2, and CMX exhibit blue shifts of 0.27, 0.35, and 0.16 eV, respectively, compared to that of MX, indicating their elevated titanium valence states, which is also shown in nitrogen doped Ti<sub>3</sub>C<sub>2</sub>T<sub>x</sub> MXene.<sup>[41]</sup> The more evident increase in titanium valence state in PMX1 and PMX2 could be ascribed to their phosphorus introduction. Titanium with higher valence states in PMX1 and PMX2 are expected to contribute more charge transfer during charge/discharge process.<sup>[36,41]</sup>

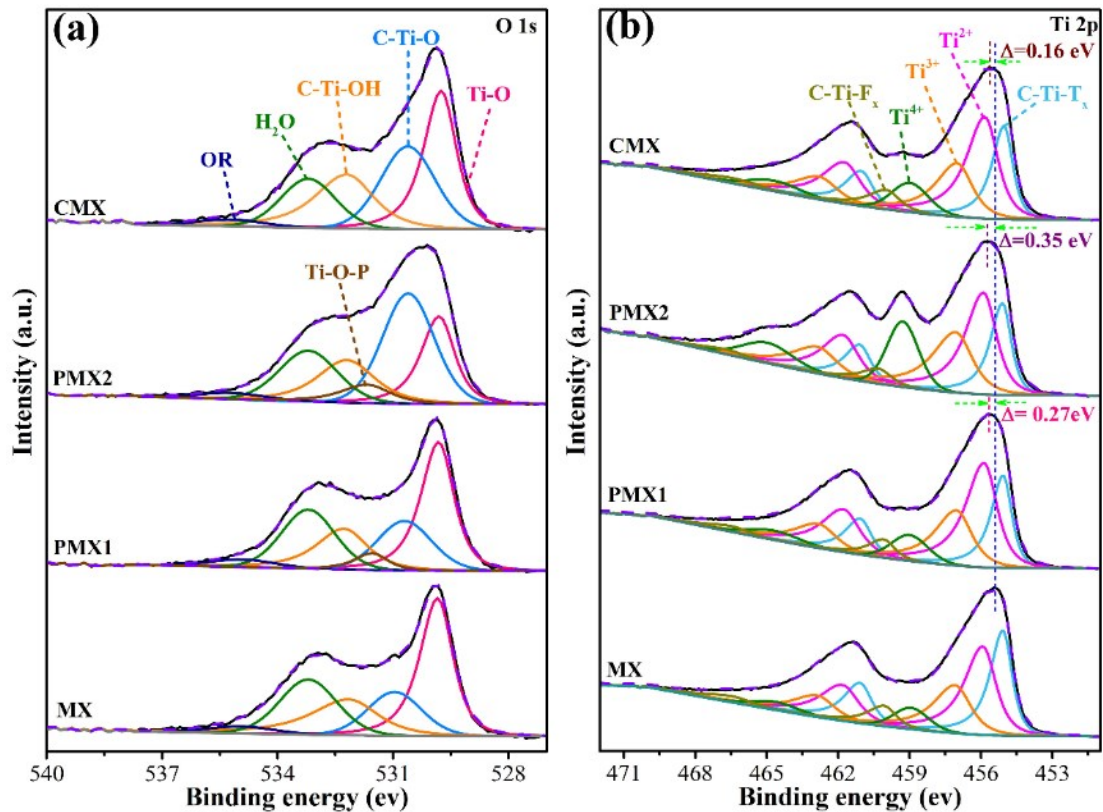


**Figure 5.10** High resolution (a) O1s and (b) Ti2p XPS spectra of MX, PMX1, PMX2 and CMX.

Surface sensitive Raman spectra of MX, PMX1, PMX2 and CMX are shown in **Figure 5.11a**. The  $E_g$  band at  $230\sim 470\text{ cm}^{-1}$  represents the in-plane vibration of surface functional groups linked with outer titanium atoms in  $\text{Ti}_3\text{C}_2\text{T}_x$  and the  $A_{1g}$  band at around  $720\text{ cm}^{-1}$  is attributed to out-of-plane vibrations of carbon.<sup>[286]</sup> The wavenumbers of the  $E_g$  band in PMX1 and PMX2 are similar ( $370\text{ cm}^{-1}$ ) but less than those ( $\sim 382\text{ cm}^{-1}$ ) of MX and CMX, suggesting that the incorporation of phosphorus engenders attenuated bond strength between functional groups and surface titanium atoms in MXene. And a larger wavenumber of  $A_{1g}$  band ( $\sim 720\text{ cm}^{-1}$ ) is observed in P-doped doped  $\text{Ti}_3\text{C}_2\text{T}_x$ , which indicates the enhanced Ti-C bond strength after doping.



The change of the  $A_{1g}$  band with applied potential can be used to investigate the charge storage behavior of  $Ti_3C_2T_x$ ,<sup>[286]</sup> which will be discussed in the following sections for differentiating energy storage behavior in P-doped  $Ti_3C_2T_x$  MXene from that in pristine MXene.

The effect of incorporated P on coordination environment of Ti in  $Ti_3C_2T_x$  is investigated via EXAFS. **Figure 5.11b** compares the Fourier-transform (FT) Ti K-edge EXAFS results of MX and PMX2. FT-EXAFS of both these two samples display two peaks in the range of 1.0–2.0 Å and 2.0–3.0 Å, in general corresponding to the Ti-O/F/C and Ti-Ti contribution, respectively.<sup>[287]</sup> However, PMX2 exhibits a much higher 2nd-shell peak than MX, which is assigned to an extra Ti-P coordination at 3.48 Å in PMX according to EXAFS fitting results (**Figure 5.11c-d** and Table 5.1) and DFT models (**Figure 5.8d**). The EXAFS Ti K-edge wavelet transform (WT) results (**Figure 5.11e**) consistently show that PMX2 exhibits increased intensity at both larger K and R space than Ti-Ti coordination compared to MX, as circled by pink line, as circled by pink line, which corresponds to Ti-P coordination. Therefore, these results collectively confirm Ti-O-P coordination in P-doped MXene.

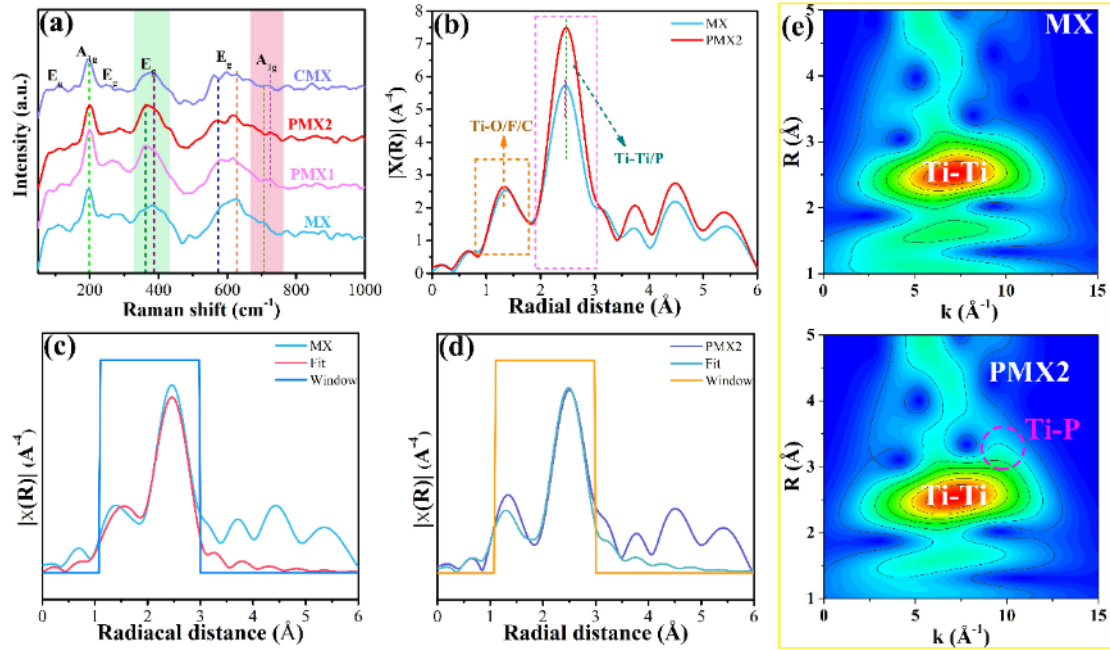


**Figure 5.11** (e) Raman spectrum of MX, PMX1, PMX2 and CMX. (b) Ti K-edge of EXAFS spectra of MX and PMX2. EXAFS fitting results for (c) MX and (d) PMX2. (e) WT-EXAFS profiles for MX and PMX2

**Table 5.1** Ti K-edge EXAFS fitting results

Sample	Path	CN	$\Delta R, \text{\AA}$	$R, \text{\AA}$	D-W factor( $\sigma^2$ ), $\text{\AA}^2$	$\Delta E_0, \text{eV}$	R-factor, %
MX	Ti-O/F	2.0(2)	0.09(2)	2.06(2)	0.004(2)	7.7	1.5
	Ti-C	4.2(6)	-0.01(1)	2.18(1)	0.009(2)	-6.5	
	Ti-Ti	7.8(4)	-0.04(2)	3.01(2)	0.009(1)	-9.2	
PMX2	Ti-O/F	1.8(2)	-0.02(2)	1.95(2)	0.003(1)	-4.9	1.2
	Ti-C	3.8(4)	0.01(1)	2.15(1)	0.003(1)	-9.7	
	Ti-Ti	5.9(2)	0.10(1)	3.03(1)	0.005(1)	-7.3	
	Ti-P	0.7(5)	0.09(3)	3.48(3)	0.012(3)	-6.9	

in which CN is the average coordination number, R is the distance from absorber atom, and  $\sigma^2$  the Debye–Waller factor. R-factor denotes a quality factor of the fitting, and  $\Delta E_0$  the energy shift from the absorption edge energy  $E_0$ .



The electrochemical performances (ECs) of the as-prepared samples were studied in 1M H<sub>2</sub>SO<sub>4</sub> with three-electrode configuration, in which Ag/AgCl (sat. KCl) and graphite bar are reference electrode and counter electrode, respectively. **Figure 5.12a** shows cyclic voltammetry (CV) profiles of MX, PMX1, PMX2 and CMX at a scan rate of 20 mV s<sup>-1</sup>. Redox peaks are observed in all of them, implying their pseudocapacitive energy storage mechanism.<sup>[36, 37]</sup> PMX1 and PMX2 exhibit larger integral areas than MX and CMX, indicative of their higher capacitances. In addition, PMX2 with richer phosphorus doping exhibits better energy storage ability than PMX1. A similar result is also shown in galvanostatic charge/discharge (GCD) curves (**Figure 5.12b**). These enhanced capacitances in PMX1 and PMX2 should be attributable to the incorporated phosphorus. The capacitances of the samples at various scan rates (2-1000 mV s<sup>-1</sup>) and current densities (2 - 20 A g<sup>-1</sup>) are compared and summarized in **Figure 5.12 c-d**. PMX2 delivers the highest capacitances of 328 F g<sup>-1</sup> and 342 F g<sup>-1</sup> at 2 mV s<sup>-1</sup> and 2 A g<sup>-1</sup> respectively, which are comparable with and even higher than those of other heteroatoms doped (N, S, V etc.) Ti<sub>3</sub>C<sub>2</sub>T<sub>x</sub> MXene, as demonstrated in Table 5.2. To investigate the effect of phosphorus doping amount on ECs, PMX8 (2.8 at. % P) and PMX20 (3.5 at. % P) were also studied, and the corresponding results are shown in **Figure 5.13**. Unfortunately, further increase in phosphorus doping does not contribute to better energy storage ability but result in the performance deterioration, which could be attributed to their degraded crystallinity (**Figure 5.6**).

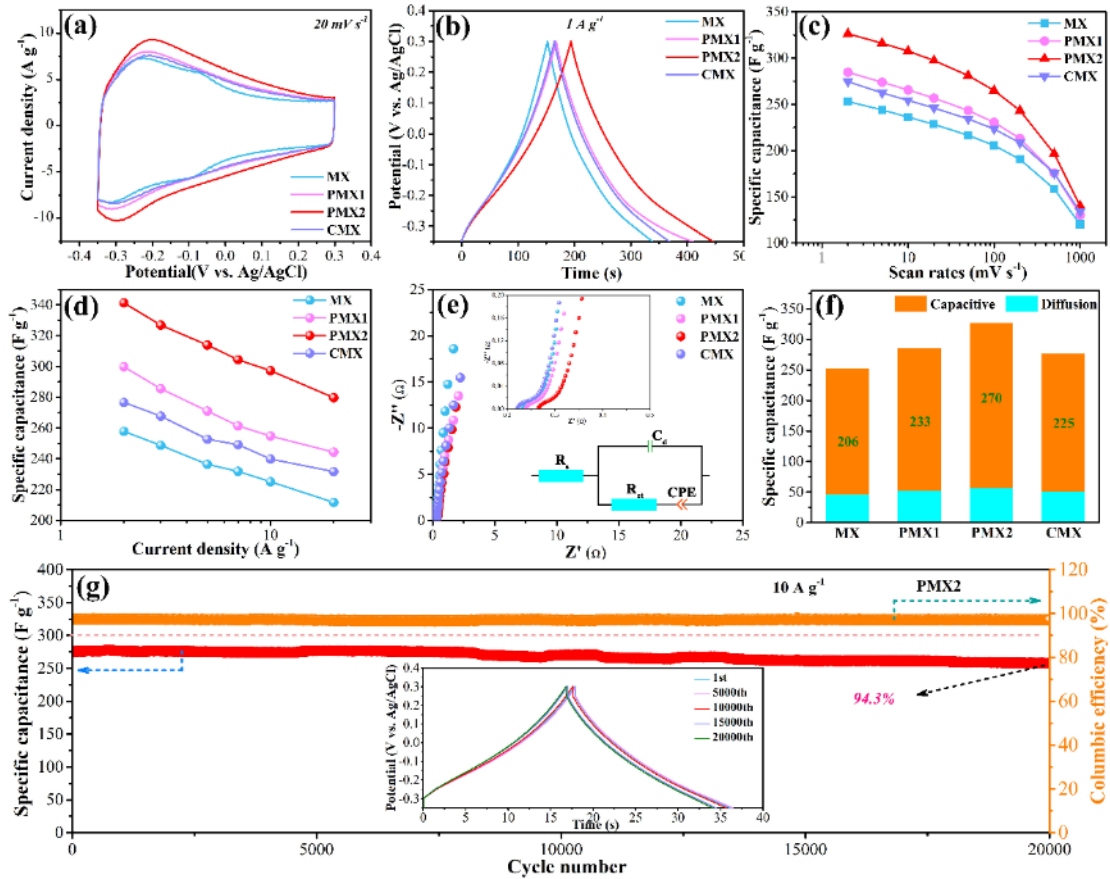


**Figure 5.12** (a) CV curves of MX, PMX1, PMX2 and CMX at the scan rate of  $20 \text{ mV s}^{-1}$  and (b) GCD curves at the current density of  $1 \text{ A g}^{-1}$  for the four samples. Specific capacitances of the samples at (c) scan rates from 2 to  $1000 \text{ mV s}^{-1}$  and (d) current densities of  $2 \sim 20 \text{ A g}^{-1}$ . (e) EIS spectra for the samples at  $-0.2 \text{ V vs. Ag/AgCl}$ . Insets are the enlarged EIS spectra at intercept with real axis and fitted equivalent circuit. (f) Capacitive contributions of the four samples at  $2 \text{ mV s}^{-1}$ . (g) Cyclic test of PMX2 at  $10 \text{ A g}^{-1}$ , the inset shows its GCD curves at different cycles.

**Table 5.2** Comparison in terms of capacitance of PMX2 along with other heteroatoms doped  $\text{Ti}_3\text{C}_2\text{T}_x$  MXene

Samples	Electrolyte	Specific capacitance	Cycling stability	References
PMX2	1 M $\text{H}_2\text{SO}_4$	$328 \text{ F g}^{-1}$ at $2 \text{ mV s}^{-1}$ and $342 \text{ F g}^{-1}$ at $2 \text{ A g}^{-1}$	94.3 % retention after 20000 cycles at $10 \text{ A g}^{-1}$	This work

N-Ti <sub>3</sub> C <sub>2</sub> T <sub>x</sub>	1 M H <sub>2</sub> SO <sub>4</sub>	192 F g <sup>-1</sup> at 1 mV s <sup>-1</sup>	92 % retention after 10000 cycles at 50 mV/s	[37]
N, S-Ti <sub>3</sub> C <sub>2</sub> T <sub>x</sub>	1 M H <sub>2</sub> SO <sub>4</sub>	340 F g <sup>-1</sup> at 1 A g <sup>-1</sup>	/	[43]
N-Ti <sub>3</sub> C <sub>2</sub> T <sub>x</sub>	6 M KOH	190 F g <sup>-1</sup> at 5 mV s <sup>-1</sup>	/	[42]
V-Ti <sub>3</sub> C <sub>2</sub> T <sub>x</sub>	2 M KCl	365.9 F g <sup>-1</sup> at 10 mV/s	95 % retention after 5000 cycles at 10 A g <sup>-1</sup>	[201]
Nb-Ti <sub>3</sub> C <sub>2</sub> T <sub>x</sub>	6 M KOH	Maximum 442.7 F g <sup>-1</sup>	70.5 % retention after 2000 cycles	[278]
P-Ti <sub>3</sub> C <sub>2</sub> T <sub>x</sub>	1M H <sub>2</sub> SO <sub>4</sub>	320 F g <sup>-1</sup> at 0.5 A g <sup>-1</sup>	93.1 % retention after 5000 cycles at 5 A g <sup>-1</sup>	[39]
N, S-Ti <sub>3</sub> C <sub>2</sub> T <sub>x</sub>	1M Li <sub>2</sub> SO <sub>4</sub>	175 F g <sup>-1</sup> at 2 mV s <sup>-1</sup>	90.1 % retention after 5000 cycles at 2 A g <sup>-1</sup>	[288]
N-Ti <sub>3</sub> C <sub>2</sub> T <sub>x</sub>	3 M H <sub>2</sub> SO <sub>4</sub>	927 F g <sup>-1</sup> at 5 mV s <sup>-1</sup>	81.7 % retention after 20000 cycles at 10 A g <sup>-1</sup>	[38]

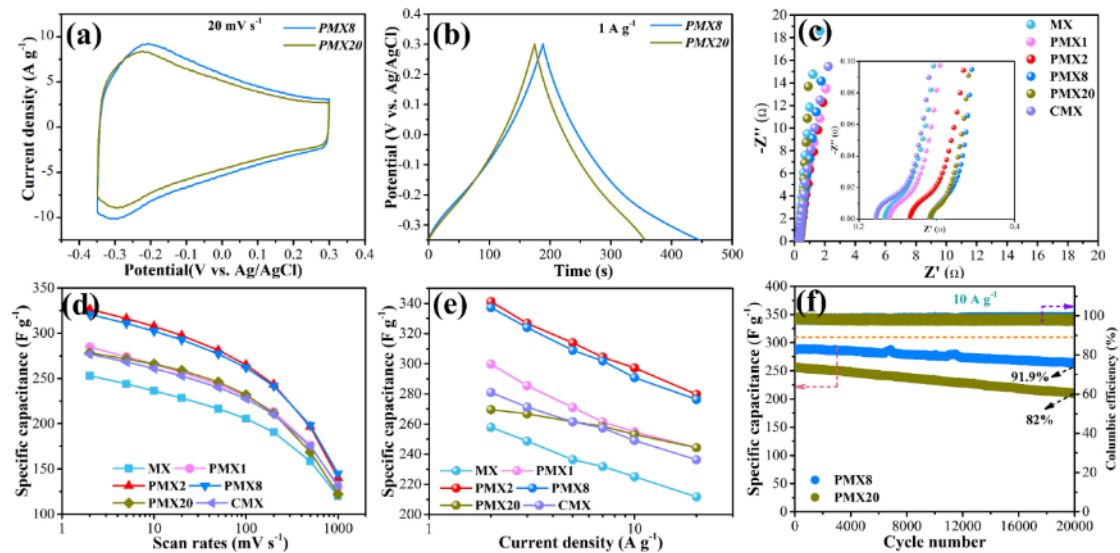


**Figure 5.13** (a) CV curves of PMX8 and PMX20 at 20 mV s<sup>-1</sup>, (b) GCD curves of the two samples at 1 A g<sup>-1</sup>, (c) EIS plots of MX, PMX1, PMX2, PMX8, PMX20 and CMX,



(6) capacitance vs. scan rates for the six samples, (e) gravimetric capacitance of the six samples at current densities from 2 to 20 A g<sup>-1</sup>, (f) cyclic stability of PMX8 and PMX20 at 10 A g<sup>-1</sup>.

Electrochemical impedance spectroscopy (EIS) results were used to evaluate redox kinetics and electrical conductivity of different samples. The Nyquist plots of MX, PMX1, PMX2 and CMX at -0.2 V vs. Ag/AgCl are shown in **Figure 5.12e**. The slope of linear part of the plots reflects ion diffusion resistance in electrode materials. The similar slope of the four samples implies that the surface grafted phosphorus atoms on Ti<sub>3</sub>C<sub>2</sub>T<sub>x</sub> do not block electrolyte ions to active sites. And the semicircle of the plots (upper inset of **Figure 5.12e**) at high frequency range denotes the charge transfer resistance ( $R_{ct}$ ) at electrode/electrolyte interface.<sup>[109]</sup> The intercept with real axis in the plots represents equivalent series resistance ( $R_s$ ), which is composed of electrical resistance of electrode material, interface resistance and ionic resistance of electrolyte. To quantitatively compare the values of  $R_{ct}$ ,  $R_s$ , an equivalent circuit (lower inset in **Figure 5.12e**) was constructed for the fitting. The higher  $R_s$  (Table S3) of PMX1 and PMX2 than MX and CMX manifests the phosphorus incorporation causes decreased electrical conductivity of MXene. This decrement in conductivity is also observed in PMX8 and PMX20 with high phosphorus content (**Figure 5.13c**). The phosphorus doping induced lattice distortion and amorphization is regarded to be responsible for the decrement in conductivity. In addition, the changed surface functionalization also leads to the decrement of density of states at Fermi level,<sup>[283]</sup> which is another reason for the decreased electrical conductivity in phosphorus-doped MXenes. It is also



observed from the **Table 5.3** that phosphorus doping contributes to smaller  $R_{ct}$ , indicative of increased active sites in PMX1 and PMX2.

**Table 5.3** EIS fitting results for MX, PMX1, PMX2 and CMX

	<b>MX</b>	<b>PMX1</b>	<b>PMX2</b>	<b>CMX</b>
<b><math>R_s/\Omega</math></b>	0.2398	0.2467	0.2726	0.2296
<b><math>C_d/F</math></b>	0.0859	0.0851	0.0805	0.0476
<b><math>R_{ct}/\Omega</math></b>	0.0607	0.0548	0.0586	0.0539
<b>CPE-T</b>	0.7027	0.9435	1.028	0.8507
<b>CPE-P</b>	0.9601	0.9369	0.9279	0.9418

The redox reactions of  $Ti_3C_2T_x$  MXene is governed by reversible proton bonding-debonding on surface -O terminations.<sup>[15, 140]</sup> Its charge storage in samples can be divided into diffusion-controlled and capacitive parts. The contribution from capacitive process to the total charge storage is investigated based on the equation below.

$$i(V) = k_1 v + k_2 v^{0.5} \tag{5-1}$$

The current density at fixed potential,  $i(V)$ , is regarded as the sum of capacitive ( $k_1 v$ ) and diffusion controlled ( $k_2 v^{0.5}$ ) components. The  $k_1$  and  $k_2$  can be confirmed by linearly fitting the plots of  $i(V)/v^{0.5}$  vs.  $v^{0.5}$ . The results show that the capacitive contributions rise with increasing scan rates in all samples and PMX2 always exhibits a higher ratio of capacitive contribution than other samples at scan rates of 2 ~ 50 mV

$s^{-1}$  (Figure 5.14). Figure 5.12f compares the contributions on total capacitance of the four samples at  $2 \text{ mV s}^{-1}$ , where the diffusion-controlled capacitance of all the samples exhibits little difference. Clear distinctions are observed from capacitive contribution. PMX2 shows the highest capacitance ( $270 \text{ F g}^{-1}$ ) from capacitive process. Therefore, one can conclude that phosphorus incorporation can boost capacitive performance (rate capability) of  $\text{Ti}_3\text{C}_2\text{T}_x$  MXene. PMX2 was cycled at  $10 \text{ A g}^{-1}$  and 94.3 % capacitance was retained after 20000 cycles, suggesting its robust structure and good prospect for supercapacitor electrode materials.

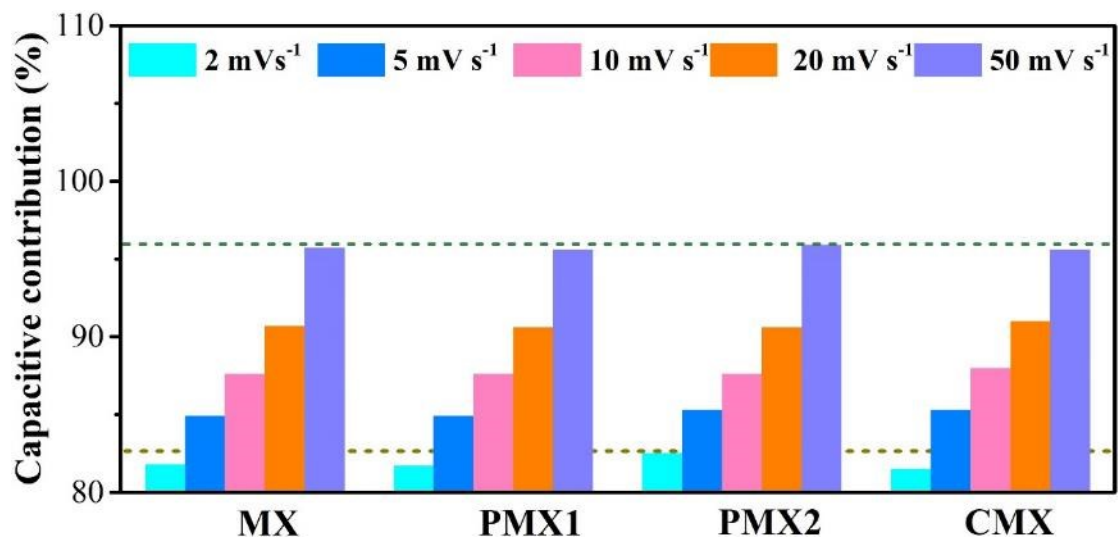


**Figure 5.14** Capacitive contribution of MX, PMX1, PMX2 and CMX at scan rates from 2 to  $50 \text{ mV s}^{-1}$

Though the boosted effect of phosphorus on EC performance of  $\text{Ti}_3\text{C}_2\text{T}_x$  MXene has been confirmed in the previous discussion, the underlying mechanism on the enhancement is still unclear. *Ex situ* XRD results (Figure 5.15) first reveal that MX, PMX2 and CMX show different interlayer distance at  $-0.35$  and  $0.3 \text{ V vs. Ag/AgCl}$ ,

indicating their intercalation pseudo-capacitance energy storage mechanism as reported in literature.<sup>[29]</sup> When the applied potentials decreases from 0.3 to -0.35 V, all the samples show a decreased interlayer spacing. Since the intercalated protons increase the electrostatic attraction between MXene layers.<sup>[29, 205]</sup>

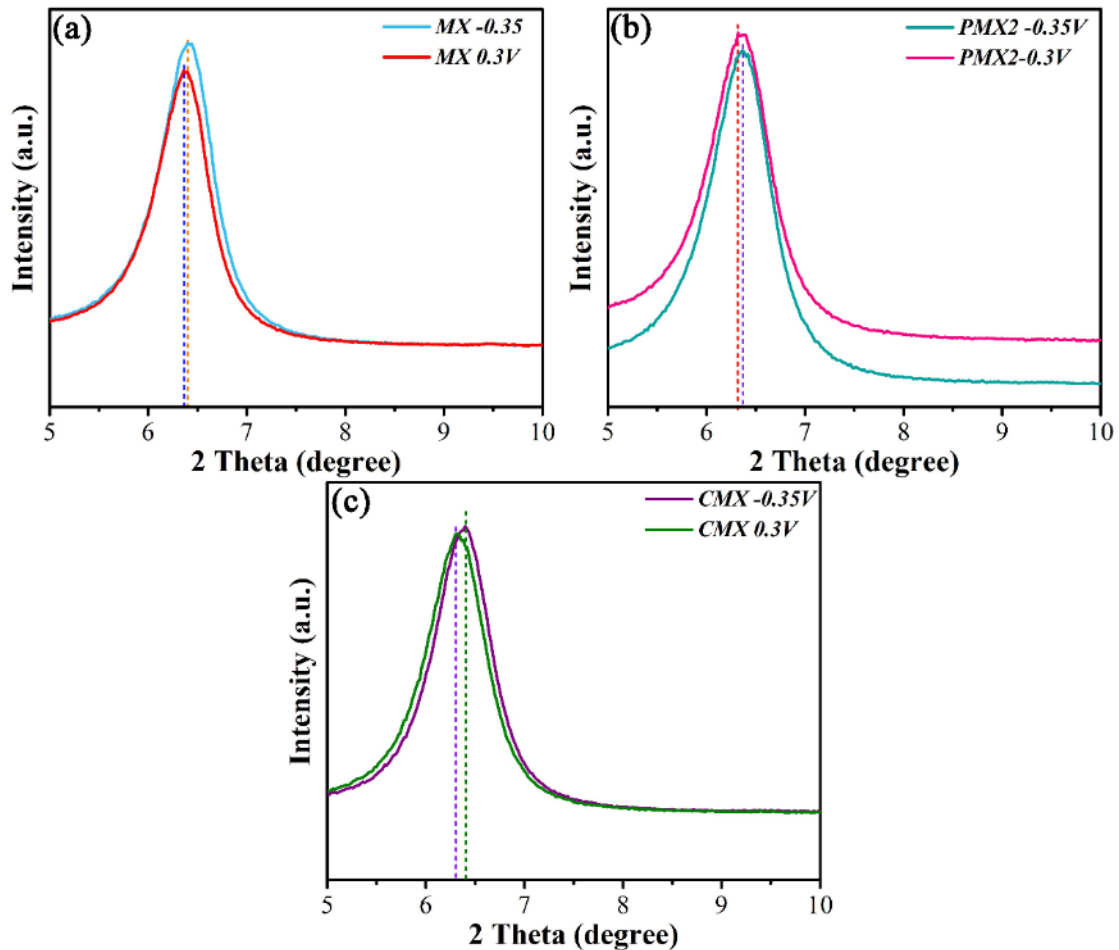


**Figure 5.15** *Ex situ* XRD spectra of (a) MX, (b) PMX2 and (c) CMX.

The redox reaction of  $Ti_3C_2T_x$  MXene involves the change of titanium valence states,<sup>[195]</sup> which has been investigated through in situ Raman,<sup>[289]</sup> ex situ XPS<sup>[163]</sup> and in situ XANES.<sup>[195]</sup> In situ Raman measurement was conducted in a custom-made device (**Figure 5.16a**). The Raman spectra of MX and PMX2 at potentials from -0.25 to 0.3 V



vs. Ag/AgCl are shown in **Figure 5.16b-c**. The  $E_g$  band located at  $230 \sim 470 \text{ cm}^{-1}$  has not shown evident shift with the potentials, while both  $E_g$  ( $500 \sim 690 \text{ cm}^{-1}$ ) and  $A_{1g}$  ( $\sim 720 \text{ cm}^{-1}$ ) bands exhibit a reversible peak shift with the applied potentials. The shift of these two bands in pristine MX is due to the bonding/debonding of protons with surface -O functional groups.<sup>[286]</sup> The similar change observed in PMX2 verifies its similar electrochemical behavior. Noting that the peak shift of  $A_{1g}$  ( $\sim 720 \text{ cm}^{-1}$ ) band can represent change of titanium valence states,<sup>[289]</sup> we compares the peak positions of  $A_{1g}$  band at potentials from -0.25 to 0.3 V vs. Ag/AgCl between the two samples in **Figure 5.16d**. The variation range on the peak position of  $A_{1g}$  band in PMX2 is  $718 \sim 736 \text{ cm}^{-1}$ , which is broader than that of MX ( $717 \sim 726 \text{ cm}^{-1}$ ), indicative of greater change of titanium valence states occurring in PMX2. To further affirm the more pronounced variation of titanium valence state in PMX2, XANES and XPS spectra of MX and PMX2 at -0.35 and 0.3 V vs. Ag/AgCl were also collected and compared. The change of white-line peak intensity in Ti K-edge XANES can reflect its varied amplitude on valence state.<sup>[290]</sup> **Figure 5.16e-f** show XANES spectra of MX and PMX2. And one can observe that the white-line peak of PMX2 exhibits a higher intensity difference than MX (0.037 vs.0.02) between -0.35 and 0.3V vs. Ag/AgCl potentials, validating the larger variation amplitude of titanium valence state in PMX2.

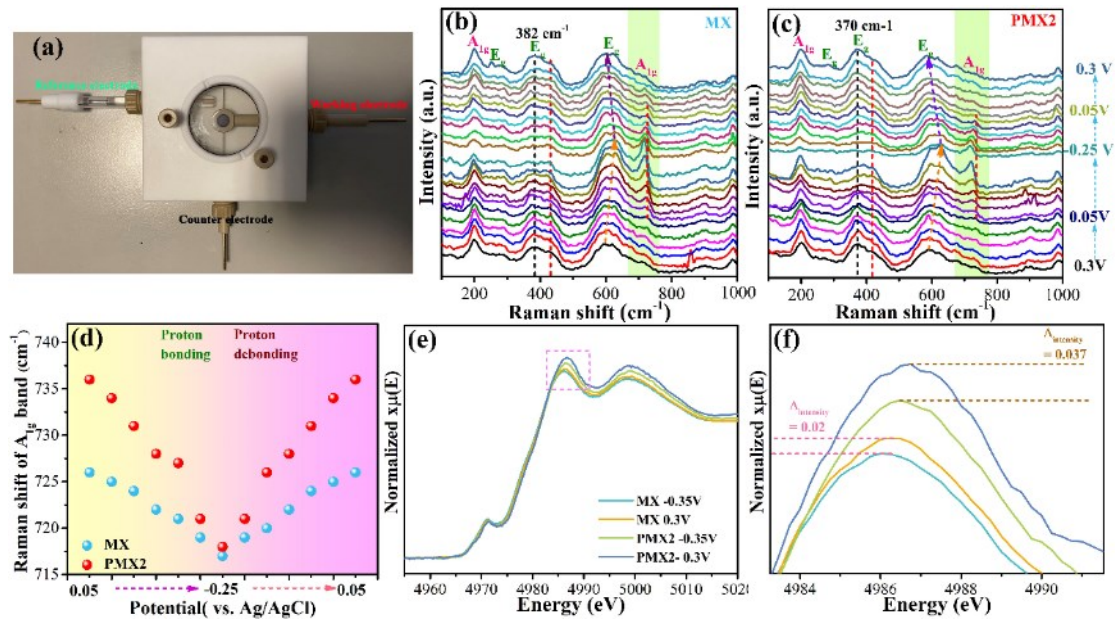


**Figure 5.16** (a) Photo for in-situ Raman device. *In situ* Raman spectra of (b) MX and (c) PMX2 at potential range of -0.25 ~ 0.3 V versus Ag/AgCl reference electrode. (d) Raman shift of  $A_{1g}$  band of MX and PMX2 with applied potential. (e) Ti K-edge XANES spectra of MX and PMX2 at -0.35 and 0.30 V versus Ag/AgCl, and (f) enlarged profile of the rectangular area in (e).

Consistently, *ex situ* XPS results (Figure S15) also demonstrate the identical trend. S 2p XPS spectra of residual sulfate radicals ( $SO_4^{2-}$ ) in all samples were used for calibration because of its nonparticipation in the redox action. The shift of right edge in normalized Ti 2p<sub>3/2</sub> peaks were used to compare the change of titanium valence state (Figure 5.17a-c). The edge shifts in MX and PMX2 are confirmed as 0.13 and 0.07 eV, respectively, also indicating the more electron gain and loss in PMX2 during the charge/discharge process. In addition, the P2p XPS spectra of PMX2 at -0.35 and 0.30 V vs. Ag/AgCl were also studied, as presented in Figure 5.17d. A 0.15 eV difference in binding energy between the two spectra elucidates that surface grafted phosphorus involve in the energy storage process. The reaction between phosphorus on P-doped MXene and protons is verified by DFT calculations (Figure 5.17e). Hydrogen atoms

exhibit a strong binding effect with P atoms. Two H atoms can adsorb one P atom stably with the binding energy of -2.43 eV, which is consistent with the fact that multivalent ion P electronic arrangement rules. It also reveals that phosphorus with lower electronegativity can bond with more protons than pure oxygen terminations do, resulting in more charge storage.

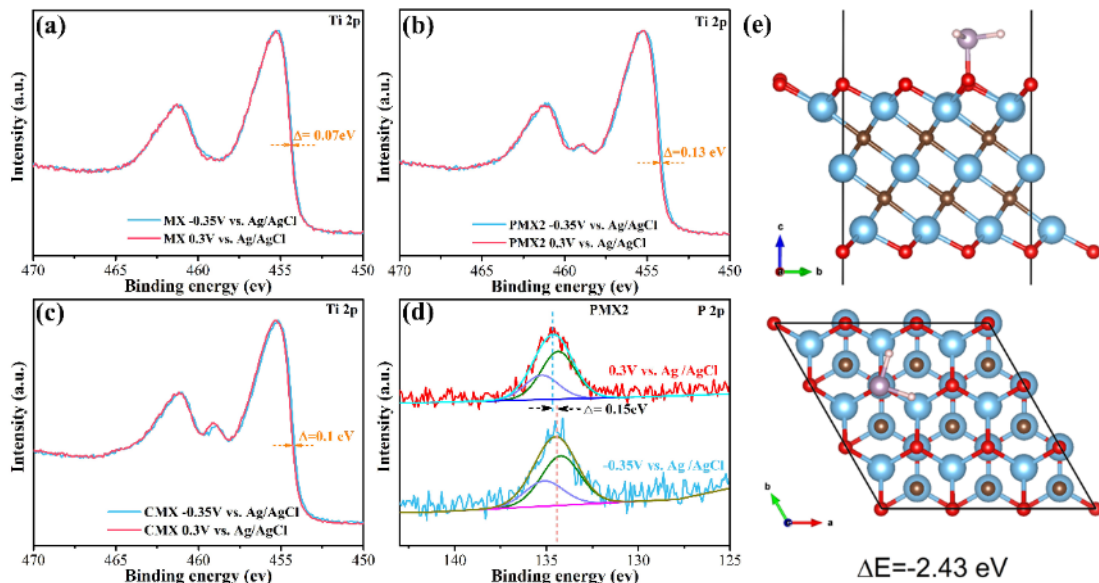


**Figure 5.17** Ti2p XPS spectra of (a) MX, (b) PMX2 and (c) CMX at potentials of -0.35 and 0.3 V vs. Ag/AgCl reference electrode. (d) P 2p XPS spectrum of PMX2 at -0.35 and 0.3 V versus Ag/AgCl. (e) Top and side views of the hydrogen adsorbed in  $Ti_3C_2O_2$ -P system.

In addition, the differential charge density results (**Figure 5.18a**) show that the grafting a phosphorus atom on surface oxygen atom of  $Ti_3C_2T_x$  MXene leads to the 0.91 electron loss for phosphorus and 1.85 electron loss for the titanium linked with oxygen and phosphorus. By comparison, when extra two protons bind with the surface grafted phosphorus atom, 1.48 electron and 1.88 electron loss are observed in phosphorus and the titanium linked with oxygen and phosphorus, respectively. Therefore, it can be concluded that the grafted phosphorus bonding with two protons will also induce charge

transfer in titanium of  $\text{Ti}_3\text{C}_2\text{T}_x$  MXene.

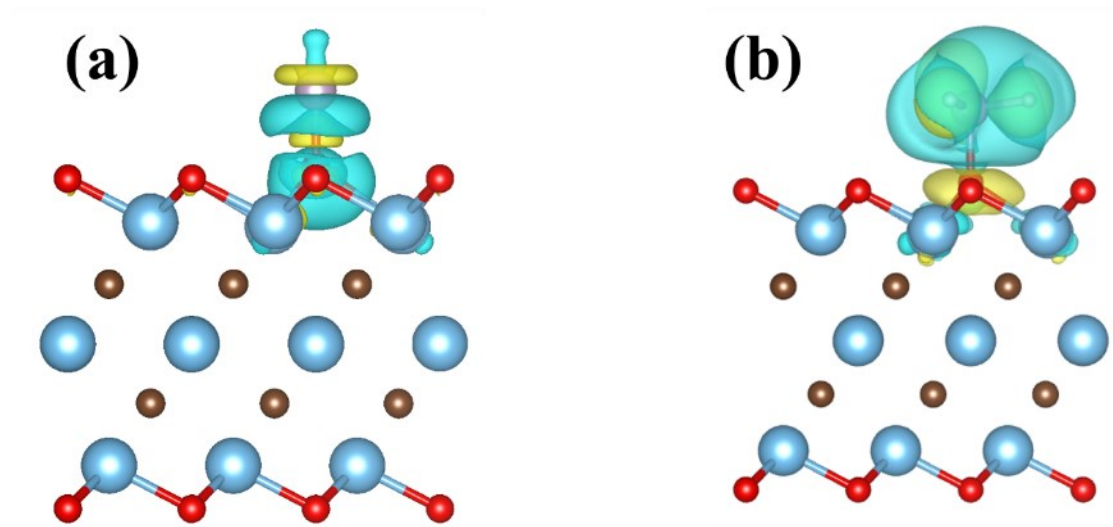


**Figure 5.18** Differential charge density distributions of  $\text{Ti}_3\text{C}_2\text{O}_2\text{-P}$  before (a) and after (b) the surface P bonding with two protons. The yellow and blue regions indicate electron accumulation and depletion, respectively.

Based on above results and discussions, it can be summarized that the surface grafted phosphorus atoms on  $\text{Ti}_3\text{C}_2\text{T}_x$  MXene serves as new active sites to enable two-proton bonding/debonding process, which can boost greater change of titanium valence state in  $\text{Ti}_3\text{C}_2\text{T}_x$  and lead to more charge transfer during its charge/discharge process, contributing to enhanced specific capacitance.

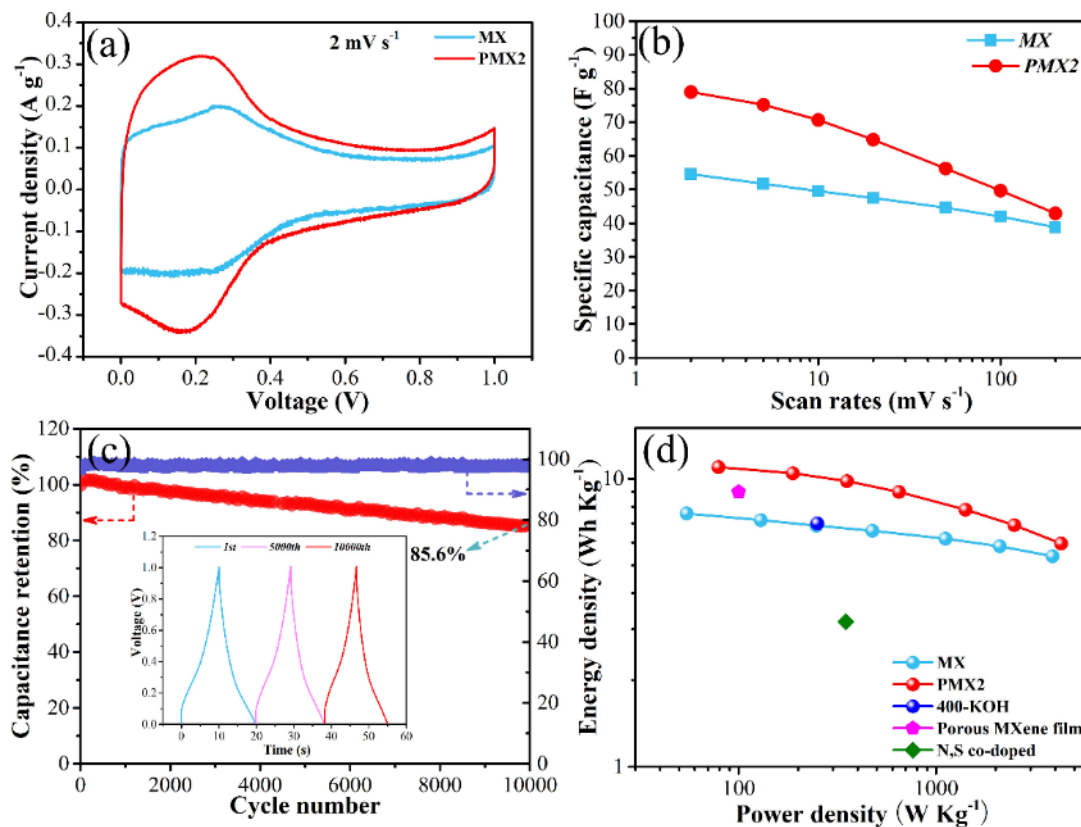


**Figure 5.19** (a) CV curves of MX and PMX2 based symmetric supercapacitors at  $2 \text{ mV s}^{-1}$ , (b) specific capacitance vs. scan rates for MX and PMX2 assembled symmetric supercapacitors, (c) cyclic stability of PMX2-based supercapacitors at  $10 \text{ A g}^{-1}$ , its inset shows GCD curves at 1<sup>st</sup>, 5000<sup>th</sup> and 10000<sup>th</sup> cycles (d) energy density vs. power density plot for MX and PMX2 based symmetric supercapacitors.

Finally, PMX2 was selected to assemble a symmetric supercapacitor to evaluate the practicability of phosphorus doped  $\text{Ti}_3\text{C}_2\text{T}_x$  MXene. The resultant device exhibits a voltage window of 1 V and delivers a highest capacitance of  $79 \text{ F g}^{-1}$  based on the total mass of two electrodes at  $2 \text{ mV s}^{-1}$ , superior to the device assembled with MX, as shown in **Figure 5.19a-b**. The PMX2-based supercapacitor delivers the 85.6% initial capacitance after 10000 GCD cycles at  $10 \text{ A g}^{-1}$  (**Figure 5.19c**), justifying the remarkable stability of PMX2 for a supercapacitor electrode material. In addition, the Ragone plots (**Figure 5.19d**) show that the PMX2-based device exhibits a highest



energy density of  $11.2 \text{ Wh Kg}^{-1}$  at the power density of  $79 \text{ W Kg}^{-1}$  and retains  $5.96 \text{ Wh Kg}^{-1}$  at  $4290 \text{ W Kg}^{-1}$ , which not only excels those of MX-based device, but also outperforms KOH washing + annealing modified  $\text{Ti}_3\text{C}_2\text{T}_x$  MXene ( $7.2 \text{ Wh Kg}^{-1}$  at  $250 \text{ W Kg}^{-1}$ ),<sup>[163]</sup> porously modified  $\text{Ti}_3\text{C}_2\text{T}_x$  MXene film ( $9.2 \text{ Wh Kg}^{-1}$  at  $100 \text{ W Kg}^{-1}$ )<sup>[33]</sup> and N, S co-doped  $\text{Ti}_3\text{C}_2\text{T}_x$  MXene ( $3.19 \text{ Wh Kg}^{-1}$  at  $349 \text{ W Kg}^{-1}$ ),<sup>[43]</sup> proving the competent role of grafting phosphorus on  $\text{Ti}_3\text{C}_2\text{T}_x$  MXene in boosting its supercapacitor performance.

### 5.3 Conclusions

In summary, we have demonstrated that grafting phosphorus atoms onto  $\text{Ti}_3\text{C}_2\text{T}_x$  surface through oxygen bridging, forming Ti-O-P surface terminations, can boost its capacitance for supercapacitor application. And the underlying improvement mechanism is also revealed. The resultant PMX2 exhibits enhanced EC performance than pristine MXene and delivers a highest capacitance of  $348 \text{ F g}^{-1}$  at  $2 \text{ mV s}^{-1}$  in  $1\text{M H}_2\text{SO}_4$  aqueous electrolyte along with excellent stability (94.3% capacitance retention after 20000 cycles). The surface doped phosphorus atoms on  $\text{Ti}_3\text{C}_2\text{T}_x$  MXene serve as new active sites for two-proton bonding-debonding, contributing to more charge transfer and the improved energy storage ability in P-doped  $\text{Ti}_3\text{C}_2\text{T}_x$  MXene. In addition, experimental and DFT calculation results suggest that high phosphorus surface doping would damage crystal structure of MXene, explaining why the specific capacitance of MXene cannot be further enhanced by merely increasing doping amount of P. It is



believed that our work paves a way for doping MXene with other heteroatoms to achieve performance modulation.



## Chapter 6 Oxygen-rich surface and narrow interlayer space endow $\text{Ti}_3\text{C}_2\text{T}_x$ MXene with enhanced capacitance and oxidation resistance ability

$\text{Ti}_3\text{C}_2\text{T}_x$  MXene delivers high pseudo-capacitance in acid solution via surface -O terminations bonding with protons. Numerous efforts have been devoted to engineer more -O for improved charge storage or expand interlayer gallery of MXene to boost ion intercalation. However, narrow interlayer space favors proton transport with Grotthuss mechanism and strengthens the interaction between intercalated protons and material interface, which is commonly neglected in optimizing MXene supercapacitive performance. Herein, a novel strategy combining surface modification and interlayer shrinkage of MXene is proposed to boost its energy storage ability. The modified MXene is rich in -O surface groups along with substantial removal of detrimental -F species, and the interlayer space becomes narrower than its pristine counterpart. It exhibits not only a high capacitance of  $375 \text{ F g}^{-1}$  ( $338 \text{ C g}^{-1}$ ), but also much enhanced oxidation resistance and excellent cyclic stability. Multiple *in situ* and *ex situ* characterization results reveal that only monolayer interstitial water is formed during its charge/discharge process, which boosts proton transport into interlayer space and strengthens host-ion interaction, contributing to the charge storage. And the rich oxygen groups are responsible for its superior oxidation resistance. The assembled asymmetric supercapacitor with modified MXene and Prussian blue analogue can deliver a high



energy density of  $19.7 \text{ Wh Kg}^{-1}$ . This work proposes a novel strategy to simultaneously enhance the energy storage capability and oxidation resistance of MXene for supercapacitor applications.

## 6.1 Introduction

Pseudocapacitors (PCs) are a kind of energy storage devices that can deliver high energy densities at fast charge/discharge rates, thus promising to be the next generation energy storage devices by replacing batteries.<sup>[291]</sup> Different from electrical double layer capacitors (EDLCs) that store charge through physical ion adsorption on electrode surface, PCs store energy via fast redox reaction on electrode materials surface or fast ion intercalation into the interlayer space of active materials with faradic charge transfer yet no phase transformation.<sup>[94]</sup> The energy storage characteristic of PCs requires the electrode material to be highly conductive, redox-active and robust for sustaining cyclic measurement. Transition metal oxides ( $\text{MnO}_2$ ,<sup>[102]</sup>  $\text{RuO}_2$ <sup>[18]</sup>) and conducting polymers (CPs)<sup>[292]</sup> have been widely used for pseudocapacitive electrode materials. But poor conductivity ( $\text{MnO}_2$ ), high cost ( $\text{RuO}_2$ ) and inferior cyclin performance (PCs) restricts their wide applications, respectively.<sup>[33, 140]</sup> It is thus highly demanded to develop other electrode materials that can bypass the above issues.

$\text{Ti}_3\text{C}_2\text{T}_x$  MXene is regarded as a promising pseudocapacitive material due to its metallic



electrical conductivity, high capacitance and robust cycle life in aqueous acid solution. This novel 2D material is synthesized by selectively etching off aluminum layer in stratified  $Ti_3AlC_2$  precursor using HF,<sup>[25]</sup> the mixture of LiF and HCl,<sup>[154]</sup> molten salt<sup>[106]</sup> as etchants or applying certain potential in  $NH_4Cl$ <sup>[173]</sup> and  $HCl$ <sup>[174]</sup> etc. solutions. The residual  $Ti_3C_2$  slabs after the etching procedure are grafted with -O, -OH, -Cl and -F functional groups via surface titanium atoms, which correspond to the T in  $Ti_3C_2T_x$  formula.<sup>[275]</sup> Its redox reaction proceeds via proton bonding/debonding with surface -O terminations, and other functional groups (mainly -F) hinders the electrolyte ion transport.<sup>[45, 149, 163]</sup>  $Ti_3C_2T_x$  MXene, surface was modified with N-butyllithium,<sup>[36]</sup> ammonium persulfate,<sup>[211]</sup> potassium hydroxide<sup>[163]</sup> to engineer more -O groups and decrease -F terminals on the surface to boost redox reactions. And the interlayer paths between MXene sheets are also broadened through delamination,<sup>[196]</sup> preintercalation of transition metal ions<sup>[198]</sup> etc. strategies to expose more active sites and accelerate ion transport within the interlayer space. The enhanced capacitance and rate capability are indeed observed after conducting these optimized methods on  $Ti_3C_2T_x$  MXene.

Note that the protons move through a Grotthuss mechanism in aqueous electrolyte, which hop via hydrogen bond network formed among water molecules of electrolytes.<sup>[28, 104, 224]</sup> Hydrogen ions move from electrolyte to interlayer space of  $Ti_3C_2T_x$  is thought as the intercalation of hydronium ions ( $H_3O^+$ ), corresponding to intercalation pseudocapacitance.<sup>[28, 293]</sup> The interaction between intercalated hydronium



ions and MXene surface behaves like an electric double layer capacitance at high potential ranges from its CV plots. Then the protons in the hydroniums would chemically bond with surface -O terminals of MXene with the decrement of potentials, leading to appearance the redox peak in CV curves, which correspond to pseudocapacitive charge storage.<sup>[211, 293, 294]</sup> However, the transport mechanism about protons from electrolyte to active site within the interlayer space and the interaction between intercalated ions and  $Ti_3C_2T_x$  MXene surface are generally neglected when optimizing its supercapacitive performance. Ultrafast proton transport can be achieved in sub-one-nanometer carbon nanotubes due to confinement effect,<sup>[224]</sup> and highly confined one-layer interlayer water of MXene has also been proved to enable much higher redox rates than more layers of interstitial water by first-principles methods.<sup>[44]</sup> Inspired by these experiment and calculation results, shrinking interlayer space of  $Ti_3C_2T_x$  MXene could be a feasible direction to boost proton intercalation and redox rates, which is opposite to typical thoughts that focus on broadening interlayer path of MXene. In addition, stronger interaction between interstitial ions and MXene surface can also be expected due to this contractive interlayer space.<sup>[15]</sup> And note that surface -F functional groups of  $Ti_3C_2T_x$  will disturb the continuity of hydrogen bond network at the interface, adverse to proton transport within the interlayer space.<sup>[28]</sup>

Therefore, herein a novel strategy is proposed to modify MXene for ameliorative energy storage ability from two aspects, (1) narrowing interlayer distance for forming



one-layer confined water molecules, (2) removing surface -F and -OH on MXene to ensure continuous hydrogen bond within the interlayer space. Namely, this strategy combines the ‘interlayer engineering’ in Chapter 4 and surface modification in Chapter 5. Few-layered  $\text{Ti}_3\text{C}_2\text{T}_x$  MXene was heated at a higher temperature ( $600^\circ\text{C}$ ) than Chapter 5 in phosphine and argon mixed atmosphere. The resultant MXene is rich in surface oxygen functional groups along with greatly decreased -F surface groups and shows narrower interlayer space than pristine counterpart. The results show that modified MXene not only exhibits an enhanced capacity of  $375 \text{ F g}^{-1}$  ( $338 \text{ C g}^{-1}$ ) than pristine  $\text{Ti}_3\text{C}_2\text{T}_x$  MXene, but also delivers better rate capability along with much ameliorative oxidation resistance ability and outstanding cyclic stability. *Ex situ* X-ray diffraction (XRD) and electrochemical impedance spectra (EIS) results collectively uncover that only one layer of water molecules in the modified sample during its charge and discharge process and proton intercalation into the interlayer space proceeds with Grotthuss mechanism at high potential range (**Figure 6.1**). The narrower interlayer gallery and faster proton transport contributes to its enhanced capacitance. The rich surface oxygen terminations are responsible for its superior oxidation resistance ability. This work demonstrates a novel strategy to boost supercapacitive performance of  $\text{Ti}_3\text{C}_2\text{T}_x$  MXene and intensify its oxidation resistance stability, which is promising for its practical applications.

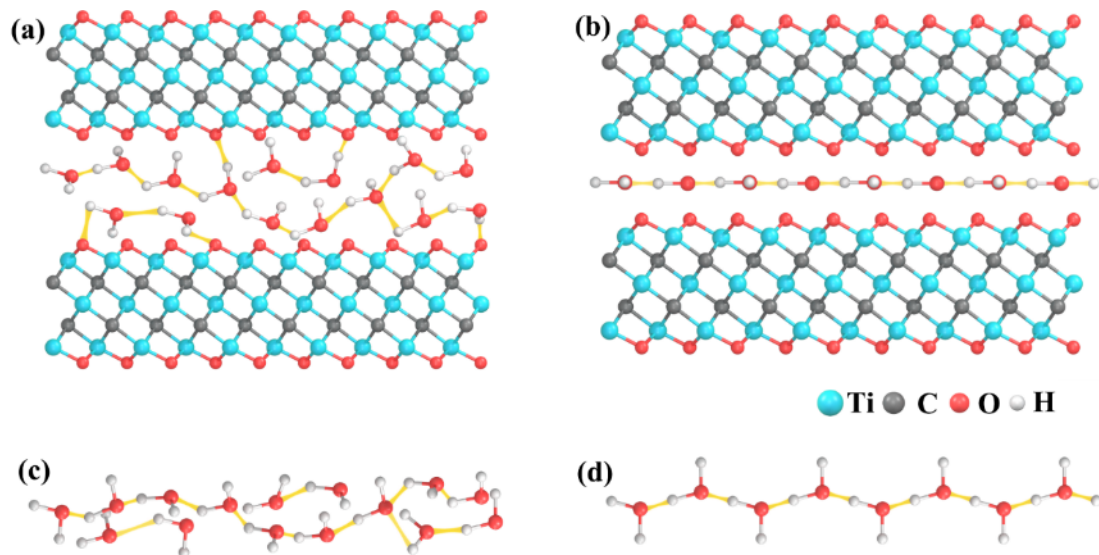


**Figure 6.1** Side view of (a) pristine MXene and (b) modified  $\text{Ti}_3\text{C}_2\text{T}_x$  MXene with interlayer water molecules. Top view of water molecules between pristine  $\text{Ti}_3\text{C}_2\text{T}_x$  (c) and modified  $\text{Ti}_3\text{C}_2\text{T}_x$  (d) interlayer space.

## 6.2 Results and discussions

To detach -F on  $\text{Ti}_3\text{C}_2\text{T}_x$  and shrink its interlayer space, few-layered  $\text{Ti}_3\text{C}_2\text{T}_x$  MXene aerogel was heated under the continuous flow of the argon and phosphine mixed gas with the higher temperature (600-700 °C) than that used in Chapter 5. The fluorine terminals on  $\text{Ti}_3\text{C}_2\text{T}_x$  will be greatly removed at temperature higher than 500 °C. <sup>[295]</sup> And the interlayer space of MXene would become narrower due to the removal of surface functional groups and interstitial water molecules during the heating procedures. The addition of phosphine in the heating atmosphere is for retarding the oxidation of  $\text{Ti}_3\text{C}_2\text{T}_x$  MXene and simultaneously serves as a surface phosphorus doping source to graft phosphorus on MXene surface, as shown in Chapter 5. These grafted phosphorus atoms are expected to avoid excessive shrinkage of interlayer space in MXene sheets

due to pillar effect. **Figure 6.2** shows the scanning electron microscope (SEM) figures of pristine  $Ti_3C_2T_x$  aerogel (MX), the aerogel samples heated at 600 °C (PMX600) and 700 °C (PMX700) in Ar+ $PH_3$  atmosphere and the control sample that MXene aerogel is only heated in pure argon at 600 °C (CMX600). Macroporous structure is observed in all of the four samples, but CMX600 shows some smaller white sheets than rest samples, as pointed by yellow arrows in **Figure 6.2d**. This result indicates  $Ti_3C_2T_x$  sheets tend to damage at the absence of  $PH_3$ , reconfirming the critical role of phosphine in sustaining the integrity of  $Ti_3C_2T_x$  MXene sheet, which is also consistent with the previous results on heating  $Ti_3C_2T_x$  MXene at 400°C with provision of the mixed Ar and phosphine gas in chapter 5 (**Figure 5.3a-d**).

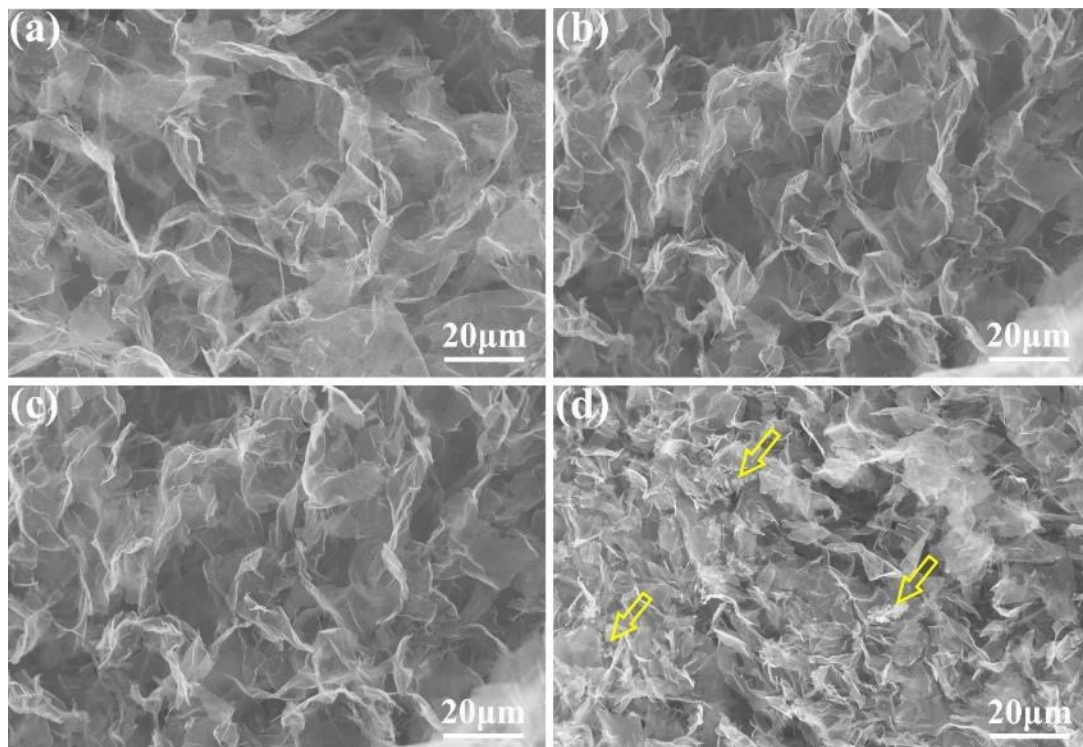


**Figure 6.2** SEM figures for (a) MX, (b) PMX600, (c) PMX700 and (d) CMX600



The phase composition and interlayer distance and in the samples are investigated by XRD patterns. The peaks ascribing to titanium oxides is evidently observed in PX700, but invisible in PMX600 and CMX600 as shown **Figure 6.3a**, indicating the severe oxidation of  $Ti_3C_2T_x$  heated at  $700^\circ C$  even if phosphine involves in the heating procedure. The peak value of (002) planes can be used to calculate the interlayer distance between MXene sheets and enlarged (002) peaks of the samples are shown in **Figure 6.3b**. The (002) peak of MX locates at  $6.02^\circ$ , corresponding to a interlayer distance of  $14.67 \text{ \AA}$ , while the (002) peaks of PMX600, PMX700 and CMX600 left shift to  $6.98^\circ$ ,  $7.25^\circ$  and  $7.14^\circ$ , respectively, indicating their narrower interlayer distance ( $12.66 \text{ \AA}$ ,  $12.19 \text{ \AA}$  and  $12.37 \text{ \AA}$ , respectively) than MX. We also note that PMX600 exhibits a broader interlayer than CMX600, which proves the pillar effect of doped phosphorus atoms to resist the shrinkage of the interlayer space between  $Ti_3C_2T_x$  sheets. The least interlayer space in PMX700 could be ascribed to the evident oxidation of  $Ti_3C_2T_x$  MXene. A sharper peak at 2theta of around  $28^\circ$  corresponding to (008) planes is shown in PMX600, PMX700 and CMX600 than in pristine MX, implying improved stacking order among MXene sheets after their heating processes. As a whole, XRD results demonstrate that  $600^\circ C$  heating technology with phosphine involvement can shrink the interlayer distance between  $Ti_3C_2T_x$  MXene sheets with phosphorus atoms as pillars and restrain the degradation of  $Ti_3C_2T_x$  MXene, which meets our design requirement on interlayer space. It also can be expected that the narrower space in all heated samples can contribute to the stronger interplay between MXene surface and



intercalated ions.

The specific area and pore size distributions of the samples were analyzed via nitrogen gas adsorption/desorption at 77K (**Figure 6.3c-d**). Brunauer–Emmett–Teller (BET) surface area of pristine MX is  $98 \text{ m}^2 \text{ g}^{-1}$ , while the values of PMX600, PMX700 and CMX600 decrease to 70.4, 75.5 and  $79.6 \text{ m}^2 \text{ g}^{-1}$  respectively (**Figure 6.3c**). The similar hierarchical pore size distributions are observed in all the samples, but PMX600, PMX700 and CMX600 underwent high temperature heating show less differential pore volume at pore size from 2 to 60 nm than MX as shown in **Figure 6.3d**. This result indicates the less specific area of PMX600, PMX700 and CMX600 is due to collapse of pores during their heating procedures. The larger BET specific areas of PMX700 and CMX600 than PMX600 could be attributed to their oxidation and breakage of  $\text{Ti}_3\text{C}_2\text{T}_x$  MXene sheets.

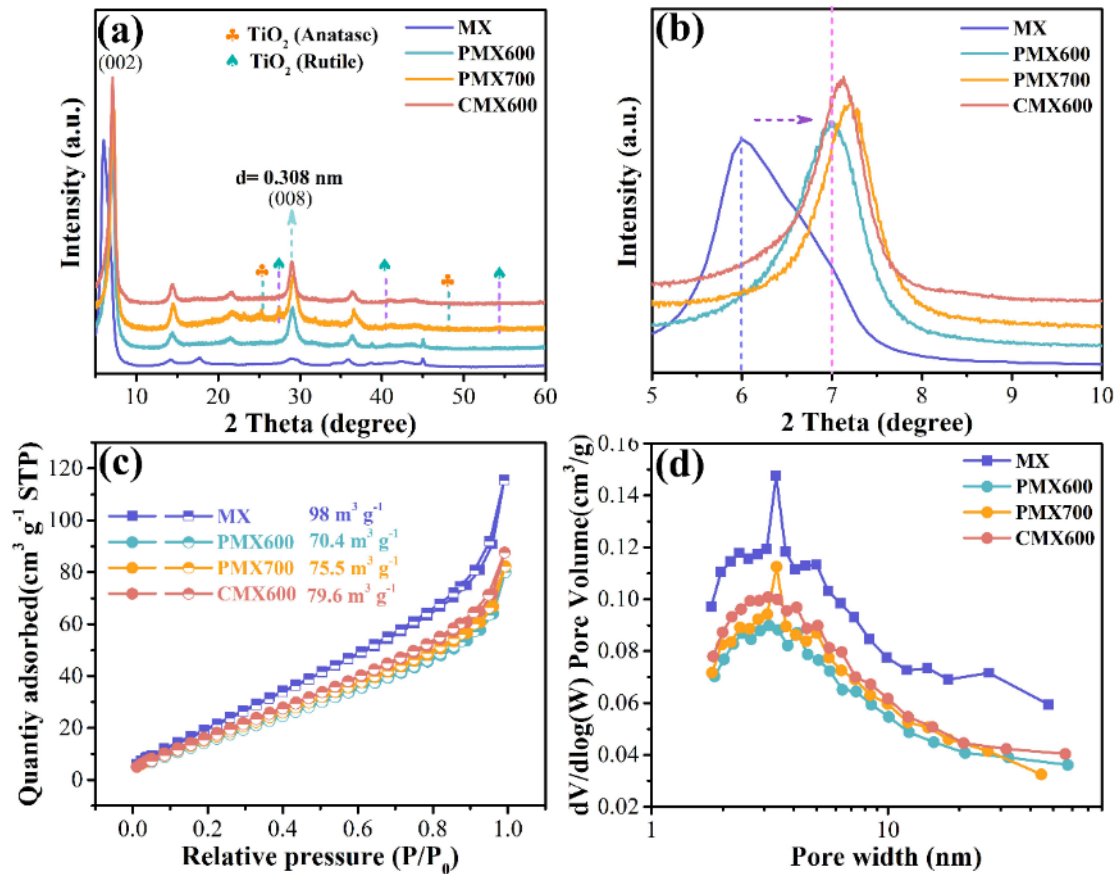


**Figure 6.3** (a) XRD plots of the samples, (b) enlarged (002) peak in (a), (c) nitrogen isothermal adsorption/desorption curves and (d) corresponding pore width distribution curves of MX, PMX600, PMX700 and CMX600

The interplanar distance of (010) planes for MX is 0.253 nm from its high resolution transmission electron microscope (HRTEM) image and the selected area electron diffraction (SAED) shows its hexagonal symmetry along with [00c] axis (**Figure 6.4a**). PMX600 exhibits a similar (010) planar distance with MX and retains the identical crystal symmetry with MX, shown in **Figure 6.4b**. However, both PMX700 and CMX600 exhibit a decreased (010) planar spacing compared to MX and polycrystalline diffraction rings can be observed from their SAED results but with evident diffraction points of titanium oxides in PMX700 (**Figure 6.4c-d**). The shrinking lattice parameter

of (010) planes in CMX600 and PMX700 could be attributed to partial oxidation of MXene sheets. And their diffraction rings indicate the fracture of MXene sheets due to oxidation, which is consistent with previous BET results.

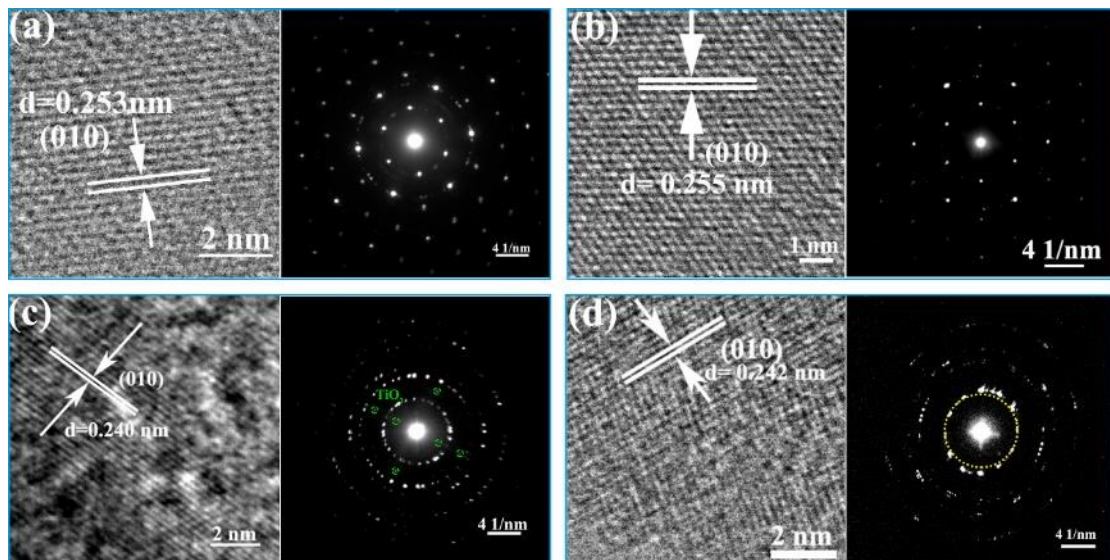


**Figure 6.4** HRTEM images and corresponding SAED patterns for (a) MX, (b) PMX600, (c) PMX700 and (d) CMX600.

Raman spectra is sensitive to the function group composition of  $Ti_3C_2T_x$  MXene, and Raman spectra of the samples are compared in **Figure 6.5a**. The  $A_{1g}$  band at around  $200\text{ cm}^{-1}$  corresponds to the out-of-plane vibration of outer-layer titanium atoms, carbon and surface functional groups.<sup>[286]</sup> This  $A_{1g}$  band in PMX600, PMX700 and CMX600 locates at the right side of that in MX, implying the stronger chemical bond strength between the outer-layer titanium and carbon/functional species in all heated samples. It is also expected that these robust chemical bonds can contribute to the crystal stability of  $Ti_3C_2T_x$  MXene, which will be verified in the following electrochemical oxidation experiments. The  $E_g$  band between  $250$  and  $450\text{ cm}^{-1}$  is related to the in-plane vibrations of surface functional groups linked with outer titanium atoms. The high  $E_g$  band value



( $\sim 397\text{ cm}^{-1}$ ) represents the vibrations of surface -OH groups, while the low band value ( $\sim 361\text{ cm}^{-1}$ ) corresponds to the vibrations of -O species on  $\text{Ti}_3\text{C}_2\text{T}_x$ . It can be observed that PMX600, PMX700 and CMX600 possess a lower peak value of the  $E_g$  band ( $352\text{ cm}^{-1}$ ) than MX ( $386\text{ cm}^{-1}$ ), which indicates their richer surface oxygen functional groups. In addition, the change of the  $E_g$  band value should be also connected to the amount of -F groups on MXene surface.

To further investigate the change of surface species on MXene, X-ray photoelectron spectroscopy (XPS) characterization was conducted. XPS survey spectra results (**Figure 6.5b**) shows that fluorine amount in MX is 14.0 at. %, but those of PMX600, PMX700 and CMX600 greatly decreases to 2.4 at. %, 1.3 at. % and 1.2 at. % respectively, verifying that our strategy can successfully remove surface fluorine terminations. And oxygen accounts for 29.3 at. %, 36.7 at. %, 33.7 at. % in PMX600, PMX700 and CMX600, respectively, which are much higher than that of MX (17.4 at. %). The richer oxygen content in all these heated samples could be due to reabsorption of oxygen on the bare outer titanium resulting from the detachment of -F groups. And their O 1s high resolution spectra can be deconvoluted into Ti-O ( $\text{TiO}_2$ ), C-Ti-O, C-Ti-OH,  $\text{H}_2\text{O}$  and organics (OR), which have the binding energies of 529.9, 531.9, 532, 532.9 and 533.8 eV, respectively, shown in **Figure 6.5c**.<sup>[35, 268, 284]</sup> The ratio of C-Ti-O to Ti-O( $\text{TiO}_2$ ) in MX, PMX600, PMX700 and CMX600 are 0.17, 0.38, 0.69 and 0.28 respectively, indicative of more surface -O groups on PMX600, PMX700 and



CMX600 than on MX, which is agreement with the previous discussion on the Raman  $E_g$  band peaking at  $352\sim 397\text{ cm}^{-1}$ . In the meantime, the higher content of C-Ti-OH in PMX600, PMX700 and CMX600 (**Table 6.1**) implies that the hydroxyl species will be reabsorbed on the  $\text{Ti}_3\text{C}_2$  slab even if they are removed during the heating procedure. A higher content of absorbed water is also observed from the O1s fitting result. These results indicate that higher oxygen concentration in all samples underwent the heating procedure dominantly originates from the reabsorbed -OH and  $\text{H}_2\text{O}$  molecules. The comparison on Ti2p XPS spectra of different samples is shown in **Figure 6.5d**. The Ti 2p3 in PMX600, PMX700 and CMX600 show a blue shift of 0.85, 0.9 and 0.76 eV, respectively in comparison to MX, indicating their higher average titanium valence states. The larger shift values in PMX600 than CMX600 could be attributed to the phosphorus incorporation, which is also seen in chapter 5 on grafting phosphorus on  $\text{Ti}_3\text{C}_2\text{T}_x$  at  $400^\circ\text{C}$  (**Figure 5.10b**). And oxidation of  $\text{Ti}_3\text{C}_2\text{T}_x$  and phosphorus doping are collectively responsible for the largest titanium valence variation in PMX700.

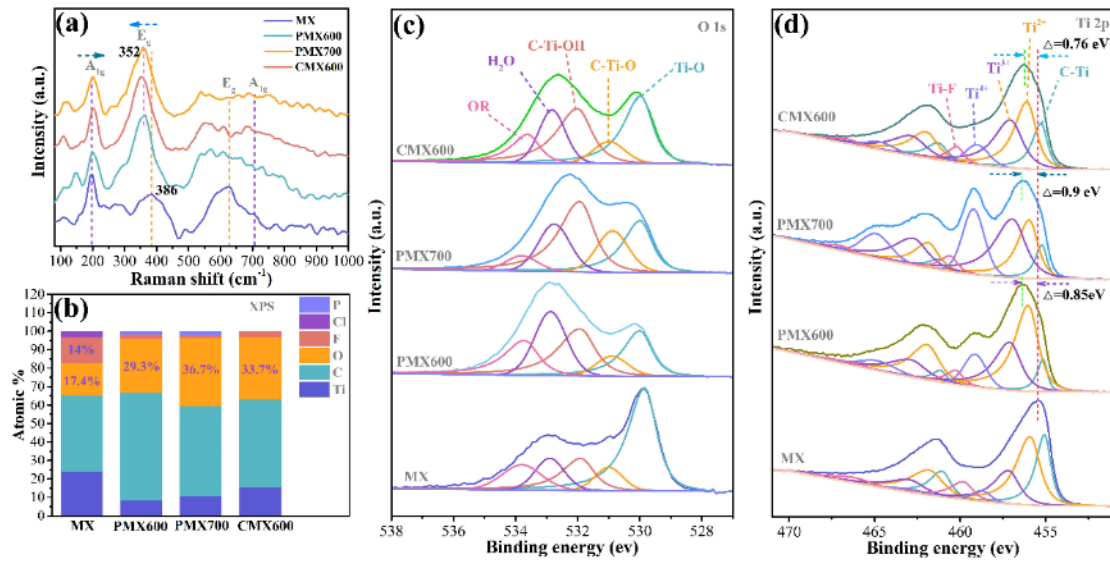


**Figure 6.5** (a) Raman spectra for MX, PMX600, PMX700 and CMX600. (b) composition analysis for the samples from XPS survey spectra. High resolution O1s (c) and Ti2p (d) of MX, PMX600, PMX700 and CMX600.

**Table 6.1** deconvolution results for O1s XPS spectra.

Sample	Concentration (%)				
	Ti-O	C-Ti-O	C-Ti-OH	H <sub>2</sub> O	OR
	529.9 eV	531.9 eV	532 eV	532.9 eV	533.8 eV
MX	49.25	8.37	17.12	12.20	13.06
PMX600	20.65	7.83	27.39	25.23	18.90
PMX700	22.59	15.7	37.73	18.11	5.87
CMX600	30.84	8.65	30.28	17.49	12.73
Reference	[35, 284]	[35, 284]	[35, 284]	[268]	[268]

P2p XPS spectra results (**Figure 6.6a**) shows a binding energy of 134 eV in PMX600 and PMX700, indicative of P-O<sub>x</sub> species in them.<sup>[296]</sup> Here the binding energy is higher

than that (133.5 eV) of PMX1 and PMX2 (**Figure 5.8b**), which can be attributed to more oxygen linking with doped phosphorus atoms. These results indicate that the surface doped phosphorus tend to bond with more oxygen atoms at high temperature and its electron donor ability will be degraded correspondingly. The detailed coordination environment on phosphorus will be further investigated via X-ray Absorption Spectroscopy (XAS) in the future work.

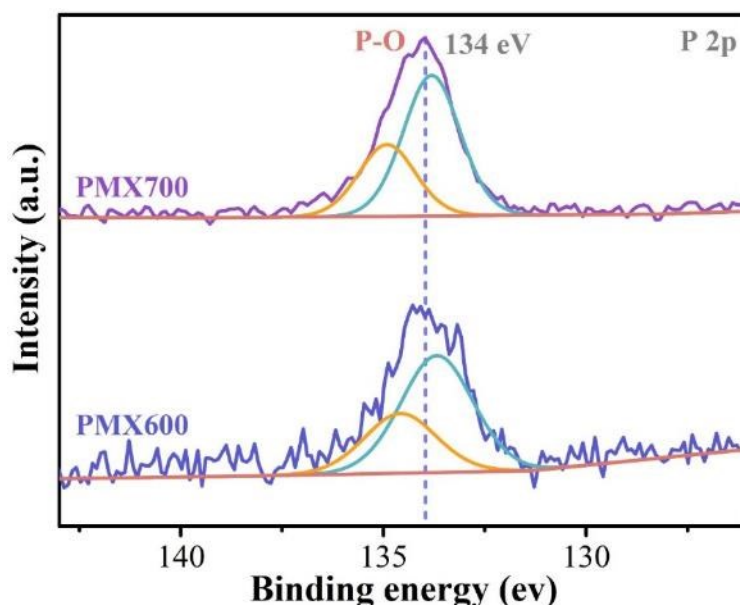


**Figure 6.6** (a) P2p high resolution spectra of PMX600 and PMX700

The electrochemical performances (ECs) of the as-prepared samples were studied using three-electrode configuration in 1M H<sub>2</sub>SO<sub>4</sub>, where Ag/AgCl (sat. KCl) and graphite bar serve as reference electrode and counter electrode, respectively. **Figure 6.7a** compares cyclic voltammetry (CV) profiles of MX, PMX600, PMX700 and CMX600 at a scan rate of 2 mV s<sup>-1</sup>. A new pair of redox peaks are observed in all heated samples, and PMX600 exhibits the identical potential window (-0.6~0.3 V vs. Ag/AgCl) with MX.



However, potential windows in PMX700 and CMX600 are -0.4~0.3 and -0.35~0.3V vs. Ag/AgCl, respectively, which could be attributed to their narrower interlayer distance and oxidation of MXene sheets.<sup>[163]</sup> It is worth noting that PMX600, PMX700 and CMX700 exhibit higher integrated area in the potential range of -0.25-0.3 V vs. Ag/AgCl than MX along with a pair of new redox peaks, indicating their ameliorative energy storage compared to pristine MXene within this potential range. And it is also can be observed that similar CV shapes are shown in MX and PMX600 within the potential range of -0.6-0.3 V vs. Ag/AgCl from **Figure 6.7a**, which represents their same intercalation pseudo capacitance in the low potential range. In summary, all modified samples (PMX600, PMX700 and CMX600) exhibit enhanced charge storage ability at the potential range of -0.25-0.3V vs. Ag/AgCl but only PMX600 retains the same working potential range with MX. Galvanostatic charge/discharge (GCD) plots of the samples at 2 A g<sup>-1</sup> are shown in **Figure 6.7b**, in which PMX600 delivers the longest charge-discharge time duration, indicating its highest capacitance among all of samples. The capacities (C g<sup>-1</sup>) of MX, PMX600, PMX700 and CXM600 at various scan rates and current densities are summarized in **Figure 6.7c-d**. PMX600 always exhibits the superior specific capacity compared to other samples at various scan rates and current densities. It delivers the highest specific capacity of 338 C g<sup>-1</sup> (376 F g<sup>-1</sup>) at 2 mV s<sup>-1</sup> and can retains 165 C g<sup>-1</sup> (183 F g<sup>-1</sup>) even if the scan rate increases to 1000 mV s<sup>-1</sup>, suggesting its good rate capability.



Electrochemical impedance spectroscopy (EIS) results were used to evaluate redox kinetics and electrical conductivity of different samples. The Nyquist plots of MX PMX-600, PMX-700 and CMX-600 at -0.2 V vs. Ag/AgCl are shown in **Figure 6.7e**. The slope of linear part of the plots reflects ion diffusion resistance in electrode materials.<sup>[109]</sup> The sharpest slope of PMX600 among the four samples implies its fastest proton intercalation process. The intercept with real axis in plots represents equivalent series resistance ( $R_s$ ), which is composed of electrical resistance of electrode material, interface resistance and ionic resistance of electrolyte. The higher  $R_s$  in PMX600, PMX700 and CMX600 manifest their decreased conductivities after the heating process, among which the decreased extent in PMX600 is the least. This should be ascribed to its intact crystal structure. In addition, the changed surface functionalization with richer -OH and P-O<sub>x</sub> species also leads to the decrement of density of states at Fermi level,<sup>[283]</sup> which is another reason for the decreased electrical conductivity in PMX600 and PMX700 and CMX600. The inferior conductivities of all heated samples to pristine MXene excludes that the enhanced of capacity is from boosted charge transport ability.

The stored charge in electrode materials can be divided into capacitive and diffusion-controlled contributions, which can be calculated using the equation below.

$$i(V) = k_1 v + k_2 v^{0.5} \quad (6-1)$$

Where the current,  $i(V)$ , at certain potential (V) is composed of capacitive ( $k_1 v$ ) and diffusion-controlled ( $k_2 v^{0.5}$ ) two components. The linear fitting on  $i(V)/v^{0.5}$  vs.  $v^{0.5}$  can



obtain the values of  $k_1$  and  $k_2$ . The capacitive contributions of the samples at scan rates from 2 to 50  $\text{mV s}^{-1}$  are shown in **Figure 6.7f**. PMX600 possesses the higher capacitive proportion than the rest samples, indicating its superior capacitive performance (rate capability) and availability of active sites to other samples, consistent with the EIS results. **Figure 6.7g** compares the capacity contributions from the two components. It can be observed that the difference of capacity between the samples mainly originates from capacitive contributions. PMX600 delivers the greatest capacity from capacitive process and PMX600 and CMX600 also shows the superior capacitive charge storage than MX. It can be concluded that that our modified strategy to  $\text{Ti}_3\text{C}_2\text{T}_x$  that narrow the interlayer space and eliminate surface -F can greatly boost the capacitive charge storage. Repetitive GCD measurements at 10  $\text{A g}^{-1}$  were conducted to evaluate the stability of samples. PMX600 retains the 94.1 % of initial capacity after 20000 cycles, which is higher than that of CMX600 (86.5%), shown in **Figure 6.7h**, reconfirming the critical role of phosphine in keeping crystal integrity of  $\text{Ti}_3\text{C}_2\text{T}_x$  MXene and whereby ensuring its cyclic stability. CV and GCD plots of PMX600 after different cycles (inset of **Figure 6.7h**) also proves its robust nature for energy storage. In addition, PMX600 exhibits the comparable and even superior energy storage ability to other reported methods (**Figure 6.7i**), including 400°C  $\text{NH}_3$  gas N-doping ( $342 \text{ C g}^{-1}$  at  $2 \text{ mV s}^{-1}$ ),<sup>[41]</sup> KOH washing+400°C annealing ( $300 \text{ C g}^{-1}$  at  $1 \text{ mV s}^{-1}$ ),<sup>[163]</sup>  $\text{NH}_4\text{F}$  N-doping ( $291 \text{ C g}^{-1}$  at  $2 \text{ mV s}^{-1}$ ),<sup>[297]</sup> surface reduction ( $270 \text{ C g}^{-1}$  at  $2 \text{ mV s}^{-1}$ )<sup>[35]</sup>, N-Butyllithium-Treated ( $314 \text{ C g}^{-1}$  at  $2 \text{ mV s}^{-1}$ ),<sup>[36]</sup> N, S co-doping ( $238 \text{ C g}^{-1}$  at  $20 \text{ mV s}^{-1}$ ),<sup>[43]</sup> partial oxidation( $182 \text{ C g}^{-1}$  at  $2 \text{ mV s}^{-1}$ ),<sup>[211]</sup>

200°C NH<sub>3</sub> gas N-doping (105.6 C g<sup>-1</sup> at 1mVs<sup>-1</sup>),<sup>[37]</sup> and 500°C P-doping (102C g<sup>-1</sup> at 2 mVs<sup>-1</sup>).<sup>[39]</sup> These results indicate that our strategy is an efficient but competent way to boost supercapacitive performance of Ti<sub>3</sub>C<sub>2</sub>T<sub>x</sub> MXene.

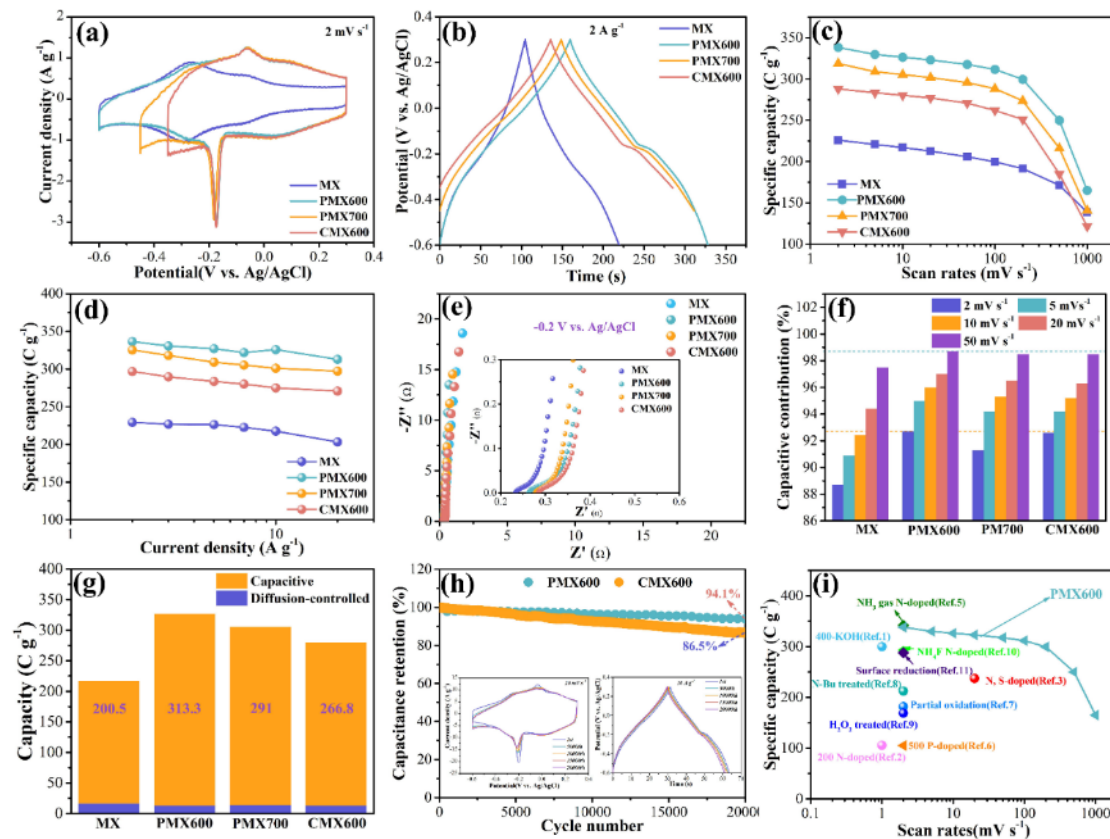


**Figure 6.7** Electrochemical performance of MX, PMX600, PMX700 and CMX600. (a) CV curves at the scan rate of 2 mV s<sup>-1</sup>. (b) GCD plots at the current density of 2A g<sup>-1</sup>. (c), (d) capacity of the samples at various scan rates (c) and (d) current densities. (e) EIS plot and its inset shows intercept with real axis. (f) capacitive contributions of the sample at scan rates from 2 to 50 mV s<sup>-1</sup> and (f) shows the capacity composition at the scan rate of 2 mV s<sup>-1</sup>. (h) cyclic test of PMX600 and CMX600 at 10 A g<sup>-1</sup> and its inset shows the CV and GCD plots of PMX600 after different cycle times. (i) Specific capacity vs. scan rates for PMX600 and the plots of capacities using other modified methods.

The blue shift of A<sub>1g</sub> Raman band in PMX600, PMX700 and CMX600 compared to MX (Figure 6.5a) indicates the strengthened chemical bonds. It is expected that this feature may endow them with improved oxidation resistance ability. Ti<sub>3</sub>C<sub>2</sub>T<sub>x</sub> MXene would



start being electrochemically oxidized when the applied potential surpass 0.3V vs. Ag/AgCl.<sup>[298]</sup> To evaluate the oxidation resistance of PMX-600, a wider potential window (-0.6-0.6V vs. Ag/AgCl) than that of routine EC characterization (-0.6-0.3V vs. Ag/AgCl) was selected to conduct many-time CV measurements. Pristine MX shows fast performance degradation with cycle times and large oxidation current within the potential of 0.4-0.6V vs. Ag/AgCl is observed in first ten cycles (**Figure 6.8a**), which indicates the inferior oxidation resistance ability of MX. By contrast, little CV shape variation was observed in PM600 after 20 cycles with the same wider potential range, as shown in **Figure 6.8b**, indicative of its much superior oxidation resistance ability to MX. Therefore, one can conclude that the enhanced chemical bonds indeed contribute to the oxidation resistance of MXene. The rich oxygen terminations on  $Ti_3C_2T_x$  should be responsible for the much-boosted oxidation resistance capability in all heated MXene.<sup>[299, 300]</sup> To our best knowledge, the enhancement about oxidation resistance of MXene is rarely reported in other modified methods, highlighting the merits of our modified strategy. The improvement of oxidation resistance ability should also be favorable for the storage of MXene in air, which will be verified in the future experiments. To here, the F-deficient, oxygen-rich MXene with narrower interlayer path is confirmed in PMX600, PMX700, CMX600.

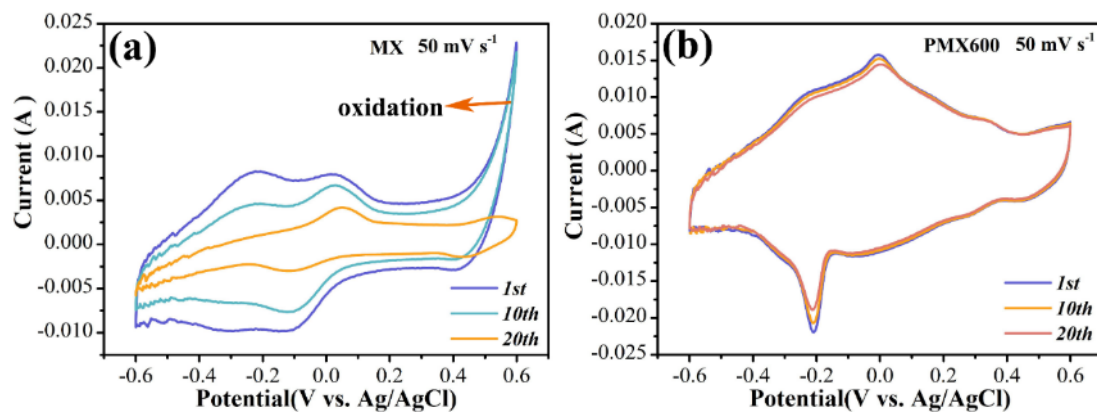


**Figure 6.8** CV curves of MX (a) and PMX600 (b) at different cycle times within potential window of -0.6-0.6V vs. Ag/AgCl.

All modified samples show a pair of new redox peaks in CV curves compared to pristine MXene. To confirm the origin of the new redox peaks, *ex situ* XRD characterizations on MX and PMX600 were conducted, and corresponding results are shown in **Figure 6.9a-b**. No appearance of new XRD peaks in both MX and PMX600 with change of potentials indicates that their charge storage all belongs to capacitive process. The CV curves of MX and PMX600 in 3M HCl, 1M Li<sub>2</sub>SO<sub>4</sub> and 3M LiCl electrolytes show are compared in **Figure 6.9d-f** to further figure out which electrolyte ion is responsible for the new redox peaks. The results show that only acid solution can endow PMX600 with the new redox peaks compared to MX, as pointed by green arrows in **Figure 6.9d**. Therefore, the new redox peaks are ascribed to the proton chemically bonding/debonding with Ti<sub>3</sub>C<sub>2</sub>T<sub>x</sub> MXene surface. And the change of (002) peaks with applied potentials for MX and PMX600 are shown in **Figure 6.9c**. 2theta value for (002) peak in MX vibrate around at 6.4° with a amplitude of 0.5°, which correspond to 13.79 Å, indicating 1-2 layer water molecules within the interlayer space.<sup>[44, 301]</sup> PMX600

exhibits a larger 2theta value of (002) XRD peak than MX, which vibrates along 7°, suggesting monolayer water situating in the interlayer space. [44, 301]

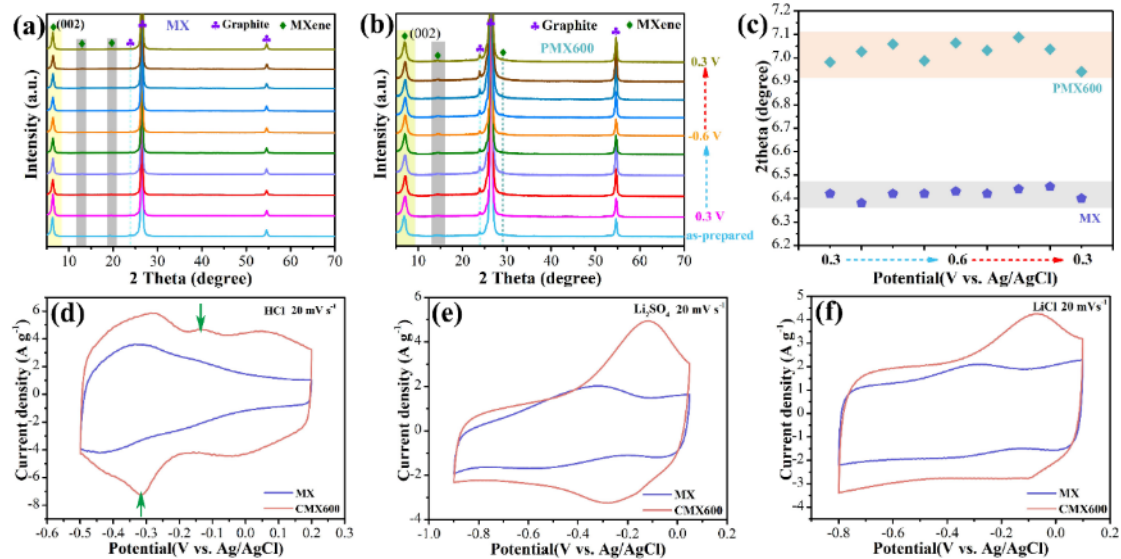


**Figure 6.9** ex situ XRD patten of (a) MX and PMX600. (c) (002) peak value vs. potential plots for MX and PMX600. CV curves of MX and PMX600 in 3M HCl, 1M Li<sub>2</sub>SO<sub>4</sub> and LiCl at 20 the scan rate of 20 mV s<sup>-1</sup>

The ion diffusion behaviors in MX and PMX600 are investigated via *in situ* electrochemical impedance spectra (EIS), shown in **Figure 6.10a-b**. The linear slope of MX varies with applied potentials and when the potential is lower than -0.3V, the slope value decreases significantly with decrement of applied potentials (**Figure 6.10a**). This result suggests that proton intercalation is dependent on the applied potentials in MX, which should be due to the simultaneous intercalation of water molecules.<sup>[28]</sup> The interlayer space containing 1-2 layer water molecules (**Figure 6.9c**) also supports the hydronium intercalation during its charge-discharge process. However, almost identical slope for the linear part of EIS plots at the potential range of -0.2-0.3V vs. Ag/AgCl is observed in PMX600, and its linear part also become much less steep when the applied



potentials reduce to  $-0.3\text{V}$  and below vs. Ag/AgCl (**Figure 6.10b**). Monolayer water molecules were formed within the interlayer space of PMX600 from its previous *ex situ* XRD results (**Figure 6.9c**). The protons transport through Grotthuss mechanism via hydrogen bond network formed among these water molecules. The same linear slope for EIS plots of PMX600 at potential range of  $-0.2\sim 0.3\text{V}$  vs. Ag/AgCl demonstrates the direct intercalation of protons without the help of extra water molecules, which can be explained as Grotthuss transport mechanism. The lower slope in EIS plots of PMX600 at lower potential ranges ( $< -0.3\text{V}$  vs. Ag/AgCl) indicates inferior proton intercalation behavior. It could be due to the formed  $-\text{OH}$  on MXene from the redox reactions at high potential range, which disturbs the continuity of interstitial hydrogen bond network, leading to the degraded proton intercalation at lower potential range. Therefore, one can conclude that the energy storage in PMX600 is divided into two stages. The proton intercalation into the interlayer space of MXene in a potential range of around  $-0.2\sim 0.3\text{V}$  vs. Ag/AgCl proceeds via Grotthuss mechanism. The second stage is that the proton transport to interlayer space is more like a normal intercalation process when the potential is further reduced. But MX shows intercalation pseudocapacitance in whole potential range ( $-0.6\sim 0.3\text{V}$  vs. Ag/AgCl).

In addition to the difference on proton transport behavior to interlayer active site, MX and PMX600 also shows distinct CV shapes at high potential range ( $-0.25\sim 0.3\text{V}$  vs. Ag/AgCl). MX exhibits electric double layer capacitance (EDLC) at potential range of



0.1-0.3 V vs. Ag/AgCl, followed by a pair of redox peaks appear at -0.2-0.1 V vs. Ag/AgCl (**Figure 6.10c**). However, broad peaks at -0.05~0.3V vs. Ag/AgCl are shown in PMX600, manifesting its pseudocapacitance energy storage behavior, which is different from the EDLC in MX. This result shows that our modified strategy makes the energy storage of MXene transform from EDLC to pseudo capacitance at high potential range (**Figure 6.10c**). The transition can be explained from that (1) highly confined monolayer water enable fast transport of protons to interlayer active sites with Grotthus mechanism,<sup>[224]</sup> and (2) intercalated protons within monolayer interstitial water have more chances to encounter active sites on MXene surface than those within two or three layer interstitial water,<sup>[44]</sup> contributing to the redox reaction of protons with MXene surface. In addition, the substantial removal of surface -F groups is also another the factor to ensure the continuity of hydrogen bonds within interlayer space,<sup>[28]</sup> which is also beneficial to interstitial proton transport in MXene sheets.

In summary, the confinement effect is critical for the interaction between host and intercalated ions. The confined monolayer water molecules within the interlayer path space of  $Ti_3C_2T_x$  MXene boost the proton intercalation and strengthen the interaction between intercalated protons and host materials.<sup>[95, 302]</sup>

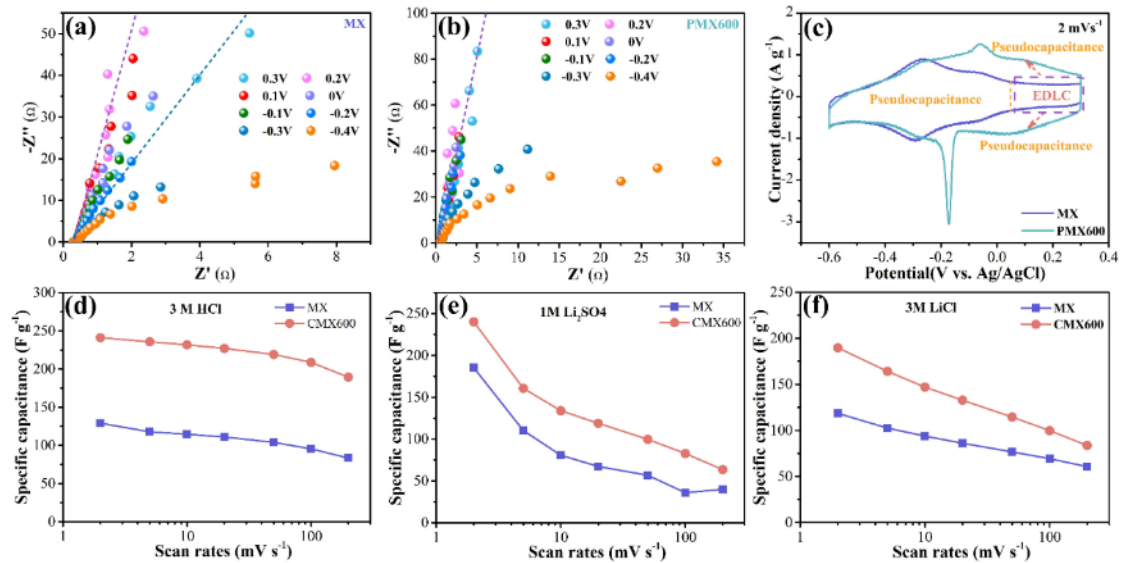


**Figure 6.10** Electrochemical impedance spectra of MX (a) and PMX600 (b) at different potentials. (c) CV curves of MX and PMX600 at the scan rate of 2 mV s<sup>-1</sup> to elucidate the difference of energy storage behavior between them. (d)-(f) Rate capability of MX and PMX600 in 3M HCl(d), 1M Li<sub>2</sub>SO<sub>4</sub> (e) and 3M LiCl (f).

To validate the uniformity of our modified strategy to improve supercapacitive performance of MXene, the electrochemical characterization of MX and PMX600 in 3M HCl, 1M Li<sub>2</sub>SO<sub>4</sub> and 3M LiCl was also conducted. PMX600 delivers the highest capacitance of 241, 240 and 190 F g<sup>-1</sup> at 2 mV s<sup>-1</sup> in the three electrolytes, respectively, which are higher those of MX (129, 185 and 119 F g<sup>-1</sup>), as shown in **Figure 6.10d-f**. And PMX600 always exhibits the superior energy storage ability to MX at various scan rates. These results our strategy is a universal method to enhance the energy storage ability of MXene. And the improved performance could be attributed to the fast but stronger interaction between MXene and intercalated cations.

Before characterizing the energy storage ability of the devices assembled with as-prepared samples, one find that Ti<sub>3</sub>C<sub>2</sub>T<sub>x</sub> MXene-based symmetric supercapacitors

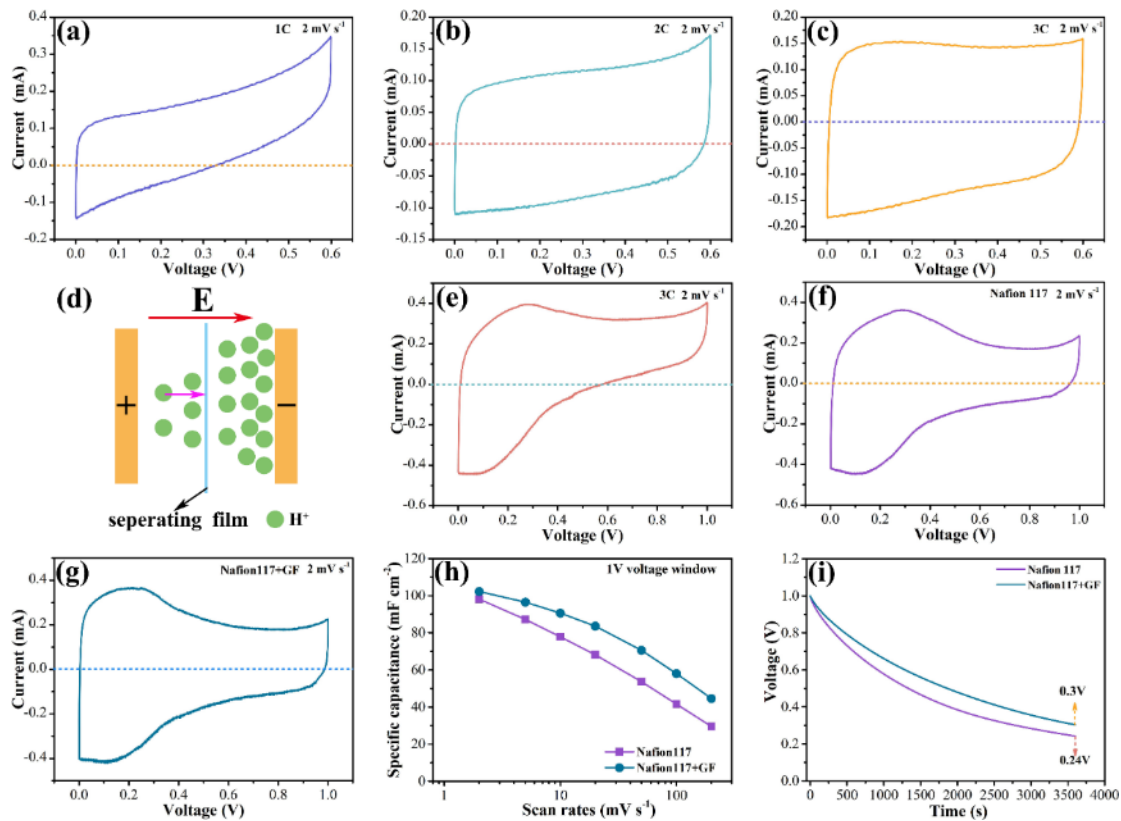


exhibit different voltage windows from 0.6 to 1V in different literature.<sup>[33, 38, 141, 249, 272, 303]</sup> There is also no report about why they use various voltage windows. Thus, it is necessary to figure out what factors lead to the difference before evaluation of modified MXene based devices. Note that only separating films are diverse in the devices of literature. So, we first use 1-3 pieces of Celgard 3501(C) films as separating films to assemble  $\text{Ti}_3\text{C}_2\text{T}_x$  MXene film based symmetric supercapacitors. Their CV curves (0.6V voltage window) at  $2 \text{ mV s}^{-1}$  are shown in **Figure 6.11a-c**. Very low columbic efficiency is observed in 1C-based device, but the efficiency of the devices increases with the number of separating films. The charge storage of  $\text{Ti}_3\text{C}_2\text{T}_x$  only involve the interaction between protons and material surface due to.<sup>[304]</sup> Therefore, when the device is charged, the protons in cathode will deintercalated and move to anode, which will cause the proton concentration gradient along with electric field direction (**Figure 6.11d**). When one separating film is used, the high concentration protons at the anode side will easily diffuse back to the cathode side, leading to self-discharge and low columbic efficiency behavior. The greater number of separating films can better separate the protons at both sides. That is why the supercapacitor with 3C separating films can exhibits almost 100% columbic efficiency in  $2\text{mV s}^{-1}$  CV curve (**Figure 6.11c**). But when the voltage window is further increase to 1V, the 3C separating film device still delivers the low columbic efficiency ( $\sim 64.5\%$ ), as shown in **Figure 6.11e**. It should be due to the higher proton concentration difference between two electrode is needed for 1V voltage window than that with only 0.6V. In this case, 3C separating



films are not enough to isolate the influence of proton at both sides.

Nafion film is a good media for proton transport and can separate the electrolytes at its both sides and may be a good candidate separating film for MXene-based symmetric supercapacitors. Thus, Nafion 117 with a thickness of 85 $\mu$ m was finally selected and the assembled device show a columbic efficiency of 98.6% (**Figure 6.11f**) for 1V voltage window, much higher than the 3C based supercapacitor (~64.5%). Considering that the Nafion 117 film is rigid thus not favorable for the electrolyte storage and electrode wetting, Nafion117 combines with glass fiber (GF) to serves as the composite separating film. The assembled device exhibits a higher columbic efficiency (99.5%), better rate capability and self-discharge resistance behavior than that with only Nafion 117, as shown in **Figure 6.11 g-i**. Therefore, Nafion117+GF is the good candidate separating film enabling that the  $Ti_3C_2T_x$ -based symmetric supercapacitors can work with 1V voltage window and almost 100% columbic efficiency. All devices in this chapter were all assembled with the composite film as separating diaphragms.



**Figure 6.11** CV curves of MX-based symmetric supercapacitors at the scan rate of  $2 \text{ mV s}^{-1}$  with 1C (a), 2C (b) and 3C (d) separating film. (d) The schematic diagram of proton transport within the device when charged. (e)-(g) CV curves of the supercapacitor at  $2 \text{ mV s}^{-1}$  and with 1V voltage window using 3C (e), Nafion117 (f) and Nafion117+GF (g) as separating films respectively. (h) specific capacitance vs. scan rate plots for two MX based symmetric supercapacitors with Nafion117 and Nafion117+GF as separating films, respectively. (i) self-discharge behavior of the two energy storage devices.

MX, PMX600 and CMX600 based symmetric supercapacitors were assembled to evaluate their practicability. **Figure 6.12a-c** shows the CV curves of the devices with 0.6V, 0.8V and 1V voltages windows, respectively. PMX600-based device always possesses the higher integrated areas than the devices of rest two samples in these three voltage windows, indicating its superior energy storage ability. GCD curves at  $0.5 \text{ A g}^{-1}$  also show the similar trend (**Figure 6.12d-f**). The maximum capacitances for PMX600 based supercapacitor are 64.5, 75.7 and  $72.8 \text{ F g}^{-1}$  at  $2 \text{ mV s}^{-1}$  for 0.6, 0.8V and 1V

windows, respectively, and the device shows the better energy storage ability than other assembled with other samples at various scan rates (2-200  $\text{mV s}^{-1}$ ) for different windows

(Figure 6.12g-i)

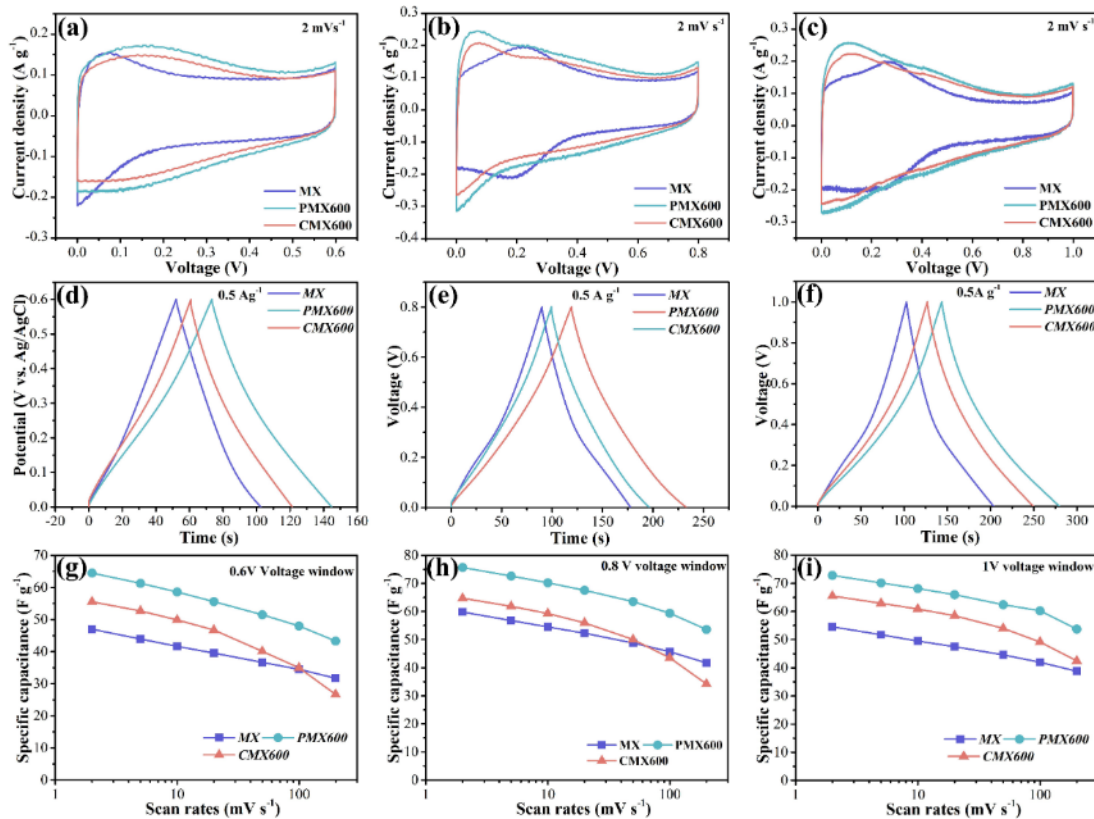


**Figure 6.12** Electrochemical performance of MX, PMX600 and CMX600 based symmetric supercapacitors. CV curves at the scan rate of 2  $\text{mV s}^{-1}$  for the samples with voltage window of 0.6V (a), 0.8V (b) and 1V (c). GCD plots at the current density of 0.5  $\text{A g}^{-1}$  for 0.6V (d), 0.8V (e) and 1V (f) voltage window. Specific capacities of the symmetric supercapacitors at the scan rates from 2 to 200  $\text{mV s}^{-1}$  with 0.6V (g), 0.8V(h) and 1V (i) voltage windows, respectively.

Self-discharge rate is a very important factor for the practical application of supercapacitors,<sup>[248, 250, 305]</sup> which is rarely evaluated in the reported MXene-based supercapacitors. Self-discharge refers to a spontaneous voltage decay process under the open circuit condition of supercapacitors. The low self-discharge rate means the voltage



of supercapacitors slowly decrease with time after being fully charged and is highly demanded for energy storage devices. Herein, MX, PMX600 and CMX600 based devices are fully charged using a current density of  $0.5 \text{ A g}^{-1}$  to 0.6V, 0.8V and 1V, then their plots of open circuit potential vs. time were collected, as shown in **Figure 6.13** a-c. PMX600 based device decreases from 0.6 V to 0.23 V within 1h after being charged to 0.6V, and decay from 0.8V to 0.26V with the same time duration after being fully charged to 0.8V, which are superior those of MX and CMX600 supercapacitors. These results indicate our modified strategy for  $\text{Ti}_3\text{C}_2\text{T}_x$  MXene not only boost its capacitance, but also resist self-discharge behavior of the assembled device. However, the superiority on self-discharge resistance ability of PMX600 based device to the supercapacitors assembled with other samples is less evident for 1V voltage window (**Figure 6.13c**), which should be due to the more severe oxidation of MXene cathodes for all 1 V devices. <sup>[303]</sup> The plots of energy density vs. power density for all supercapacitors are compared in **Figure 6.13d**. The symmetric supercapacitors using PMX600 as electrodes shows the highest energy density of  $10.11 \text{ Wh Kg}^{-1}$  at power density of  $121.33 \text{ W Kg}^{-1}$ .

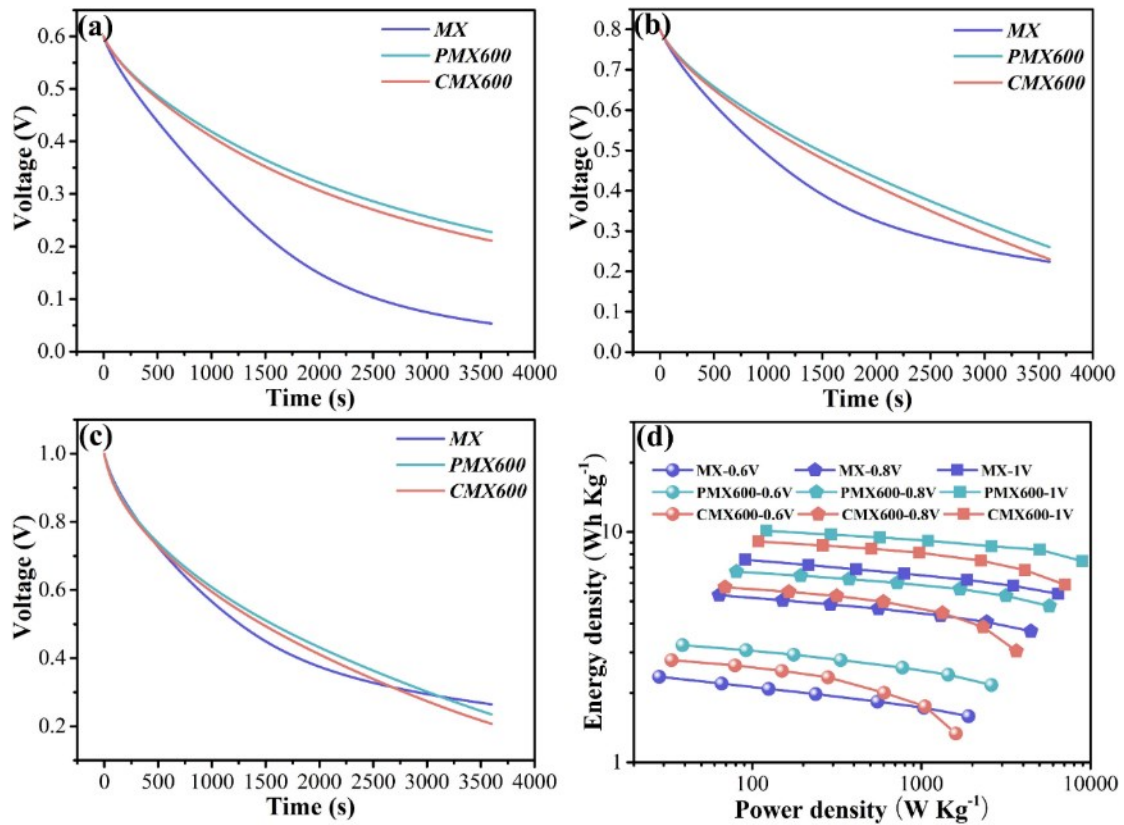


**Figure 6.13** self-discharge behavior of MX and PMX600 and CMX600 based symmetric supercapacitors with 0.6V(a), 0.8V(b) and 1V(c) voltage windows. (d) Ragone plots for the assembled devices with different voltage windows.

Given the fast voltage decay with time for all assembled MXene based symmetric supercapacitors, redox active copper hexacyanoferrate Prussian blue analogue (PBA) in acid media is selected to serve as cathode to assemble asymmetric supercapacitors with PMX600 as anode. The assembled device is expected to show further increased energy density due to wider voltage window and slow self-discharge rate resulting from both redox-active nature in both electrodes.<sup>[250]</sup> First, XRD pattern (**Figure 6.14a**) shows that PBA was successfully prepared due to peaks matching well with JCPD 01-86-0513. Its CV curves (**Figure 6.14b**) shows a main pair of redox peaks along with some smaller peaks, which correspond to the redox reactions of  $\text{Cu}^{2+}/\text{Cu}^+$  and  $\text{Fe}^{3+}/\text{Fe}^{2+}$

due to the intercalation of protons.<sup>[104, 306]</sup> **Figure 6.14 c** shows the GCD plots at current density from 1 to 20 A g<sup>-1</sup>. Their almost symmetric shapes suggest the good reversibility of the redox actions in PBA. It delivers the maximum capacity of 104 C g<sup>-1</sup> at 1 A g<sup>-1</sup> and retains 37 C g<sup>-1</sup> when the current density increases to 20 A g<sup>-1</sup> (**Figure 6.14d**). To assemble the asymmetric device, the mass ratio between cathode and anode is confirmed according to the equation below,<sup>[241]</sup>

$$\frac{m_{cathode}}{m_{anode}} = \frac{C_{anode} \cdot U_{anode}}{C_{cathode} \cdot U_{cathode}} \quad (6-2)$$

where, C<sub>cathode</sub> and C<sub>anode</sub> represent the capacitance of cathode and anode, respectively, and U<sub>cathode</sub> and U<sub>anode</sub> are their potentials windows.

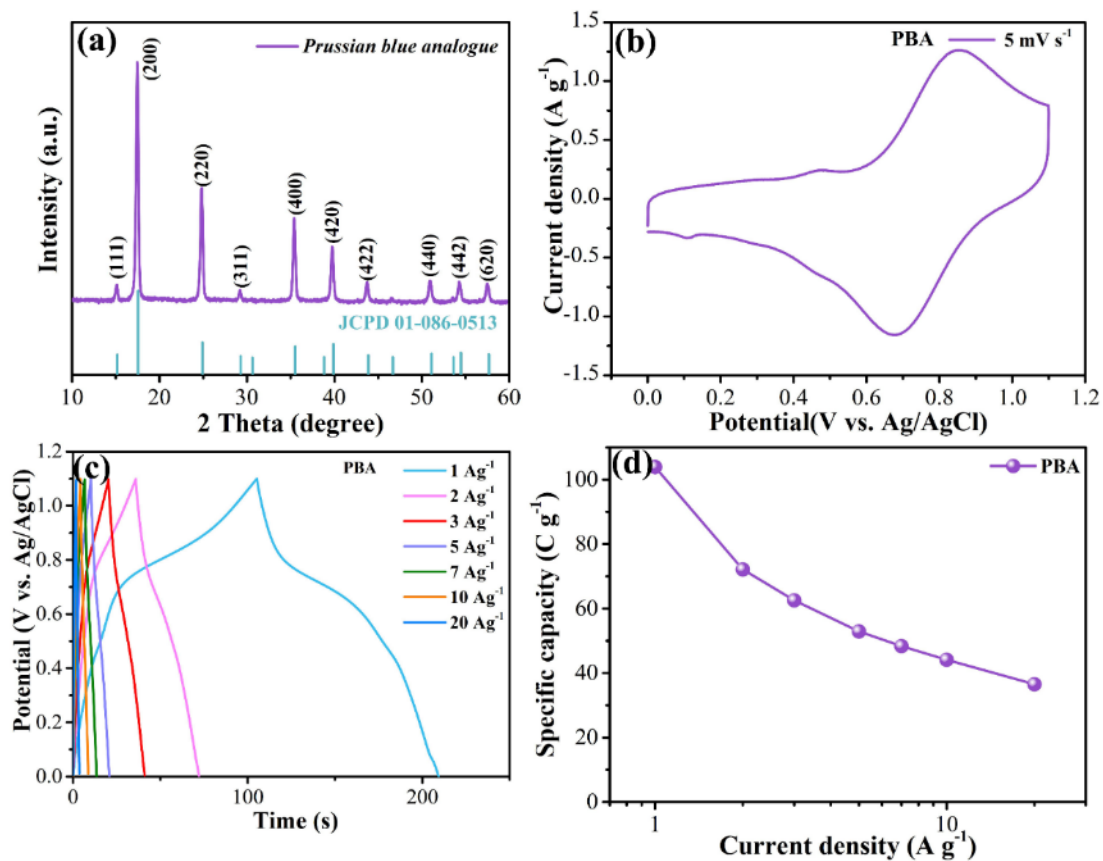


**Figure 6.14** (a) XRD patterns of PBA. (b) CV curve of PBA in 1M H<sub>2</sub>SO<sub>4</sub> at 5 mVs<sup>-1</sup> and (c) its GCD plots at current density from 1 to 20 A g<sup>-1</sup>. (d) The plots of specific



capacity vs. current density for PBA.

**Figure 6.15a** shows the CV curve of assembled asymmetric supercapacitor at  $5 \text{ mV s}^{-1}$ . The broaden redox peaks suggest its pseudocapacitive energy storage behavior. The good reversibility of redox reactions in the device is confirmed through symmetric GCD shape at  $0.1\text{-}5 \text{ A g}^{-1}$  (**Figure 6.15 b,d**). The broaden peaks can be all observed at scan rates from  $2$  to  $200 \text{ mVs}^{-1}$ , indicating the redox reaction proceeding at both the cathode and anode. The almost vertical tend for plots of low frequency in EIS image proves the good capacitive performance of the assembled supercapacitor. It exhibits the maximum capacitance of  $49.1 \text{ F g}^{-1}$  at  $2 \text{ mV s}^{-1}$  and retains  $17 \text{ F g}^{-1}$  when the scan rate increases to  $200 \text{ mVs}^{-1}$ . To evaluate its self-discharge resistance ability, a current density of  $0.5 \text{ A g}^{-1}$  was applied to charge to  $1.8 \text{ V}$ , followed by  $2 \text{ min}$  standing, then the plots of open circuit potential vs. time was collected shown in **Figure 6.15g**. A voltage of  $1.54 \text{ V}$  is kept after the standing and the supercapacitor still keeps  $1 \text{ V}$  voltage after  $1 \text{ h}$  duration, which is much superior to all assembled symmetric supercapacitors (**Figure 6.13a-c**). Ragone plots compare (**Figure 6.15h**) the energy density and power density of PMX600-PBA asymmetric supercapacitors with other assembled supercapacitors in this research and some reported MXene-based devices. The PMX600-PBA device can provide the highest energy density of  $19.7 \text{ Wh Kg}^{-1}$  at the power density of  $83.6 \text{ W Kg}^{-1}$  and still delivers an energy density of  $6.8 \text{ Wh Kg}^{-1}$  when the power density reaches up to  $2885 \text{ W kg}^{-1}$ , which is comparable to MXene-PANI ( $17 \text{ Wh Kg}^{-1}$  at  $200 \text{ W kg}^{-1}$ ),<sup>[23]</sup> and superior to MXene-MnO<sub>2</sub> ( $6.4 \text{ Wh Kg}^{-1}$  at  $1107 \text{ W}$

$\text{Kg}^{-1}$ )<sup>[18]</sup>, MXene-AC ( $7 \text{ Wh Kg}^{-1}$  at  $698 \text{ W Kg}^{-1}$ ),<sup>[279]</sup> MX-MX ( $7.6 \text{ Wh Kg}^{-1}$  at  $91 \text{ W Kg}^{-1}$ ), PMX2-PMX2 ( $11.2 \text{ Wh Kg}^{-1}$  at  $79 \text{ W Kg}^{-1}$ ) and PMX600-PMX600 ( $10.1 \text{ Wh Kg}^{-1}$  at  $121 \text{ W Kg}^{-1}$ ), indicative of the competence of the assembled device. Two PMX600-PBA after being charged with a current density of  $0.2 \text{ A g}^{-1}$  in series can light up a red and green LED light bulb, as shown in **Figure 6.15i**, proving the good prospect for real application of the PMX600-PBA asymmetric supercapacitor.

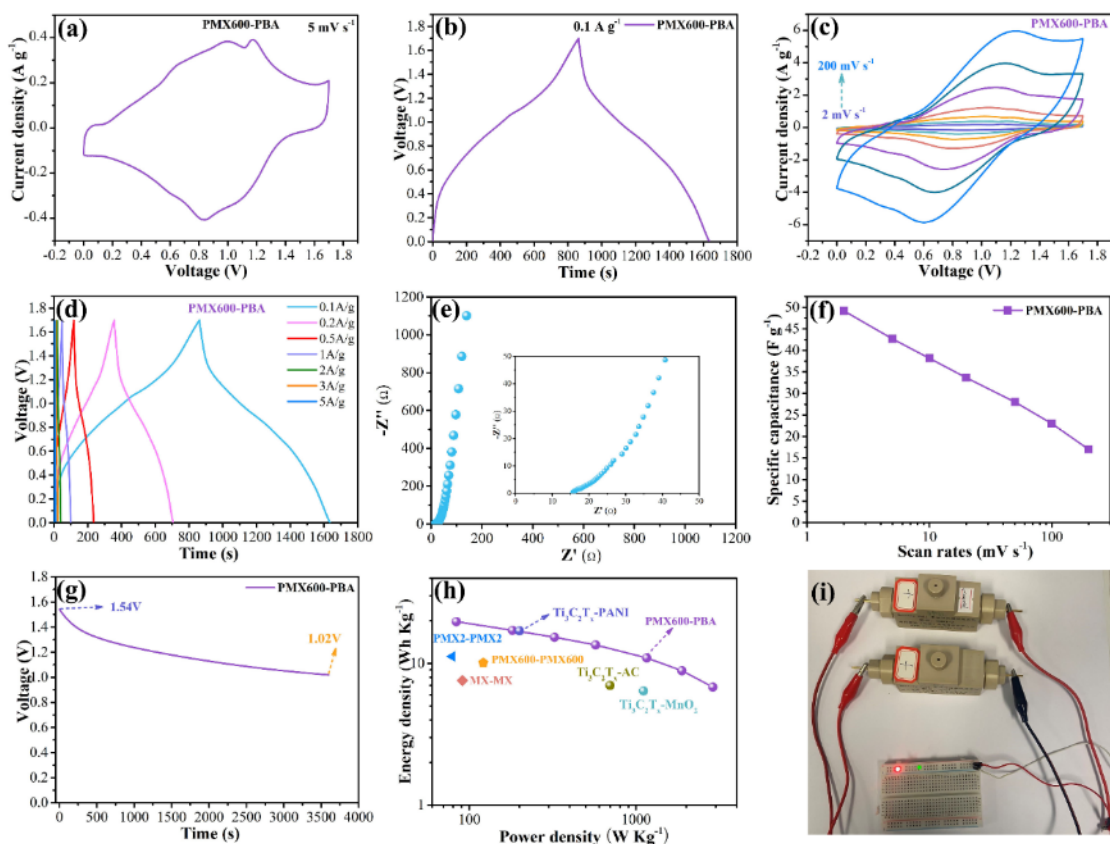


**Figure 6.15** Electrochemical performance of PMX600-PBA supercapacitors. (a) CV curve at  $5 \text{ mV s}^{-1}$  and GCD plot at  $0.1 \text{ A g}^{-1}$  of the assembled device. (c) CV curves of the device at scan rates from 2 to  $200 \text{ mV s}^{-1}$ , and (d) GCD curves at current density from 0.1 to  $5 \text{ A g}^{-1}$  for the supercapacitor. (e) EIS spectra for the PMX600-PBA supercapacitor. (f) Specific capacitance vs. scan rates for the device. (g) the plot of open circuit potential vs. time for the device. (h) Ragone plots of the energy density vs. power density for PMX600-PBA supercapacitor and other reported device. (i) The photo of two in-series PMX60-PBA devices lighting a red and a green LED bulb.



### 6.3 Conclusions

In summary, we have demonstrated a novel optimized strategy that combines removing surface -F groups, adding more -O on MXene and narrowing interlayer space to boost MXene supercapacitors applications. The modified MXene not only exhibits an enhanced capacity of  $375 \text{ F g}^{-1}$  ( $338 \text{ C g}^{-1}$ ) at  $2 \text{ mVs}^{-1}$  along with a new pair of redox peaks, but also shows much ameliorative oxidation resistance ability and outstanding cyclic stability. Multiple *ex situ* and *in situ* characterization methods reveals that the ameliorative energy storage ability is due to monolayer interstitial water, which boost proton transport into interlayer space and strengthen host-ion interaction, contributing to charge storage. The rich surface oxygen groups and strengthen chemical bonds in modified MXene are responsible for its much superior oxidation resistance ability to pristine MXene. In addition, it is uncovered that energy storage in the modified samples can be divided into two stages that protons intercalation proceeds with Grotthuss mechanism at high potential range and intercalation pseudo capacitance is shown in lower potential ranges. Eventually the assembled asymmetric supercapacitor with modified PMX600 and PBA can deliver a maximum energy density of  $19.7 \text{ Wh Kg}^{-1}$ , proving its good prospect for practical application. This work demonstrates a new strategy to boost energy storage ability of MXene and intensify its oxidation resistance ability, which is promising for its practical applications.

## Chapter 7 Conclusions and Prospect

### 7.1 Conclusions

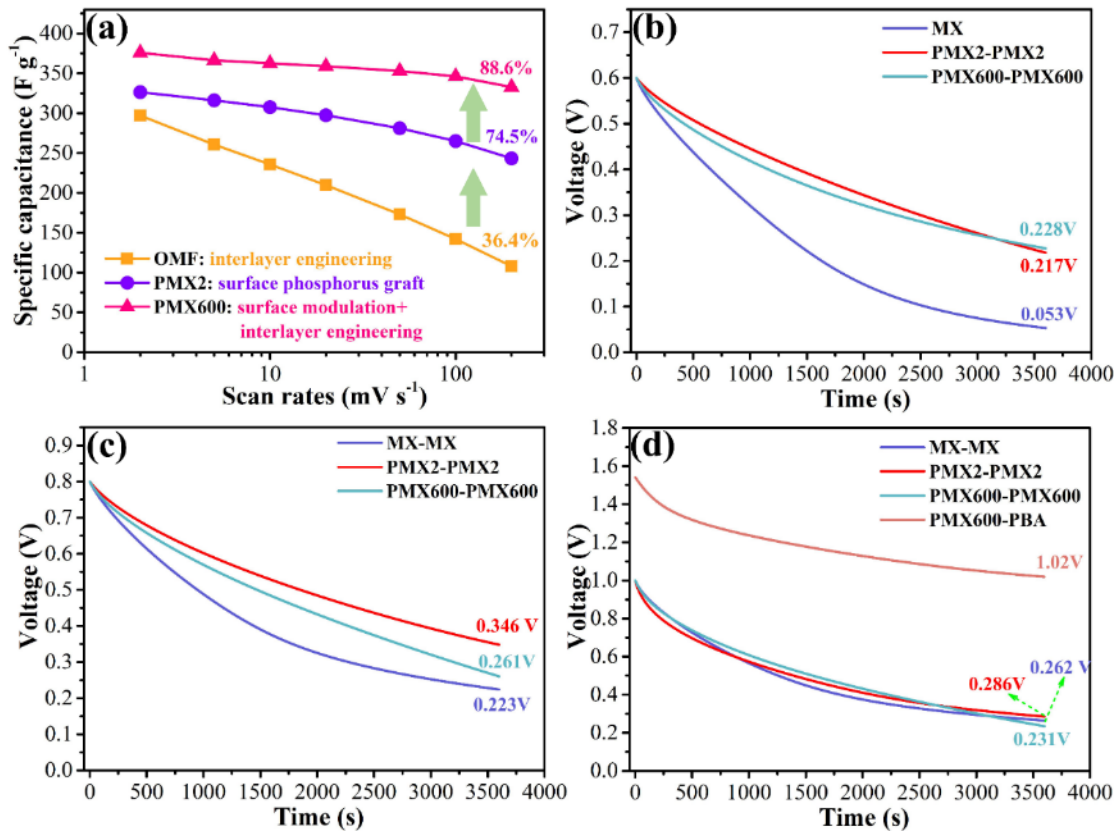


**Figure 7.1** (a) Rate capability of OMF, PMX2, PMX600. (b)-(c) Self-discharge behavior of MX-, PMX2- and PMX600-based symmetric supercapacitors with voltage windows of 0.6 V (b) and 0.8 V (c). (d) The plots of open-circuit potential vs. time for MX, PMX2 and PMX600-based symmetric supercapacitors with 1V voltage window and PMX600-PBA asymmetric supercapacitor.

This research focuses on the modulation of  $\text{Ti}_3\text{C}_2\text{T}_x$  MXene from the perspective of (1) optimization of interlayer path, (2) surface phosphorus doping and (3) simultaneous modulation of interlayer path and surface groups. With three strategies, the specific capacitance of MXene shows a step-by-step improvement as shown in **Figure 7.1a**. In addition, both second and third strategies can not only improve the capacitance of

$Ti_3C_2T_x$  MXene, but also resist its self-discharge behavior (**Figure 7.1b-c**). To boost the practical application of  $Ti_3C_2T_x$ , the PMX600-PBA asymmetric supercapacitor was assembled to further increase energy density and resist self-discharge behavior of  $Ti_3C_2T_x$  MXene-based supercapacitors (**Figure 7.1d**). In addition, comparison of cyclic stability (**Figure 7.2**) demonstrates that the suitable phosphorus surface doping and the combination of surface modulation and interlayer engineering would not lead to the degradation of robustness of  $Ti_3C_2T_x$  MXene. As a whole, this thesis is devoted to strengthening the energy storage ability of  $Ti_3C_2T_x$  MXene with interlayer engineering and surface modulation methods to push its practical applications. The conclusions for the three works in this research are as follows.

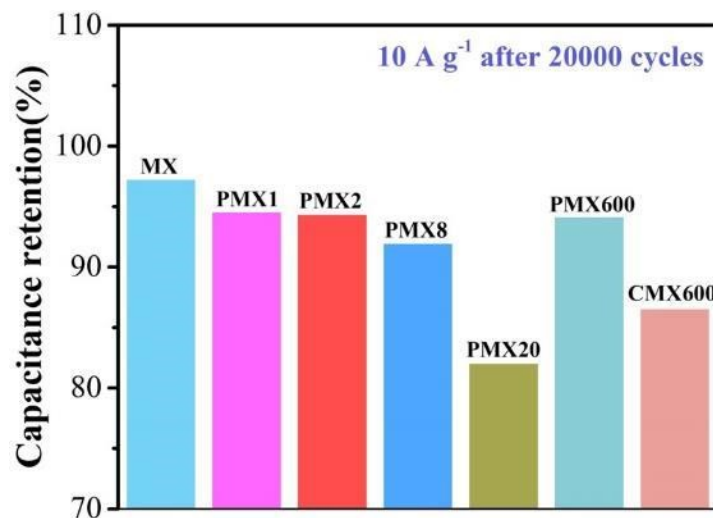


**Figure 7.2** Comparison of cyclic stability between MX and other modified samples

A facile method employing the ester reaction between ethanol and phosphoric acid to optimize the interlayer path of restacked  $Ti_3C_2T_x$  films is proposed for supercapacitor application in the first work. The optimized  $Ti_3C_2T_x$  film owns molecular scale



expanded but more uniform interlayer path as compared with pristine film, which endows it with more available active sites to electrolyte, faster ion diffusion kinetics and accelerated redox reaction kinetics, contributing to its enhanced gravimetric capacitance and rate capability. Furthermore, unlike those conventional methods that resist restacking among  $\text{Ti}_3\text{C}_2\text{T}_x$  sheets via constructing porous structure, our method introduces only mild interlayer expansion that will not decrease its volumetric capacitance. Instead, the volumetric capacitance of OMF is raised due to its improved interlayer gallery. Therefore, the proposed strategy is promising to alleviate the restacking of  $\text{Ti}_3\text{C}_2\text{T}_x$  sheets while sustaining high volumetric energy storage ability of the assembled films, capable of being extended to other assembled 2D material films for faster interlayer ion diffusion kinetics and preferable energy storage ability.

Then, I demonstrate that grafting phosphorus atoms onto  $\text{Ti}_3\text{C}_2\text{T}_x$  surface through oxygen bridging to form Ti-O-P surface terminations can boost its capacitance for supercapacitor application in the second work. The underlying improvement mechanism is also revealed. The resultant PMX2 exhibits enhanced EC performance than pristine MXene and delivers the highest capacitance of  $348 \text{ F g}^{-1}$  at  $2 \text{ mV s}^{-1}$  in  $1 \text{ M H}_2\text{SO}_4$  aqueous electrolyte along with excellent stability (94.3% capacitance retention after 20,000 cycles). The surface doped phosphorus atoms on  $\text{Ti}_3\text{C}_2\text{T}_x$  MXene serve as new active sites for two-proton bonding-debonding, contributing to more charge transfer and the improved energy storage ability in P-doped  $\text{Ti}_3\text{C}_2\text{T}_x$  MXene. In addition,



experimental and DFT calculation results suggest that high phosphorus surface doping would damage crystal structure of MXene, explaining why the specific capacitance of MXene cannot be further enhanced by merely increasing doping amount of P. It is believed that this work paves a way for doping MXene with other heteroatoms to achieve performance modulation.

In the third work, I demonstrate a novel optimization strategy that combines removing surface -F groups, adding more -O on MXene surface and narrowing interlayer space to boost its supercapacitor applications. The modified MXene not only exhibits an enhanced capacity of  $375 \text{ F g}^{-1}$  ( $338 \text{ C g}^{-1}$ ) at  $2 \text{ mVs}^{-1}$  along with a new pair of redox peaks, but also shows much ameliorative oxidation resistance ability and outstanding cyclic stability. Multiple *ex situ* and *in situ* characterizations reveal that the ameliorated energy storage ability is due to monolayer interstitial water, which boosts proton transport into interlayer space and strengthens host-ion interaction, synergistically contributing to its charge storage. And the rich surface oxygen groups and strengthened chemical bonds in modified MXene are responsible for the much superior oxidation resistance ability to pristine MXene. In addition, it is uncovered that energy storage in the modified samples can be divided into two stages, i.e., proton intercalation with Grotthuss mechanism at high potential range and intercalative pseudo capacitance in low potential range. Eventually the assembled asymmetric supercapacitor with modified PMX600 and PBA can deliver a maximum energy density of  $19.7 \text{ Wh Kg}^{-1}$ .



This work demonstrates a new strategy to boost energy storage ability of MXene and intensify its oxidation resistance ability, which is promising for its practical applications.

## 7.2 Prospects

Though PMX600 shows improvement in both capacitance and oxidation resistance, it still has the following issues that need further exploration.

- (1) What specific redox reactions contribute to its new redox peaks? *In situ* Raman and XPS may be applied to solve the problem.
- (2) The proton intercalation behavior within PMX600 and MX should be further compared through *in situ* XRD measurements and electrochemical quartz crystal microbalance (EQCM).
- (3) DFT calculation and extra experiments are needed to uncover the origin of the much-enhanced oxidation resistance ability in PMX600.

In addition, the electrochemical performance of PBA is lower than that of relevant literature, optimization of its synthesis is hence required for assembling a new PMX600-PBA supercapacitor with superior energy storage ability to the current one.

MXene is good storage media of protons thus could be a promising material for proton batteries. With the current strategies, the proton storage ability can be boosted. It is expected that the modified strategy reported here can also boost MXene application in



proton batteries, which will be further verified in my postdoc work.

## References

- [1] J. M. Chen, *Innovation (Camb)* **2021**, 2, 100127.
- [2] V. Smil, *Encyclopedia of Energy* **2004**, 6.
- [3] B. U. Haq and S. R. Schutter, *Science* **2008**, 322, 64.
- [4] Z. Liu, Z. Deng, G. He, H. Wang, X. Zhang, J. Lin, Y. Qi and X. Liang, *Nature Reviews Earth & Environment* **2021**, 3, 141.
- [5] J. Zhao, A. K. Patwary, A. Qayyum, M. Alharthi, F. Bashir, M. Mohsin, I. Hanif and Q. Abbas, *Energy* **2022**, 238.
- [6] A. González, E. Goikolea, J. A. Barrena and R. Mysyk, *Renewable and Sustainable Energy Reviews* **2016**, 58, 1189.
- [7] P. Simon and Y. Gogotsi, *Nat. Mater.* **2020**, 19, 1151.
- [8] L. M. Da Silva, R. Cesar, C. M. R. Moreira, J. H. M. Santos, L. G. De Souza, B. M. Pires, R. Vicentini, W. Nunes and H. Zanin, *Energy Storage Materials* **2020**, 27, 555.
- [9] Y. Ji, Z. W. Yin, Z. Yang, Y. P. Deng, H. Chen, C. Lin, L. Yang, K. Yang, M. Zhang, Q. Xiao, J. T. Li, Z. Chen, S. G. Sun and F. Pan, *Chem. Soc. Rev.* **2021**, 50, 10743.
- [10] Q. Li, H. Li, Q. Xia, Z. Hu, Y. Zhu, S. Yan, C. Ge, Q. Zhang, X. Wang, X. Shang, S. Fan, Y. Long, L. Gu, G. X. Miao, G. Yu and J. S. Moosera, *Nat. Mater.* **2021**, 20, 76.
- [11] Y. Shao, M. F. El-Kady, J. Sun, Y. Li, Q. Zhang, M. Zhu, H. Wang, B. Dunn and R. B. Kaner, *Chem Rev* **2018**, 118, 9233.
- [12] I. H. Panhwar, K. Ahmed, M. Seyedmahmoudian, A. Stojcevski, B. Horan, S. Mekhilef, A. Aslam and M. Asghar, *IEEE Access* **2020**, 8, 189747.
- [13] R. Kořtz and M. Carlen, *Electrochimica Acta* **2000**, 45, 2483.
- [14] W. C. de Carvalho, R. P. Bataglioli, R. A. S. Fernandes and D. V. Coury, *Electric Power Systems Research* **2020**, 184.
- [15] S. Fleischmann, Y. Zhang, X. Wang, P. T. Cummings, J. Wu, P. Simon, Y. Gogotsi, V. Presser and V. Augustyn, *Nat. Energy* **2022**, 7, 222.
- [16] C. Zhong, Y. Deng, W. Hu, J. Qiao, L. Zhang and J. Zhang, *Chem. Soc. Rev.* **2015**, 44, 7484.
- [17] W. Lu, J. Shen, P. Zhang, Y. Zhong, Y. Hu and X. W. D. Lou, *Angew. Chem. Int. Ed. Engl.* **2019**, 58, 15441.
- [18] Q. Jiang, N. Kurra, M. Alhabeib, Y. Gogotsi and H. N. Alshareef, *Adv. Energy Mater.* **2018**, 8, 1703043.
- [19] H. Jin, L. Zhou, C. L. Mak, H. Huang, W. M. Tang and H. L. Wa Chan, *J. Mater. Chem. A* **2015**, 3, 15633.
- [20] Y. Liu, N. Fu, G. Zhang, M. Xu, W. Lu, L. Zhou and H. Huang, *Adv. Funct. Mater.* **2017**, 27.
- [21] X. Su, Q. He, Y.-e. Yang, G. Cheng, D. Dang and L. Yu, *Diamond Relat. Mater.* **2021**, 114.
- [22] K. Li, X. Wang, X. Wang, M. Liang, V. Nicolosi, Y. Xu and Y. Gogotsi, *Nano Energy* **2020**, 75.
- [23] M. Boota and Y. Gogotsi, *Adv. Energy Mater.* **2019**, 9.
- [24] Y. Gogotsi and B. Anasori, *ACS Nano* **2019**, 13, 8491.
- [25] M. Naguib, M. Kurtoglu, V. Presser, J. Lu, J. Niu, M. Heon, L. Hultman, Y. Gogotsi and M. W. Barsoum, *Adv. Mater.* **2011**, 23, 4248.



- [26] M. Hu, H. Zhang, T. Hu, B. Fan, X. Wang and Z. Li, *Chem. Soc. Rev.* **2020**, 49, 6666.
- [27] S. Wan, X. Li, Y. Chen, N. Liu, Y. Du, S. Dou, L. Jiang and Q. Cheng, *Science* **2021**, 374.
- [28] H. Shao, K. Xu, Y.-C. Wu, A. Iadecola, L. Liu, H. Ma, L. Qu, E. Raymundo-Piñero, J. Zhu, Z. Lin, P.-L. Taberna and P. Simon, *ACS Energy Lett.* **2020**, 5, 2873.
- [29] X. Mu, D. Wang, F. Du, G. Chen, C. Wang, Y. Wei, Y. Gogotsi, Y. Gao and Y. Dall'Agnese, *Adv. Funct. Mater.* **2019**, 29, 1902953.
- [30] A. Qian, J. Y. Seo, H. Shi, J. Y. Lee and C. H. Chung, *ChemSusChem* **2018**, 11, 3719.
- [31] Y. Wang, X. Wang, X. Li, Y. Bai, H. Xiao, Y. Liu, R. Liu and G. Yuan, *Adv. Funct. Mater.* **2019**, 29.
- [32] E. Kim, B.-J. Lee, K. Maleski, Y. Chae, Y. Lee, Y. Gogotsi and C. W. Ahn, *Nano Energy* **2021**, 81.
- [33] P. Zhang, Q. Zhu, R. A. Soomro, S. He, N. Sun, N. Qiao and B. Xu, *Adv. Funct. Mater.* **2020**, 30.
- [34] Y. Deng, T. Shang, Z. Wu, Y. Tao, C. Luo, J. Liang, D. Han, R. Lyu, C. Qi, W. Lv, F. Kang and Q. H. Yang, *Adv. Mater.* **2019**, 31, 1902432.
- [35] A. Saha, N. Shpigel, Rosy, N. Leifer, S. Taragin, T. Sharabani, H. Aviv, I. Perelshtein, G. D. Nessim, M. Noked and Y. Gogotsi, *Adv. Funct. Mater.* **2021**, 31.
- [36] X. Chen, Y. Zhu, M. Zhang, J. Sui, W. Peng, Y. Li, G. Zhang, F. Zhang and X. Fan, *ACS Nano* **2019**, 13, 9449.
- [37] Y. Wen, T. E. Rufford, X. Chen, N. Li, M. Lyu, L. Dai and L. Wang, *Nano Energy* **2017**, 38, 368.
- [38] C. Yang, Y. Tang, Y. Tian, Y. Luo, M. Faraz Ud Din, X. Yin and W. Que, *Adv. Energy Mater.* **2018**, 8.
- [39] Y. Wen, R. Li, J. Liu, Z. Wei, S. Li, L. Du, K. Zu, Z. Li, Y. Pan and H. Hu, *J. Colloid Interface Sci.* **2021**, 604, 239.
- [40] M. Q. Zhao, C. E. Ren, Z. Ling, M. R. Lukatskaya, C. Zhang, K. L. Van Aken, M. W. Barsoum and Y. Gogotsi, *Adv. Mater.* **2015**, 27, 339.
- [41] M. Hu, R. Cheng, Z. Li, T. Hu, H. Zhang, C. Shi, J. Yang, C. Cui, C. Zhang, H. Wang, B. Fan, X. Wang and Q. H. Yang, *Nanoscale* **2020**, 12, 763.
- [42] C. Lu, L. Yang, B. Yan, L. Sun, P. Zhang, W. Zhang and Z. Sun, *Adv. Funct. Mater.* **2020**, 30, 2000852.
- [43] L. Liao, D. Jiang, K. Zheng, M. Zhang and J. Liu, *Adv. Funct. Mater.* **2021**, 31, 2103960.
- [44] Y. Sun, C. Zhan, P. R. C. Kent, M. Naguib, Y. Gogotsi and D. E. Jiang, *ACS Appl. Mater. Interfaces* **2020**, 12, 763.
- [45] Z. Wang, Z. Xu, H. Huang, X. Chu, Y. Xie, D. Xiong, C. Yan, H. Zhao, H. Zhang and W. Yang, *ACS Nano* **2020**, 14, 4916.
- [46] G. Wang, L. Zhang and J. Zhang, *Chem. Soc. Rev.* **2012**, 41, 797.
- [47] J. Liu, J. Wang, C. Xu, H. Jiang, C. Li, L. Zhang, J. Lin and Z. X. Shen, *Adv Sci (Weinh)* **2018**, 5, 1700322.
- [48] A. Muzaffar, M. B. Ahamed, K. Deshmukh and J. Thirumalai, *Renewable and Sustainable Energy Reviews* **2019**, 101, 123.
- [49] I. I. Gurten Inal and Z. Aktas, *Appl. Surf. Sci.* **2020**, 514.



- [50] B. Xu, Y. Chen, G. Wei, G. Cao, H. Zhang and Y. Yang, *Mater. Chem. Phys.* **2010**, 124, 504.
- [51] G. Xu, C. Zheng, Q. Zhang, J. Huang, M. Zhao, J. Nie, X. Wang and F. Wei, *Nano Research* **2011**, 4, 870.
- [52] L. Yu, L. Hu, B. Anasori, Y.-T. Liu, Q. Zhu, P. Zhang, Y. Gogotsi and B. Xu, *ACS Energy Lett.* **2018**, 3, 1597.
- [53] H. Pan, J. Li and Y. Feng, *Nanoscale Res Lett* **2010**, 5, 654.
- [54] J. Chmiola, C. Largeot, P. L. Taberna, P. Simon and Y. Gogotsi, *Science* **2010**, 328, 480.
- [55] M. Heon, S. Lofland, J. Applegate, R. Nolte, E. Cortes, J. D. Hettinger, P.-L. Taberna, P. Simon, P. Huang, M. Brunet and Y. Gogotsi, *Energy Environ. Sci.* **2011**, 4, 135.
- [56] M. F. El-Kady and R. B. Kaner, *Nat Commun* **2013**, 4, 1475.
- [57] M. Reina, A. Scalia, G. Auxilia, M. Fontana, F. Bella, S. Ferrero and A. Lamberti, *Advanced Sustainable Systems* **2021**, 6.
- [58] P. Simon and A. Burke, *The Electrochemical Society Interface* **2008**, 17, 38.
- [59] P. Simon and Y. Gogotsi, *Nat. Mater.* **2008**, 7, 845.
- [60] A. G. Pandolfo and A. F. Hollenkamp, *J. Power Sources* **2006**, 157, 11.
- [61] X. L. Chen, W. S. Li, C. L. Tan, W. Li and Y. Z. Wu, *J. Power Sources* **2008**, 184, 668.
- [62] Y. S. Yun, G. Yoon, K. Kang and H.-J. Jin, *Carbon* **2014**, 80, 246.
- [63] Z. G. Cambaz, G. N. Yushin, Y. Gogotsi, K. L. Vyshnyakova and L. N. Pereselentseva, *J. Am. Ceram. Soc.* **2006**, 89, 509.
- [64] Y. Gogotsi, A. Nikitin, H. Ye, W. Zhou, J. E. Fischer, B. Yi, H. C. Foley and M. W. Barsoum, *Nat. Mater.* **2003**, 2, 591.
- [65] Y. Zhao, W. Wang, D.-B. Xiong, G. Shao, W. Xia, S. Yu and F. Gao, *Int. J. Hydrogen Energy* **2012**, 37, 19395.
- [66] A. E. Kravchik, J. A. Kukushkina, V. V. Sokolov and G. F. Tereshchenko, *Carbon* **2006**, 44, 3263.
- [67] J. Chmiola, G. Yushin, Y. Gogotsi, C. Portet, P. Simon and P. L. Taberna, *Science* **2006**, 313, 1760.
- [68] Y. B. Tan and J.-M. Lee, *J. Mater. Chem. A* **2013**, 1.
- [69] K. S. Novoselov, A. K. Geim, S. V. Morozov, D. Jiang, Y. Zhang, S. V. Dubonos, I. V. Grigorieva and A. A. Firsov, *Science* **2004**, 306, 666.
- [70] H. Kim, I. Song, C. Park, M. Son, M. Hong, Y. Kim, J. S. Kim, H.-J. Shin, J. Baik and H. C. Choi, *ACS Nano* **2013**, 7, 6575.
- [71] S. Pei, Q. Wei, K. Huang, H. M. Cheng and W. Ren, *Nat Commun* **2018**, 9, 145.
- [72] Y. Zhu, S. Murali, M. D. Stoller, K. J. Ganesh, W. Cai, P. J. Ferreira, A. Pirkle, R. M. Wallace, K. A. Cychoz, M. Thommes, D. Su, E. A. Stach and R. S. Ruoff, *Science* **2011**, 332, 1537.
- [73] X. He, H. Ma, J. Wang, Y. Xie, N. Xiao and J. Qiu, *J. Power Sources* **2017**, 357, 41.
- [74] Y. Shao, M. F. El-Kady, C. W. Lin, G. Zhu, K. L. Marsh, J. Y. Hwang, Q. Zhang, Y. Li, H. Wang and R. B. Kaner, *Adv. Mater.* **2016**, 28, 6719.
- [75] S. R. C. Vivekchand, C. S. Rout, K. S. Subrahmanyam, A. Govindaraj and C. N. R. Rao, *Journal of Chemical Sciences* **2008**, 120, 9.
- [76] C. Liu, Z. Yu, D. Neff, A. Zhamu and B. Z. Jang, *Nano Lett.* **2010**, 10, 4863.
- [77] C. Prehal, C. Koczwarra, N. Jäckel, A. Schreiber, M. Burian, H. Amenitsch, M. A. Hartmann, V.



- Presser and O. Paris, *Nat. Energy* **2017**, 2.
- [78] Alexander C. Forse, John M. Griffin, C. Merlet, J. Carretero-Gonzalez, A.-Rahman O. Raji, Nicole M. Trease and Clare P. Grey, *Nat. Energy* **2017**, 2.
- [79] A. C. Forse, C. Merlet, J. M. Griffin and C. P. Grey, *J. Am. Chem. Soc.* **2016**, 138, 5731.
- [80] J. M. Griffin, A. C. Forse, W. Y. Tsai, P. L. Taberna, P. Simon and C. P. Grey, *Nat. Mater.* **2015**, 14, 812.
- [81] C. Merlet, B. Rotenberg, P. A. Madden, P. L. Taberna, P. Simon, Y. Gogotsi and M. Salanne, *Nat. Mater.* **2012**, 11, 306.
- [82] W. Y. Tsai, P. L. Taberna and P. Simon, *J. Am. Chem. Soc.* **2014**, 136, 8722.
- [83] N. Shpigel, M. D. Levi, S. Sigalov, L. Daikhin and D. Aurbach, *Acc. Chem. Res.* **2018**, 51, 69.
- [84] N. Jäckel, P. Simon, Y. Gogotsi and V. Presser, *ACS Energy Lett.* **2016**, 1, 1262.
- [85] R. Yan, M. Antonietti and M. Oschatz, *Adv. Energy Mater.* **2018**, 8.
- [86] R. Futamura, T. Iiyama, Y. Takasaki, Y. Gogotsi, M. J. Biggs, M. Salanne, J. Segalini, P. Simon and K. Kaneko, *Nat. Mater.* **2017**, 16, 1225.
- [87] Y. M. Liu, C. Merlet and B. Smit, *ACS Cent Sci* **2019**, 5, 1813.
- [88] J. M. Black, G. Feng, P. F. Fulvio, P. C. Hillesheim, S. Dai, Y. Gogotsi, P. T. Cummings, S. V. Kalinin and N. Balke, *Adv. Energy Mater.* **2014**, 4.
- [89] V. Sudha and M. V. Sangaranarayanan, *J. Phys. Chem. B* **2002**, 106, 2699.
- [90] B. E. Conway, V. Birss and J. Wojtowicz, *J. Power Sources* **1997**, 66, 1.
- [91] J. W. Long, K. E. Swider, C. I. Merzbacher and D. R. Rolison, *Langmuir* **1999**, 15, 780.
- [92] K. Naoi and P. Simon, *The Electrochemical Society Interface* **2008**, 17, 34.
- [93] M. Toupin, T. Brousse and D. Be' langer, *Chem. Mater.* **2004**, 16, 3184.
- [94] V. Augustyn, J. Come, M. A. Lowe, J. W. Kim, P. L. Taberna, S. H. Tolbert, H. D. Abruña, P. Simon and B. Dunn, *Nat. Mater.* **2013**, 12, 518.
- [95] W. Chen, J. Gu, Q. Liu, M. Yang, C. Zhan, X. Zang, T. A. Pham, G. Liu, W. Zhang, D. Zhang, B. Dunn and Y. Morris Wang, *Nature Nanotechnology* **2022**, 17, 153.
- [96] K. Naoi, K. Kisu, E. Iwama, S. Nakashima, Y. Sakai, Y. Orikasa, P. Leone, N. Dupré, T. Brousse, P. Rozier, W. Naoi and P. Simon, *Energy & Environmental Science* **2016**, 9, 2143.
- [97] R. Amisse, M. T. Sougrati, L. Stievano, C. Davoisne, G. Dražič, B. Budič, R. Dominko and C. Masquelier, *Chem. Mater.* **2015**, 27, 4261.
- [98] M. Okubo, E. Hosono, J. Kim, M. Enomoto, N. Kojima, T. Kudo, H. Zhou and I. Honma, *Journal of the American Chemical Society* **2007**, 129, 7444.
- [99] H. S. Kim, J. B. Cook, H. Lin, J. S. Ko, S. H. Tolbert, V. Ozolins and B. Dunn, *Nat. Mater.* **2017**, 16, 454.
- [100] J. Yang, X. Xiao, P. Chen, K. Zhu, K. Cheng, K. Ye, G. Wang, D. Cao and J. Yan, *Nano Energy* **2019**, 58, 455.
- [101] J. B. Mitchell, N. R. Geise, A. R. Paterson, N. C. Osti, Y. Sun, S. Fleischmann, R. Zhang, L. A. Madsen, M. F. Toney, D.-e. Jiang, A. I. Kolesnikov, E. Mamontov and V. Augustyn, *ACS Energy Lett.* **2019**, 4, 2805.
- [102] S. Boyd, K. Ganeshan, W. Y. Tsai, T. Wu, S. Saeed, D. E. Jiang, N. Balke, A. C. T. van Duin and V. Augustyn, *Nat. Mater.* **2021**, 20, 1689.
- [103] P. Ball, *Nat. Mater.* **2021**, 20, 1588.



- [104] X. Wu, J. J. Hong, W. Shin, L. Ma, T. Liu, X. Bi, Y. Yuan, Y. Qi, T. W. Surta, W. Huang, J. Neufeind, T. Wu, P. A. Greaney, J. Lu and X. Ji, *Nat. Energy* **2019**, 4, 123.
- [105] S. Dong, N. Lv, Y. Wu, G. Zhu and X. Dong, *Adv. Funct. Mater.* **2021**, 31.
- [106] Y. Li, H. Shao, Z. Lin, J. Lu, L. Liu, B. Duployer, P. O. A. Persson, P. Eklund, L. Hultman, M. Li, K. Chen, X. H. Zha, S. Du, P. Rozier, Z. Chai, E. Raymundo-Pinero, P. L. Taberna, P. Simon and Q. Huang, *Nat. Mater.* **2020**, 19, 894.
- [107] J. Chen and P. S. Lee, *Adv. Energy Mater.* **2020**, 11.
- [108] D. Cai, B. Liu, D. Wang, L. Wang, Y. Liu, H. Li, Y. Wang, Q. Li and T. Wang, *J. Mater. Chem. A* **2014**, 2.
- [109] K. Tao, Y. Gong and J. Lin, *Nano Energy* **2019**, 55, 65.
- [110] D. W. Wang, F. Li, L. C. Yin, X. Lu, Z. G. Chen, I. R. Gentle, G. Q. Lu and H. M. Cheng, *Chemistry* **2012**, 18, 5345.
- [111] J. Joseph, R. Rajagopalan, S. S. Anoop, V. Amruthalakshmi, A. Ajay, S. V. Nair and A. Balakrishnan, *RSC Adv.* **2014**, 4, 39378.
- [112] K. Fic, G. Lota, M. Meller and E. Frackowiak, *Energy Environ. Sci.* **2012**, 5, 5842.
- [113] M. J. Deng, K. W. Chen, Y. C. Che, I. J. Wang, C. M. Lin, J. M. Chen, K. T. Lu, Y. F. Liao and H. Ishii, *ACS Appl. Mater. Interfaces* **2017**, 9, 479.
- [114] Y. Cai, B. Zhao, J. Wang and Z. Shao, *J. Power Sources* **2014**, 253, 80.
- [115] W.-H. Qu, F. Han, A.-H. Lu, C. Xing, M. Qiao and W.-C. Li, *J. Mater. Chem. A* **2014**, 2.
- [116] Z. B. Zhou, H. Matsumoto and K. Tatsumi, *Chemistry* **2004**, 10, 6581.
- [117] J. G. Huddleston, A. E. Visser, W. M. Reichert, H. D. Willauer, G. A. Broker and R. D. Rogers, *Green Chemistry* **2001**, 3, 156.
- [118] N. Handa, T. Sugimoto, M. Yamagata, M. Kikuta, M. Kono and M. Ishikawa, *J. Power Sources* **2008**, 185, 1585.
- [119] J. Feng, Y. Wang, Y. Xu, Y. Sun, Y. Tang and X. Yan, *Energy & Environmental Science* **2021**, 14, 2859.
- [120] H. Kurig, M. Vestli, K. Tönurist, A. Jänes and E. Lust, *J. Electrochem. Soc.* **2012**, 159, A944.
- [121] K. Li, J. Zhao, A. Zhussupbekova, C. E. Shuck, L. Hughes, Y. Dong, S. Barwich, S. Vaesen, I. V. Shvets, M. Mobius, W. Schmitt, Y. Gogotsi and V. Nicolosi, *Nat Commun* **2022**, 13, 6884.
- [122] H. Jin, L. Zhou, C. L. Mak, H. Huang, W. M. Tang and H. L. W. Chan, *Nano Energy* **2015**, 11, 662.
- [123] K. F. Chiu and S. H. Su, *Thin Solid Films* **2013**, 544, 144.
- [124] Z. Ma, G. Shao, Y. Fan, M. Feng, D. Shen and H. Wang, *ACS Sustainable Chemistry & Engineering* **2017**, 5, 4856.
- [125] M.-F. Hsueh, C.-W. Huang, C.-A. Wu, P.-L. Kuo and H. Teng, *J. Phys. Chem. C* **2013**, 117, 16751.
- [126] L.-Q. Fan, Q.-M. Tu, C.-L. Geng, Y.-L. Wang, S.-J. Sun, Y.-F. Huang and J.-H. Wu, *Int. J. Hydrogen Energy* **2020**, 45, 17131.
- [127] Y. Yin, J. Zhou, A. N. Mansour and X. Zhou, *J. Power Sources* **2011**, 196, 5997.
- [128] S. P. M. S. Thayyil, M. P. Pillai and T. K.K., *J. Mol. Liq.* **2019**, 294.
- [129] H. Fei, C. Yang, H. Bao and G. Wang, *J. Power Sources* **2014**, 266, 488.
- [130] H. Gao and K. Lian, *J. Electrochem. Soc.* **2013**, 160, A505.



- [131] C.-S. Lim, K. H. Teoh, C.-W. Liew and S. Ramesh, *Mater. Chem. Phys.* **2014**, 143, 661.
- [132] C.-W. Huang, C.-A. Wu, S.-S. Hou, P.-L. Kuo, C.-T. Hsieh and H. Teng, *Adv. Funct. Mater.* **2012**, 22, 4677.
- [133] G. Ayalneh Tiruye, D. Muñoz-Torrero, J. Palma, M. Anderson and R. Marcilla, *J. Power Sources* **2015**, 279, 472.
- [134] N. Shirshova, A. Bismarck, S. Carreyette, Q. P. V. Fontana, E. S. Greenhalgh, P. Jacobsson, P. Johansson, M. J. Marczewski, G. Kalinka, A. R. J. Kucernak, J. Scheers, M. S. P. Shaffer, J. H. G. Steinke and M. Wienrich, *J. Mater. Chem. A* **2013**, 1.
- [135] H. Zhou, H. Li, L. Li, T. Liu, G. Chen, Y. Zhu, L. Zhou and H. Huang, *Materials Today Energy* **2022**, 24, 100924.
- [136] S. T. Senthilkumar, R. K. Selvan, M. Ulaganathan and J. S. Melo, *Electrochim. Acta* **2014**, 115, 518.
- [137] A. Abdisattar, M. Yeleuov, C. Daulbayev, K. Askaruly, A. Tolyzbekov, A. Taurbekov and N. Prikhodko, *Electrochem. Commun.* **2022**, 142.
- [138] A. Davies, P. Audette, B. Farrow, F. Hassan, Z. Chen, J.-Y. Choi and A. Yu, *J. Phys. Chem. C* **2011**, 115, 17612.
- [139] J. Xiao, S. Yang, L. Wan, F. Xiao and S. Wang, *J. Power Sources* **2014**, 245, 1027.
- [140] M. R. Lukatskaya, S. Kota, Z. Lin, M.-Q. Zhao, N. Shpigel, M. D. Levi, J. Halim, P.-L. Taberna, M. W. Barsoum, P. Simon and Y. Gogotsi, *Nat. Energy* **2017**, 2, 17105.
- [141] X. Wang, L. Dong, W. Liu, Y. Huang, X. Pu, J. Wang, F. Kang, J. Li and C. Xu, *Journal of Energy Chemistry* **2020**, 48, 233.
- [142] K. Tönurist, T. Thomberg, A. Jänes, I. Kink and E. Lust, *Electrochem. Commun.* **2012**, 22, 77.
- [143] W. Cao, Y. Li, B. Fitch, J. Shih, T. Doung and J. Zheng, *J. Power Sources* **2014**, 268, 841.
- [144] Y. M. Shulga, S. A. Baskakov, V. A. Smirnov, N. Y. Shulga, K. G. Belay and G. L. Gutsev, *J. Power Sources* **2014**, 245, 33.
- [145] C. N. Rao, A. K. Sood, K. S. Subrahmanyam and A. Govindaraj, *Angew. Chem. Int. Ed. Engl.* **2009**, 48, 7752.
- [146] M. Guo, W.-C. Geng, C. Liu, J. Gu, Z. Zhang and Y. Tang, *Chem. Mater.* **2020**, 32, 8257.
- [147] L. Xiu, Z. Wang, M. Yu, X. Wu and J. Qiu, *ACS Nano* **2018**, 12, 8017.
- [148] F. Shahzad, M. Alhabeab, C. B. Hatter, B. Anasori, S. Hong, C. Koo and Y. Gogotsi, *science* **2016**, 353.
- [149] Q. Tang, Z. Zhou and P. Shen, *J. Am. Chem. Soc.* **2012**, 134, 16909.
- [150] R. Meng, J. Huang, Y. Feng, L. Zu, C. Peng, L. Zheng, L. Zheng, Z. Chen, G. Liu, B. Chen, Y. Mi and J. Yang, *Adv. Energy Mater.* **2018**, 8.
- [151] Y. Cao, Y. Zhang, H. Chen, S. Qin, L. Zhang, S. Guo and H. Yang, *Adv. Funct. Mater.* **2021**, DOI: 10.1002/adfm.202108574.
- [152] J. Shi, Y. Hou, Z. Liu, Y. Zheng, L. Wen, J. Su, L. Li, N. Liu, Z. Zhang and Y. Gao, *Nano Energy* **2022**, 91.
- [153] A. VahidMohammadi, M. Mojtavavi, N. M. Caffrey, M. Wanunu and M. Beidaghi, *Adv. Mater.* **2019**, 31, 1806931.
- [154] M. Ghidui, M. R. Lukatskaya, M. Q. Zhao, Y. Gogotsi and M. W. Barsoum, *Nature* **2014**, 516, 78.



- [155] A. Lipatov, M. Alhabebe, H. Lu, S. Zhao, M. J. Loes, N. S. Vorobeve, Y. Dall'Agnese, Y. Gao, A. Gruverman, Y. Gogotsi and A. Sinititskii, *Advanced Electronic Materials* **2020**, 6.
- [156] G. Deyscher, C. E. Shuck, K. Hantanasirisakul, N. C. Frey, A. C. Foucher, K. Maleski, A. Sarycheva, V. B. Shenoy, E. A. Stach, B. Anasori and Y. Gogotsi, *ACS Nano* **2020**, 14, 204.
- [157] A. Shayesteh Zeraati, S. A. Mirkhani, P. Sun, M. Naguib, P. V. Braun and U. Sundararaj, *Nanoscale* **2021**, 13, 3572.
- [158] V. Kamysbayev, A. S. Filatov, H. Hu, X. Rui, F. Lagunas, D. Wang, R. F. Klie and D. V. Talapin, *science* **2020**, 369.
- [159] L. Liao, D. Jiang, K. Zheng, M. Zhang and J. Liu, *Adv. Funct. Mater.* **2021**, DOI: 10.1002/adfm.202103960.
- [160] J. Yang, M. Naguib, M. Ghidui, L. M. Pan, J. Gu, J. Nanda, J. Halim, Y. Gogotsi, M. W. Barsoum and Y. Zhou, *J. Am. Ceram. Soc.* **2015**, 99, 660.
- [161] C. Wang, H. Shou, S. Chen, S. Wei, Y. Lin, P. Zhang, Z. Liu, K. Zhu, X. Guo, X. Wu, P. M. Ajayan and L. Song, *Adv. Mater.* **2021**, DOI: 10.1002/adma.202101015, e2101015.
- [162] B. Anasori, M. R. Lukatskaya and Y. Gogotsi, *Nature Reviews Materials* **2017**, 2.
- [163] J. Li, X. Yuan, C. Lin, Y. Yang, L. Xu, X. Du, J. Xie, J. Lin and J. Sun, *Adv. Energy Mater.* **2017**, 7.
- [164] H. Wang, Y. Wu, J. Zhang, G. Li, H. Huang, X. Zhang and Q. Jiang, *Mater. Lett.* **2015**, 160, 537.
- [165] J. Halim, M. R. Lukatskaya, K. M. Cook, J. Lu, C. R. Smith, L. A. Naslund, S. J. May, L. Hultman, Y. Gogotsi, P. Eklund and M. W. Barsoum, *Chem. Mater.* **2014**, 26, 2374.
- [166] O. Mashtalir, M. Naguib, V. N. Mochalin, Y. Dall'Agnese, M. Heon, M. W. Barsoum and Y. Gogotsi, *Nat Commun* **2013**, 4, 1716.
- [167] M. Alhabebe, K. Maleski, B. Anasori, P. Lelyukh, L. Clark, S. Sin and Y. Gogotsi, *Chem. Mater.* **2017**, 29, 7633.
- [168] C. J. Zhang, S. Pinilla, N. McEvoy, C. P. Cullen, B. Anasori, E. Long, S.-H. Park, A. Seral-Ascaso, A. Shmeliov, D. Krishnan, C. Morant, X. Liu, G. S. Duesberg, Y. Gogotsi and V. Nicolosi, *Chem. Mater.* **2017**, 29, 4848.
- [169] V. Natu, R. Pai, M. Sokol, M. Carey, V. Kalra and M. W. Barsoum, *Chem* **2020**, 6, 616.
- [170] T. Li, L. Yao, Q. Liu, J. Gu, R. Luo, J. Li, X. Yan, W. Wang, P. Liu, B. Chen, W. Zhang, W. Abbas, R. Naz and D. Zhang, *Angew. Chem. Int. Ed. Engl.* **2018**, 57, 6115.
- [171] J. Xuan, Z. Wang, Y. Chen, D. Liang, L. Cheng, X. Yang, Z. Liu, R. Ma, T. Sasaki and F. Geng, *Angew. Chem. Int. Ed. Engl.* **2016**, 55, 14569.
- [172] W. Sun, S. A. Shah, Y. Chen, Z. Tan, H. Gao, T. Habib, M. Radovic and M. J. Green, *J. Mater. Chem. A* **2017**, 5, 21663.
- [173] S. Yang, P. Zhang, F. Wang, A. G. Ricciardulli, M. R. Lohe, P. W. M. Blom and X. Feng, *Angew. Chem. Int. Ed. Engl.* **2018**, 57, 15491.
- [174] S. Y. Pang, Y. T. Wong, S. Yuan, Y. Liu, M. K. Tsang, Z. Yang, H. Huang, W. T. Wong and J. Hao, *J. Am. Chem. Soc.* **2019**, 141, 9610.
- [175] X. Li, M. Li, Q. Yang, G. Liang, Z. Huang, L. Ma, D. Wang, F. Mo, B. Dong, Q. Huang and C. Zhi, *Adv. Energy Mater.* **2020**, 10.
- [176] J. Chen, M. Chen, W. Zhou, X. Xu, B. Liu, W. Zhang and C. Wong, *ACS Nano* **2022**, 16, 2461.



- [177] M. Naguib, V. Presser, D. Tallman, J. Lu, L. Hultman, Y. Gogotsi, M. W. Barsoum and Y. Zhou, *J. Am. Ceram. Soc.* **2011**, 94, 4556.
- [178] H. Fashandi, M. Dahlqvist, J. Lu, J. Palisaitis, S. I. Simak, I. A. Abrikosov, J. Rosen, L. Hultman, M. Andersson, A. Lloyd Spetz and P. Eklund, *Nat. Mater.* **2017**, 16, 814.
- [179] M. Li, J. Lu, K. Luo, Y. Li, K. Chang, K. Chen, J. Zhou, J. Rosen, L. Hultman, P. Eklund, P. O. Å. Persson, S. Du, Z. Chai, Z. Huang and Q. Huang, *J. Am. Chem. Soc.* **2019**, 141, 4730.
- [180] K. Arole, J. W. Blivin, S. Saha, D. E. Holta, X. Zhao, A. Sarmah, H. Cao, M. Radovic, J. L. Lutkenhaus and M. J. Green, *iScience* **2021**, 24, 103403.
- [181] H. Jin, Q. Gu, B. Chen, C. Tang, Y. Zheng, H. Zhang, M. Jaroniec and S.-Z. Qiao, *Chem* **2020**, 6, 2382.
- [182] Z. Sun, M. Yuan, L. Lin, H. Yang, C. Nan, H. Li, G. Sun and X. Yang, *ACS Materials Letters* **2019**, 1, 628.
- [183] J. Mei, G. A. Ayoko, C. Hu, J. M. Bell and Z. Sun, *Sustainable Materials and Technologies* **2020**, 25.
- [184] L. Liang, L. Niu, T. Wu, D. Zhou and Z. Xiao, *ACS Nano* **2022**, 16, 7971.
- [185] A. E. Ghazaly, H. Ahmed, A. R. Rezk, J. Halim, P. O. Å. Persson, L. Y. Yeo and J. Rosen, *ACS Nano* **2021**, 15, 4287.
- [186] H. Shi, P. Zhang, Z. Liu, S. Park, M. R. Lohe, Y. Wu, A. Shaygan Nia, S. Yang and X. Feng, *Angew. Chem. Int. Ed. Engl.* **2021**, 60, 8689.
- [187] A. Jawaid, A. Hassan, G. Neher, D. Nepal, R. Pachter, W. J. Kennedy, S. Ramakrishnan and R. A. Vaia, *ACS Nano* **2021**, 15, 2771.
- [188] C. Xu, L. Wang, Z. Liu, L. Chen, J. Guo, N. Kang, X. L. Ma, H. M. Cheng and W. Ren, *Nat. Mater.* **2015**, 14, 1135.
- [189] D. Geng, X. Zhao, Z. Chen, W. Sun, W. Fu, J. Chen, W. Liu, W. Zhou and K. P. Loh, *Adv. Mater.* **2017**, 29.
- [190] Y. Fan, L. Li, Y. Zhang, X. Zhang, D. Geng and W. Hu, *Adv. Funct. Mater.* **2022**, 32.
- [191] Q. Jiang, Y. Lei, H. Liang, K. Xi, C. Xia and H. N. Alshareef, *Energy Storage Materials* **2020**, 27, 78.
- [192] L. Liu, M. Orbay, S. Luo, S. Duluard, H. Shao, J. Harmel, P. Rozier, P. L. Taberna and P. Simon, *ACS Nano* **2021**, DOI: 10.1021/acsnano.1c08498.
- [193] J. Ma, Y. Cheng, L. Wang, X. Dai and F. Yu, *Chem. Eng. J.* **2020**, 384.
- [194] X. Huang and P. Wu, *Adv. Funct. Mater.* **2020**, 30.
- [195] M. R. Lukatskaya, S.-M. Bak, X. Yu, X.-Q. Yang, M. W. Barsoum and Y. Gogotsi, *Adv. Energy Mater.* **2015**, 5.
- [196] Y. Dall'Agnese, M. R. Lukatskaya, K. M. Cook, P.-L. Taberna, Y. Gogotsi and P. Simon, *Electrochem. Commun.* **2014**, 48, 118.
- [197] X. Zhang, Y. Liu, S. Dong, J. Yang and X. Liu, *Electrochim. Acta* **2019**, 294, 233.
- [198] S. Li, Q. Shi, Y. Li, J. Yang, T. H. Chang, J. Jiang and P. Y. Chen, *Adv. Funct. Mater.* **2020**, 30.
- [199] M. Okubo, A. Sugahara, S. Kajiyama and A. Yamada, *Acc. Chem. Res.* **2018**, 51, 591.
- [200] C. Yang, Y. Tang, Y. Tian, Y. Luo, Y. He, X. Yin and W. Que, *Adv. Funct. Mater.* **2018**, 28.
- [201] Z. W. Gao, W. Zheng and L. Y. S. Lee, *Small* **2019**, 15, 1902649.
- [202] S.-Y. Lin and X. Zhang, *J. Power Sources* **2015**, 294, 354.



- [203] Q. Zhang, J. He, X. Fu, S. Xie, R. Fan, H. Lai, W. Cheng, P. Ji, J. Sheng, Q. Liao, W. Zhu and H. Li, *Chem. Eng. J.* **2022**, 430.
- [204] S. Xu, G. Wei, J. Li, Y. Ji, N. Klyui, V. Izotov and W. Han, *Chem. Eng. J.* **2017**, 317, 1026.
- [205] M. R. Lukatskaya, O. Mashtalir, C. E. Ren, Y. Dall'Agnese, P. Rozier, P. L. Taberna, M. Naguib, P. Simon, M. W. Barsoum and Y. Gogotsi, *Science* **2013**, 341, 1502.
- [206] K. Liang, R. A. Matsumoto, W. Zhao, N. C. Osti, I. Popov, B. P. Thapaliya, S. Fleischmann, S. Misra, K. Prenger, M. Tyagi, E. Mamontov, V. Augustyn, R. R. Unocic, A. P. Sokolov, S. Dai, P. T. Cummings and M. Naguib, *Adv. Funct. Mater.* **2021**, 31.
- [207] X. Wang, T. S. Mathis, K. Li, Z. Lin, L. Vlcek, T. Torita, N. C. Osti, C. Hatter, P. Urbankowski, A. Sarycheva, M. Tyagi, E. Mamontov, P. Simon and Y. Gogotsi, *Nat. Energy* **2019**, 4, 241.
- [208] X. Wang, T. S. Mathis, Y. Sun, W. Y. Tsai, N. Shpigel, H. Shao, D. Zhang, K. Hantanasirisakul, F. Malchik, N. Balke, D. E. Jiang, P. Simon and Y. Gogotsi, *ACS Nano* **2021**, 15, 15274.
- [209] Z. H. Fu, Q. F. Zhang, D. Legut, C. Si, T. C. Germann, T. Lookman, S. Y. Du, J. S. Francisco and R. F. Zhang, *Physical Review B* **2016**, 94.
- [210] Y. Lee, S. J. Kim, Y.-J. Kim, Y. Lim, Y. Chae, B.-J. Lee, Y.-T. Kim, H. Han, Y. Gogotsi and C. W. Ahn, *J. Mater. Chem. A* **2020**, 8, 573.
- [211] M. Zhang, X. Chen, J. Sui, B. S. Abraha, Y. Li, W. Peng, G. Zhang, F. Zhang and X. Fan, *Inorg. Chem. Front.* **2020**, 7, 1205.
- [212] H. Hwang, S. Byun, S. Yuk, S. Kim, S. H. Song and D. Lee, *Appl. Surf. Sci.* **2021**, 556.
- [213] G. Zhou, M. C. Li, C. Liu, Q. Wu and C. Mei, *Adv. Funct. Mater.* **2021**, DOI: 10.1002/adfm.202109593.
- [214] W. Tian, A. VahidMohammadi, M. S. Reid, Z. Wang, L. Ouyang, J. Erlandsson, T. Pettersson, L. Wagberg, M. Beidaghi and M. M. Hamedi, *Adv. Mater.* **2019**, 31, e1902977.
- [215] X. Wang, H. Li, H. Li, S. Lin, W. Ding, X. Zhu, Z. Sheng, H. Wang, X. Zhu and Y. Sun, *Adv. Funct. Mater.* **2020**, 30.
- [216] J. Yan, C. E. Ren, K. Maleski, C. B. Hatter, B. Anasori, P. Urbankowski, A. Sarycheva and Y. Gogotsi, *Adv. Funct. Mater.* **2017**, 27.
- [217] G. Wu, T. Li, Z. Wang, M. Li, B. Wang and A. Dong, *Angew. Chem. Int. Ed. Engl.* **2020**, 59, 20628.
- [218] A. VahidMohammadi, J. Moncada, H. Chen, E. Kayali, J. Orangi, C. A. Carrero and M. Beidaghi, *J. Mater. Chem. A* **2018**, 6, 22123.
- [219] W. Zheng, J. Halim, A. El Ghazaly, A. S. Etman, E. N. Tseng, P. O. A. Persson, J. Rosen and M. W. Barsoum, *Adv Sci (Weinh)* **2021**, 8, 2003656.
- [220] A. Al-Temimy, K. Prenger, R. Golnak, M. Lounasvuori, M. Naguib and T. Petit, *ACS Appl. Mater. Interfaces* **2020**, 12, 15087.
- [221] K. Prenger, Y. Sun, K. Ganeshan, A. Al-Temimy, K. Liang, C. Dun, J. J. Urban, J. Xiao, T. Petit, A. C. T. van Duin, D.-e. Jiang and M. Naguib, *ACS Applied Energy Materials* **2022**, DOI: 10.1021/acsaem.2c00653.
- [222] N. Sun, Z. Guan, Q. Zhu, B. Anasori, Y. Gogotsi and B. Xu, *Nanomicro Lett* **2020**, 12, 89.
- [223] A. Esfandiari, B. Radha, F. C. Wang, Q. Yang, S. Hu, S. Garaj, R. R. Nair, A. K. Geim and K. Gopinadhan, *Science* **2017**, 358, 511.
- [224] R. H. Tunuguntla, F. I. Allen, K. Kim, A. Belliveau and A. Noy, *Nat Nanotechnol* **2016**, 11, 639.



- [225] E. Kayali, A. VahidMohammadi, J. Orangi and M. Beidaghi, *ACS Appl. Mater. Interfaces* **2018**, 10, 25949.
- [226] M. Q. Zhao, X. Xie, C. E. Ren, T. Makaryan, B. Anasori, G. Wang and Y. Gogotsi, *Adv. Mater.* **2017**, 29.
- [227] X. Zhang, X. Liu, S. Dong, J. Yang and Y. Liu, *Applied Materials Today* **2019**, 16, 315.
- [228] W. Bao, X. Tang, X. Guo, S. Choi, C. Wang, Y. Gogotsi and G. Wang, *Joule* **2018**, 2, 778.
- [229] W. Yang, J. J. Byun, J. Yang, F. P. Moissinac, Y. Peng, G. Tontini, R. A. W. Dryfe and S. Barg, *Energy & Environmental Materials* **2020**, 3, 380.
- [230] X. Yang, Y. Yao, Q. Wang, K. Zhu, K. Ye, G. Wang, D. Cao and J. Yan, *Adv. Funct. Mater.* **2021**, 32, 2109479.
- [231] Z. Lin, J. Liu, W. Peng, Y. Zhu, Y. Zhao, K. Jiang, M. Peng and Y. Tan, *ACS Nano* **2020**, 14, 2109.
- [232] Z. Zhao, S. Wang, F. Wan, Z. Tie and Z. Niu, *Adv. Funct. Mater.* **2021**, 31.
- [233] Y. Xia, T. S. Mathis, M.-Q. Zhao, B. Anasori, A. Dang, Z. Zhou, H. Cho, Y. Gogotsi and S. Yang, *Nature* **2018**, 557, 409.
- [234] J. Tang, T. Mathis, X. Zhong, X. Xiao, H. Wang, M. Anayee, F. Pan, B. Xu and Y. Gogotsi, *Adv. Energy Mater.* **2020**, 11, 2003025.
- [235] Y. Luo, C. Yang, Y. Tian, Y. Tang, X. Yin and W. Que, *J. Power Sources* **2020**, 450.
- [236] C. Liu, Y. Bai, W. Li, F. Yang, G. Zhang and H. Pang, *Angew. Chem. Int. Ed. Engl.* **2022**, 61, e202116282.
- [237] H. Jiang, Z. Wang, Q. Yang, M. Hanif, Z. Wang, L. Dong and M. Dong, *Electrochim. Acta* **2018**, 290, 695.
- [238] R. Zhang, J. Dong, W. Zhang, L. Ma, Z. Jiang, J. Wang and Y. Huang, *Nano Energy* **2022**, 91.
- [239] R. Zhao, M. Wang, D. Zhao, H. Li, C. Wang and L. Yin, *ACS Energy Lett.* **2017**, 3, 132.
- [240] J. Zhang, N. Kong, S. Uzun, A. Levitt, S. Seyedin, P. A. Lynch, S. Qin, M. Han, W. Yang, J. Liu, X. Wang, Y. Gogotsi and J. M. Razal, *Adv. Mater.* **2020**, 32, 2001093.
- [241] Z. Pan, F. Cao, X. Hu and X. Ji, *J. Mater. Chem. A* **2019**, 7, 8984.
- [242] G. Kresse and J. Furthmüller, *Physical review B* **1996**, 54, 11169.
- [243] G. Kresse and D. Joubert, *Physical review b* **1999**, 59, 1758.
- [244] J. P. Perdew, K. Burke and M. Ernzerhof, *Physical review letters* **1996**, 77, 3865.
- [245] A. Jain, S. P. Ong, G. Hautier, W. Chen, W. D. Richards, S. Dacek, S. Cholia, D. Gunter, D. Skinner and G. Ceder, *APL materials* **2013**, 1, 011002.
- [246] W. Tang, S. Chill and G. Henkelman, *Journal*, 1970.
- [247] K. Fan, Y. Ying, X. Luo and H. Huang, *Physical Chemistry Chemical Physics* **2020**, 22, 16665.
- [248] W. Zheng, J. Halim, Z. Sun, J. Rosen and M. W. Barsoum, *Energy Storage Materials* **2021**, 38, 438.
- [249] W. Zheng, J. Halim, J. Rosen and M. W. Barsoum, *Advanced Energy and Sustainability Research* **2021**, 3.
- [250] K. Liu, C. Yu, W. Guo, L. Ni, J. Yu, Y. Xie, Z. Wang, Y. Ren and J. Qiu, *Journal of Energy Chemistry* **2021**, 58, 94.
- [251] H. Wang, J. Chen, R. Fan and Y. Wang, *Sustainable Energy & Fuels* **2018**, 2, 2727.
- [252] L. Shi, S. Lin, L. Li, W. Wu, L. Wu, H. Gao and X. Zhang, *Ceram. Int.* **2018**, 44, 13901.



- [253] X. Wang, Q. Fu, J. Wen, X. Ma, C. Zhu, X. Zhang and D. Qi, *Nanoscale* **2018**, 10, 20828.
- [254] L. Yao, Q. Wu, P. Zhang, J. Zhang, D. Wang, Y. Li, X. Ren, H. Mi, L. Deng and Z. Zheng, *Adv. Mater.* **2018**, 30, 1706054.
- [255] D. Sheberla, J. C. Bachman, J. S. Elias, C. J. Sun, Y. Shao-Horn and M. Dinca, *Nat. Mater.* **2017**, 16, 220.
- [256] L. Qin, Y. Liu, S. Xu, S. Wang, X. Sun, S. Zhu, L. Hou and C. Yuan, *Small Methods* **2020**, 4, 2000630.
- [257] J. Liu, H. B. Zhang, R. Sun, Y. Liu, Z. Liu, A. Zhou and Z. Z. Yu, *Adv. Mater.* **2017**, 29, 1702367.
- [258] A. VahidMohammadi, J. Rosen and Y. Gogotsi, *Science* **2021**, 372, eabf1581.
- [259] X. Hui, X. Ge, R. Zhao, Z. Li and L. Yin, *Adv. Funct. Mater.* **2020**, 30, 2005190.
- [260] Y. Ando, M. Okubo, A. Yamada and M. Otani, *Adv. Funct. Mater.* **2020**, 30, 2000820.
- [261] F. Han, S. Luo, L. Xie, J. Zhu, W. Wei, X. Chen, F. Liu, W. Chen, J. Zhao, L. Dong, K. Yu, X. Zeng, F. Rao, L. Wang and Y. Huang, *ACS Appl. Mater. Interfaces* **2019**, 11, 8443.
- [262] L. Popovi, D. de Waal and J. C. A. Boeyens, *J. Raman Spectrosc.* **2005**, 36, 2.
- [263] G. Lv, J. Wang, Z. Shi and L. Fan, *Mater. Lett.* **2018**, 219, 45.
- [264] H. Sun, L. Zhang, W. Xia, L. Chen, Z. Xu and W. Zhang, *Appl. Phys. A* **2016**, 122.
- [265] R. K. Brow, *J. Non-Cryst. Solids* **1996**, 194, 267.
- [266] M. Han, X. Yin, H. Wu, Z. Hou, C. Song, X. Li, L. Zhang and L. Cheng, *ACS Appl. Mater. Interfaces* **2016**, 8, 21011.
- [267] M. Halim, K. Lukatskaya, J. L. Cook, S. CR, N. L-Å and M. SJ, *Chem. Mater* **2014**, 26, 2374.
- [268] J. Halim, K. M. Cook, M. Naguib, P. Eklund, Y. Gogotsi, J. Rosen and M. W. Barsoum, *Appl. Surf. Sci.* **2016**, 362, 406.
- [269] Y. Wang, X. Wang, X. Li, X. Li, Y. Liu, Y. Bai, H. Xiao and G. Yuan, *Adv. Funct. Mater.* **2020**, 31, 2008185.
- [270] Z. Fan, J. Yan, T. Wei, L. Zhi, G. Ning, T. Li and F. Wei, *Adv. Funct. Mater.* **2011**, 21, 2366.
- [271] H. Li, R. Chen, M. Ali, H. Lee and M. J. Ko, *Adv. Funct. Mater.* **2020**, 30, 2002739.
- [272] F. Ran, T. Wang, S. Chen, Y. Liu and L. Shao, *Appl. Surf. Sci.* **2020**, 511, 145627.
- [273] X. Zhang, Y. Liu, S. Dong, J. Yang and X. Liu, *J. Alloys Compd.* **2019**, 790, 517.
- [274] S. Fleischmann, J. B. Mitchell, R. Wang, C. Zhan, D. E. Jiang, V. Presser and V. Augustyn, *Chem Rev* **2020**, 120, 6738.
- [275] Y. Wei, P. Zhang, R. A. Soomro, Q. Zhu and B. Xu, *Adv. Mater.* **2021**, 33, 2103148.
- [276] M. Benchakar, L. Loupias, C. Garnero, T. Bilyk, C. Morais, C. Canaff, N. Guignard, S. Morisset, H. Pazniak, S. Hurand, P. Chartier, J. Pacaud, V. Mauchamp, M. W. Barsoum, A. Habrioux and S. Célérier, *Appl. Surf. Sci.* **2020**, 530.
- [277] T. Schultz, N. C. Frey, K. Hantanasirisakul, S. Park, S. J. May, V. B. Shenoy, Y. Gogotsi and N. Koch, *Chem. Mater.* **2019**, 31, 6590.
- [278] M. Fatima, J. Fatheema, N. B. Monir, A. H. Siddique, B. Khan, A. Islam, D. Akinwande and S. Rizwan, *Front Chem* **2020**, 8, 168.
- [279] H. Li, H. Zhou, L. Zhuang, T. Liu, W. Han and H. Huang, *Advanced Energy and Sustainability Research* **2022**, 3, 2100216.
- [280] W. Liu, Y. Zheng, Z. Zhang, Y. Zhang, Y. Wu, H. Gao, J. Su and Y. Gao, *J. Power Sources* **2022**, 521.



- [281] M. Naguib, O. Mashtalir, J. Carle, V. Presser, J. Lu, L. Hultman, Y. Gogotsi and M. W. Barsoum, *ACS Nano* **2012**, 6, 1332.
- [282] H. Pazniak, M. Benchakar, T. Bilyk, A. Liedl, Y. Busby, C. Noel, P. Chartier, S. Hurand, M. Marteau, L. Houssiau, R. Larciprete, P. Lacovig, D. Lizzit, E. Tosi, S. Lizzit, J. Pacaud, S. Celerier, V. Mauchamp and M. L. David, *ACS Nano* **2021**, 15, 4245.
- [283] J. L. Hart, K. Hantanasirisakul, A. C. Lang, B. Anasori, D. Pinto, Y. Pivak, J. T. van Omme, S. J. May, Y. Gogotsi and M. L. Taheri, *Nat Commun* **2019**, 10, 522.
- [284] V. Natu, M. Benchakar, C. Canaff, A. Habrioux, S. Célérier and M. W. Barsoum, *Matter* **2021**, 4, 1224.
- [285] F. Zhou, X.-S. Yang, J. Liu, J. Liu, R. Hu, L. Ouyang and M. Zhu, *J. Power Sources* **2021**, 485.
- [286] A. Sarycheva and Y. Gogotsi, *Chem. Mater.* **2020**, 32, 3480.
- [287] N. Zhao, Y. Yang, D. Yi, Y. Xiao, K. Wang, W. Cui and X. Wang, *Chem. Eng. J.* **2021**, 422.
- [288] C. Yang, W. Que, Y. Tang, Y. Tian and X. Yin, *J. Electrochem. Soc.* **2017**, 164, A1939.
- [289] P. Salles, D. Pinto, K. Hantanasirisakul, K. Maleski, C. E. Shuck and Y. Gogotsi, *Adv. Funct. Mater.* **2019**, 29.
- [290] Y. Tang, Y. Zhang, O. I. Malyi, N. Bucher, H. Xia, S. Xi, Z. Zhu, Z. Lv, W. Li, J. Wei, M. Srinivasan, A. Borgna, M. Antonietti, Y. Du and X. Chen, *Adv. Mater.* **2018**, 30, 1802200.
- [291] S. Mahala, K. Khosravinia and A. Kiani, *Journal of Energy Storage* **2023**, 67.
- [292] A. M. Bryan, L. M. Santino, Y. Lu, S. Acharya and J. M. D'Arcy, *Chem. Mater.* **2016**, 28, 5989.
- [293] X. Mu, D. Wang, F. Du, G. Chen, C. Wang, Y. Wei, Y. Gogotsi, Y. Gao and Y. Dall'Agnesse, *Adv. Funct. Mater.* **2019**, 29.
- [294] C. Zhan, M. Naguib, M. Lukatskaya, P. R. C. Kent, Y. Gogotsi and D. E. Jiang, *J Phys Chem Lett* **2018**, 9, 1223.
- [295] M. Seredych, C. E. Shuck, D. Pinto, M. Alhabeab, E. Precetti, G. Deysher, B. Anasori, N. Kurra and Y. Gogotsi, *Chem. Mater.* **2019**, 31, 3324.
- [296] C. Hao, B. Yang, F. Wen, J. Xiang, L. Li, W. Wang, Z. Zeng, B. Xu, Z. Zhao, Z. Liu and Y. Tian, *Adv. Mater.* **2016**, 28, 3194.
- [297] Y. Tian, W. Que, Y. Luo, C. Yang, X. Yin and L. B. Kong, *J. Mater. Chem. A* **2019**, 7, 5416.
- [298] J. Tang, T. S. Mathis, N. Kurra, A. Sarycheva, X. Xiao, M. N. Hedhili, Q. Jiang, H. N. Alshareef, B. Xu, F. Pan and Y. Gogotsi, *Angew. Chem. Int. Ed. Engl.* **2019**, 58, 17849.
- [299] X. Zhao, D. E. Holta, Z. Tan, J.-H. Oh, I. J. Echols, M. Anas, H. Cao, J. L. Lutkenhaus, M. Radovic and M. J. Green, *ACS Applied Nano Materials* **2020**, 3, 10578.
- [300] X. Zhao, A. Vashisth, E. Prehn, W. Sun, S. A. Shah, T. Habib, Y. Chen, Z. Tan, J. L. Lutkenhaus, M. Radovic and M. J. Green, *Matter* **2019**, 1, 513.
- [301] S. Célérier, S. Hurand, C. Garnero, S. Morisset, M. Benchakar, A. Habrioux, P. Chartier, V. Mauchamp, N. Findling, B. Lanson and E. Ferrage, *Chem. Mater.* **2018**, 31, 454.
- [302] P. Simon and Y. Gogotsi, *Joule* **2022**, 6, 28.
- [303] Y. Tian, C. Yang, Y. Luo, H. Zhao, Y. Du, L. B. Kong and W. Que, *ACS Applied Energy Materials* **2020**, 3, 5006.
- [304] N. Shpigel, A. Chakraborty, F. Malchik, G. Bergman, A. Nimkar, B. Gavriel, M. Turgeman, C. N. Hong, M. R. Lukatskaya, M. D. Levi, Y. Gogotsi, D. T. Major and D. Aurbach, *J. Am. Chem. Soc.* **2021**, 143, 12552.



- [305] Z. Wang, X. Chu, Z. Xu, H. Su, C. Yan, F. Liu, B. Gu, H. Huang, D. Xiong, H. Zhang, W. Deng, H. Zhang and W. Yang, *J. Mater. Chem. A* **2019**, *7*, 8633.
- [306] Y. Tian, B. Que, Y. Luo, M. Ju, Y. Tang, X. Lou, Z. Chen and W. Que, *J. Power Sources* **2021**, 495.